DIEGO ALEXIS ARAGÓN SOTELO | Control methods and stability analysis of electricity networks strongly dominated by electronic power converters

Mondragon Unibertsitatea

**DOCTORAL THESIS**

# CONTROL METHODS AND STABILITY ANALYSIS OF ELECTRICITY NETWORKS STRONGLY DOMINATED BY ELECTRONIC POWER CONVERTERS

**DIEGO ALEXIS ARAGÓN SOTELO | Arrasate-Mondragón, 2023**



*Dissertation*

# Control methods and stability analysis of electricity networks strongly dominated by power electronic converters

**Diego Alexis Aragón Sotelo**

Mondragon Goi Eskola Politeknikoa
Electronics and Computing Department

Arrasate-Mondragón, 12th December 2022



# Control methods and stability analysis of electricity networks strongly dominated by power electronic converters

Diego Alexis Aragón Sotelo

Supervisors:

Dr. Jon Andoni Barrena, Dr. Salvador Ceballos and Dr. Eneko Unamuno
Electronics and Computing Department
Mondragon Unibertsitatea

*Submitted in partial fulfilment of the requirements*
*for the Degree of Doctor Philosophy under the program:*
*Applied Engineering*

**Thesis Committee:**
President: Dr. Oriol Gomis
Vocal: Dr. Jef Beerten
Vocal: Dr. Adolfo Anta
Vocal: Dra. Maider Santos
Secretary: Dr. Gonzalo Abad

Director: Dr. Jon Andoni Barrena
Co-director: Dr. Salvador Ceballos
Co-director: Dr. Eneko Unamuno

Arrasate-Mondragón, 12th December 2022

*Dedication*

*A mi familia, amigas y a la gente del "sur global".*

*To my family, friends and the "global south" people.*

*“ En nombre del desarrollo nos han empobrecido y nos han violentado. En nombre del desarrollo, esclavizaron a mis ancestros”*
Francia Márquez Mina

*“We have been impoverished and attacked in the name of development. In the name of development, they enslaved my ancestors”*
Francia Márquez Mina

# Abstract

Contemporary society faces significant energy challenges due to the accumulation of greenhouse gases in the atmosphere. This scenario has been driven mainly by the use of fossil fuels for energy generation, population growth and exponential technological development. In response, the scientific community has focused its efforts on reducing dependence on fossil fuels in the energy matrix. In this direction, new non-conventional energy sources, such as wind, solar photovoltaic, and geothermal, have been integrated into the power system.

The integration of such renewables into the electricity system is progressively replacing synchronous machine-based generation, resulting in a transformation of the electrical system. The reason is that most non-conventional renewables are connected to the grid via electronic converters, eliminating the rotating components of the system. Converters have the advantage of controlling the bi-directional power flow between the grid and the energy source, thereby reducing power losses and thus providing precise control of the non-conventional renewable sources. Conversely, the increasing integration of such renewables is causing new challenges for the system operation by manipulating the various system dynamics. Consequently, this transformation in the power system is leading to a reduction of the total mechanical inertia supplied by the rotating elements of the synchronous machines. Likewise, the fast converter dynamics means that the classical small and large signal stability studies based on phasor models do not represent the true behaviour of the converter-dominated networks. The reason is that the dynamics of the inverters interact with the grid's passive elements, i.e., transmission lines and loads— endangering the system's stability.

Inspired by these challenges, the main objective of this thesis is to analyse the stability and control of the electrical networks strictly dominated by the converters, ensuring their correct operation in terms of transient response and steady state, and avoiding adverse interactions between the converter and the grid. To achieve this objective, initially, a methodology for analysing small- and large-signal stability through accurate models of the inverter-dominated networks using electromagnetic models (EMT) is discussed. Subsequently, the grid-supporting control strategy called "Second-order filter-based inertia emulation (SOFIE)" is proposed to provide frequency support employing primary control, inertia emulation and oscillation damping. The SOFIE control is compared against the classical inertia emulation control in grid-supporting converters, demonstrating that the developed control solves several stability problems caused by the adverse interactions between the inverter controls and the LC resonances of the grid. It is worth mentioning that each of the control strategies developed in this thesis have been carefully designed to improve the stability limits of the power system, as well as to increase the number of converter services in the grid.

Among other contributions of this thesis, the small-signal stability based comparison of the various grid-forming control approaches under different network conditions is also highlighted. This class of converters demonstrate the need to improve the damping of power oscillations to increase the stability limits in stiff grids.

# Laburpena

Gaur egungo gizarteak energia-erronka handiak ditu atmosferan berotegi-efektuko gasak metatzen direlako. Eszenatoki hau energia sortzeko, biztanleriaren hazkunderako eta garapen teknologiko esponentzialerako erregai fosilen erabilerak bultzatu du batez ere. Horren harira, komunitate zientifikoak energia matrizean erregai fosilekiko menpekotasuna murrizteko ahaleginak bideratu ditu. Norabide horretan, energia-iturri ez-konbentzional berriak, hala nola eolikoa, eguzki fotovoltaikoa eta geotermikoa, sistema elektrikoan integratu dira.

Energia berriztagarri horiek sistema elektrikoan txertatzeak makinetan oinarritutako sorkuntza sinkronoa ordezkatzen ari da pixkanaka, sistema elektrikoaren eraldaketa eraginez. Arrazoia da berriztagarri ez-konbentzional gehienak sarera konektatzen direla bihurgailu elektronikoen bidez, sistemaren osagai birakariak ezabatuz. Bihurgailuek sarearen eta energia iturriaren arteko noranzko biko potentzia-fluxua kontrolatzeko abantaila dute, eta, horrela, potentzia-galerak murrizten dituzte eta, horrela, iturri berriztagarri ez-konbentzionalen kontrol zehatza eskaintzen dute. Aitzitik, berriztagarri horien gero eta integrazioa sistemaren funtzionamendurako erronka berriak eragiten ari da sistemaren dinamika ezberdinak manipulatuz. Ondorioz, potentzia-sistemaren eraldaketa honek makina sinkronoen elementu birakariek ematen duten inertzia mekaniko osoaren murrizketa dakar. Era berean, bihurgailu bizkorreko dinamikak esan nahi du fasore ereduetan oinarritutako seinale txiki eta handien egonkortasunaren azterketa klasikoek ez dutela bihurgailuek menperatutako sareen benetako portaera adierazten. Arrazoia da inbertsoreen dinamikak sareko elementu pasiboekin, hau da, transmisio-lerroekin eta kargarekin elkarreragiten duela— sistemaren egonkortasuna arriskuan jarriz.

Erronka hauek bultzatuta, tesi honen helburu nagusia bihurgailuek zorrozki nagusi diren sare elektrikoen egonkortasuna eta kontrola aztertzea da, haien funtzionamendu zuzena bermatuz erantzun iragankorrean eta egoera egonkorrean, eta bihurgailuaren eta bihurgailuaren arteko interakzio kaltegarriak saihestuz. sareta. Helburu hori lortzeko, hasiera batean, eredu elektromagnetikoak (EMT) erabiliz inbertsoreak nagusi diren sareen eredu zehatzen bidez seinale txiki eta handien egonkortasuna aztertzeko metodologia bat aztertzen da. Gerora, "Bigarren ordenako iragazkietan oinarritutako inertziaren emulazioa (SOFIE)"izeneko sarearen euskarriaren kontrol-estrategia proposatzen da, maiztasun-euskarria emateko, kontrol primarioa, inertziaren emulazioa eta oszilazio moteltzea erabiliz. SOFIE kontrola sarearen euskarria duten bihurgailuetan inertziaren emulazio kontrol klasikoarekin alderatzen da, garatutako kontrolak inbertsorearen kontrolen eta sarearen LC erresonantziaren arteko interakzio kaltegarriek eragindako egonkortasun-arazo batzuk konpontzen dituela frogatuz. Aipatzekoa da tesi honetan garatutako kontrol-estrategietako bakoitza arreta handiz diseinatu dela potentzia-sistemaren egonkortasun-mugak hobetzeko, baita sareko bihurgailuen zerbitzuen kopurua handitzeko ere.

Tesi honen beste ekarpen batzuen artean, sare-baldintza desberdinetan sareak eratzeko kontrol-ikuspegi ezberdinen arteko seinale txikian egonkortasunean oinarritutako konparaketa ere nabarmentzen da. Bihurgailu-klase honek potentzia-oszilazioen moteltzea hobetzeko beharra erakusten du sare zurrunetan egonkortasun-mugak handitzeko.

# Resumen

La sociedad contemporánea se enfrenta a importantes retos energéticos debido a la acumulación de gases de efecto invernadero en la atmósfera. Este escenario ha sido impulsado principalmente por el uso de combustibles fósiles para la generación de energía, el crecimiento de la población y el desarrollo tecnológico exponencial. Como respuesta, la comunidad científica ha centrado sus esfuerzos en reducir la dependencia de los combustibles fósiles en la matriz energética. En esta dirección, se han integrado en el sistema energético nuevas fuentes de energía no convencionales, como la eólica, la solar fotovoltaica y la geotérmica.

La integración de estas energías renovables en el sistema eléctrico está sustituyendo progresivamente a la generación basada en máquinas síncronas, lo que supone una transformación del sistema eléctrico. La razón es que la mayoría de las energías renovables no convencionales se conectan a la red a través de convertidores electrónicos, eliminando los componentes rotativos del sistema. Los convertidores tienen la ventaja de controlar el flujo de potencia bidireccional entre la red y la fuente de energía, reduciendo así las pérdidas de potencia y proporcionando un control preciso de las fuentes renovables no convencionales. A la inversa, la creciente integración de estas energías renovables está provocando nuevos retos en el funcionamiento del sistema al manipular las distintas dinámicas del mismo. En consecuencia, esta transformación del sistema de potencia está conduciendo a una reducción de la inercia mecánica total suministrada por los elementos giratorios de las máquinas síncronas. Asimismo, la rápida dinámica de los convertidores hace que los estudios clásicos de estabilidad de pequeña y gran señal basados en modelos fasoriales no representen el verdadero comportamiento de las redes dominadas por los convertidores. La razón es que la dinámica de los convertidores interactúa con los elementos pasivos de la red, es decir, las líneas de transmisión y las cargas— poniendo en peligro la estabilidad del sistema.

Inspirado en estos retos, el objetivo principal de esta tesis es analizar la estabilidad y el control de las redes eléctricas dominadas estrictamente por los convertidores, asegurando su correcto funcionamiento en términos de respuesta transitoria y estado estacionario, y evitando interacciones adversas entre el convertidor y la red. Para lograr este objetivo, inicialmente se discute una metodología para analizar la estabilidad de pequeña y gran señal mediante precisos modelos de las redes dominadas por los convertidores utilizando modelos electromagnéticos (EMT). Posteriormente, se propone la estrategia de control grid-following denominada 'Second-Order Filter Based Inertia Emulation (SOFIE)" para proporcionar apoyo a la frecuencia empleando el control primario, la emulación de inercia y la amortiguación de las oscilaciones. El control SOFIE se compara con el control clásico de emulación de inercia en convertidores grid-following, demostrando que el control desarrollado resuelve varios problemas de estabilidad causados por las interacciones adversas entre los controles del inversor y las resonancias LC de la red. Cabe destacar que cada una de las estrategias de control desarrolladas en esta tesis ha sido cuidadosamente diseñada para mejorar los límites de estabilidad del sistema de potencia, así como para aumentar el número de servicios del convertidor en la red.

Entre otras aportaciones de esta tesis, también se destaca la comparación basada en la estabilidad de pequeña señal de los distintos enfoques de control grid-forming en diferentes condiciones de red. Esta clase de convertidores demuestra la necesidad de mejorar la amortiguación de las oscilaciones de potencia para aumentar los límites de estabilidad en redes rígidas.

## Acknowledgement

Es imposible no empezar este texto sin recordar los momentos difíciles que han traído estos años de academia y pensar en todas las personas que ayudaron a que esta tesis llegara a buen término. Gracias a los bien llamados, Dr. Ceballos, Dr. Unamuno y Dr. Barrena por verme como un ser humano y no como un estudiante de doctorado. Gracias por el tiempo que se tomaron para asesorar mi tesis y siempre dar sus críticas objetivas a mi trabajo. De nuevo gracias al Dr. Salvador Ceballos, por darme la oportunidad de estar en su grupo de trabajo en Tecnalia; por responder a cada una de mis preguntas por básicas que fuera y por apoyarme en los modelos matemáticos que algunas veces no lograba obtener. Siento que, de estos cuatro años de reuniones semanales, me llevo a tres amigos y colegas para la vida.

Gracias a la familia Boyacá —familia nuclear— que durante los últimos dos años han decidió romper un poco sus dinámicas, para incluirme, compartiendo cada uno de sus momentos conmigo. Entre estos, gracias a Nicolás y Arturo, mis amigos que me han enseñado la dignidad de vivir lejos de casa y a ser un adulto más funcional. Gracias por esas conversaciones políticas, psicológicas y personales que han iluminado mi ser político. Estos dos años no habrían sido lo mismo sin nuestras fiestas.

Como dije antes, este trabajo no ha sido sencillo. Más allá de dedicar cientos de horas de simulación, análisis, escritura e implementación en tiempo real (implementación que literalmente me saco lágrimas). La parte más difícil ha sido lograr mantener la constancia y dedicación sin perder el ánimo, aun en los momentos más difíciles. Esto ha sido posible gracias al apoyo incondicional brindado por mis amigas. Ellas que siempre estuvieron disponibles para "maternarme"; mediante una conversación telefónica, escuchando mis constantes quejas, mis crisis de ansiedad y mis problemas relacionados con el desarraigo. Es por eso que siento que a cada una de ellas debo darles una merecida mención en este trabajo.

Gracias a la filósofa, mamerta y feminista Carolina Camacho. Mujer que durante estos cuatro años ha compartido cada uno de sus días conmigo, pese a la distancia y a las diferencias horarias. Gracias por el amor incondicional que nos brindamos.

A Johanna Florián —mujer y amiga incansable— por esos golpes que siempre se nos fueron al piso y por ayudarnos mutuamente a construirnos como actores politicos. Gracias a mi comandante Tfarrah —ideóloga política de mi organización y autora de "Devenir Seiba"— que entre más insultos que risas, logró ganarse un espacio gigante en mi corazón sudaka. Gracias al Dr. Andrés Cortés por ser mi amigo y compañero de doctorado; nos llevaremos estos años de convivencia en Bilbao para la vida. Así mismo, a mis amigas residentes en Colombia que siempre estuvieron ahí, así fuera para ir a tomar un té: Daniela Cely, Paula Valderrama, Pauline Cabrejo, Alejandra Triana, Nicole Porto, Yennyfer León, Lina Barbosa, Lina Bajonero, Juliana Padilla, Lorena Valero y Tatiana Muñoz. Gracias porque siempre hicieron que volver a mi casa valiera la pena.

Finalmente, y no menos importante, gracias a mi padre Jorge Aragón, por heredarme la profesión y a mi madre Claudia Sotelo por estar todos los días de estos 6 años de migración pendiente de mí. Gracias a ellos, por ser esa llamada cuando ya no podía más y por ser siempre el estandarte para sostenerme. Gracias porque sin su esfuerzo, seguramente no hubiera logrado el primer doctorado de la familia. Gracias a mis hermanos y amigos naturales de la vida, Natali, Jorge y Camilo. Además, una mención especial a mi sobrina Sofía.

*Arakiruma.*

# Contents

# Nomenclature

ACE Area Control Error

AGC Automatic Generation Control

APC Active Power Control

CCM Component Connection Method

CSTEP Converter Stability Tool for Electric Power System

DAE Differential-Algebraic Equations

DC-SOFIE Direct current Second-Order Filter-Based Inertia Emulation

DSOFIE Dual Second-Order Filter-Based Inertia Emulation

dVOC Dispatchable Virtual Oscillator

EMT Electromagnetic Transient Models

ePLL Enhanced Phase-Locked Loop

FFR Fast Frequency Response

FOFIE First-Order Filter-Based Inertia Emulation

GFL Grid-Following Converter

GFM Grid-Forming Converter

GSC Grid-supporting Converter

HIL Hardware-in-the-Loop

HVDC High Voltage Direct Current

IE Inertia Emulation

MC Matching control

MPP Maximum Power Point

MTDC Multi-Termianl Direct Current

nRES Non-Conventional Renewable Sources

OPF Optimal Power Flow

PCC Point of Common Coupling

PLL Phase-Locked Loop

PV Solar Photovoltaic

PWM Pulse Width Modulator

QSS Quasi-Steady-State

RMS Phasor Models

RoCoF Rate of change of frequency

RoCoV Rate of change of voltage

RPC Reactive Power Control

SCR Short-Circuit Ratio

SFR Synchronous Reference Frame

SM Synchronous Machine

SME Synchronous Machine Emulation

SOF Second-Order Filter

SOFIE Second-Order Filter-Based Inertia Emulation

SOGI Second-Order Generalised Integrators

SV Synchronverter

SVPWM Space Vector Modulation

VCVSM Voltage Controlled Virtual Synchronous Machine

VSC Voltage Source Converter

# Chapter 1

# Introduction

*This chapter describes the transformation of electricity systems due to the massive integration of non-conventional renewable energies and their main challenges at the analysis, control and operation levels. Moreover, it describes the main objectives and contributions of this thesis.*

## 1.1 Background

The economic growth and the population increase over the last 30 years have led to a growing electric energy consumption reaching 28214 TWh/yr in 2021 [1], and the International Renewable Energy Agency (IRENA) estimates that more than 55000 TWh/year will be needed by 2030 [2]. An essential share of this energy is produced nowadays by conventional fossil fuel-based generation systems, which are the major sources of carbon emissions in the atmosphere [2]. Consequently, the average earth's surface temperature has risen by 1.2ºC compared to the pre-industrial period of 1880-1900 [2]. Scientists are investigating ways to lessen the emission of greenhouse gases and prevent the devastating consequences of a future global temperature rise. One way to reduce these emissions is to replace conventional fossil fuel-based energy sources with renewable technologies such as wind, solar photovoltaic (PV), and geothermal [3]. In this sense, renewable energies have experienced a meteoric development in the electricity sector, and now generate 25% energy to cover the demand. It is estimated that by 2050, renewable energy generation will account for 86% of the total power generation [2]. Non-conventional renewable energy sources (nRES), such as PV and wind power, are expected to see an increase in installed capacity of between eight and thirteen times; covering 60% of the power consumption, as shown in Figure 1.1.

### 1.1.1 Transformation of electrical power systems

Traditional power systems are designed to reliably and efficiently meet the requirements established by the electricity demand. For several decades, electricity has been produced by

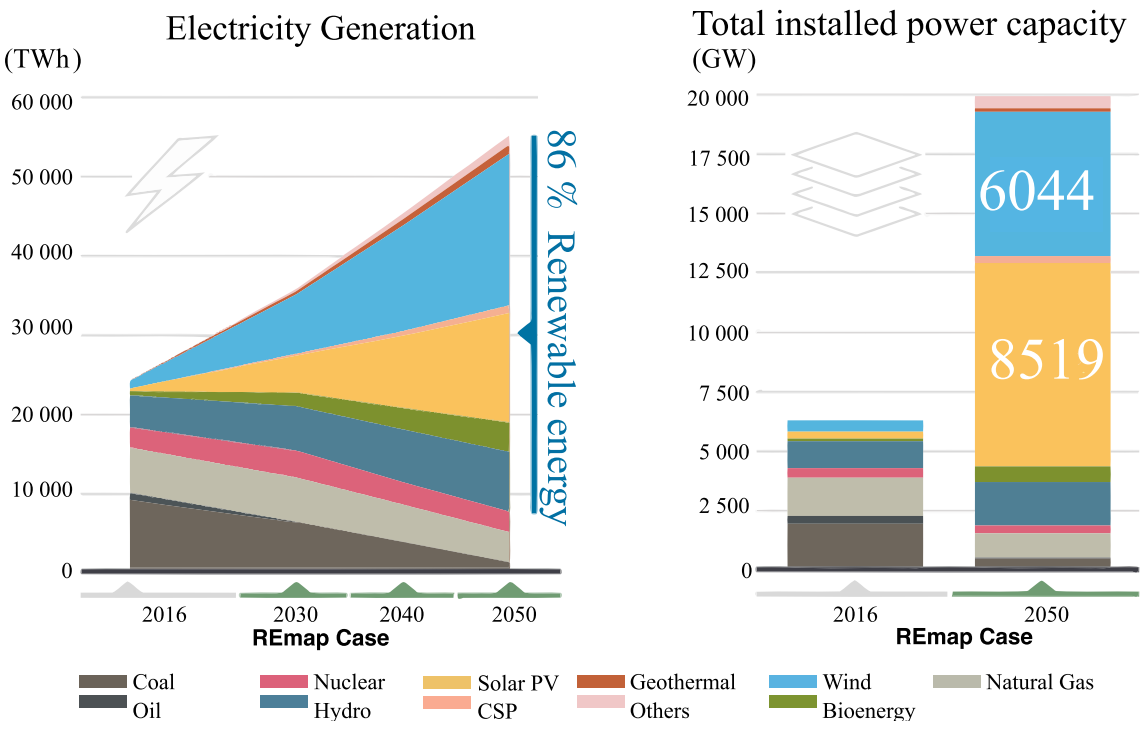


**Figure 1.1:** Electricity generation mix (TWh) and power generation installed capacity (GW) by fuel, REmap Case, 2016-2050 [2].

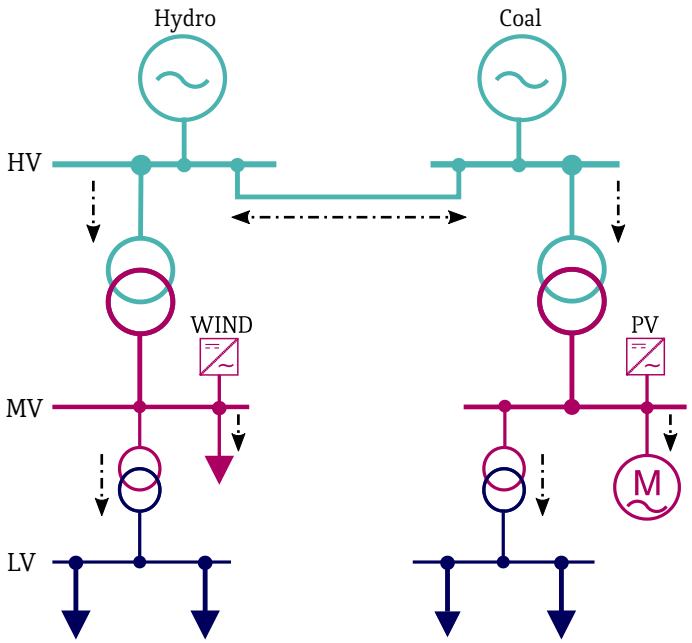


**Figure 1.2:** One-line diagram of a classical power system.

large fossil fuels, and conventional renewables energies such as hydro-power are interconnected by long-distance high-voltage transmission lines and distributed to the consumers via medium and low-voltage lines, as shown in Fig. 1.2. In this so-called "top-down" scenario, the energy flows in a single direction, from power plants to industrial, residential, and commercial consumers. Each stage of the electricity system is carefully monitored by the system operators, ensuring that the grid is at a safe operating point and maintaining the balance between generation and demand.

Power generation via fossil fuels is considered the primary source of carbon emissions, raising global concern over the worsening climate situation in recent years. A paradigm shift in energy production from conventional sources to renewables is therefore necessary [4]. The use of renewable generation sources such as solar and wind is considered one of the viable alternatives to curb carbon emissions and increase the reliability, sustainability and efficiency of the electricity system.

One of the main advantages of nRES integration is its versatility —most of the nRES are connected to the grid via power electronic converters, creating the new converter-dominated grids, as shown in Fig 1.3. This new power system has several benefits, such as making it possible to manage bi-directional power flows, reducing energy losses in the transmission and distribution areas, accurate active and reactive power control, or creating ac/dc island-type networks [5, 6]. Moreover, this new electricity system will enable consumers to interact with the electricity market through demand management plans easily, avoiding peaks in the daily load curve and generating new revenue streams [7].

However, the massive integration of nRES also brings new operational challenges due to the uncertainty of their daily power variation. For instance, wind and PV farms, whose generation depends on weather conditions, are not dispatchable by tertiary control [4]. In the case of wind farms, their generation fluctuates throughout the day, although their highest power ramps tend to occur at night and during intense weather conditions. On the other hand, PV

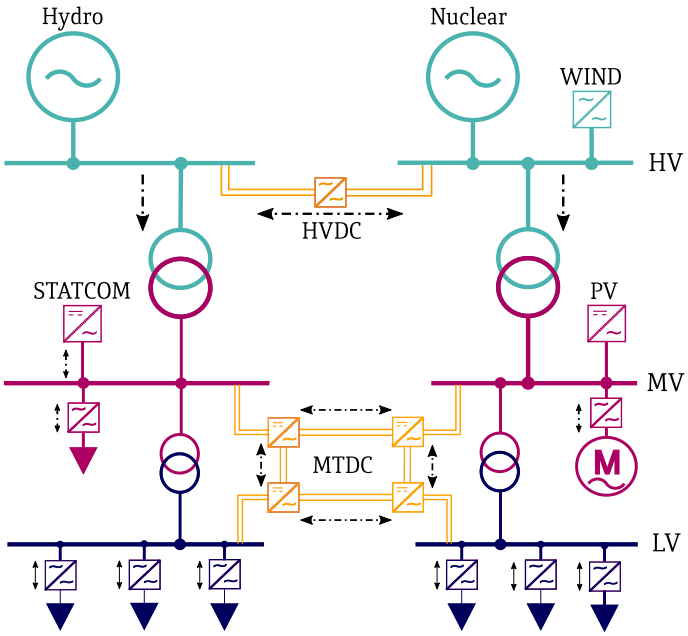


**Figure 1.3:** Electrical system based on electronic power converters.

has a behaviour characterised by the daily solar curve, whereas they do not produce energy at night. In this sense, the use of batteries is necessary to ensure the dispatch of the nRES [4]. In literature, various researchers propose sophisticated algorithms that predict weather conditions to manage reserves in tertiary control [8–10].

Beyond the challenges in operation and dispatch, there are also issues of stability and control of these new converter-dominated networks. To achieve a safe transition between the traditional electricity system to converter-based grids, a combination of the physical and control characteristics of the traditional synchronous machine-based power system and the power electronic converter-based power system is necessary.

In some countries, the massive integration of converters into the grid is already a reality today, achieving scenarios with considerable participation of nRES. The Texas power system operated by ERCOT, for instance, has a total generation capacity of approximately 86,000 MW, of which 20 % is wind energy. On average, wind energy supplies 15% of the state's demand; however, there have been occasional instances when it has provided up to 54 % of the total power [11]. The Irish system includes 5,585 MW of wind power that produced 36.3 % of the nation's energy in 2020, making it one of the greatest wind power penetration rates in the world [12]. The Australian electricity system, operated by AEMO, is recognised as being composed of several interconnected "energy islands" with an installed generating capacity of 53,535 MW, of which 45 % is wind and PV. Under specific weather and load conditions, the system has experienced instantaneous maximums of 119 % for wind and 38 % for PV [13]. However, this massive integration of nRES comes at a price. In 2016, the Australian electricity system suffered the first blackout provoked by the massive integration of renewables. This event was produced by two tornadoes that affected southern Australia, with winds of up to 160 mph that knocked down several 275 kV towers. The voltage transient generated by the disconnection of the lines activated the protections of various wind farms, causing a power imbalance of 456 MW [14]. The official report suggests that the sensitive voltage control of some wind farms caused their rapid disconnection and sudden frequency loss [13]. The

Australian case is just one example of the complexity of operating electricity grids with intense nRES penetration. Several authors have described the challenges of managing these kind of grids [4, 15].

To ensure the correct operation of the systems dominated by the electronic inverters and their friendly interaction with synchronous machines, classical control and operation techniques must be re-examined, modified and rethought to meet the technical requirements and new challenges presented by inverter-based generation systems. In this context, several projects propose to study control systems for integrating converters into the grid. The Massive InteGRATion of power Electronics devices (MIGRATE)[1], for instance, presents several control strategies to achieve 100 % converter-dominated grids. In addition, it offers new protection schemes, power quality studies and redefines stability studies. The RE-SERVE project[2] focuses on the redefinition of the control, operation and management of the European electricity system composed of 100 % renewables. One of its most important contributions relates to defining new grid codes. In the Basque Country, the Road2DC project[3] dealt with the development of mathematical tools for the analysis of hybrid ac/dc networks with a high penetration of converters. These projects exemplify how the scientific community has responded to operation, stability, electrical protection and power quality challenges.

The extensive integration of nRES connected to the grid through electronic converters raises many challenges, some of which are addressed in this thesis:

### Inertia and rate of change of frequency

In ac power systems, frequency is physically related to active power; therefore, it is the variable used to ensure the balance between energy generation and load. In this sense, the frequency must be within permissible limits to balance supply and demand. Over-frequency and under-frequency events may cause load shedding and generator tripping and sometimes cause severe outages, thereby risking the system's stability.

When a power imbalance occurs at a power system, the hierarchical control, composed of various levels of regulation, is activated to return the grid frequency to a steady state.

Figure 1.4 shows how frequency is regulated in a conventional power system when an increased load occurs. Thanks to the rotating parts of synchronous machines, the first response they give is to release the kinetic energy stored in the ratating mass (including the rotor and turbine) to opposite to frequency deviation. This phenomenon is called an inertial response, and its duration depends on the inertia of each SM and the magnitude of the perturbation. Simultaneously, to compensate for the change in the grid frequency, the primary control increases or decreases the power of the primary source to regulate the rotation speed of the turbine coupled to the shaft of the SM, thereby achieving a new steady-state operation point. It is worth noting that the primary control has a delay caused by the governor drives, which prevents it from acting instantaneously in the event of a frequency disturbance. Thus, a high amount of inertia will lead to a smooth rate of frequency of change (RoCoF), compensating for the governor's delay and avoiding a strong minimum frequency point (also known as Nadir), as shown in Fig. 1.4.

After the primary control achieves the steady-state regime, a slight deviation in frequency ($\Delta\omega$) remains due to the governor's static response. The secondary control assigns new power

[1] https://www.h2020-migrate.eu
[2] http://www.re-serve.eu
[3] https://www.mondragon.edu/en/-/concesion-del-proyecto-road2dc

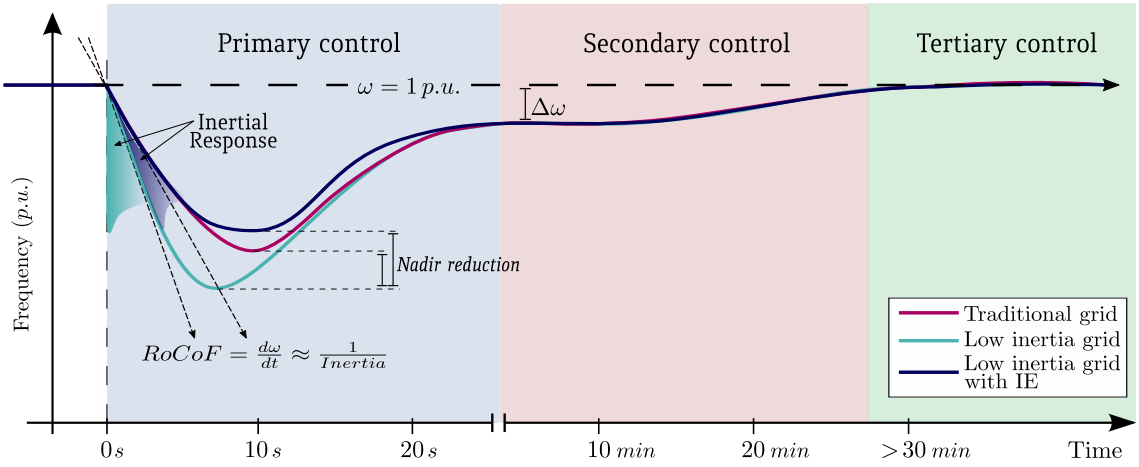


**Figure 1.4:** Involvement of inherent inertia and hierarchical control in frequency regulation of the converter-dominated grids.

references to the generators to eliminate the steady-state error left by the primary control. In large power systems, this work is performed by an integrated platform called "automatic generation control" (AGC), keeping the frequency and inter-area exchange within the set-point value by reducing the area control error (ACE). The secondary control is much slower than the governor's action and can take up to 15 to 30 minutes.

The tertiary control is the last process in the system frequency regulation; this control is several times slower than the primary and secondary control. Tertiary control is responsible for economic dispatch through optimal power flow (OPF), managing reserves, minimising operating costs, and fulfilling system operating constraints [16]. Power systems in many parts of the world correspond to a liberal market of buying and selling energy transactions. In the market structure, the tertiary control is responsible for adjusting the operating point according to the electricity market, guaranteeing the reserves of the primary control and the optimal dispatch of the secondary control [16].

As mentioned above, the classical generation systems based on rotating electrical machines are gradually displaced by non-conventional renewable energies connected to the network through power electronic converters, reducing the mechanical inertia and degrading the system stability [17]. The reason is that most grid-connected converters today are equipped with grid-following (GFL) controls, which are aimed, e.g. at maximising the energy extraction from nRES, but do not provide frequency support [18]. In Figure 1.4, the "Low inertia grid" case depicts the frequency behaviour in the event of a power imbalance; this scenario exhibits a rapid change in frequency as well as a pronounced Nadir, which could jeopardise the stability of the system [17].

Today, the problem of inertia reduction by nRES integration is manageable in large electrical systems such as the continental European electricity grid. However, in island-type power systems, as the Irish electrical system, where generation from nRES has begun to replace synchronous machines in high percentages, the loss of mechanical inertia considerably increases the risk of instabilities. Therefore, in this case, the system operator has been forced to modify the network code to allow the system to work with higher RoCoF values than usually allowed and to propose new stability studies with these new scenarios [17].

Besides, new converter control techniques have also been proposed to provide frequency

support. For instance, the British grid operator takes advantage of the invester's fast dynamics to respond quickly to frequency disturbances through primary regulation. To this end, they have proposed a package of faster-acting frequency response services composed of regulators and modifications to the grid code. It will allow the grid operator to guarantee the system's response to small and large power deviations and additional control for operating post-fault in response to significant frequency disturbances[4].

Developing such fast-frequency response and inertia emulation techniques is only one step towards the correct operation of converter-dominated electrical systems because it is necessary to include the primary energy source (wind, PV, among others), as most studies assume it is an ideal battery [20]. Regarding the transmission system, it is essential to provide HVDC and MTDC links with ancillary services that provide frequency support to improve the stability margins in networks [21].

To improve the frequency behaviour of converter-dominated grids, this thesis will address the study of different inertia emulation and fast-frequency response techniques, comparing several approaches proposed in the literature. Subsequently, several new inertia emulation methods are proposed to improve the converter's inertial response and increase the power system's stability limits.

### Adverse system interactions

Adverse interactions are undesired responses produced by the mutual action between the control dynamics responsible for maintaining the grid's frequency and voltage with other system elements. These adverse interactions are well described by the time scale separation presented in Figure 1.5. In a traditional power system, the interactions are given by the coupling between the synchronous machines, turbines and their voltage and frequency controls, which have response times around $50\,ms$ and $10\,s$, respectively. These interactions have been extensively investigated in several research studies [22–24]. Considering these dynamics, SM-based electrical systems are usually analysed using phasor models (also known as RMS models). These analyses are based only on electromechanical dynamics and assume the electromagnetic properties of transmission lines and loads as algebraic elements. RMS models have enabled the system's real-time operation, thanks to the considerable reduction in computational time.

The connection of converters to the network introduces fast dynamics that make the analysis of the system's stability more complex. The controller and filter of a given converter can interact with the controllers and filters of the adjacent ones and/or with the rest of the electrical elements of the grid, such as transmission lines or reactive compensators, among others [25]. These events lead to sub-synchronous control interactions and super-synchronous harmonic interactions that span over the grid, becoming more critical as the number of converters increases [25]. Simulations based on RMS are insufficient to assess the stability of power-converter-dominated grids because they do not consider the passive components of the system, as they are modelled as quasi-static elements. For this reason, the focus has shifted to using electromagnetic transient (EMT) models to study fast dynamics in converter-dominated

[4]https://theenergyst.com/national-grid-outlines-future-of-frequency-response/. Another solution to improve the RoCoF is to use inertia emulation technologies to maintain network inertia. These approaches are based on emulating the behaviour of the synchronous machine under power imbalances, supplying the network with synthetic inertia and increasing the RoCoF and the Nadir in low inertia grids, as shown in Figure 1.4 case—"Low inertia grid with IE". A practical example is the Australian electricity system that implemented IE from battery energy storage systems, achieving a 31% share in ancillary services [19].

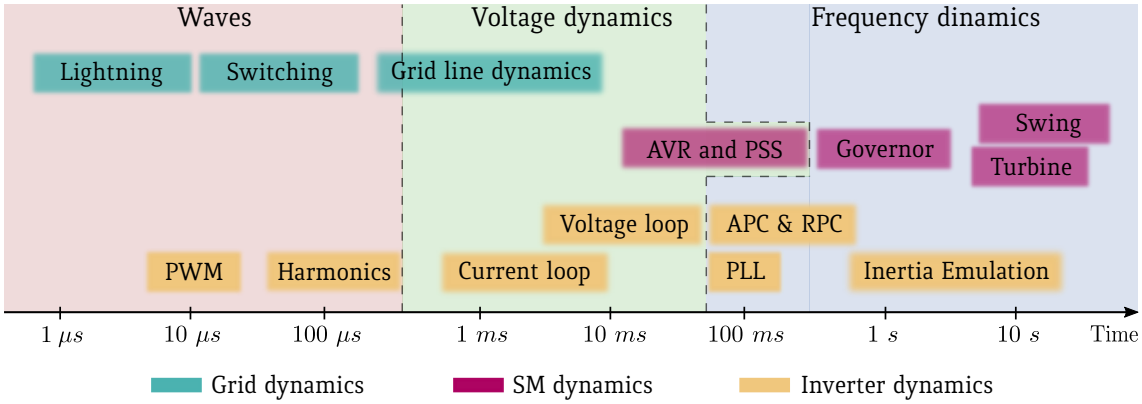


**Figure 1.5:** Timescales separation in a low inertia system [25].

grids. The Australian electricity market operator and the national grid in Great Britain have developed complete EMT models of the grid sections with high participation of converters to study system stability [26]. Nevertheless, implementing large EMT models drastically increases the computational time to solve the algebraic differential equations that describe the system performance—complicating the real-time monitoring of the system.

To address this challenge, the thesis describes a formulation to perform a small-signal stability analysis of converter-dominated power networks that does not neglect electromagnetic oscillatory modes as RMS-based approaches do. The proposed method is used to compare the dynamic operation of some of the best-known grid-forming techniques and to characterise the impact of inner loops, synchronisation methods and frequency support technologies on low inertia power systems.

## 1.2 Goals of the Thesis

Inspired by the previous challenges, this thesis puts the focus on the stability of low-inertia converter-dominated power grids as a way to i) ensure their operation in terms of transient and steady-state response and ii) to determine accurately the dynamic interactions that take place between the converters and the grid. More concisely, the objectives of the thesis can be summarised as:

**O**1. Development of analytical techniques based on EMT models to characterise adverse interactions produced by the integration of converters in the electricity grid.

**O**2. Identify and analyse the small-signal dynamics of different inertia emulation philosophies based on grid-forming and grid-supporting control.

**O**3. Development of new control techniques to provide frequency support to the power grid.

## 1.3 List of Contributions

The main research outcomes of the thesis have been published or are being considered for publication in the following journals:

### Journal Papers

J1. D. Serrano-Jiménez, E. Unamuno, A. Gil-de-Muro, D.A. Aragon, S. Ceballos, J.A. Barrena, "Stability tool for electric power systems with a high penetration of electronic power converters", *Electric Power Systems Research, Volume 210, 2022*, DOI://doi.org/10.1016/j.epsr.2022.108115.

J2. D. Aragon, E. Unamuno, S. Ceballos, and J. Barrena, "Comparative small-signal evaluation of advanced grid-forming control techniques," *Electric Power Systems Research, vol. 211, p. 108154, 2022*. DOI://doi.org/10.1016/j.epsr.2022.108154.

J3. D. Aragon, E. Unamuno, A. Gil-de-Muro, S. Ceballos, and J. Barrena, "Second-order filter-based inertia emulation (SOFIE) for low inertia power systems—Part 1: Principles and Equivalence with Synchronous Machines," *IEEE Transaction on power delivery,* ***Under Review***.

J4. D. Aragon, E. Unamuno, A. Gil-de-Muro, S. Ceballos, and J. Barrena, "Second-order filter-based inertia emulation (SOFIE) for low inertia power systems—Part 2: Analysis and Comparative Evaluation," *IEEE Transaction on power delivery,* ***Under Review***.

J5. D. Aragon, E. Unamuno, A. Khan, S. Ceballos, and J. Barrena, "Dual second-order filter-based inertia emulation (DSOFIE) for interlinking converters in low inertia power systems," ***In ellaboration***.

## 1.4 Document Outline

The thesis structure is highlighted in Figure 1.6, illustrating how objectives and the proposed contributions are related to each chapter.

**Chapter 2** provides a brief state-of-the-art overview of the main techniques for primary and low-level control of grid-connected converters. These techniques are classified according to their synchronisation method and the services they provide to the network as grid-following, grid-supporting and grid-forming. Additionally, a literature review demonstrates the technical differences between grid-supporting and grid-forming inertia emulation controls. The chapter leads to the conclusion that both approaches must be developed to guarantee the stability margins of converter-dominated grids.

**Chapter 3** presents a MATLAB-based software tool called CSTEP (Converter Stability Tool for Electric Power Systems), jointly designed by Mondragon Unibertsitatea and Tecnalia. This software uses detailed EMT modelling to construct and analyse converter-dominated power systems' small- and large-signal stability. Comparing CSTEP against commercial software (that uses RMS models) demonstrates the need for EMT modelling in converter-dominated grids. CSTEP is used in the rest of the chapters to ensure the accuracy of the findings/results while considering the need for EMT model-based studies.

**Chapter 4** aims to benchmark the small-signal properties of grid-forming controls, taking into account the internal voltage and current loops. To give a general approach, this chapter discusses the behaviour of the techniques studied under different grid types and conditions. For that purpose, the GFM converter is connected to an equivalent low-inertia grid model capable of emulating different levels of aggregated inertia, damping, and line impedances. Hardware-in-the-loop (HIL) simulations are further presented to validate the results obtained.

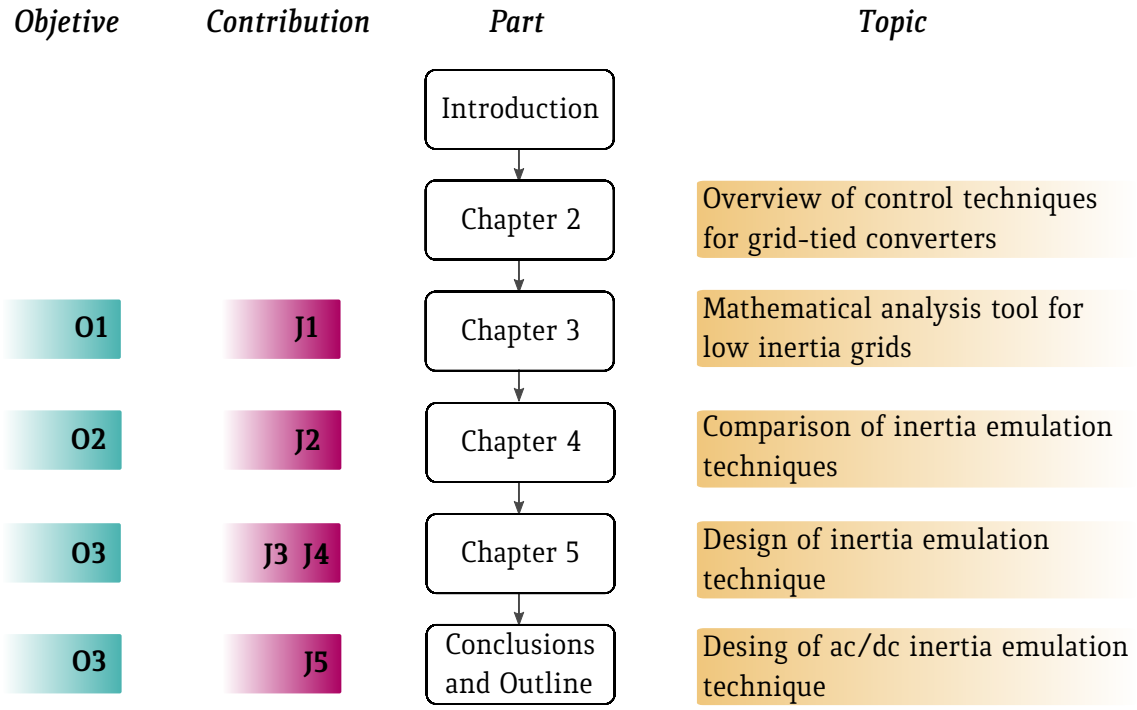


**Figure 1.6:** Structure of the chapters of the thesis and their relation to the specific objectives and main contributions.

**Chapter 5** introduces a control philosophy based on the use of second-order filters to develop new grid-supporting techniques. Based on the proposed scheme, three new Second-Order Filter-based Inertia Emulation (SOFIE) techniques, that overcome the main stability issues caused by their conventional counterparts, are derived. Their main feature is that they can accurately emulate the electromechanical behaviour of a synchronous machine by making minor modifications to the control structure of the grid-following and grid-supporting converter. A detailed comparison is done to demonstrate its superior performance over the classical emulation techniques (i.e., "First-order filter-based inertial emulation"). Finally, the study is validated using real-time simulations.

Finally, **Chapter 6** summarises the key findings and contributions of this thesis and presents lines for future work. Moreover, a preview of the topics that are currently being developed based on the innovations of this doctoral thesis is presented. The first topic is based on the development of an inertia emulation control for dc networks. While the second topic is based on an inertia emulation controller for HVDC and MTDC systems.

# Chapter 2

# Control strategies of grid tied-converters

*This chapter reviews the different control approaches for grid-connected converters, that is, grid-following, grid-supporting and grid-forming. It describes how these control approaches achieve synchronisation and load-sharing of the converter with the network. Moreover, it describes how this converter configuration will allow the converter to frequency support. Finally, a high-level comparison between grid-supporting and grid-forming control approaches is presented, to give a brief introduction to the contributions of this thesis on this issue.*

## 2.1 Introduction

The traditional top-down electricity system, characterised by an unidirectional power flow from generation plants to distribution and consumption centres, is an operation strategy concept that has been in place for more than a century. In the last two decades, however, this concept operation principle is being adapted caused by the massive integration of nRES into the power system. Emerging new technologies include distributed generation, energy storage system integration, microgrids, demand-side management or autonomous control based on artificial intelligence and communications. They are not only the interface for connecting nRES, but also for connecting ESS, electric vehicles, and even large hydroelectric power plants to increase their efficiency. Moreover, they are also used to improve the power quality of the system.

With the increase of converters on the grid, it has been necessary to develop more sophisticated control systems. Initially, methods involving communication in centralised or master/slave configuration were proposed for parallel converters that served e.g. as uninterruptible power systems. This way, the correct load-sharing, voltage and frequency stabilisation were achieved. In recent years, decentralised systems have emerged, eliminating the need for communication systems. Nonetheless, usually these type of techniques are less accurate in power-sharing, especially with non-linear loads. To overcome these drawbacks, methodologies based on virtual impedance and harmonic power-sharing have been proposed. Moreover, different droop control implementations have arisen to improve the transient response, such as voltage-current or angle droop.

The implementation of the classic droop control —originally designed on synchronous machines— in power electronic converters has been one of the significant advances in converter control systems recently. It allows decentralised power control, and has also helped in developing new converter control techniques on the grid, such as grid-forming approaches (GFM). Unlike grid-following (GFL) techniques, which synchronise with the grid using frequency estimators such as phase-locked or frequency-locked loops, droop-based GFM techniques do not require any synchronising algorithm and can establish the frequency and amplitude of the grid voltage. GFL controls were initially proposed to connect the nRES to the grid by assigning a power reference —usually provided by some kind of maximum power point tracking (MPPT) technique. Prior to the advent of GFM approaches, droop control was also incorporated into the classical GFL strategies to allow the converters to participate in the primary frequency regulation, resulting in the development of grid-supporting converters.

With the reduction of the mechanical inertia of the grid caused by the replacement of synchronous generation systems with nRES that make use of electronic converters, some of the most recent proposals are that converters not only emulate the primary response but also provide inertia and damping towards the grid as an synchronous machine (SM) does. In this regard, several synchronous machine emulation (SME) strategies have been designed in GFM converters to emulate the electromechanical behaviour of the synchronous machines, starting with the so called synchronverter and going through more complex implementations such as voltage-controlled virtual synchronous manchine (VCVSM) or the synchronous power control (SPC). Meanwhile, in GSC converters, first-order filter-based inertia emulation (FOFIE) is based on the swing equation to provide synthetic inertia. FOFIE control has been widely used in HVDC, MTDC, wind, and PV systems.

This chapter provides a brief overview of the control techniques used in grid-connected electronic converters. It begins with a description of synchronisation techniques for GFL and GSC converters. Next, it discusses GFM controls, which are classified into centralised tech-

niques based on communication, and decentralised techniques based on droop controls, followed by a brief overview of GFM techniques based on FFR and SME controls. Finally, a high-level comparison between the GSC and GFM approaches is presented based on the state–of–the–art and the contributions of this thesis.

## 2.2 Configuration of grid-connected converters

To address the challenges of converter-dominated grids, grid-tied inverters need to modify the configuration of their control loops. An example of this has been to equip the converter with the possibility of providing reactive power against voltage sags. In the same direction, the massive integration of power electronics has led to converters being equipped with new control loops to contribute to frequency regulation. For better illustration, in this thesis, voltage source converters (VSCs) are classified according to their control configuration, as shown in Fig. 2.1.

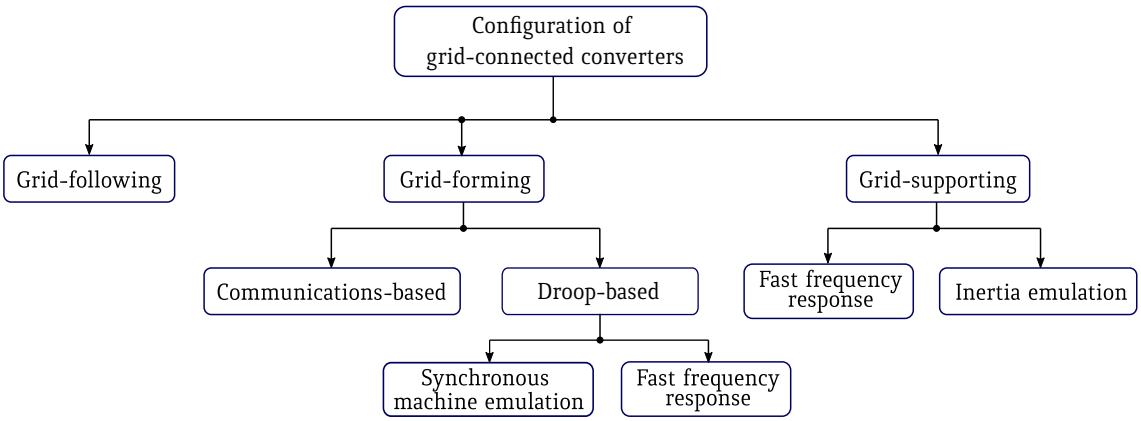


**Figure 2.1:** CSTEP structure.

### 2.2.1 Grid-following techniques

GFL strategies are the most common and well established control approaches for grid-connected converters. They are not intended to contribute to the inertial response or primary regulation but to provide active and reactive power to the electrical grid regardless of its frequency and voltage level. Therefore, they can be modelled as a current source with a high parallel output impedance. The power converters are suitable to work with other grid-following converters in grid-connected mode, and they have to be synchronised with the grid angle via a synchronisation algorithm such as a PLL [27]. Grid-following power converters exchange active and reactive power with the grid using various algorithms, such as maximum power point (MPP) or constant power supply/demand. Grid-following power converters cannot operate in island mode if there are no grid-forming units or a synchronous machine setting the voltage amplitude and frequency [28, 29].

Fig. 2.2a shows a simplified block diagram of a converter operating in grid-following mode, in which external loops are generally used for output power control, DC-link voltage control, and/or control of the current a the point of common coupling (PCC). The inner loop is usually composed of a current regulator that generates the internal voltage references for the pulse width modulator (PWM), depending on the current references set by the outer loop [30].

### Synchronisation methods in grid-following techniques

Grid-following control approaches must be synchronised with the grid voltage. Therefore, the phase angle, frequency and amplitude of the voltage need to be accurately estimated. Currently, the most used synchronisation technique is the so-called PLL, a control system that estimates the frequency, phase and magnitude with a precise way based on the instantaneous measurements of the phase voltage. Fig. 2.3 shows the diagram of the traditional synchronous reference frame PLL (SFR-PLL), where $v_{o_{abc}}$ is the voltage in ABC reference frame, $\omega_g$ is the estimated network frequency and $\theta_g$ is the estimate angle phase estimated. $\omega^*$ is the nominal frequency, $k_{p_{pll}}$ and $k_{i_{pll}}$ are the gains of the PI controller and $\omega_b$ is the base frequency in rad/s. The q-axis output of the $dq$-transformed voltages ($v_{o_q}$), which contains the phase error data, is passed through a PI controller that makes it null in steady-state. The PI controller output is the resultant estimated frequency error that is added to the nominal frequency, and the result is integrated to obtain the phase angle of the voltage.

PLLs play an important role in GFL converters as they are used to track the angle and frequency of the ac grid voltage. The angle estimated by the PLL is used in the current controller to synchronise the active and reactive components of the current with the grid voltage. Usually, PLL algorithms have a good performance in stiff grids where the voltage does not present significant disturbances in normal operating conditions. However, in weak networks, the voltage at the point of common coupling can be affected by the active and reactive currents

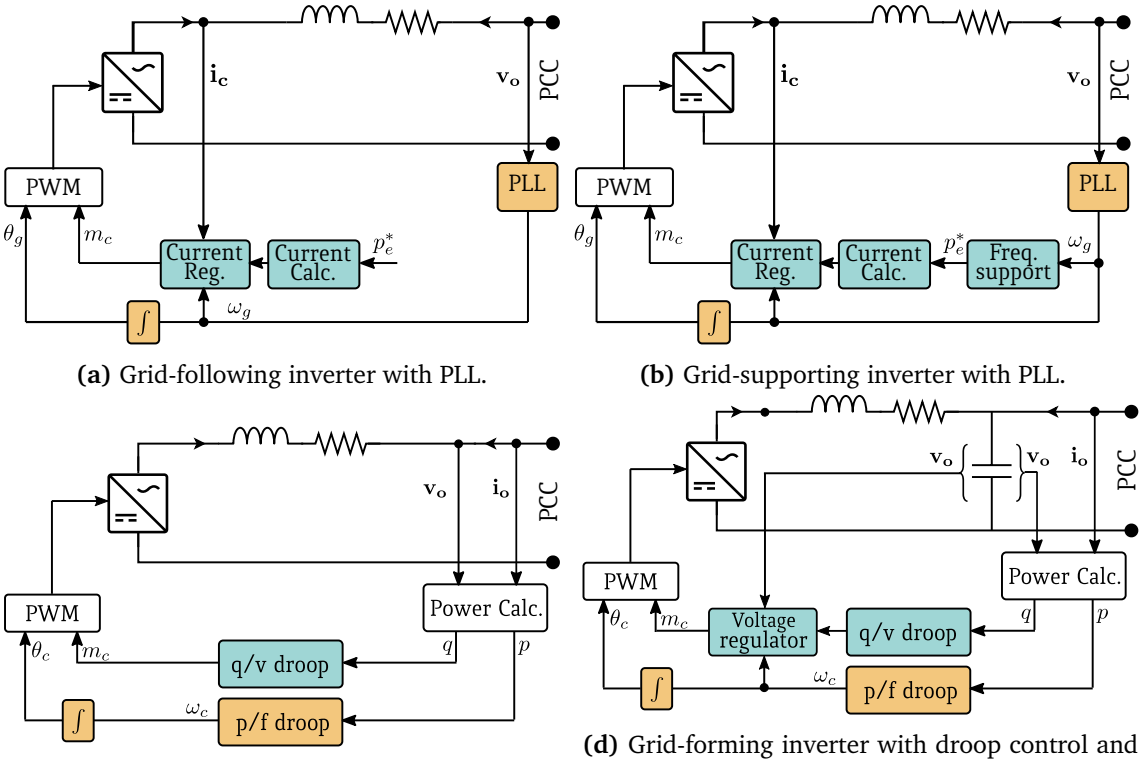


**(a)** Grid-following inverter with PLL.

**(b)** Grid-supporting inverter with PLL.

**(c)** Grid-forming inverter with droop control.

**(d)** Grid-forming inverter with droop control and inner loop.

**Figure 2.2:** Inverters and their control structures in synchronous $dq$ frame. (a) Grid-following inverter with PLL. (b) Grid-supporting inverter with PLL. (c) Grid-forming inverter with droop control. (d) Grid-forming inverter with droop control and inner loop.

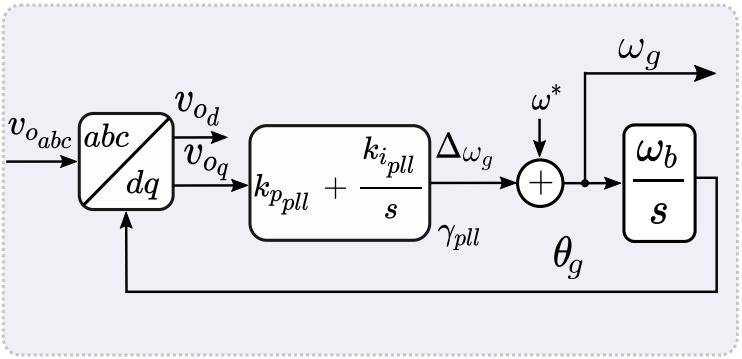


**Figure 2.3:** Diagram of conventional SRF-PLL

of the converter. This voltage perturbation is fed by the PLL back in the current control loops, which produces a change in the current that again modifies the voltage at the PCC. This positive feedback between the PLL, the current controller and the voltage, that takes place in weak grids can produce large voltage and current oscillations [31,32] or even system instabilities.

In recent years, various authors have developed more advanced three-phase PLLs. The majority of them to improve the dynamic behaviour [33–35], enhance the disturbance rejection capability of the conventional SFR-PLL [36,37] or optimise the PLL implementation using low-cost devices [38].

Among them, two of the most widespread advanced PLL techniques are those based on second-order generalised integrators (SOGI) [39] and on enhanced PLL (ePLL) [40]. In the SOGI-PLL, the conventional PLL structure is improved with a second-order generalised integrator that performs as a frequency-adaptive second-order filter providing an accurate estimation of the frequency and phase angle of the positive sequence voltage even under faulty grid conditions. On the other hand, the ePLL is a non-linear adaptive frequency synchronisation approach that provides a higher degree of immunity and insensitivity to noise, harmonics and unbalances of the input signal. It is suited for systems where the frequency has variations and noise.

### 2.2.2 Grid-supporting techniques

Grid-supporting control techniques are historically the first attempt to provide the converter with primary control, as an extension of grid-following control structures. Therefore, it retains the advantages of the classical GFL control structure based on the current regulator and PLL. To provide the frequency support, an additional external loop is added, as shown in Fig. 2.2b.

GSCs as well as GFLs, perform as current sources and are not capable of forming the grid by themselves, but they are an interesting control alternative because they can provide frequency support with minimal modifications in the original controller. Broadly speaking, GSCs can be categorised in two different groups: fast frequency response (FFR) and inertia emulation (IE).

#### Fast frequency response GSC techniques

Due to reduced inertia in the electric power system, the traditional primary response of synchronous generators may not may not be fast enough to maintain the system frequency

within tolerable ranges immediate after a power imbalance. Therefore, one of the most attractive solutions for frequency control in low inertia systems is to use the fast dynamics of VSC to respond in much shorter time frames against power imbalances.

Ref. [41] defines FFR as the controlled contribution of electrical torque from a unit which acts quickly to changes in frequency to counteract the effect of reduced inertia response. Several studies conclude that FFR [41–43] contributes to frequency regulation and reduces the frequency nadir. However, it can also excite adverse interactions between the frequency support loops and the transmission lines [25] that, if they are not properly considered during the desing phase of the controller, may deteriorate the system response.

Droop control based fast-frequency response is the most widely studied technique in grid-supporting converters, which is inspired from the traditional droop of synchronous machines. Its aims to regulate the grid frequency, avoid sharp drops, and reduce the frequency nadir. This is achieved by regulating the active power injected into the grid. The active power reference is calculated using a $p/f$ droop controller. Besides, a $v/q$ droop controller can be also used to regulate the amplitude of the voltage at the connection point. However, using this technique the RoCoF is not improved [**J**3].

### Inertia emulation

The European Network of Transmission System Operators (ENTSO-E) [44] defines synthetic inertia as "the facility provided by a power park module or HVDC system to replace the inertia effect of a synchronous power generation module to a prescribed level of performance". Therefore, the converter equipped with control techniques based on synthetic inertia must simulate the inertial response of the synchronous machine in the face of power imbalances and with the same time scales as a traditional generation station.

The inertia emulation technique for GSC converters is based on the swing equation of classical SMs [22]. The power set-point ($p_e^*$) is calculated from the grid frequency ($\omega_g$) estimated by a PLL, as follows:

$$p_e^* = -\frac{d\omega_g}{dt} 2H \tag{2.1}$$

where $H$ is the inertia constant.

Its main advantage is that it works as a SM in the case of power imbalances. Unlike grid-forming techniques based on synchronous machine emulation, the swing equation is used inversely in such a way that the electrical power reference is obtained from the grid frequency. However, that approach is prone to instabilities and noise from the PLL in a discrete system [45]. Thus, this technique is usually combined with a first-order filter with a cut-off frequency $\omega_n$ to limit the derivative and mitigate the noise. In this sense, this technique will be named first-order filter-based inertia emulation technique (FOFIE). Moreover, a droop controller with gain $k_\omega$ is often included to carry out the primary regulation. Considering these components, a FOFIE control can be described as:

$$p_e^*(s) = -2H \frac{\omega_n s}{s+\omega_n} \omega_g(s) + k_\omega (\omega^* - \omega_g(s)) + p^* \tag{2.2}$$

where $p^*$ is an external power set-point, and $\omega^*$ is the rated frequency.

FOFIE technique is a suitable approach to provide frequency support through the emulation of inertia and has been successfully applied, e.g. in wind farms [45,46], energy storage systems [47,48] or HVDC links [49,50].

### 2.2.3 Grid-forming techniques

Grid-forming techniques are a new family of control approaches that enable the converters to generate the voltage waveforms at the point of coupling. Therefore, GFM converters can work autonomously by establishing the amplitude and frequency of the ac voltage without the need of synchronous generators or additional grid-forming devices. This allows the converters to provide primary regulation to the network, thus improving the system's dynamic response against disturbances. In addition, other functions with high added value, such as load-sharing/drooping, black-start, virtual damping, inertial response and hierarchical frequency/voltage regulation [51] are also achieved.

Practical implementations of GFM converters have been traditionally used in UPS to provide grid support in island mode. However, more recently, GFM converters have been also integrated in battery energy storage systems and other applications such as type 4 wind turbines, PV plants, fuel cells, HVDC links and even controllable loads are also in the agenda [52].

Multiple grid-forming control approaches have been proposed in the literature which, broadly speaking, can be grouped into two categories as:

#### Communication based control

Grid-forming control based on communications has been used mainly in techniques such as master/slave, load sharing central or concentrated control [53, 54]. The main advantage is that precise power-sharing between each converter can be achieved. However, its main disadvantage is the increased costs and implementation of complex communication systems that decrease reliability indices and hinder grid expansion [55].

One of the most widely used communication techniques, "power lines communication", involves sending information through electrical network cables. It has some advantages, such as it provides greater reliability since it has fewer components and produces less interference compared to wireless technologies [56]. Nevertheless, it has some drawbacks, such as high cost and loss of signal quality in lines [56]. Alternatively, in recent years, wireless technology-based methods have also arisen. These methods can be classified according to the transmission distance. The cellular network is the most usual. It covers ranges of up to $50\,km$. In addition, the short-distance network that allows data processing at a maximum of $100\,m$ and the LPWAM with distances of up to $50\,km$ are other alternatives. These technologies have the problem of low data rates, high cost, and sensitivity to delays [56].

#### Droop-based grid-forming techniques

In a conventional power system, the generation has to respond automatically to power variations to ensure the balance between generation and load. In many power systems, coordination of all grid-forming units has been achieved through the implementation of active and reactive power droop-based regulators that only make use of the local frequency and voltage measurements [57]. Droop controllers have been widely used as the primary control to ensure load sharing between GFM converters and SMs in a plug-and-play manner. The main advantages of this method is its simple implementation, improved reliability as they do not require communications and fast response to power changes [58, 59].

Droop control was initially proposed in [60] as a proportional control of active power and frequency ($p/f$). It presents many modifications to adapt it to other variables or improve its

performance [61, 62]. Assuming an inductive network, the classic $p/f$ droop is given by:

$$\omega_c = \omega^* + k_\omega(p^* - p) \tag{2.3}$$

where $\omega^*$ is the frequency reference, $\omega_c$ is the frequency generated by the GFM, $p^*$ is the active power reference, $p$ is the measured active power and $k_\omega$ is the droop control gain that determines the steady-state power distribution in the grid.

Droop control has also been used to ensure the power-sharing of reactive power. Considering the relation between reactive power and voltage, the droop $q/v$ is given by:

$$v_c = \hat{v}^* + k_q(q^* - q) \tag{2.4}$$

where $v_c$ is the converter output voltage, $\hat{v}^*$ is the reference voltage amplitude, $k_q$ is the reactive power droop gain, and $q^*$ and $q$ are the reference and reactive power measurement, respectively.

However, several authors demonstrate low accuracy in ensuring reactive power-sharing [63, 68] because this approach is intended for purely inductive systems; In fact, when the system resistance becomes relevant, this approach is no longer valid. The reason is that as the ratio $R/X$ increases, so does the coupling between the $p/f$ and $q/v$ loops. Other droop approaches that improve transient response and communications-free power-sharing have been introduced to overcome these drawbacks, as shown in the table 2.1.

### Synchronous machine emulation techniques

SME techniques have gained relevance in recent years due to their ability to emulate inertia while maintaining the time scales of a traditional grid. These techniques integrate the mechanical model of the classical synchronous machine, i.e., the swing equation, into the converter control (see Fig. 2.4) as a way to provide damping and inertial response against power imbalances similar to a synchronous machine. Additionally, to eliminate the communication system, they added an active power control (APC) based on droop control to ensure power-sharing. Some of the most relevant techniques will be further analysed in Chapter 4.

An electrical model of the emulated SM and reactive power control (RPC) determines the voltage amplitude at the converter output terminals. The main difference between SME techniques concerning the real synchronous machine is that the delays caused by the governor, turbine and exciter can be avoided or modulated, thus improving the dynamics of the response.

One of the main features of SME techniques is that, as they emulate the behaviour of synchronous machines, the operation principles of the power system are not drastically modified, thus ensuring the converters interact adequately with the rest of the grid components.

**Table 2.1:** Comparison of droop-based power-sharing techniques [63]

| Droop | Cite | Implementation | Reactive power-sharing accuracy | Transient response |
|---|---|---|---|---|
| $p/f$-$q/v$ | [57, 60, 64, 65] | Easy | Inaccurate | Sluggish |
| $p/\delta$-$q/v$ | [66, 67] | Complex | Inaccurate | Sluggish |
| Virtual impedance droop | [68–71] | Easy | Accurate | Sluggish |
| Arctan $p/f$ - $q/v$ | [72] | Complex | Inaccurate | Sluggish |
| VI droop | [73] | Easy | Accurate | Improved |

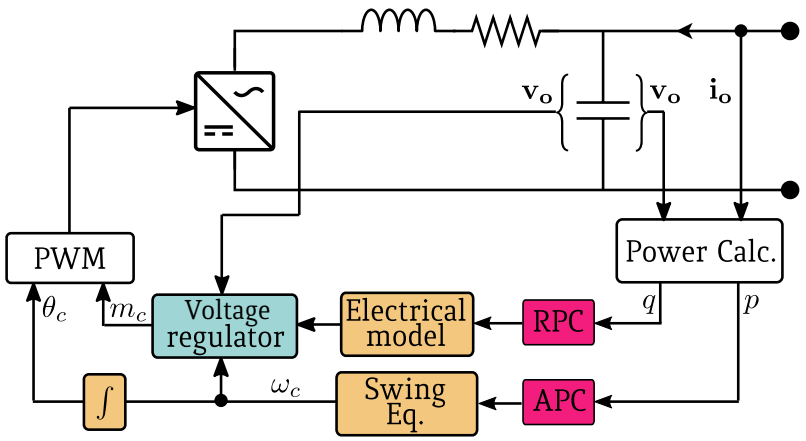


**Figure 2.4:** Overview of the converter configuration equipped with synchronous machine emulation technology

**Table 2.2:** Summary of different GFM control methods.

| Approach | Control strategy | Cite |
|---|---|---|
| SME | Voltage controlled virtual synchronous machine (VCVSM) | [74, 76–80] |
| | Current controlled virtual synchronous machine (CCVSM) | [74, 81, 82] |
| | Synchronverter (SV) | [83–87] |
| | Power synchronisation control (PSC) | [88–90] |
| | Synchronous power control (SPC) | [91–95] |
| FFR | Droop control | [96–98] |
| | Dispatchable virtual oscillator (dVOC) | [75, 99] |
| | Virtual oscillator control (VOC) | [100, 101] |
| | Matching control (MC) | [J2] |
| | Hybrid Angle Control (HAC) | [20] |

There are multiple SME implementations in the lieachines and the voltage-controlled virtual synchronous machines some of the most widely used approaches [74].

### Fast frequency response in grid-forming control

As in GSC techniques, FFR techniques in GFM approaches can respond quickly to power unbalances. However, in GFM techniques based on FFR, the converter has to ensure fast synchronisation with the grid to maintain system stability. These techniques also incorporate droop control as a strategy to ensure active power-sharing without communications. Although these control technologies are intended to provide fast synchronisation with the network, several authors use low-pass filters in the power loops to avoid suddenly set-point variations. The addition of such filters are used to maintain the time scales of the traditional power system [75], resulting in the possibility to deliver inertia to the network, as shown in section 4.5.

Table 2.2 gathers a compilation of various GFM techniques based on synchronous machine emulation and FFR.

## 2.3 Comparative analysis of GSC and GFM techniques

GFM and GSC techniques have recently emerged to provide mainly grid frequency support. Nevertheless, both control approaches exhibit significant differences concerning their implementation, synchronisation or the number of services they can provide towards the network. This subsection discusses the main differences between the two control philosophies and their limitations in aspects such as synchronisation, inertial response and damping of oscillations, which are fundamental aspects in determining the limits of stability and transient behaviour. Additionally, based on the differences and issues presented in the literature, the contributions of this doctoral thesis to these control structures are briefly described in compliance with objectives [**O**2] and [**O**3].

### 2.3.1 Synchronisation approaches

One of the most relevant differences between the GFM and GSC converters is their synchronisation method. GFMs are synchronised with the grid similar to classical grid-connected SMs by using the virtual shaft speed provided by the swing equation. GFL techniques, on the other hand, achieve their synchronisation by estimating the frequency of the network. In [102], the authors compare these synchronisation methods demonstrating their similarities. They indicate that GFM synchronisation methods, when matched with the power balance ($p \rightleftharpoons \omega$), can be assumed to be current following and voltage forming, as defined by the authors. In other words, by measuring the power at the PCC ($p = i_d\, v_d + i_q\, v_q$) of a balanced system and assuming that $v_d = 1$ is constant, while $v_q = 0$, the direct relationship between $i_d \rightleftharpoons \omega$, can be demonstrated. In contrast, PLL-based synchronisation techniques measure the grid voltage to estimate its frequency by forcing $v_q = 0$ through a PI regulator. Thus, the reactive power ($q = i_d\, v_q - i_q\, v_d$) is proportional to $v_q$ when $i_d$ is constant and $i_q = 0$. This means that $v_q \rightleftharpoons PLL$ is equivalent to $q \rightleftharpoons PLL$ [102]. Hence, PLL-synchronised converters can be assumed to be current-forming and voltage-following.

In light of the above, the synchronisation methods of the GFM and GSC techniques will be affected by the equivalent impedance at the PCC. On the one hand, as recently demonstrated, GFM converters are vulnerable to loss of stability in stiff grids due to low-frequency oscillations, as described in [102, 103]. To address these issues, chapter 4.5 discusses the importance of damping and virtual impedance management to improve the stability of GFM converters in strong networks. In contrast, PLL-synchronised converters have robust synchronisation in stiff networks due to smooth voltage fluctuations [102]. Nonetheless, as the equivalent inductance at the PCC increases (low short-circuit ratio (SCR)), the PLL begins to have difficulty accurately estimating the frequency owing to larger voltage oscillations [102]. In this sense, we consider that there is a need to compare both synchronisation approaches. Therefore, this work is carried out in chapters 4 and 5.

### 2.3.2 Inertia and virtual damping

As mentioned throughout this document, a central challenge of converter-dominated power systems is the need to provide inertia and virtual damping to ensure a smooth transient frequency control. Yet, not all SME implementations can contribute with damping to the grid due to the coupling between the droop gain and damping term (further discussed in chapter 4). Decoupling the virtual damping and constant droop is fundamental in transmission systems to ensure power-sharing and adequate steady-state frequency operation points; while

attenuating the oscillations of active power.

On the other hand, GSC techniques based solely on droop control (i.e., fast frequency response) cannot add virtual inertia to the grid. At the same time, virtual damping depends only on the droop gain. Therefore, its contribution to inertia is null, and damping to oscillations is limited, as will be further described in section 5.6.

The first-order filter-based inertial emulation techniques for GSCs has stability issues owing to undesirable interactions between the converter control and the passive elements of the system, limiting their capacity to inject synthetic inertia (as will be demonstrated in section 5.7). Additionally, this control technique fails to decouple the damping terms of the swing equation and the droop gain. Thus, several authors [49, 50] do not favour this approach. To solve these drawbacks, Chapter 5 proposes the second-order filter-based inertial emulation (SOFIE), which perfectly emulates the synchronous machine's inertial and damping behaviour. In addition, this technique solves the stability problems caused by adverse interactions, increasing its ability to provide inertia to the system. Moreover, it decouples the damping and constant droop terms, allowing precise attenuation of power oscillations.

Table 2.3 shows a brief overview of the main differences between the GSC and GFM techniques; Moreover, it shows the contributions that this thesis has made to these topics.

**Table 2.3:** Summary of the main differences between the GSC and GFM approaches.

| | GFM | GSC | Cite |
|---|---|---|---|
| Synchronisation | Power balance | Phase-locked loop | [102, 103] |
| Stability | Robust in weak grids | Robust in stiff grids | [**J**2] |
| Inertia emulation | Based on SME | Limited in FOFIE but improved with SOFIE | [**J**3, **J**4, **J**5] |
| Uncoupling damping term | Possible in some SME techniques. | Only possible whit SOFIE control. | [**J**3, **J**4] |
| Implementation | Restructure firmware | Maintains the classic control structure | [**J**2, **J**3] |

## 2.4 Summary

This chapter has shown the main control techniques for grid-connected converters. First conventional grid-following approaches, that uses the PLL to synchronise with the grid through frequency and power angle estimation have been described. Then, grid-forming techniques have been introduced, which are capable of contributing to the frequency and voltage regulation of the grid. Grid-forming is based on calculating the grid frequency, ensuring a balance between generation and load. In addition, grid-supporting techniques, which make use of the grid following structure to synchronise with the grid, delivers synthetic inertia proportionally against frequency disturbances. Finally, a brief comparison based on state–of–the–art, and the control strategies proposed in this research work/thesis is provided.

# Chapter 3

# Stability Tool for Electric Power Systems with a High Penetration of Electronic Power Converters

*One of the main challenges in converter-dominated grids is the analysis of the mutual interactions of the converter control loops and the passive elements of the power system. These interactions can be electromagnetic in nature, making the tradicional approaches to analyse the power system stability, based on phasor models, innappropriate as they do not consider them. In this context, this chapter presents a methodology developed jointly by Tecnalia and Mondragon Unibertsitatea for analysing small-signal stability in converter-dominated networks using EMT models. This methodology has been embedded in a software tool called CSTEP, which is used throughout this thesis. To assess the effectiveness of the proposed methodology, several case studies are presented, including a comparative study of RMS modelling of commercial software against EMT modelling using CSTEP. The results of this comparison demonstrate the necessity of EMT models for the correct study of converter-dominated networks.*

## 3.1 Introduction

Power system stability is among the most important new challenges of converter-dominated grids. In general, power system stability is defined as the ability of an electrical system, for a given initial condition, to regain a state of operating equilibrium after being subjected to a disturbance, with most system variables bounded [104]. Traditionally, the stability assessment has been divided into angle, frequency, and voltage, further divided into small- and large-signal analyses depending on the magnitude of the disturbance studied [104].

This division is based on a time-scale separation of the electromechanical oscillations associated with synchronous generators and the electromagnetic oscillations related to the electrical part of the grid. With the massive integration of electronic power converters and their controls, the previous assumption is no longer valid for all power systems [18]. Converters can be controlled to mimic the behaviour of classical synchronous machines but with a much faster response to ensure the stability of the power system [74].

Therefore, the converter multiscale coupling between control loops and the mutual interactions of parallel converters frequently requires the consideration of the electromagnetic as well as the electromechanical dynamics [105]. In light of this issue, an extended classification has been recently presented incorporating the term converter-driven stability to consider this type of coupling in the assessment of stability [106]. Converter-driven or converter stability can be divided into small-signal and large-signal analyses [107]. In small-signal studies, the system is linearized around an operation point and thus, the conclusions drawn are valid for small deviations from this operation point. The advantage of small-signal studies is that, since the system is linear, all the powerful linear analysis tools can be applied. Such studies can be divided into time-domain or frequency-domain, depending on the type of system representation employed [108].

Time-domain studies are carried out with state-space representations, by looking at the location of eigenvalues in the complex plane and their properties (damping factor, natural frequency, oscillation frequency, etc.). Recently, the so-called component connection method (CCM) has been proposed to facilitate the construction of systems comprised of several devices (generators, loads, converters, etc.) [109]. One of the main disadvantages of this method and similar ones is that it does not reduce these redundant states and therefore the models of devices must be modified depending on how they are connected (e.g., when connecting two nominal-pi equivalent transmission line models, the state representing the voltage at one of the terminal capacitors is redundant).

Frequency-domain studies are based on impedance-based representations, which enable the construction of power systems by means of equivalent voltage/current sources and impedances [110]. The advantages of such representations are that small-signal stability margins can be quantified, and their modularity and scalability are high. Moreover, a black-box model can be obtained using a frequency-scanning method [108].

Even though there are tools such as MATLAB that provide commands or libraries to facilitate the construction of small-signal time- and frequency-domain models for the assessment of the converter stability, there are no standardised tools to carry out such studies systematically. Each model must be constructed ad hoc, defining the equations of all the devices connected to the system under study. This means that if a device appears more than once in the system (e.g., the *RL* impedance of a line), its model cannot be reutilised and the equations have to be repeated in the overall model, but modifying the variable names. Moreover, all studies focus either on time- or frequency-domain representations but do not take full advantage of

combining both approaches.

Regarding large-signal stability analysis, two main methods can be distinguished: Lyapunov-based techniques and time-domain simulations. Considering the difficulty in generalising a method based on Lyapunov, time-domain simulations are the default solution for studying the large-signal stability of any power system scenario. As it was previously explained, in conventional power systems dominated by synchronous generators electromagnetic transients (EMT) are neglected, and RMS or quasi-steady-state (QSS) phasor simulations are used to increase the computational speed [111].

The available tools that consider EMT dynamics mainly focus on the analysis of transient values of voltages and currents for element sizing and design purposes [112], rather than on large-signal stability analyses. More general-purpose tools such as MATLAB require the development of ad hoc models of the system to be analysed [113]. The former do not provide information about the modes or eigenvalues associated with the electrical part of the system for the assessment of the small-signal stability, and the latter are usually focused on the analysis and design of controllers for electronic converters rather than on the overall analysis of the power system [74, 114–116]. Other co-simulation tools that combine electromechanical and electromagnetic dynamics have been also developed to simulate power systems with a high presence of electronic power converters in the time domain [117,118]. These tools are usually oriented to system planning but do not return the root loci of the system to carry out small-signal stability analyses.

This chapter presents a methodology jointly designed by Mondragon Unibertsitatea and Tecnalia to analyse the small- and large-signal stability of converter-dominated power systems. The mathematical foundations of the methodology are similar to other tools focused for instance on EMT simulations of electrical and electronic circuits [119]. However, this methodology incorporates a systematic formulation of state-space representations that, in addition to time-domain simulations, is aimed at small-signal stability studies by providing the root loci of the system under study. The dynamical models of the elements that comprise the test case are modelled in a library so that they can be used multiple times with different parameters. This facilitates the construction of complex systems without the need to repeat and interconnect all the equations of the individual elements. Therefore, an important contribution of the proposed methodology is found in its element-oriented modelling philosophy, which makes it a modular and flexible. A difference with other approaches is this methodology has the capacity to automatically eliminate dependent dynamic states, which is necessary to handle applications such as synchronous generators or power converters with $L$ or $LCL$ filters connected to inductive lines or transformers, or power distribution systems with meshed or ring topologies where the currents are dependent on each other.

Another advantage compared to already existing software is its symbolic engine—in addition to the numerical one—enabling the generation of parametric state-space models that can be studied analytically and evaluated iteratively, e.g., to determine the influence of parameters on the stability margins of the system. Moreover, the symbolic engine provides the analytical expressions that represent the system's dynamics, which is interesting to identify the variables and parameters that determine the evolution of the states in the time domain.

To facilitate its use, the proposed methodology has been embedded in a MATLAB-based software tool called CSTEP (Converter Stability Tool for Electric Power Systems), which additionally includes a simulation module capable of assessing the time-domain behaviour of the constructed system by simulating the original set of nonlinear equations. These simulations provide information about the large-signal stability of the system and facilitate the valida-

tion of small-signal models before the analysis phase without the necessity to reconstruct the system with another tool.

The chapter's main objective is to provide the readers with the mathematical foundations and methodology behind CSTEP for carrying out stability analyses of converter-dominated power systems. Several test cases are presented to demonstrate how a system is built in CSTEP with the proposed methodology. This doctoral thesis has contributed to the development of CSTEP by carrying out the validation of the tool throughout the implementation of multiple case studies and by comparing it with the RMS methods used in commercial software packages. As mentioned above, all the analysis developed in the thesis have been carried out using this CSTEP tool. Validation and comparison are made against PowerFactory, which uses RMS models for small-signal analysis. The results demonstrate the need to implement EMT modelling for large and small signal analysis of converter-dominated grids because the RMS models represent the passive components of the system —inductive and capacitive elements— as quasi-static models. Therefore, it is impossible to analyse the impact of the fast dynamics of the converter and its control loops with these passive network elements.

#### Description of CSTEP

The general structure of CSTEP is illustrated in Fig. 3.1. In the following sections, each of the core modules of CSTEP is described in detail. The modular nature of the tool will facilitate the integration of new modules to manipulate and broaden the study of the system equations in the future. For instance, it might be interesting to implement model order reduction (MOR) techniques to decouple states with different dynamics and to focus the subsequent analyses on the dynamics of interest [120]. The reader should not confuse MOR techniques with the reduction of redundant states mentioned in the following sections. Another interesting feature would be the implementation of a semiautomatic frequency-domain analysis tool to complement the information obtained from time-domain studies as in [121]. The core modules of CSTEP could be also extended to handle multi-harmonic models based on dynamic phasors or harmonic state-space systems [108, 122]. These functionalities have been represented in grey in Fig. 3.1.

### 3.1.1 System-building and adaptation module

The objective of the system-building and adaptation module is the definition of the system equations and the automatic construction, reduction and linearisation of the model. Since CSTEP is an element-oriented tool, the equations of the system to be modelled are obtained by means of the equations of the individual elements and their interconnections. This means that first, it is necessary to define appropriate element representations. Based on these individual models and their interconnections (predefined in a test case file), the complete system is then constructed, reduced, and (if necessary) linearized at a specific operating point.

#### Element representation

CSTEP uses three different types of variables for the element representation: internal, nodal, and port. The internal variables are used to describe the intrinsic behaviour of the element and they can be differential ($\mathbf{x}_{int}$) or algebraic ($\mathbf{z}_{int}$). On the other hand, the nodal and port variables are used to define the connections between the elements and are always algebraic. Nodes refer to the connections used to transmit power, while ports refer to the

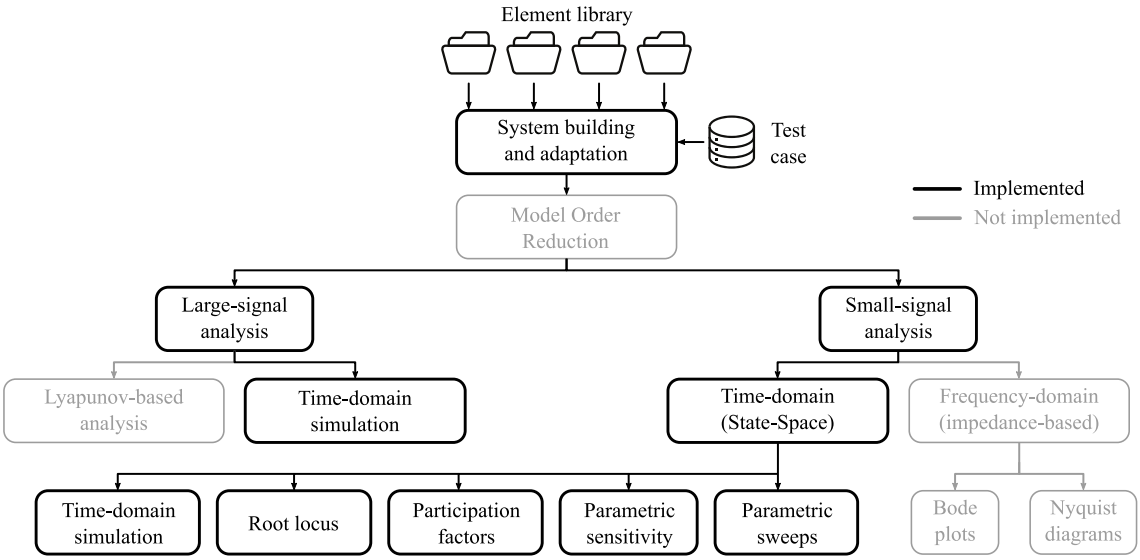


**Figure 3.1:** CSTEP Structure

connections used to transmit information (e.g., control signals). Each node has two associated variables, i.e., a potential variable ($\mathbf{z}_{pn}$) and a flow variable ($\mathbf{z}_{fn}$). In power systems, potential and flow variables are associated with voltages and currents, respectively. In other domains, an analogous representation can be made, e.g.: speed and torque in mechanical systems; temperature and heat flow in thermal circuits, or the magnetic field and flux in magnetic circuits. The formulation of CSTEP described in the following sections is kept generic so that various domains can be combined in the future. Port variables are divided into input variables ($\mathbf{z}_{ip}$) and output variables ($\mathbf{z}_{op}$). Considering all this information, the number of equations required for the representation of an element must be equal to the number of equations of internal differential variables $\mathbf{f}$, plus the number of equations of internal algebraic variables ($\mathbf{g}_1$) plus the number of equations of node variables ($\mathbf{g}_2$), plus the number of equations of output port variables ($\mathbf{g}_3$). These equations are shown in the following expressions:

$$\frac{d\mathbf{x}_{int}^{E_i}}{dt} = \mathbf{f}^{E_i}\left(\mathbf{x}_{int}^{E_i}, \mathbf{z}_{int}^{E_i}, \mathbf{z}_{pn}^{E_i}, \mathbf{z}_{fi}^{E_i}, \mathbf{z}_{ip}^{E_i}, \mathbf{z}_{op}^{E_i}, \mathbf{u}^{E_i}\right) \tag{3.1}$$

$$\mathbf{0} = \mathbf{g}_1^{E_i}\left(\mathbf{x}_{int}^{E_i}, \mathbf{z}_{int}^{E_i}, \mathbf{z}_{pn}^{E_i}, \mathbf{z}_{fi}^{E_i}, \mathbf{z}_{ip}^{E_i}, \mathbf{z}_{op}^{E_i}, \mathbf{u}^{E_i}\right) \tag{3.2}$$

$$\mathbf{0} = \mathbf{g}_2^{E_i}\left(\mathbf{x}_{int}^{E_i}, \mathbf{z}_{int}^{E_i}, \mathbf{z}_{pn}^{E_i}, \mathbf{z}_{fi}^{E_i}, \mathbf{z}_{ip}^{E_i}, \mathbf{z}_{op}^{E_i}, \mathbf{u}^{E_i}\right) \tag{3.3}$$

$$\mathbf{0} = \mathbf{g}_3^{E_i}\left(\mathbf{x}_{int}^{E_i}, \mathbf{z}_{int}^{E_i}, \mathbf{z}_{pn}^{E_i}, \mathbf{z}_{fi}^{E_i}, \mathbf{z}_{ip}^{E_i}, \mathbf{z}_{op}^{E_i}, \mathbf{u}^{E_i}\right) \tag{3.4}$$

where the superscript $E_i$ represents the $i-th$ element.

### Nonreduced system representation

As it was previously explained, the system representation is obtained by means of the system models and their interconnections. The first step is for CSTEP to generate the nonreduced system representation consisting of the concatenation of the equations of the elements. This process leads to equations $\mathbf{f}^s$, $\mathbf{g}_1^s$, $\mathbf{g}_2^s$ and $\mathbf{g}_3^s$ shown in Eqs. (3.5)-(3.8). These expressions have a greater number of variables than the number of equations. To complete the system of equations, the system node potential variables (**np**) and the system port potential variables (**pp**) are defined based on the node and port variables of the individual elements. With these new variables, the relation between the node potential, input port and output port variables for each element is defined, obtaining equations $\mathbf{g}_4^s$, $\mathbf{g}_5^s$ and $\mathbf{g}_6^s$ shown in expressions (3.9)–(3.12). The current flow on each node of the system is defined according to Kirchhoff's current law to obtain $\mathbf{g}_7^s$. Finally, an additional reference node potential ($np_o$) is included and set to zero as shown in Eq. (3.13). This equation defines a common reference voltage for all the nodes in the system, which will be necessary to solve the system of equations.

$$\frac{d\mathbf{x}^S}{dt} = \mathbf{f}^S \Leftrightarrow \left[\mathbf{x}_{int}^{E_1}, ..., \mathbf{x}_{int}^{E_n}\right] = \left[\mathbf{f}^{E_1}, ..., \mathbf{f}^{E_n}\right] \tag{3.5}$$

$$\mathbf{0} = \mathbf{g}_1^S \Leftrightarrow \left[\mathbf{0}_{g_1}^{E_1}, ..., \mathbf{0}_{g_1}^{E_n}\right] = \left[\mathbf{g}_1^{E_1}, ..., \mathbf{g}_1^{E_n}\right] \tag{3.6}$$

$$\mathbf{0} = \mathbf{g}_2^S \Leftrightarrow \left[\mathbf{0}_{g_2}^{E_1}, ..., \mathbf{0}_{g_2}^{E_n}\right] = \left[\mathbf{g}_2^{E_1}, ..., \mathbf{g}_2^{E_n}\right] \tag{3.7}$$

$$\mathbf{0} = \mathbf{g}_3^S \Leftrightarrow \left[\mathbf{0}_{g_3}^{E_1}, ..., \mathbf{0}_{g_3}^{E_n}\right] = \left[\mathbf{g}_3^{E_1}, ..., \mathbf{g}_3^{E_n}\right] \tag{3.8}$$

$$\mathbf{0} = \mathbf{g}_4^S = \left[\mathbf{g}_4^{E_1}\left(\mathbf{z}_{pn}^{E_1}, \mathbf{np}\right), ..., \mathbf{g}_4^{E_n}\left(\mathbf{z}_{pn}^{E_n}, \mathbf{np}\right)\right] \tag{3.9}$$

$$\mathbf{0} = \mathbf{g}_5^S = \left[\mathbf{g}_5^{E_1}\left(\mathbf{z}_{ip}^{E_1}, \mathbf{pp}\right), ..., \mathbf{g}_5^{E_n}\left(\mathbf{z}_{ip}^{E_n}, \mathbf{pp}\right)\right] \tag{3.10}$$

$$\mathbf{0} = \mathbf{g}_6^S = \left[\mathbf{g}_5^{E_1}\left(\mathbf{z}_{po}^{E_1}, \mathbf{pp}\right), ..., \mathbf{g}_5^{E_n}\left(\mathbf{z}_{po}^{E_n}, \mathbf{pp}\right)\right] \tag{3.11}$$

$$\mathbf{0} = \mathbf{g}_7\left(\mathbf{z}_{fn}^{E_1}, ..., \mathbf{z}_{f_n}^{E_n}\right) \tag{3.12}$$

$$0 = np_0 \tag{3.13}$$

where the superscript $S$ denotes system-level equations.

Expressions (3.5)–(3.13) describe the dynamic performance of the electric power system. It is called a nonreduced representation because the algebraic variables are still present in the equations. To provide a more compact fashion of these equations, algebraic variables of individual elements and node and port potential variables are grouped into $\mathbf{z}^S$ and Eqs. (3.6)–(3.13) are grouped into $\mathbf{g}^S$, leading to the following nonreduced system representation:

$$\begin{aligned} \frac{d\mathbf{x}^S}{dt} &= \mathbf{f}^S\left(\mathbf{x}^S, \mathbf{z}^S, \mathbf{u}^S\right) \\ \mathbf{0} &= \mathbf{g}^S\left(\mathbf{x}^S, \mathbf{z}^S, \mathbf{u}^S\right) \end{aligned} \tag{3.14}$$

### Reduced and linearized system representation

The nonreduced system representation may also contain redundant (linearly dependent) differential and algebraic equations [119]. Some typical examples where redundant variables appear are synchronous generators or electronic power converters with $L$ or $LCL$ filters connected in series to transformers or transmission lines, cutsets formed by inductors and/or current sources in closed loops (e.g. in meshed or ring power system topologies) [123] or the cascaded interconnection of $\pi$ or $T$ transmission line models. To systematically identify and reduce these redundancies, Eq. (3.14) is first represented in the matrix form as:

$$\begin{aligned} \frac{d\mathbf{x}^S}{dt} &= \mathbf{E}\mathbf{x}^S + \mathbf{F}\mathbf{z}^S + \mathbf{G}\mathbf{u}^S \\ \mathbf{0} &= \mathbf{H}\mathbf{x}^S + \mathbf{K}\mathbf{z}^S + \mathbf{L}\mathbf{u}^S \end{aligned} \tag{3.15}$$

where the matrices are obtained by partially differentiating the equations in Eq. (3.15) with respect to state variables ($\mathbf{x}^S$), algebraic variables ($\mathbf{z}^S$) and inputs ($\mathbf{u}^S$):

$$\begin{aligned} \mathbf{E} &= \frac{\partial \mathbf{f}^S}{\partial \mathbf{x}^S} \quad \mathbf{F} = \frac{\partial \mathbf{f}^S}{\partial \mathbf{z}^S} \quad \mathbf{G} = \frac{\partial \mathbf{f}^S}{\partial \mathbf{u}^S} \\ \mathbf{H} &= \frac{\partial \mathbf{g}^S}{\partial \mathbf{x}^S} \quad \mathbf{K} = \frac{\partial \mathbf{g}^S}{\partial \mathbf{z}^S} \quad \mathbf{L} = \frac{\partial \mathbf{g}^S}{\partial \mathbf{u}^S} \end{aligned} \tag{3.16}$$

At this point, it is worth noting that, if the original system in Eq. (3.14) is nonlinear, obtaining the matrices by means of the partial derivatives as in Eq. (3.16) will linearise the equations. The mathematical explanation behind this linearisation is based on the Taylor series expansion of Eq. (3.14), which is detailed in Appendix A. The linearisation of the model is a necessary step to represent the equations in matrix form and to apply classical linear analysis techniques to perform a small-signal stability assessment. When equations are linearized, Eq. (3.15) becomes:

$$\begin{aligned} \frac{d\Delta\mathbf{x}^S}{dt} &= \mathbf{E}\Delta\mathbf{x}^S + \mathbf{F}\Delta\mathbf{z}^S + \mathbf{G}\Delta\mathbf{u}^S \\ \mathbf{0} &= \mathbf{H}\Delta\mathbf{x}^S + \mathbf{K}\Delta\mathbf{z}^S + \mathbf{L}\Delta\mathbf{u}^S \end{aligned} \tag{3.17}$$

where $\Delta$ represents variations around the equilibrium point as explained in Appendix A. For the sake of generality, the symbol $\Delta$ is not included in the following equations.

When dynamical systems are represented by sinusoidal magnitudes, it is not possible to find a constant steady-state equilibrium point, and therefore CSTEP makes it possible to model these systems in a $dq$ rotatory frame such that the sinusoidal variables become constant. The

zero sequence could be also considered in the analyses, as long as the employed library models include the equations that represent this sequence. However, most of the studies related to the assessment of the small-signal stability of power systems consider symmetrical and balanced situations and average power converter models, where the zero sequence can be safely neglected. Since it is out of the scope of the thesis, the assessment of the stability of power systems with zero sequence components or unbalances is left as a future research activity. In the next step, the redundant states of the system are reduced and the dependencies between the variables are identified. The process consists of arranging the equations in (3.15) in a matrix form as follows:

$$\mathbf{U} = \begin{bmatrix} \mathbf{I} & \vdots & \mathbf{F} & \mathbf{E} & \mathbf{G} \\ \cdots & \cdots & \cdots & \cdots & \cdots \\ \mathbf{0} & \vdots & \mathbf{K} & \mathbf{H} & \mathbf{L} \end{bmatrix} \tag{3.18}$$

A Gauss-Jordan elimination method is used and the matrix $\mathbf{U}$ is reduced to a row echelon form. The resulting matrix can be represented as:

$$\mathbf{U_r} = \begin{bmatrix} \mathbf{I_r} & \vdots & \mathbf{F_r} & \mathbf{E_r} & \mathbf{G_r} \\ \cdots & \cdots & \cdots & \cdots & \cdots \\ \mathbf{0} & \vdots & \mathbf{K_r} & \mathbf{H_r} & \mathbf{L_r} \end{bmatrix} \tag{3.19}$$

where the subscript $r$ represents the reduced form of the matrices. This matrix can be also rewritten as a differential and algebraic system of equations:

$$\begin{aligned} \frac{d\mathbf{x}_r^S}{dt} &= \mathbf{E}_r\mathbf{x}_r^S + \mathbf{F}_r\mathbf{z}_r^S + \mathbf{G}_r\mathbf{u}^S \\ \mathbf{0} &= \mathbf{H}_r\mathbf{x}_r^S + \mathbf{K}_r\mathbf{z}_r^S + \mathbf{L}_r\mathbf{u}^S \end{aligned} \tag{3.20}$$

where $\mathbf{x}_r^S$ and $\mathbf{z}_r^S$ represent the reduced vector of states and algebraic variables, respectively. CSTEP offers the possibility to carry out this process either numerically or symbolically. The former is faster and makes it possible to apply most classical analysis techniques, but unlike the symbolic approach, it is not capable of retaining all the information to carry out a parametric sensitivity analysis or to identify the variables that determine the dynamic behaviour of the system.

### 3.1.2 Small-signal system representation

The last step in the system-building and adaptation module is to obtain the simplified small-signal representation of the system in the form:

$$\frac{\mathbf{x}_r^S}{dt} = \mathbf{A}\mathbf{x}_r^S + \mathbf{B}\mathbf{u}^S \tag{3.21}$$

For that purpose, the algebraic variables are first isolated from the algebraic equations in (3.21):

$$\mathbf{z}^S = -\mathbf{K}_r^{-1}\left(\mathbf{H}_r\mathbf{x}^S + \mathbf{L}_r\mathbf{u}^S\right) \tag{3.22}$$

Note that when obtaining the row echelon form $\mathbf{U}_r$ in Eq. (3.19), $\mathbf{K}_r$ becomes an upper-diagonal square matrix whose diagonal terms are different from zero, meaning that $\mathbf{K}_r$ will be invertible.

Then, the right-hand side of (3.22) is incorporated into the differential equations in (3.20) as:

$$\frac{d\mathbf{x}_r^S}{dt} = \mathbf{E}_r\mathbf{x}_r^S - \mathbf{F}_r\mathbf{K}_r^{-1}\left(\mathbf{H}_r\mathbf{x}_r^S + \mathbf{L}_r\mathbf{u}^S\right) + \mathbf{G}_r\mathbf{u}^S \tag{3.23}$$

From Eq. (3.23), $\mathbf{A}$ and $\mathbf{B}$ can be calculated as:

$$\begin{aligned}\mathbf{A} &= \mathbf{E}_r - \mathbf{F}_r\mathbf{K}_r^{-1}\mathbf{H}_r \\ \mathbf{B} &= \mathbf{G}_r - \mathbf{F}_r\mathbf{K}_r^{-1}\mathbf{L}_r\end{aligned} \tag{3.24}$$

### 3.1.3 Large-signal analysis module

The large-signal module has two main objectives: the calculation of the time-domain response of the system and the validation of the small-signal state-space model when the system is nonlinear. To perform the nonlinear simulation, the reduced system of equations in Eq. (3.14) is dynamically solved. For that purpose, the vector of input variables is defined as a time -dependent array— since the inputs vary during the simulation—and the $ode15i$ solver provided by MATLAB is used to solve the system of equations.

### 3.1.4 Small-signal analysis module

The analysis module is used to carry out a small-signal stability analysis of the system from the time-domain representation of equations.

#### Time-domain simulation

To simulate the linearized system, the representation shown in Eq. (3.21) is solved via the $lsim$ function from MATLAB. The results from this simulation are represented on top of the results from the large-signal analysis to corroborate the correctness of the linearized model.

#### Root locus

The small-signal stability analysis is based on the study of the location of the eigenvalues in the complex plane. If the real part of the eigenvalues is negative, the system is stable, and it will reach a new equilibrium point under a small disturbance. The tool returns the root locus of the system for the operation point provided by the user.

#### Participation factors

To analyse the system dynamics, CSTEP calculates the participation factors (**pf**), which provide the incidence of the system eigenvalues on the state variables and vice versa. These participation factors are calculated according to the following expression:

$$\mathbf{pf} = \mathbf{\Phi}^{\mathsf{T}} \odot \mathbf{\Psi} \tag{3.25}$$

where $\odot$ denotes the element-by-element or Hadamard product of the left and right eigenvectors of the state matrix **A**. The tool also calculates the weighted participation factors (**wpf**) as in [115] to represent that incidence in a percentage or 0–1 scale:

$$\mathbf{wpf}\left(x_l, \lambda_j\right) = \frac{\left|\mathbf{pf}\left(x_l, \lambda_j\right)\right|}{\sum_{\mu}\left|\mathbf{pf}\left(\mu, \lambda_j\right)\right|} \tag{3.26}$$

where $\mu$ depicts the set of states for the eigenvalue $\lambda_j$.

#### Parametric sensitivity

CSTEP provides a couple of tools to estimate the influence of parameters on the system stability: a parametric sensitivity matrix (**bf**) and an iterative parametric sweep function. The so-called parametric sensitivities are calculated to study the movement of eigenvalues with respect to variations of any parameter of the system [115]. This matrix is obtained as follows:

$$ps_{jk} = \frac{\partial \lambda_j}{\partial \rho_k} = \frac{\boldsymbol{\Phi}_j^{\mathsf{T}} \dfrac{\partial \mathbf{A}}{\partial \rho_k} \boldsymbol{\Psi}_j}{\boldsymbol{\Phi}_j^{\mathsf{T}} \boldsymbol{\Psi}_j} \tag{3.27}$$

The use of symbolic notation in CSTEP makes it possible to calculate the exact sensitivity of each of the studied operation points.

#### Parametric sweeps

Parametric sweeps, on the other hand, can be carried out either using the symbolic or the numeric representation of the system. In the former, even though constructing the system model symbolically requires a higher computational effort than doing it numerically, the final symbolic expressions can be efficiently used afterwards to carry out iterative studies such as parametric sweeps without the need to reconstruct the linearized system matrices in Eq. (3.15) each iteration.

## 3.2 Validation and application of CSTEP

The aim of this section is threefold. Firstly, the purpose is to illustrate step-by-step how a very simple example is constructed and reduced with CSTEP (Use case I). Secondly, the tool is validated by comparing the time-domain response and eigenvalues of a 5-bus IEEE benchmark system to the same model developed in DigSilent PowerFactory (Use case II). Moreover, with this example, the incongruencies that might arise in terms of converter stability in both models for certain operating points due to the reduction of the electromechanical states are shown. Thirdly, the potential applications of CSTEP are demonstrated with a more complex CIGRÉ distribution system comprised of 14 buses (Use case III).

### 3.2.1 Use case I – Simple ac system

This benchmark is comprised of an ideal voltage source (Generator 1), an *RL* transmission line (Line 1), and an *RL* load (Load 1). The general diagram is illustrated in Fig. 3.2-a.

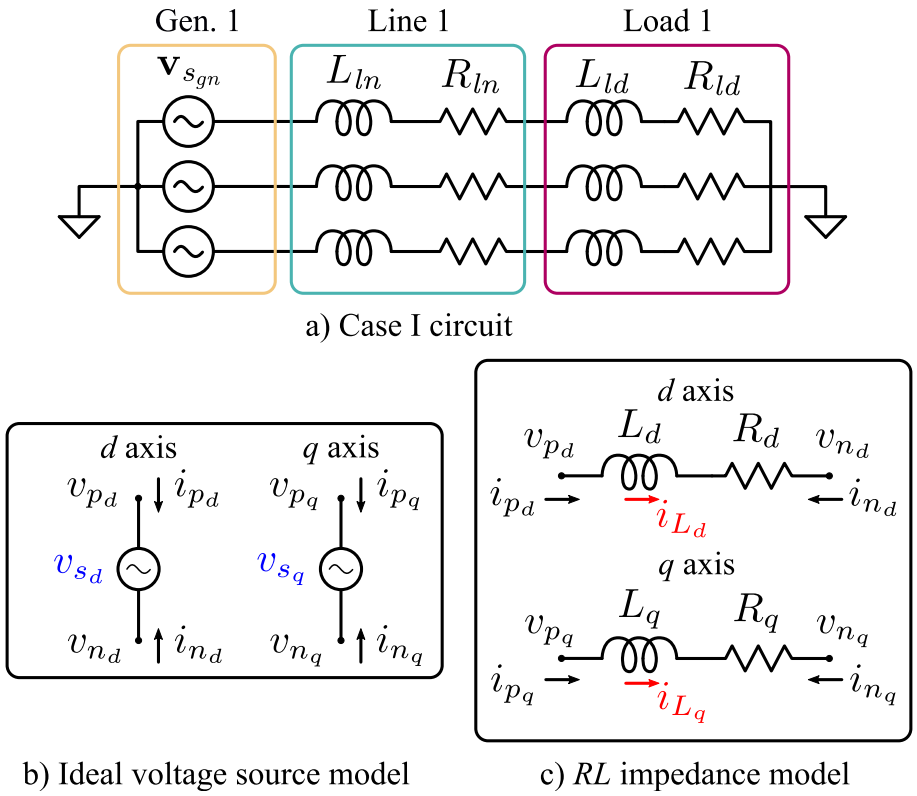


**Figure 3.2:** Use case I: a) simplified ac system scenario, b) ideal voltage source library model, and c) RL impedance library model

In CSTEP, the ideal voltage source is modelled according to Fig. 3.2-b. The model has a $d$ and $q$ component, and there are no dynamic states. Since the element only has four node potential variables, it can be represented with the following four algebraic equations:

$$v_{s_d} = v_{p_d} - v_{n_d}; \quad v_{s_q} = v_{p_q} - v_{n_q}; \quad i_{p_d} = -i_{n_d}; \quad i_{p_q} = -i_{n_q} \tag{3.28}$$

where $v_{s_d}$ and $v_{s_q}$ are considered global inputs of the system.

Similarly, the line and load of the circuit can be modelled with the same $RL$ library component (Fig. 3.2-c). In this case, there are two states associated with the inductances and four node potential variables, so the element of the $RL$ impedance can be represented with the following set of differential-algebraic equations (DAE):

$$\begin{aligned}
\frac{di_{L_d}}{dt} &= \frac{1}{L_d}\left(v_{p_d} - R_d i_{L_d} - v_{n_d}\right) + \omega i_{L_q} \\
\frac{di_{L_q}}{dt} &= \frac{1}{L_q}\left(v_{p_q} - R_q i_{L_q} - v_{n_q}\right) - \omega i_{L_d} \\
i_{p_d} &= i_{L_d}; \quad i_{n_d} = -i_{L_d}; \quad i_{p_q} = i_{L_q}; \quad i_{n_q} = -i_{L_q}
\end{aligned} \tag{3.29}$$

where the coupling terms $\omega i_{L_d}$ and $-\omega i_{L_q}$ appear due to the conversion to the rotating $dq$ reference frame. In this case, $\omega$ is considered a global input of the system.

### Nonreduced system representation

Based on these library elements, the concatenated element equations (Eqs. (3.5)–(3.8)) can be represented as follows:

$$\frac{d\mathbf{x}^S}{dt} = \begin{bmatrix} \frac{di_{L_d}^{\mathrm{Ln}_1}}{dt} \\ \frac{di_{L_q}^{\mathrm{Ln}_1}}{dt} \\ \frac{di_{L_d}^{\mathrm{Ld}_1}}{dt} \\ \frac{di_{L_q}^{\mathrm{Ld}_1}}{dt} \end{bmatrix} = \begin{bmatrix} \frac{1}{L_d^{\mathrm{Ln}_1}}\left(v_{p_d}^{\mathrm{Ln}_1} - R_d^{\mathrm{Ln}_1} i_{L_d}^{\mathrm{Ln}_1} - v_{n_d}^{\mathrm{Ln}_1}\right) + \omega i_{L_q}^{\mathrm{Ln}_1} \\ \frac{1}{L_q^{\mathrm{Ln}_1}}\left(v_{p_q}^{\mathrm{Ln}_1} - R_q^{\mathrm{Ln}_1} i_{L_q}^{\mathrm{Ln}_1} - v_{n_q}^{\mathrm{Ln}_1}\right) - \omega i_{L_d}^{\mathrm{L}_1} \\ \frac{1}{L_d^{\mathrm{Ld}_1}}\left(v_{p_d}^{\mathrm{Ld}_1} - R_d^{\mathrm{Ld}_1} i_{L_d}^{\mathrm{Ld}_1} - v_{n_d}^{\mathrm{Ld}_1}\right) + \omega i_{L_q}^{\mathrm{Ld}_1} \\ \frac{1}{L_q^{\mathrm{Ld}_1}}\left(v_{p_q}^{\mathrm{Ld}_1} - R_q^{\mathrm{Ld}_1} i_{L_q}^{\mathrm{Ld}_1} - v_{n_q}^{\mathrm{Ld}_1}\right) - \omega i_{L_d}^{\mathrm{Ld}_1} \end{bmatrix} \tag{3.30}$$

$$\mathbf{g}_2^S = \begin{bmatrix} v_{s_d}^{\mathrm{Gn}_1} = v_{p_d}^{\mathrm{Gn}_1} - v_{n_d}^{\mathrm{Gn}_1} \\ v_{s_q}^{\mathrm{Gn}_1} = v_{p_q}^{\mathrm{Gn}_1} - v_{n_q}^{\mathrm{Gn}_1} \\ i_{p_d}^{\mathrm{Gn}_1} = -i_{n_d}^{\mathrm{Gn}_1} \\ i_{p_q}^{\mathrm{Gn}_1} = -i_{n_q}^{\mathrm{Gn}_1} \\ i_{p_d}^{\mathrm{Ln}_1} = i_{L_d}^{\mathrm{Ln}_1} \\ i_{n_d}^{\mathrm{Ln}_1} = -i_{L_d}^{\mathrm{Ln}_1} \\ i_{p_q}^{\mathrm{Ln}_1} = i_{L_q}^{\mathrm{Ln}_1} \\ i_{n_q}^{\mathrm{Ln}_1} = -i_{L_q}^{\mathrm{Ln}_1} \\ i_{p_d}^{\mathrm{Ld}_1} = i_{L_d}^{\mathrm{Ld}_1} \\ i_{n_d}^{\mathrm{Ld}_1} = -i_{L_d}^{\mathrm{Ld}_1} \\ i_{p_q}^{\mathrm{Ld}_1} = i_{L_q}^{\mathrm{Ld}_1} \\ i_{n_q}^{\mathrm{Ld}_1} = -i_{L_q}^{\mathrm{Ld}_1} \end{bmatrix}; \quad \mathbf{g}_4^S = \begin{bmatrix} v_{p_d}^{\mathrm{Gn}_1} = np_1 \\ v_{p_q}^{\mathrm{Gn}_1} = np_2 \\ v_{n_d}^{\mathrm{Gn}_1} = np_0 \\ v_{n_q}^{\mathrm{Gn}_1} = np_0 \\ v_{p_d}^{\mathrm{Ln}_1} = np_1 \\ v_{n_d}^{\mathrm{Ln}_1} = np_3 \\ v_{p_q}^{\mathrm{Ln}_1} = np_2 \\ v_{n_q}^{\mathrm{Ln}_1} = np_4 \\ v_{p_d}^{\mathrm{Ld}_1} = np_3 \\ v_{n_d}^{\mathrm{Ld}_1} = np_0 \\ v_{p_q}^{\mathrm{Ld}_1} = np_4 \\ v_{n_q}^{\mathrm{Ld}_1} = np_0 \end{bmatrix} \tag{3.31}$$

$$\mathbf{g}_7^S = \begin{bmatrix} 0 = i_{p_d}^{\mathrm{Gn}_1} + i_{p_d}^{\mathrm{Ln}_1} \\ 0 = i_{p_q}^{\mathrm{G}_1} + i_{p_q}^{\mathrm{Ln}_1} \\ 0 = i_{n_d}^{\mathrm{Ln}_1} + i_{p_d}^{\mathrm{Ld}_1} \\ 0 = i_{n_q}^{\mathrm{Ln}_1} + i_{p_q}^{\mathrm{Ld}_1} \end{bmatrix}; \quad 0 = pn_0 \tag{3.32}$$

### Reduced system representation

From Fig. 3.2 it is evident that the current of the line and the load is the same, meaning that in Eq. (3.30) there are two linearly dependent (redundant) differential equations. By reducing these equations and substituting the algebraic equations from (3.31) and (3.32) the following system of equations is obtained:

$$\frac{d\mathbf{x}_r^S}{dt} = \begin{bmatrix} \dfrac{di_{L_d}^{\mathrm{Ln}_1}}{dt} \\ \dfrac{di_{L_q}^{\mathrm{Ln}_1}}{dt} \end{bmatrix} = \begin{bmatrix} \dfrac{v_{s_d}^{\mathrm{Gn}_1} - \left(R_d^{\mathrm{Ln}_1} + R_d^{\mathrm{Ld}_1}\right) i_{L_d}^{\mathrm{Ln}_1}}{L_d^{\mathrm{Ln}_1} + L_d^{\mathrm{Ld}_1}} + \omega i_{L_q}^{\mathrm{Ln}_1} \\ \dfrac{v_{s_q}^{\mathrm{Gn}_1} - \left(R_q^{\mathrm{Ln}_1} + R_q^{\mathrm{Ld}_1}\right) i_{L_q}^{\mathrm{Ln}_1}}{L_q^{\mathrm{Ln}_1} + L_q^{\mathrm{Ld}_1}} - \omega i_{L_d}^{\mathrm{Ln}_1} \end{bmatrix} \tag{3.33}$$

This system is therefore comprised of two state variables and three inputs:

$$\mathbf{x}_r^S = \begin{bmatrix} i_{L_d}^{\mathrm{Ln}_1} & i_{L_q}^{\mathrm{Ln}_1} \end{bmatrix}^{\mathsf{T}}; \quad \mathbf{u} = \begin{bmatrix} v_{s_d}^{\mathrm{Gn}_1} & v_{s_q}^{\mathrm{Gn}_1} & \omega \end{bmatrix} \tag{3.34}$$

where $i_{L_d}^{\mathrm{Ln}_1} = i_{L_d}^{\mathrm{Ld}_1}$ and $i_{L_q}^{\mathrm{Ln}_1} = i_{L_q}^{\mathrm{Ld}_1}$ are the reduced dependent state variables.

### Linear system representation

From Eq. (3.33) it is noticeable that the system appears to be nonlinear, due to the multiplication between the inductor current and the reference frame rotation frequency ($\omega$). The reason is that $\omega$ is defined as an input of the system, so that frequency variations can be performed if necessary. If this frequency was considered to be constant, the system in Eq. (3.33) would be linear and would not need any linearisation. Following the process in Appendix A, by partially differentiating the equations in Eq. (3.33) with respect to (3.34), the linearized representation of the system can be obtained:

$$\begin{aligned} \mathbf{A} &= \begin{bmatrix} \dfrac{-\left(R_d^{\mathrm{Ln}_1} + R_d^{\mathrm{Ld}_1}\right)}{L_d^{\mathrm{Ln}_1} + L_d^{\mathrm{Ld}_1}} & \bar{\omega} \\ -\bar{\omega} & \dfrac{-\left(R_q^{\mathrm{Ln}_1} + R_q^{\mathrm{Ld}_1}\right)}{L_q^{\mathrm{Ln}_1} + L_q^{\mathrm{Ld}_1}} \end{bmatrix} \\ \mathbf{B} &= \begin{bmatrix} \dfrac{1}{L_d^{\mathrm{Ln}_1} + L_d^{\mathrm{Ld}_1}} & 0 & \dfrac{L_d^{\mathrm{Ln}_1}\bar{i}_{L_q^{\mathrm{Ln}_1}} + L_d^{\mathrm{Ld}_1}\bar{i}_{L_q\mathrm{Ld}_1}}{L_d^{\mathrm{Ln}_1} + L_d^{\mathrm{Ld}_1}} \\ 0 & \dfrac{1}{L_q^{\mathrm{Ln}_1} + L_q^{\mathrm{Ld}_1}} & -\dfrac{L_q^{\mathrm{Ln}_1}\bar{i}_{L_d^{\mathrm{Ln}_1}} + L_q^{\mathrm{Ld}_1}\bar{i}_{L_d\mathrm{Ld}_1}}{L_q^{\mathrm{Ln}_1} + L_q^{\mathrm{Ld}_1}} \end{bmatrix} \end{aligned} \tag{3.35}$$

where the upper bar denotes the steady-state value obtained by setting the derivative terms in Eq. (3.33) to zero (i.e., $\mathbf{x}_r^S = 0$) and by solving the remaining system of algebraic equations.

### Validation of the linearized state-space model

To ensure that the linearized system is representative of the original nonlinear system, a time-domain simulation is carried out with CSTEP, and the response of both systems with a voltage variation in the voltage source is compared. The initial parameters of the simulation are given in Table 3.1:

**Table 3.1:** Parameters of Case I

| Param. | Value | Param. | Value | Param. | Value |
|---|---|---|---|---|---|
| $v_{s_d}^{Gn_1}$ | 100 V | $L_d^{\mathrm{Ln}_1}$ | 0.1 mH | $R_d^{\mathrm{Ln}_1}$ | 0.1 Ω |
| $v_{s_q}^{Gn_1}$ | 0 V | $L_q^{\mathrm{Ln}_1}$ | 0.1 mH | $R_q^{\mathrm{Ln}_1}$ | 0.1 Ω |
| $\omega$ | 100 $\pi$ rad7s | $L_d^{\mathrm{Ld}_1}$ | 30 mH | $R_d^{\mathrm{Ld}_1}$ | 20 Ω |
| | | $L_q^{\mathrm{Ld}_1}$ | 30 mH | $R_q^{\mathrm{Ld}_1}$ | 20 Ω |

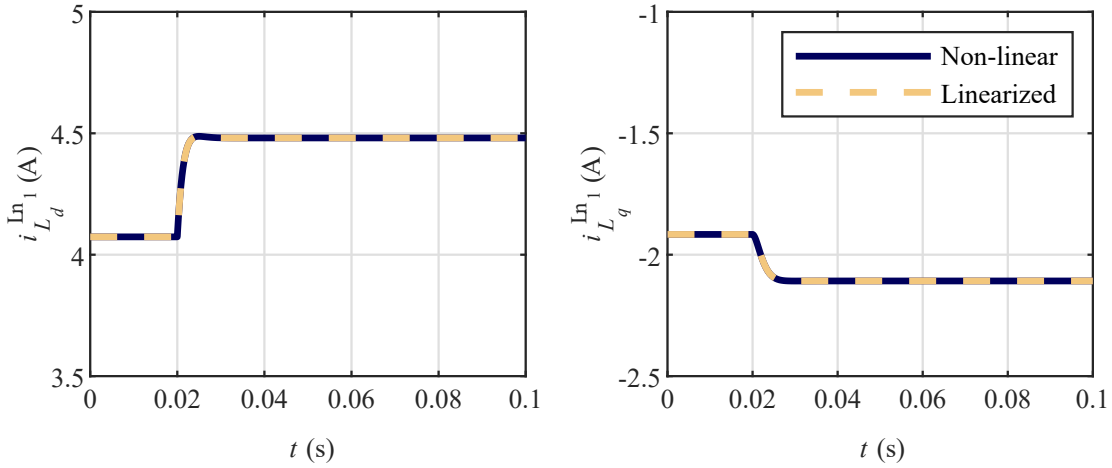


**Figure 3.3:** Time-domain evolution of the system states in Case I for a 0.1 $p.u.$ voltage variation

The time-domain evolution of the states of the system (the current in this case) for a 0.1 $p.u.$ d-axis voltage variation can be observed in Fig. 3.3.

The results show that the linearized model is correctly representing the time-domain behaviour of the system even when moving out of the point at which the linearization is made. This means that the matrices in Eq. (3.35) can be employed to carry out a detailed modal analysis.

### Modal analysis

The system has two eigenvalues and their properties have been gathered in Table 3.2. The oscillation frequency is the same as the reference frame rotation frequency, and the high damping values explain the overdamped response observed in Fig. 3.3. The following two tables show the weighted participation factors (**wpf**) and the real part of the parametric sensitivity ($\Re\{\mathbf{ps}\}$ or **rps** ) of the two eigenvalues.

**Table 3.2:** Eigenvalues of Case I and their properties

| Eigenvalue ($\lambda_j$) | Damping ($\zeta_j$) | Osc. Freq. ($f_{o_i}$) | Nat. Freq. ($f_{n_i}$) |
|---|---|---|---|
| $-667.77 \pm 314.14i$ | 0.9 | 50 Hz | 117.45 Hz |

The participation factors show that the eigenvalues and the states are equally related,

| **wpf** | $\lambda_j$ | |
|---|---|---|
| $x_l$ | 0.5 | 0.5 |
| | 0.5 | 0.5 |

| **rps** | $R_d^{\mathrm{Ln}_1}$ | $R_q^{\mathrm{Ln}_1}$ | $L_d^{\mathrm{Ln}_1}$ | $L_q^{\mathrm{Ln}_1}$ | $R_q^{\mathrm{Ln}_1}$ | $R_q^{\mathrm{Ld}_1}$ | $L_d^{\mathrm{Ld}_1}$ | $L_q^{\mathrm{Ld}_1}$ |
|---|---|---|---|---|---|---|---|---|
| $x_l$ | $-16.6$ | $-16.6$ | $1.1^4$ | $1.1^4$ | $-16.6$ | $-16.6$ | $1.1^4$ | $1.1^4$ |
| | $-16.6$ | $-16.6$ | $1.1^4$ | $1.1^4$ | $-16.6$ | $-16.6$ | $1.1^4$ | $1.1^4$ |

whereas the parametric sensitivity demonstrates that the inductances are the parameters that mostly influence the movement of eigenvalues in the complex plane. This can be also corroborated by carrying out a parametric sweep of the load resistance and inductance (see Fig. 3.4). A small variation of the inductance causes the poles to move significantly in the real axis compared to higher variations in the resistance.

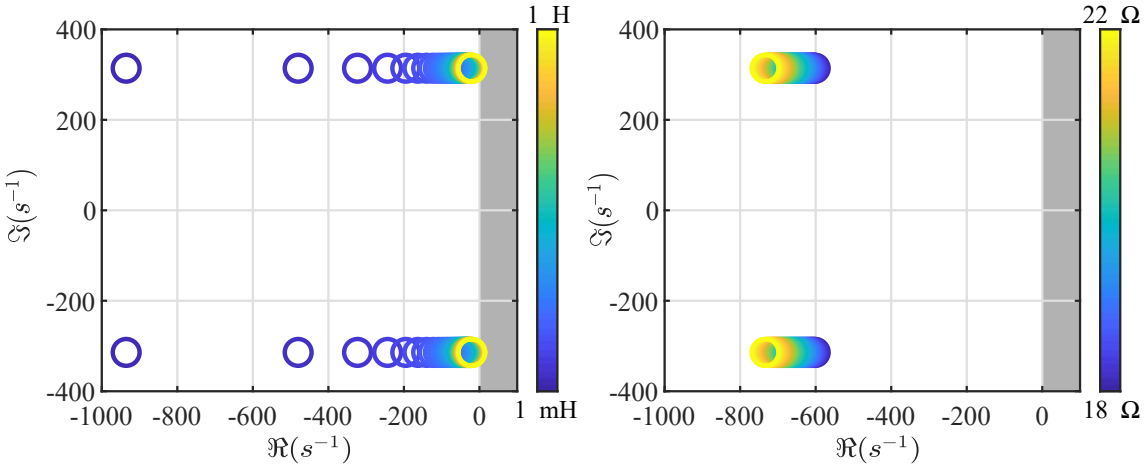


**Figure 3.4:** Parametric sweep in Use case I: a) load inductance (from 1 mH to 1 H) and b) load resistance (from 18 Ω to 22 Ω)

### 3.2.2 Use case II – IEEE 5-bus benchmark system

The single-line diagram of this use case is illustrated in Fig. 3.5, where the black boxes represent the sources (in this case electronic converters), and the gray triangles represent the loads. The values of the line impedances and the passive loads are indicated in the figure. The employed voltage and power base values are 138 kV and 100 MVA, respectively.

The converters are responsible for controlling the frequency of the grid by means of a grid-forming control strategy (Fig. 3.6). In this case, the active power controller consists of a low-pass filter (equivalent to a virtual inertia) and a $p/f$ droop regulator with gain $k_p$. The reactive power controller also includes a low-pass filter and a $q/v$ droop regulator ($k_q$).

The voltage amplitude and angle of the grid-forming control are used to obtain the converter reference voltage ($\mathbf{v}_{cv}^*$). The dc bus voltage of converters is assumed to be constant, and the switching operation is neglected by considering an average model of the converter as in [120]. This way, the converter output voltage ($\mathbf{v}_{cv}$) is decoupled from dc bus oscillations so

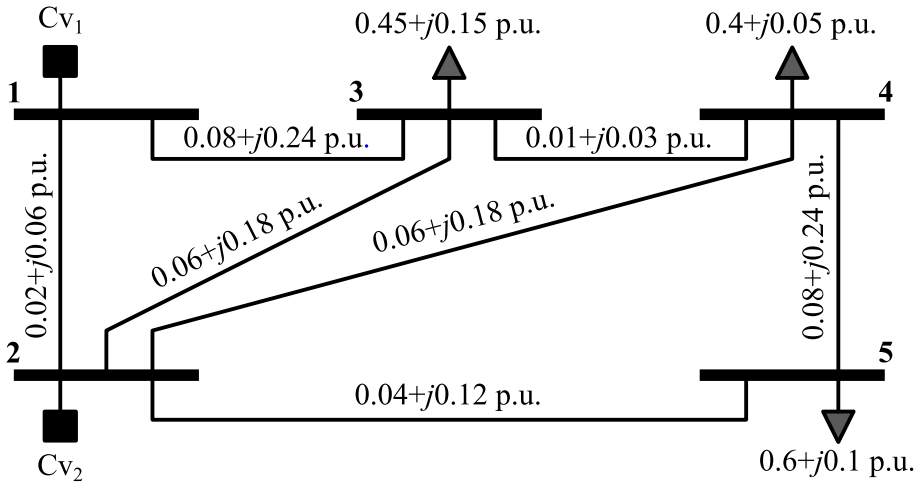


**Figure 3.5:** IEEE 5-bus benchmark system (Use case II)

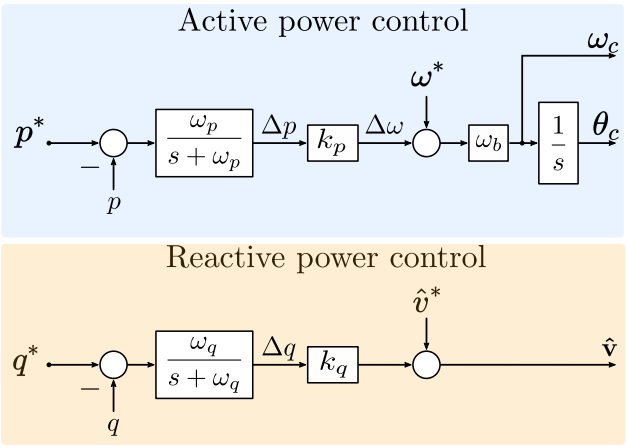


**Figure 3.6:** $p/f$ droop grid-forming control

that $\mathbf{v}_{cv}^* \approx \mathbf{v}_{cv}$. Moreover, an $LC$ filter is included in the output of converters.

This use case has been constructed in CSTEP as well as in PowerFactory. Fig. 3.7 represents the eigenvalues and the time-domain response of the system for a variation of $0.1\,p.u.$ in the resistive part of the load connected to node 5. In the case of PowerFactory, the results obtained from the RMS model are represented, since the eigenvalues of the system cannot be obtained from the EMT model to carry out the small-signal stability analysis.

In Fig. 3.7a, it is observed that the eigenvalues represented by PowerFactory match correctly with the eigenvalues associated with the slowest states—i.e., with the lowest frequency obtained with CSTEP. The reason for having such slow eigenvalues with converters is that the controllers are aimed at emulating the behaviour of classical generators. In addition, CSTEP provides the eigenvalues associated with the faster electromagnetic states of the system. If the small-signal stability is assessed with the results from both tools, it can be concluded that the system is stable, but it can also be noted that the dominant eigenvalues (i.e., with less damping) differ significantly in both cases. In classical power systems where electromagnetic modes do not interact with fast-acting converters—e.g. when they are dominated by synchronous generators—the oscillations they cause are damped rapidly, and therefore such modes can

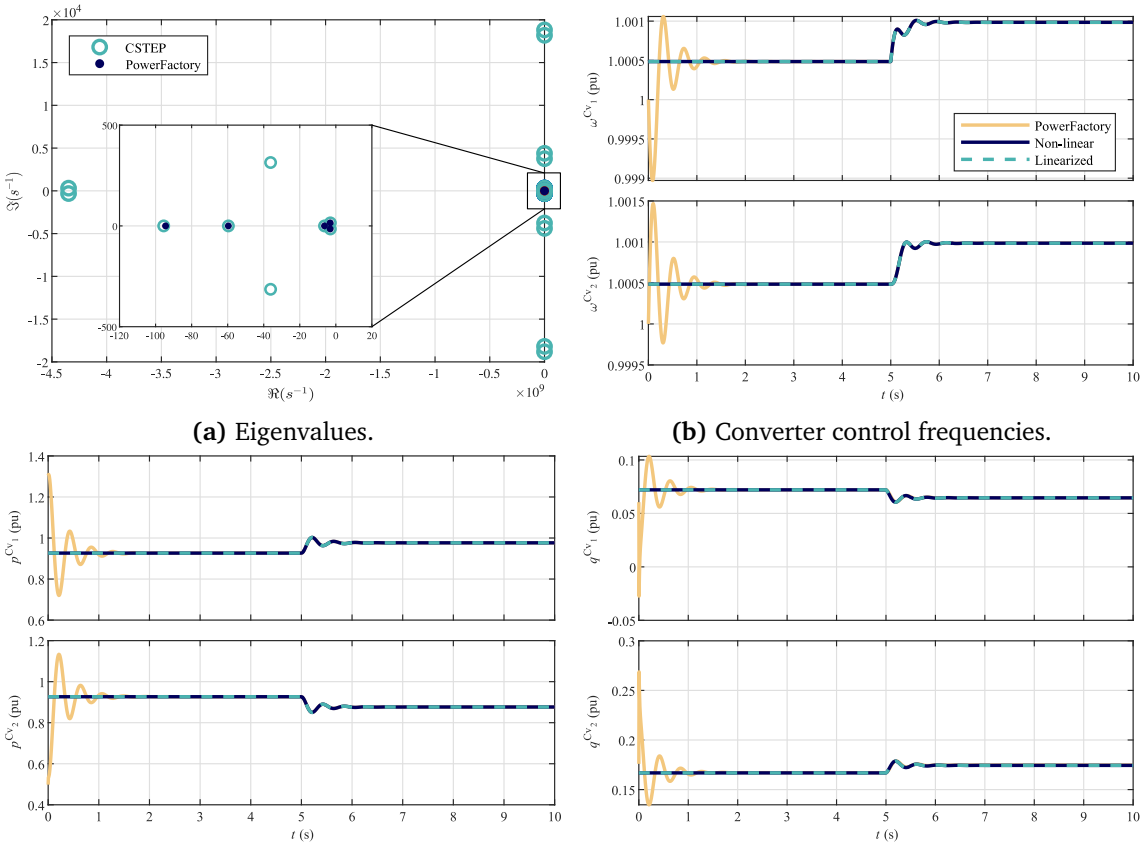


**(a)** Eigenvalues.

**(b)** Converter control frequencies.

**(c)** Converter active powers.

**(d)** Converter reactive powers.

**Figure 3.7:** Results of the IEEE 5-bus benchmark system: a) eigenvalues, b) converter control frequencies, c) converter active powers, d) converter reactive powers

be neglected.

This can be observed for instance in the results from the time-domain simulation in Fig. 3.7, where the evolution of converter frequencies and their active and reactive power are illustrated, respectively. Apart from the initial transient caused by the differences in the initial operating point in PowerFactory, the time-domain results show a very good match not only in steady-state, but also in the transient response after a load disturbance. Moreover, the nonlinear and the linearized models obtained in CSTEP also exhibit a good matching. These results validate the correctness of the core modules of CSTEP and mean that the conclusions obtained from the small-signal stability assessment are valid near the chosen equilibrium point. One of the main contributions of CSTEP compared to already available tools arises when the controllers of electronic converters start interacting with faster states associated with the electric part of the grid, causing the eigenvalues to approach the unstable area. To illustrate this case, the reactive power droop gain from one of the converters in the 5-bus use case is modified, causing the dominant eigenvalues to move to the unstable area for certain points of operation (Fig. 3.8a).

As it can be observed, the eigenvalues obtained from the RMS model in PowerFactory still coincide with the slower modes in CSTEP. However, in this case, PowerFactory does not consider the two dominant eigenvalues that make the system unstable, thus providing an incorrect

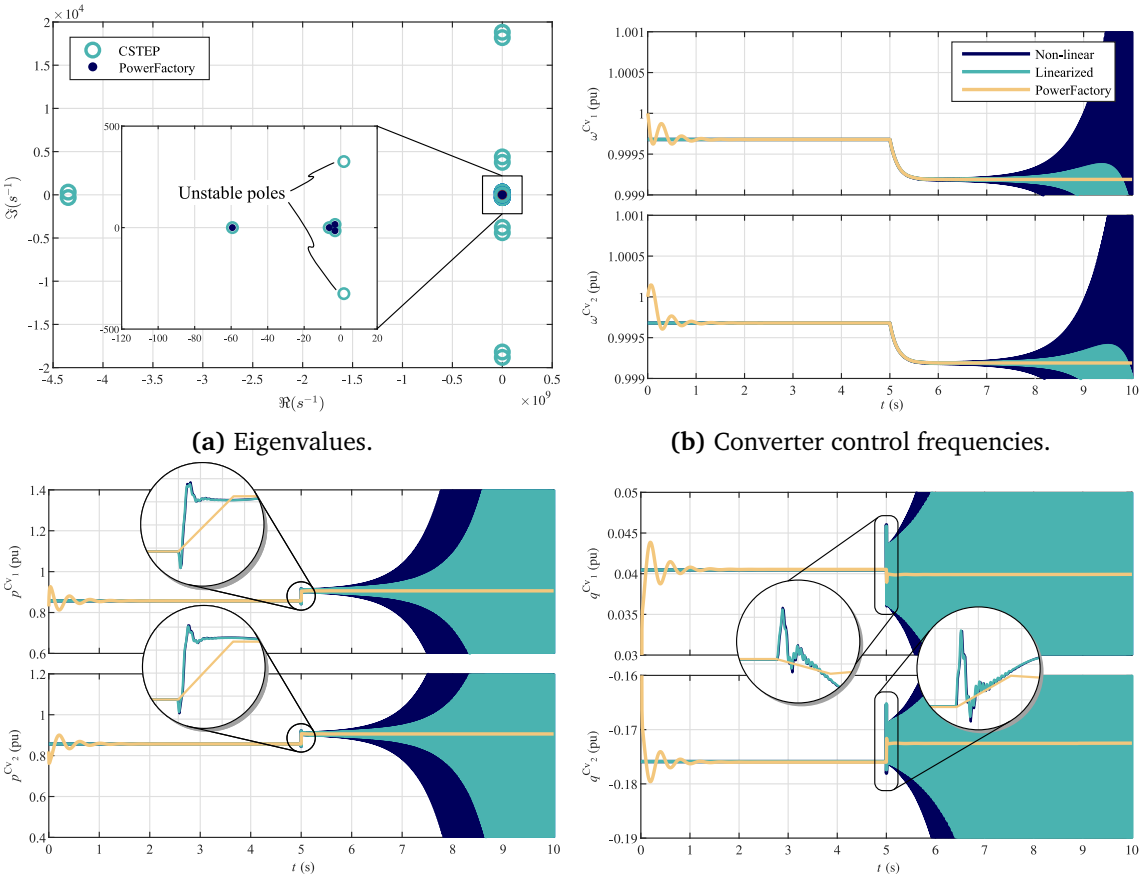


**(a)** Eigenvalues.

**(b)** Converter control frequencies.

**(c)** Converter active powers.

**(d)** Converter reactive powers.

**Figure 3.8:** Results of the IEEE 5-bus benchmark system for an unstable point of operation: a) eigenvalues, b) converter control frequencies, c) converter active powers, d) converter reactive powers

conclusion in the assessment of the small-signal stability. This can be further corroborated by looking at the time-domain response of the system in both tools (Fig 3.8b-d). The simulation is started from a stable point of operation, where CSTEP and PowerFactory provide almost the same results. At the instant $t = 5\,s$ the disturbance in the load causes the system poles to cross to the unstable area, causing the time-domain response to approach infinity. However, the RMS model in PowerFactory from which eigenvalues are obtained converges to a new stable operating point. The differences of the modes considered in CSTEP and PowerFactory can be also observed in the transient after the disturbance at $t = 5\,s$; the enlarged sections in Fig. 3.8c-d show the transient with different frequency components obtained in CSTEP, compared to the few points provided by the RMS model. Although this transient and the instability could be represented with more detail via an EMT simulation in PowerFactory, there is no option to calculate the eigenvalues from PowerFactory EMT model.

### 3.2.3 Use case III – CIGRÉ distribution system

The purpose of this use case is to illustrate the potential applications of CSTEP with a more complex use case. The scenario is based on the medium-voltage distribution network proposed

by the CIGRÉ Task Force C6.04.02 in [124]. The topology is comprised of two feeders and 14 buses, as illustrated in Fig. 3.9.

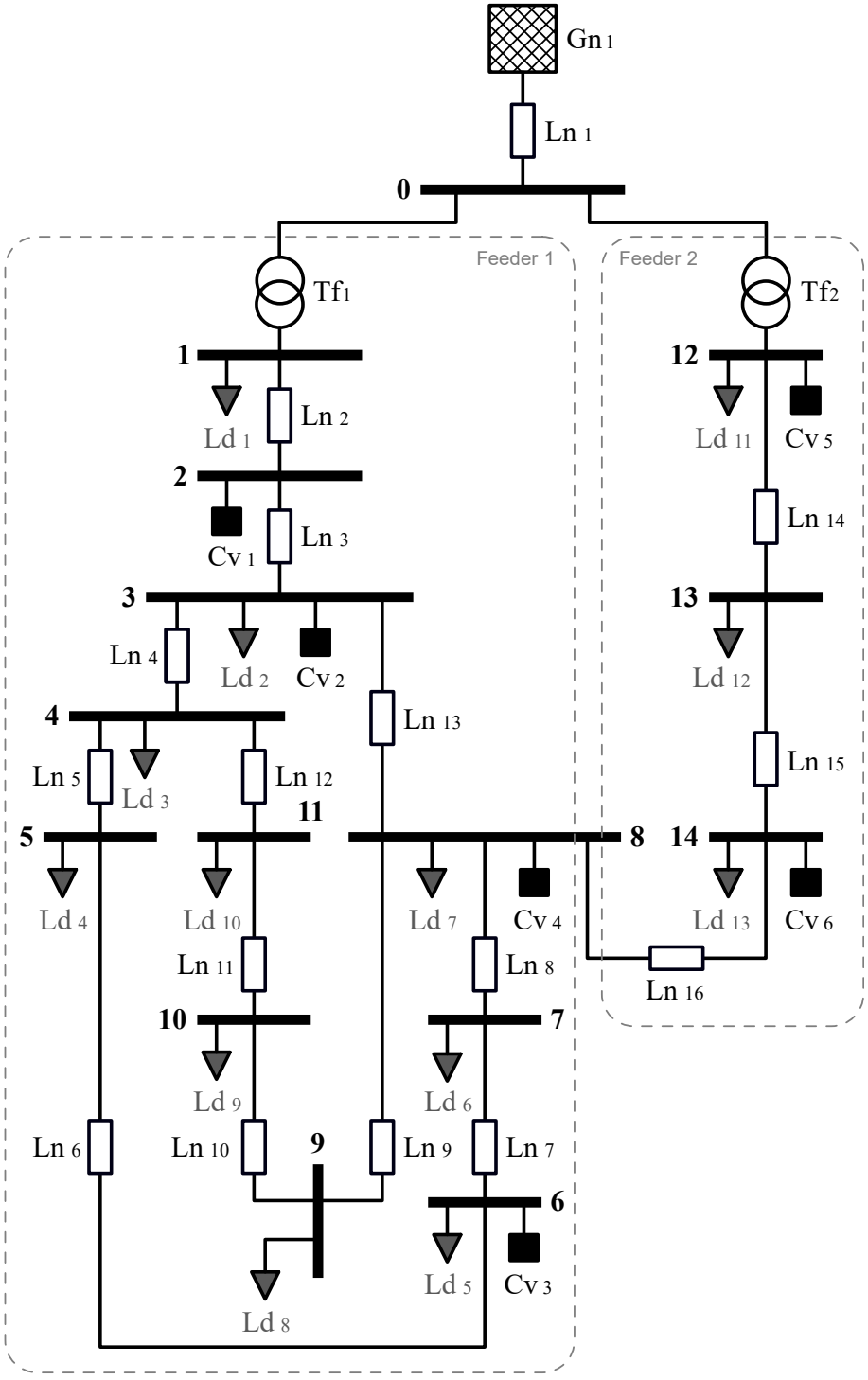


**Figure 3.9:** CIGRÉ medium-voltage distribution network (Use case II)

The transformers and loads are modelled as equivalent *RL* impedances. On the other hand, transmission lines are modelled with two different fidelity levels to observe their effect

on the small-signal stability. One benchmark variant is modelled with *RL* transmission lines (named Variant 1), whereas the second one is modelled with nominal $\pi$ transmission line circuits (Variant 2). The parameters of the transmission lines and transformers, as well as the generated/demanded power values, have been gathered from [124].

The use of simple element models for the considered test cases is justified since the objective of the chapter is to illustrate the operation and functionalities of the tool rather than analysing the accuracy of the obtained results. On the other hand, converter-driven stability is closely linked to distributed generation, and thus to distribution lines. When the frequency spectrum of the signals involved is not too wide, and assuming frequency-independent line parameters, distribution lines are commonly represented in literature as cascaded $\pi$ circuits. However, this approach has been also analysed for frequency-dependent transmission lines with satisfactory results in [125, 126].

In Variant 1 there are 62 state variables, whereas in Variant 2 there are 122. These are automatically reduced by CSTEP to a representation of 34 and 88 state variables, respectively. The reason for this significant reduction is that many currents of the system depend on other ones (e.g., the current from loads depends on the line current), and that the capacitors of adjacent $\pi$ equivalent transmission lines are connected in parallel (meaning that their voltage is equal). In other tools, the construction of such state-space models would have to be done either by manually writing all the equations (grouping adjacent inductors and capacitors) or by alternatively cascading $\pi$ and $T$ line models to avoid redundant states in the first place. Another alternative is the addition of "phantom" components to avoid the appearance of redundant states [119], but these parasitic elements introduce undesired dynamics and fictitious poles in the complex plane.

The root loci of the two benchmarks are illustrated in Fig. 3.10. The right side of the figure shows that both systems exhibit some relatively damped modes at similar locations in the complex plane. These are primarily related to the inductances of the lines and loads. In addition to these, the left side of Fig. 3.10 shows that Variant 2 exhibits several eigenvalues with an extremely low damping factor. In this case, their high imaginary component is caused by the low capacitance of the $\pi$ equivalent transmission lines. Such low damping factors will cause high-frequency oscillations under power disturbances in the system.

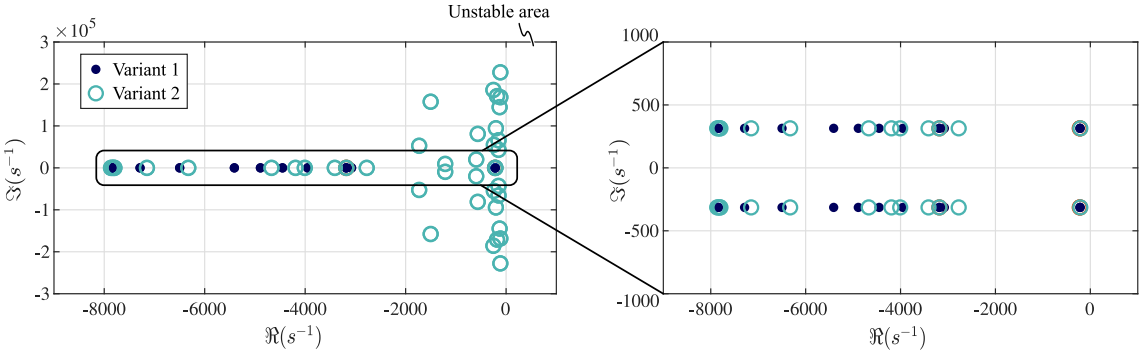


**Figure 3.10:** Use case II: root loci of the CIGRÉ benchmark for *RL* transmission lines and $\pi$ equivalent lines

The participation factor analysis of the eigenvalues shows that the most poorly damped eigenvalues—the so-called dominant modes—are associated with the state variables of transmission lines 2, 13 and 16 in Variant 1, and to 7, and 11 and 12 in Variant 2. This means that

the buses adjacent to these lines are more prone to oscillate under the same load or generation variation. The frequency of these oscillations will be the same as the frequency of the eigenvalues, but the amplitude will be dependent on how these modes are excited. From this study, it can be already seen that the fidelity of transmission lines returns different dominant oscillation modes for the same benchmark.

Since another potential application of CSTEP is the study of the integration of converters in the grid, 6 converter-interfaced devices have been included in Variants 1 and 2 of Use case III. These converters are connected to the grid by means of $LC$ filters and their location is shown in Fig. 3.9. Their control consists of a classical power controller based on $dq$ current PI regulators. The converters are equipped with a SRF-PLL to synchronize with the grid. The root loci of Variants 1 and 2 including these converters are shown in Fig. 3.11. Apart from increasing the number of oscillatory modes, on the right side of the figure, it can be observed that the converters generate less damped oscillation modes compared to the previous results. This might lead to a more oscillatory behaviour under power disturbances. To study the effect of these additional modes, the simulation module provided by CSTEP is used.

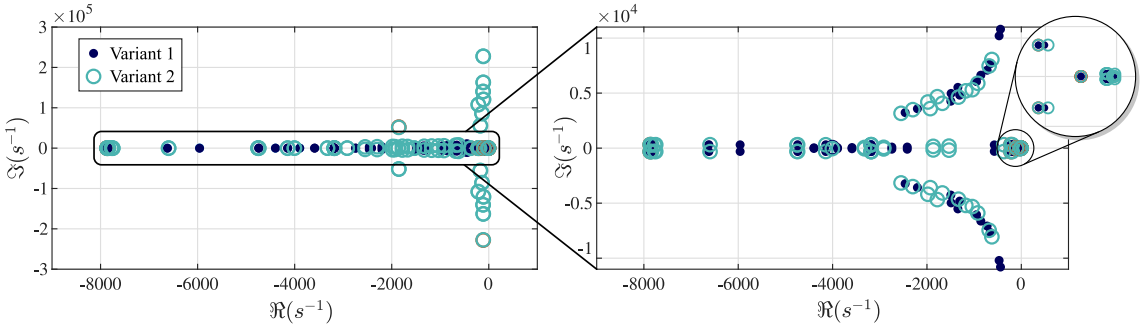


**Figure 3.11:** Use case II: root loci of the CIGRÉ benchmark for the penetration of electronic power converters

Figure 3.12 shows the dynamic response of the current through line 1 for a $0.05\,p.u.$ and a $-0.1\,p.u.$ power reference variation of $C_{v_3}$ at instants $t = 1\,s$ and $3\,s$, respectively. The comparison between the linearized (LIN) and nonlinear (NL) representations of Variants 1 and 2 shows that the small-signal models are accurate even for a $0.1\,p.u.$ disturbance.

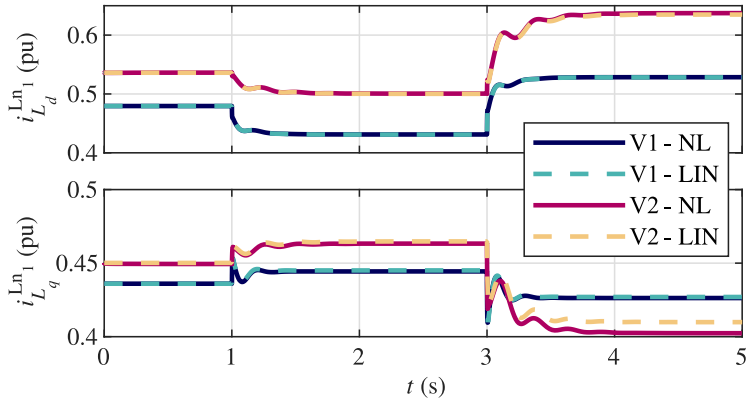


**Figure 3.12:** Use case II: line 1 current evolution under $0.05\,p.u.$ and $-0.1\,p.u.$ current perturbation of the inverter at instants $t = 1\,s$ and $3\,s$

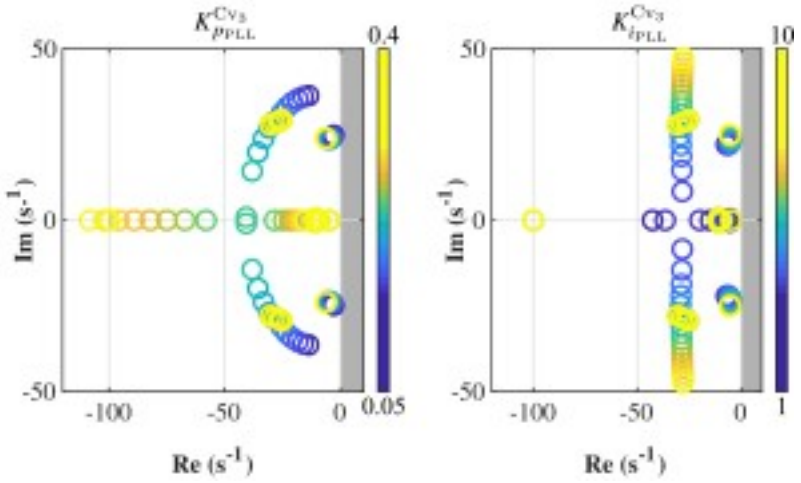


**Figure 3.13:** Use case II-Variant 2: parametric sweep of PLL proportional and integral gains

Depending on the type of model employed for transmission lines, the system exhibits a different transient response under the same power disturbance, and the currents converge to different operation points in steady-state. In fact, Variant 2 exhibits a more oscillatory current response, and the q-axis term has a larger transient response and current excursion after the perturbation at $t = 3s$ .

Following the example of Use case I the analysis can be extended, for example, by studying the effect of varying controller parameters on the movement of eigenvalues. Fig. 3.13 shows the movement of eigenvalues in the complex plane for variations of the proportional and integral gains of the PLL of $C_{v_3}$. For instance, a slight modification of the proportional gain can significantly change the damping and hence the stability margins of the system. This brings out the necessity not only to automatically build small-signal models, but also to provide a time-domain study to corroborate the analytical results. This does not make the small-signal model invalid or useless, because it can still be used to identify which are the states and parameters associated to the unstable modes, modify the design of the system and increase the stability margins. Regarding the integral gain, the damping of poles varies for different values of the parameter. However, in this case, they do not tend to approach the unstable region. The results elucidate that the topology of the studied system, the fidelity with which the transmission lines are modelled, or control parameters play a key role in the dynamic behaviour of the system. Other aspects such as the type of control employed at the converters, the model fidelity of transformers, or the consideration of a nonstiff grid in the system will also modify the dynamic properties of the system. However, since the purpose of this chapter is to show the potential applications and advantages offered by CSTEP, these studies are left for future research activities. CSTEP is providing information that might be challenging to get otherwise, since most available tools either 1) do not provide an automatic method for connecting element models, 2) do not consider the dynamics of line impedance, filters and converter controllers in the assessment of converter stability, and/or 3) they simulate the electromagnetic transients with a high level of detail for a short period but do not provide any analysis of the oscillation modes.

## 3.3 Summary

Power systems are suffering one of the most significant paradigm shifts because of the massive integration of electronic power converters. Even though there are a wide number of tools capable of carrying out stability analyses of conventional power systems, these tools do not consider the faster dynamics introduced by the electrical part of the grid or by power converters. This chapter has described a new converter stability analysis tool called CSTEP to simulate and analyse the stability of power systems with a considerable penetration of converters. This tool makes it possible to consider not only the electromechanical dynamics of machines, but also the electromagnetic dynamics of the grid and the effect of converter topology and controllers.

In the chapter, the mathematical foundations of the tool that enable to automatically construct and reduce the system of equations representing a specific use case have been introduced, based on the individual element models. Moreover, the time-domain simulation module and the analysis module of CSTEP have been described. The former is useful to simulate the original nonlinear representation and the linearized small-signal model of the system, which facilitates the validation of the linearized models for further analyses and provides information under large disturbances.

The functionalities and potential applications of CSTEP have been proved by means of a simplified ac use case, a converter-dominated system following the 5-bus IEEE benchmark and the CIGRE medium voltage grid. The performance of CSTEP has been compared against RMS-based small-signal stability analysis tools used in commercial softwares. This comparison has demonstrated the need to use EMT modelling to perform the small-stability analysis of converter-dominated networks. Otherwise, critical oscillatory modes can be neglected leading to erroneous stability assessments.

# Chapter 4

# Comparative small-signal evaluation of advanced grid-forming control techniques

*A brief overview of the control techniques in grid-connected converters and the need for EMT models for stability analysis of electronically dominated grid have been presented in previous chapters. This chapter presents the small-signal modelling and analysis of the most recent grid-forming control techniques, namely the matching control (MC) and the dispatchable virtual oscillator (dVOC). These are compared to more classical SME techniques, such as synchronverters (SV) and voltage-controlled virtual synchronous machines (VCVSM) under different grid conditions. Besides studying their time-domain response (inertial behaviour, steady-state operation point, etc.), a thorough evaluation of the dominant eigenvalues of each control is carried out by obtaining the participation factors and the sensitivity to physical and control parameter variations. Simulation results are obtained for a grid-forming converter connected to a dynamic grid model that emulates different properties of low-inertia power systems—e.g. primary reserve, inertial strength, grid impedance, etc. Besides, hardware-in-the-loop experimental results are presented to validate the analysis.*

## 4.1 Introduction

As it has already been said, one of the main challenges to massively connect converters to the network is that—unlike classical synchronous machines with big inertia—they do not inherently respond under voltage or frequency variations [127]. Additionally, converters introduce much faster dynamics than synchronous machines, which may cause interoperability problems affecting the frequency and voltage regulation [25]. In response to these challenges, one of the solutions proposed by the research community is to control converters as GFM.

In recent years, a full range of GFM control techniques have been proposed to contribute to the regulation of the grid [128], starting from the droop control classically employed to regulate the speed of synchronous machines [129], to SME techniques [74] which incorporate the swing equation of a synchronous machine in the controller to deliver a synthetic inertial response under power imbalances. A more recent example is the so-called matching control (MC) [130], which takes advantage of the physics of the converter to deliver the energy stored in the dc-link in the event of changes in the grid frequency. Another recent approach is the dispatchable virtual oscillator (dVOC) [131], which guarantees almost global asymptotic stability for converter-based networks [132].

To correctly integrate these new control strategies into the power grid, it is necessary to ensure the system's proper operation in steady state and transient regimes. In this context, the small-signal analysis is one of the most used techniques to assess the dynamic behaviour of conventional networks and the stability with a high integration of nRES, since it allows to identify the location of the eigenvalues in the complex plane. In the field of grid-forming converters, the assessment of the small-signal stability has been used, e.g., to compare the equivalence of a virtual synchronous machine and the droop control, concluding that they are equivalent from the perspective of stability [65]. Another study analyses the SME techniques implemented with dynamic and quasi-dynamic models [133], while others compare their behaviour against classical SM [74, 134]. Nevertheless, when assessing the stability of the system, these studies model the grid as a single-machine, infinite-bus system with a fixed frequency.

The gradual integration of GFM converters in the grid has caused the necessity to employ grid models that considers dynamic variations of the frequency under power perturbations. In [135], for instance, the eigenvalues of a GFM-based network are studied and sensitivity analyses are carried out by considering load and line dynamics and GFM converters with internal voltage and current loops. Similarly, in [25] a small-signal study of a droop-based GFM converter connected to a dynamic grid model is carried out, where the dynamics of transmission lines are also included. In [136] the frequency stability of a SM and various GFM control approaches are discussed, but the study is limited to time-domain simulations.

This chapter aims to benchmark the small-signal properties of MC and dVOC control techniques against well-established SME strategies synchronverters (SV) and voltage-controlled virtual synchronous machines (VCVSM), taking into account the internal voltage and current loops. To this date, most small-signal stability studies have either considered the power system to be a stiff voltage source, or have been focused on a single control strategy. This chapter aims to go one step further by evaluating and comparing the behaviour of several GFM control strategies under different grid types and conditions. For that purpose, the GFM converter is connected to an equivalent low-inertia grid model capable of emulating different levels of aggregated inertia, damping, and lines impedances [25, 137, 138]. In addition to evaluating the time-domain response of the four GFM controllers, several parametric sensitivity analyses

are carried out to reveal the inherent small-signal properties of the controllers and to evaluate their performance under different grid conditions.

The operation points have been first analysed through time-domain simulations. Then, small-signal models are obtained to compare the critical modes, participation factors and parameter sensitivity of the GFM control parameters. After that, the dynamic properties of the controllers under different load variations, equivalent grid impedance, total inertia and level of converter penetration are analysed.

The results of the study have been experimentally corroborated by means of real-time hardware-in-the-loop (HIL) tests, where the controllers are implemented in an external Texas Instruments F28739D launchpad control hardware.

## 4.2 Use case modelling

In this section, a description of the scenario under study and the mathematical formulation of the converter and the equivalent grid model is included.

### 4.2.1 General system description

The scenario shown in Fig. 4.1 consists of a GFM converter connected to a low-inertia power system. Unlike in other studies where the grid is considered to be stiff, in this case it is represented by an aggregated grid model based on a simplified synchronous machine. The purpose of this non-stiff grid model is to emulate several grid conditions and grid types by representing different levels of aggregated inertia, damping or line impedances. The mathematical foundations of this model are explained in Section 4.2.2.

In addition to the GFM control algorithm, the converter model includes the output *LC* filter and inner current and voltage loops. Moreover, the dc-link capacitor dynamics and its regulation are also considered in this study. The details of this model are explained in Section 4.2.3.

To ensure the correct operation of the system, the converter dynamics are adjusted to satisfy the time scales of the synchronous machines.

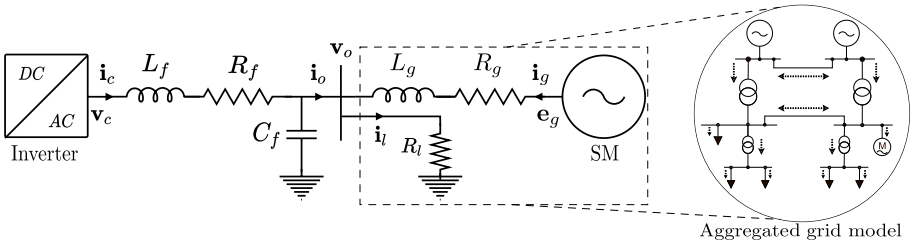


**Figure 4.1:** One-bus system comprised of GFM and aggregated grid model

### 4.2.2 Aggregated grid model

The electromagnetic behaviour of the aggregated grid model is represented by a simplified synchronous machine model that takes into account the dynamics of a governor and a turbine (Fig. 4.2).

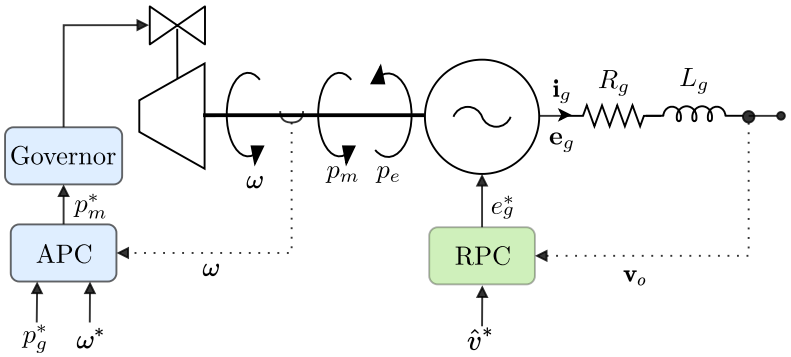


**Figure 4.2:** Synchronous generator model.

The electromechanical behaviour of the grid frequency is represented by the swing equation ($\omega$) [22]:

$$\frac{d\omega}{dt} = \left[p_m - p_e - k_{d_g}(\omega - \omega^*)\right] \frac{1}{2H_g} \tag{4.1}$$

where $p_e$ and $p_m$ are the electrical and mechanical power, respectively. $k_{d_g}$ is the damping constant of the frequency, $H_g$ the inertia constant and $\omega^*$ is the frequency reference.

The mechanical power is established by an aggregated turbine model, which in this case is modelled as a first-order transfer function:

$$\frac{dp_m}{dt} = \frac{1}{t_t}(g - p_m) \tag{4.2}$$

where $t_t$ represents the time constant of the equivalent turbine.

The input flow $g$ of this equivalent turbine is dependent on the governor, which has been also modelled as a first-order transfer function:

$$\frac{dg}{dt} = \frac{1}{t_g}\left(p_m^* - g\right) \tag{4.3}$$

where $t_g$ is the time constant of the governor.

The mechanical power reference $p_m^*$ is calculated with a $p/\omega$ droop regulator as follows:

$$p_m^* = p_g^* + k_{\omega_g}(\omega^* - \omega) \tag{4.4}$$

where $p_g^*$ is the output power reference.

The electrical behaviour of the grid currents is represented as a series *RL* impedance, given by:

$$\frac{d\mathbf{i}_g}{dt} = \frac{\omega_b}{L_g}\left[\mathbf{e}_g - \mathbf{v}_o - \left(R_g + j\,\omega L_g\right)\mathbf{i}_g\right] \tag{4.5}$$

where $L_g$ and $R_g$ are the equivalent grid-side inductance and resistance, respectively. $\mathbf{e}_g$ is the vector representing the voltage of the grid, which is controlled via a RPC.

The RPC generates the voltage reference with a $q/v$ droop controller with gain $k_v$:

$$e_s^* = \hat{v}_o^* + k_v\left(q_g^* - q_g\right) \tag{4.6}$$

where $\hat{v}_o^*$ is the voltage reference.

The grid voltage components are obtained as:

$$e_{s_d} = e_s^* \quad e_{s_q} = 0$$

### 4.2.3 Inverter with *LC* filter and inner loops

The dc-ac inverter model employed is a detailed representation of an average model represented in the SRF as shown in Fig. 4.3.

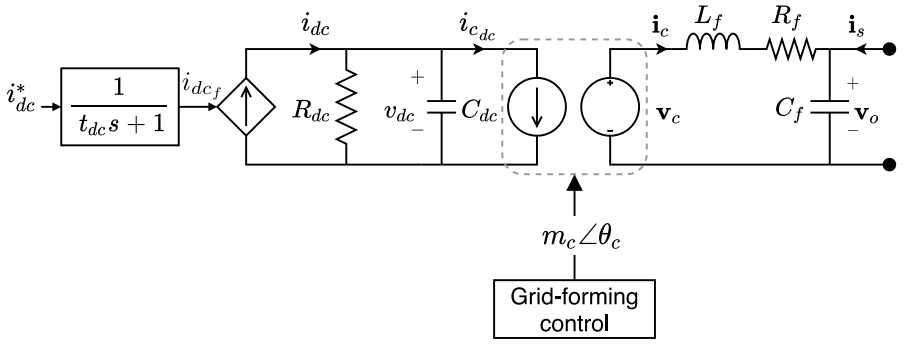


**Figure 4.3:** Converter model in SFR.

$L_f$, $R_f$ and $C_f$ are the inductance, series resistance and capacitance of the output filter of the converter, respectively. The current flowing through the filter inductor is modelled as follows:

$$\frac{d\mathbf{i}_c}{dt} = \frac{\omega_b}{L_f}\left[\mathbf{v}_c - \mathbf{v}_o - \left(R_f + j\omega L_f\right)\mathbf{i}_c\right] \tag{4.7}$$

where $\omega_b$ is the base frequency for the per-unit representation and $\omega$ is the frequency of the SRF. Vector notation with boldfaced symbols is used to represent variables that contain $d$ and $q$-axis components, e.g., $\mathbf{i_c} = i_{c_d} + ji_{c_q}$.

Since the inverter is represented with an average model, the converter output voltage $\mathbf{v}_c$ depends on the modulation index ($\mathbf{m}_c$) as follows:

$$\mathbf{v}_c = \mathbf{m}_c\, v_{dc} \tag{4.8}$$

where $v_{dc}$ is the dc bus voltage.

The voltage across the filter capacitor is modelled as:

$$\frac{d\mathbf{v}_o}{dt} = \frac{\omega_b}{C_f}\left[\mathbf{i}_c - \mathbf{i}_o - j\omega C_f\,\mathbf{v}_o\right] \tag{4.9}$$

Most of the studies in the literature assume that the bus voltage of inverters is constant. However, to obtain a more accurate representation of the voltage dynamics, the dc-bus is represented by a capacitor $C_{dc}$ and a parallel resistance $R_{dc}$ that accounts for the converter losses. This representation allows taking into account the voltage variations of the dc-bus. The voltage across the dc-bus capacitor is expressed as follows:

$$\frac{dv_{dc}}{dt} = \frac{\omega_b}{C_{dc}}\left[i_{dc} - i_{c_{dc}} - \frac{v_{dc}}{R_{dc}}\right] \tag{4.10}$$

where $i_{c_{dc}}$ is the dc-side converter current, which is obtained from the average inverter model as:

$$i_{c_{dc}} = \frac{v_{c_d}\, i_{c_d} + v_{c_q}\, i_{c_q}}{v_{dc}} \tag{4.11}$$

The dc current source, $i_{dc}$, is determined by a dc voltage control as proposed in [136]. This control is comprised by a proportional regulator and a feed-forward term of active power to compensate for the losses of the *LC* filter. The elimination of the steady-state error is taken into account to ensure correct synchronisation of the matching control and improve the voltage regulation of the rest of GFM approaches considered in this study:

$$i_{dc}^{*} = k_{dc}\left(v_{dc}^{*} - v_{dc}\right) + \frac{p^{*}}{v_{dc}^{*}} + \frac{v_{dc}}{R_{dc}} + \frac{p_c - p_o}{v_{dc}^{*}} \tag{4.12}$$

where $k_{dc}$ is the proportional gain, $p_c$ is the power passing through the converter, $p_o$ is the power measured at the PCC, $p^{*}$ is the reference of the output active power, $v_{dc}/R_{dc}$ is the current that flows through the resistor $R_{dc}$ that is added to compensate the losses on the dc side.

The generated current reference is then passed through a first-order filter that represents the dynamics of the dc bus current controller:

$$\frac{di_{dc_f}}{dt} = \frac{1}{t_{dc}}(i_{dc}^{*} - i_{dc_f}) \tag{4.13}$$

The grid-forming controllers considered in this study make use of the active and reactive power of the converter. These magnitudes are measured and then filtered with a first-order filter as shown in Fig. 4.3. The output of the controller is the modulation index $\mathbf{m_c}$, which is used in the average model of the inverter.

The modulation index is determined by an inner control loop composed of a PI voltage regulator in cascade to a PI current regulator, to control the output voltage and currents of the *LC* filter, respectively (Fig. 4.4). Although in the literature these internal loops have been treated mainly for the VCVSM, they are used in the SV, dVOC and MC in several studies because they provide a way to limit the voltage and current of the converter in the controller [136, 139, 140].

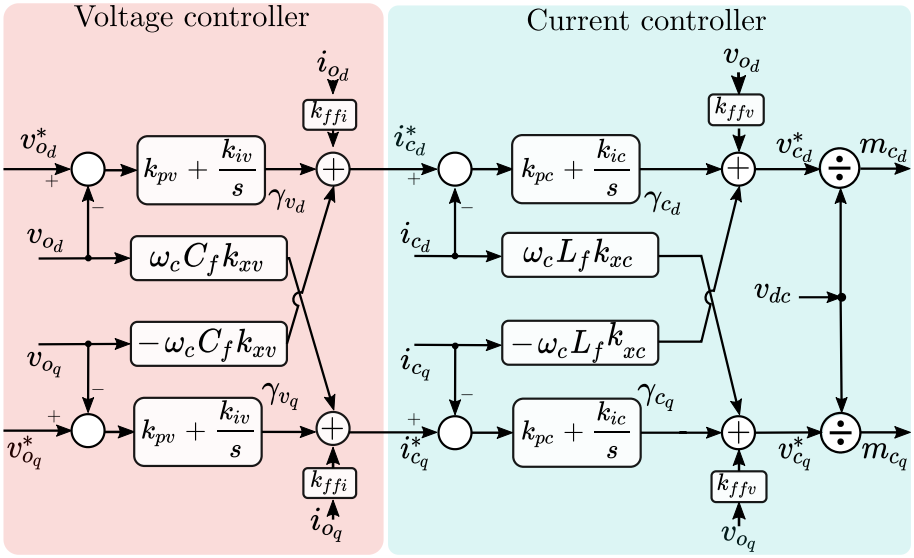


**Figure 4.4:** Block diagram of the inner loops.

## 4.3 Overview of grid-forming control techniques

### Synchronverter

Synchronverters (SVs) are the most straightforward technique to mimic the behaviour of a classical synchronous machine, since they usually do not include any inner voltage/current loop, and they do not estimate the grid frequency with a synchronising algorithm such as a PLL to determine the damping. Instead, it is assumed that the grid frequency is fixed in $\omega^*$, avoiding the use of frequency estimators [141]. A streamlined version is shown in Fig. 4.5.

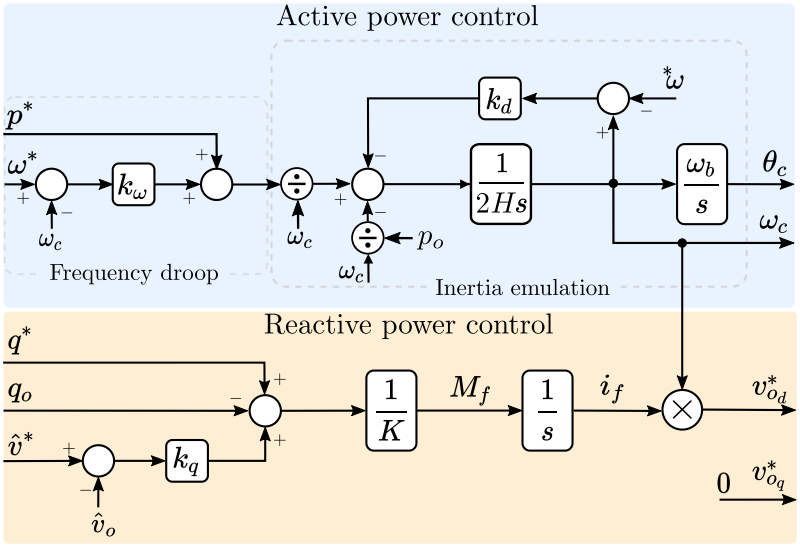


**Figure 4.5:** Synchronverter block diagram.

A SV, as other SMEs, is comprised by a frequency droop control with a gain $k_\omega$ and a damping term $k_d$. The control of the reactive power is usually carried out by a voltage droop control with gain $k_q$. The final reactive power reference is multiplied by a $1/K$ gain, integrated and multiplied by the angular speed to emulate the inner voltage of the synchronous machine.

### Voltage-controlled virtual synchronous machine

Voltage-controlled virtual synchronous machines (VCVSM) have been widely studied in the literature [65, 74], and the typical structure of active and reactive power loops can be observed in Fig. 4.6.

Compared to the SV, the higher number of control loops complicates the tuning of the control parameters, but at the same time it provides more degrees of freedom to adapt the dynamic behaviour of the converter. For the regulation of the active power, the controller includes a frequency droop with gain $k_\omega$ and the swing equation as in the SV. The difference is that VCVSMs also include a PLL to estimate the grid frequency that is used to calculate the damping term and a static virtual-impedance. The block diagram of the PLL shown in Fig. 4.6 follows the same configuration as the one used in [65], but other PLL approaches are also valid. Regarding the reactive power regulation, VCVSMs employ a voltage droop with gain $k_q$.

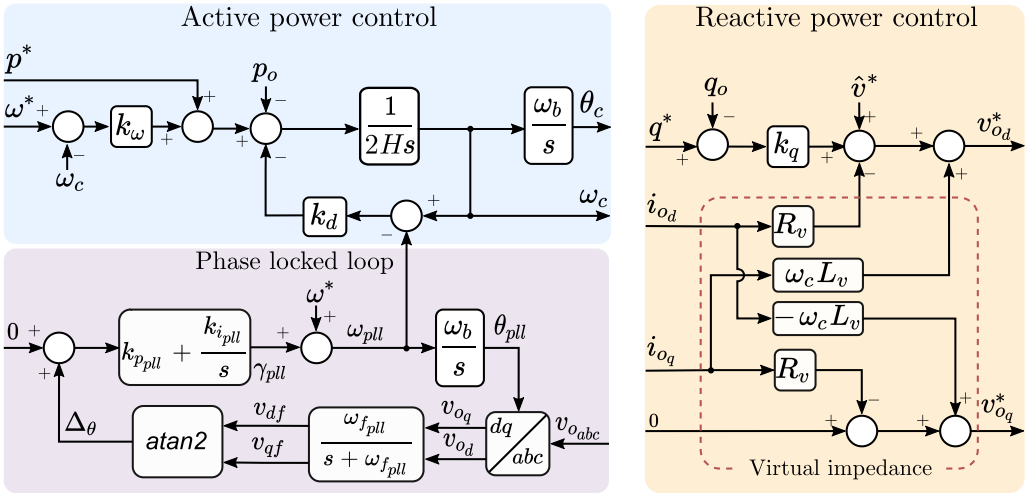


**Figure 4.6:** Active and reactive control of the voltage-controlled virtual synchronous machine block diagram.

### 4.3.1 Matching control

Matching control (MC) is a new control philosophy proposed initially in [142] and further studied in [130, 143, 144]. This control is different from classical SME techniques because it is based on the analogy between the rotor dynamics of synchronous machine ($\omega_r$) and the dc-link voltage dynamics ($v_{dc}$) of two-level inverters. These equivalences can be observed through the following expressions:

$$\underbrace{\frac{d\omega_r}{dt} = \left[\frac{\tau_m}{\omega_r} - \frac{\tau_e}{\omega_r} - k_d(\omega_r - \omega^*)\right]\frac{1}{2H}}_{\text{SM}} \leftrightharpoons \underbrace{\frac{dv_{dc}}{dt} = \frac{i_{dc}}{C_{dc}} - \frac{i_{c_{dc}}}{C_{dc}} - \frac{i_{R_{dc}}}{C_{dc}}}_{\text{2—level inverter}} \tag{4.14}$$

MC techniques are based on establishing a correlation between the speed of synchronous machine and the bus voltage as follows:

$$\frac{d\theta_c}{dt} = \psi\, v_{dc}\, \omega_b = \omega_c\, \omega_b \tag{4.15}$$

where $\psi = \omega^*/v^*_{dc}$. Considering the analogy between the dynamic equations established in 4.14 and the correlation between speed and bus voltage in 4.15, it is possible to define the remaining parameters as $k_d = \psi^2/R_{dc}$, $T_m = i_{dc}/\psi$ and $T_e = i_{c_{dc}}/\psi$.

In other words, the MC uses the energy stored in the bus capacitor to release it when there is a power imbalance in the ac grid, while the power losses caused by $R_{dc}$ behave as the damping term of the synchronous machine. Fig. 4.7 shows a possible implementation of the MC. This control does not have a reactive power controller, but a PI regulator with $k_{p\hat{v}}$ and $k_{i\hat{v}}$ constants to control the voltage at the PCC.

In this technique, the converter that regulates the dc voltage acts as a governor, so the dc-link control has to be based on a droop regulator that allows power-sharing.

### 4.3.2 Dispatchable virtual oscillator control

The techniques described above were designed to operate electronic converters as a synchronous machine to maintain scaling times of a traditional power system. Nevertheless, the

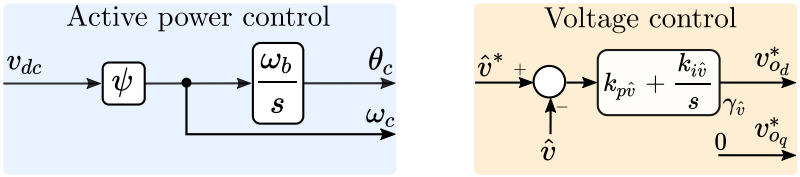


**Figure 4.7:** Matching control diagram block.

dispatchable virtual oscillator (dVOC) is based on the theory behind non-linear oscillators, allowing the synchronisation between converter-based networks. One notable feature of dVOC is its capability to rapidly stabilise the oscillator, i.e., reach the sinusoidal steady-state of the inverter output voltage from any initial condition [145].

Fig. 4.8 illustrates the block diagram of a dVOC in rectangular coordinates and for an inductive system ($\kappa = \pi/2$), where active and reactive power control loops can be distinguished.

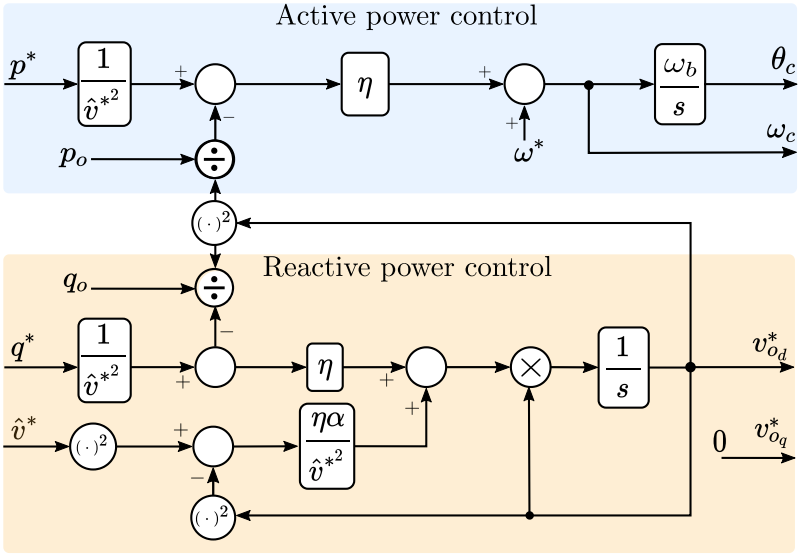


**Figure 4.8:** Dispatchable virtual oscillator block diagram.

## 4.4 Model validation, performance tests and modal analysis

To analyse the small-signal behaviour of the control techniques presented in Section 4.3, the methodology implemented in [74], which consists of modelling, validation of the small-signal model, and evaluation of the dynamic behaviour in response to power reference changes and grid frequency variations, is followed.

### 4.4.1 Small-signal modelling

The models of the generator, load, converter and each of the control approaches introduced in the previous section are first described via a set of DAE. The state vector of the system where the converter is controlled with an SV technique ($\mathbf{x}_{\text{SV}}$) contains 20 states, 29 states for the VCVSM ($\mathbf{x}_{\text{VCVSM}}$), 18 states for the MC ($\mathbf{x}_{\text{MC}}$) and 19 for the dVOC ($\mathbf{x}_{\text{dVOC}}$).

$$\mathbf{x}_{\text{SV}} = \left[ i_{g_d}\, i_{g_q}\, \omega\, p_m\, g\, i_{c_d}\, i_{c_q}\, v_{o_d}\, v_{o_q}\, v_{dc}\, p_o\, q_o\, i_{dc}\, \gamma_{v_d}\, \gamma_{v_q}\, \gamma_{c_d}\, \gamma_{c_q}\, \omega_c\, \theta_c\, i_f \right]$$

$$\mathbf{x}_{\text{VCVSM}} = \left[ i_{g_d}\, i_{g_q}\, \omega\, p_m\, g\, i_{c_d}\, i_{c_q}\, v_{o_d}\, v_{o_q}\, v_{dc}\, p_o\, q_o\, i_{dc}\, \gamma_{v_d}\, \gamma_{v_q}\, \gamma_{c_d}\, \gamma_{c_q}\, v_{dc}\, \gamma_{c_d}\, \gamma_{c_q}\, \gamma_{v_d}\, \omega_c\, \theta_c\, v_{df}\, v_{qf}\, \gamma_{pll}\, \theta_{pll} \right]$$

$$\mathbf{x}_{\text{MC}} = \left[ i_{g_d}\, i_{g_q}\, \omega\, p_m\, g\, i_{c_d}\, i_{c_q}\, v_{o_d}\, v_{o_q}\, v_{dc}\, \theta_c\, p_o\, q_o\, i_{dc}\, \gamma_{\hat{v}}\, \gamma_{c_q}\, \gamma_{v_d}\, \gamma_{v_q}\, \gamma_{c_d} \right]$$

$$\mathbf{x}_{\text{dVOC}} = \left[ i_{g_d}\, i_{g_q}\, \omega\, p_m\, g\, i_{c_d}\, i_{c_q}\, v_{o_d}\, v_{o_q}\, v_{dc}\, p_o\, q_o\, i_{dc}\, \gamma_{v_d}\, \gamma_{v_q}\, \gamma_{c_d}\, \gamma_{c_q}\, \theta_c\, v_{o_d}^* \right]$$

The input vector ($\mathbf{u}$) for the four cases is identical, and is defined as follows:

$$\mathbf{u} = \left[ p_g^*\, v_{dc}^*\, q^*\, p^*\, \omega^*\, \hat{v}^* \right]$$

Some of the equations that describe the dynamics of these state variables are non-linear, meaning that they have to be linearized around an operating point to obtain their state-space matrix form. To obtain the operating point, the time derivatives are made equal to zero and the resulting system of equations are solved. The equations are then linearized by applying the Taylor series expansion to obtain the small-signal model given in the form:

$$\Delta\mathbf{x} = \mathbf{A}(\mathbf{x}_0)\,\Delta\mathbf{x} + \mathbf{B}(\mathbf{x}_0)\,\Delta\mathbf{u} \tag{4.16}$$

where $\Delta$ represents the small signal variation and $\mathbf{x}_0$ is the operating point. The linearisation process and the time-domain and eigenvalue analysis is carried out in the software CSTEP, presented in the chapter 3.

### 4.4.2 Parameter values

The system parameters and the default set-points are listed in Appendix B - Tab. B.1. The base power $S_b$ is the power value employed to calculate all the system per-unit parameters and variables (Appendix C describes the methodology for defining the base values.). In this case, it has been defined to be equal to the rated power of the inverter (2.75MVA). The rated power of the equivalent grid model is not explicitly defined, since all aggregated parameters (inertia, damping, series impedance, etc.) are defined according to the base power. By modifying these $p.u.$ values, a more or less strong grid can be emulated with respect to the inverter. On the other hand, to provide a fair comparison and to guarantee the correct integration of the GFM converter in the system, the four control techniques are tuned to provide a similar steady-state and transient response (i.e., the rate of change of the output frequency or RoCoF). The methodology employed in [136] is used to adjust the droop gains of each technique. The internal voltage and current loops are the same for the four control strategies. The current loop parameters are designed with the modulus optimum criterion. The voltage loop and the PLL are tuned according to the symmetrical optimum criterion to ensure the maximum phase margin [146]. However, the $k_{iv}$ gain of the voltage loop (see Fig. 4.4) has been readjusted employing a parametric sweep.

### 4.4.3 Model validation and performance tests

#### Active power reference variation

Fig. 4.9 presents the behaviour of the linearized and non-linear model of the system described in Fig. 4.1 for a variation in the active power reference of the converter of $0.1\,p.u.$

The curves reveal that the linearized (small-signal) models and the original non-linear models coincide in their transient response for a step-shaped variation in the active power reference. The strong transient in the dVOC is due to this approach's disadvantage in adding synthetic inertia to the network without modifying the structure of the original control. Regarding the SV, the fluctuations have a frequency of oscillation which is very similar to that of the VCVSM. Nevertheless, the values of the SV in steady-state are different compared to the rest of GFM implementations because the damping factor term acts upon the virtual frequency and not the system frequency ($k_d(\omega_c - \omega^*)$). This might entail a disadvantage in grids where the SV plays a significant role in frequency regulation because it affects the power-sharing with respect to the rest of grid-forming systems. A different situation occurs with the VCVSM, which, by attaching the PLL to estimate the grid frequency and using it in the damping term, uncouples the effect of the damping and the droop and manages to take full advantage of this physical characteristic of synchronous machines to damp the oscillations in the power system. The MC exhibits a relatively clean and oscillation-free behaviour because its synchronisation is fast since the synthetic inertia delivered by the converter is limited by the size of the dc bus capacitor. These results also demonstrate that the small-signal models adequately represent the dynamics of the original models even for a significant deviation from the initial point of operation. Therefore, these small-signal models will be used to study further the oscillation modes and the influence of parameter variations in the following sections.

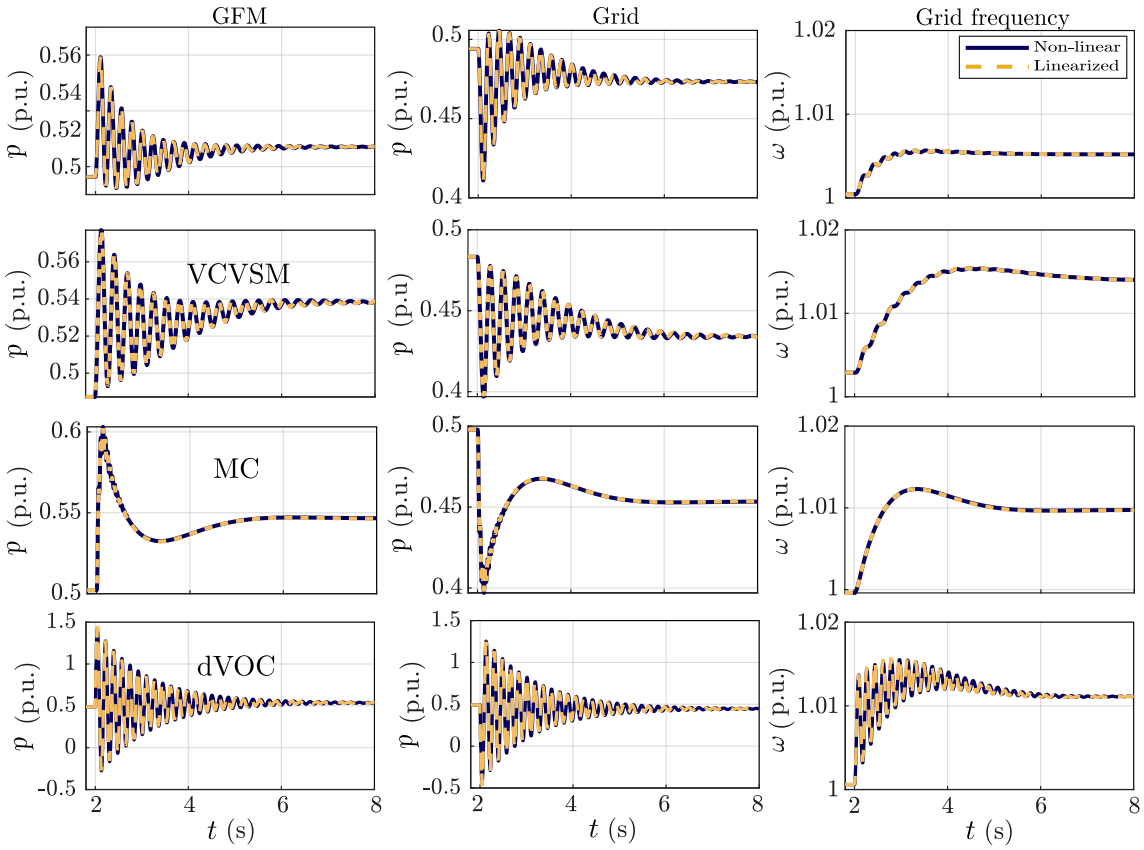


**Figure 4.9:** Validation of small-signal models under active power reference variations. From left to right, GFM power, SM power and grid frequency in each case.

### Load power variation

To analyse the frequency response against power imbalances, a change on the active power of the load ($R_l$ in Fig. 4.1) of $0.1\,p.u.$ is assumed at $t = 2s$. Fig. 4.10 a and b show the active power behaviour of the converter and the grid, respectively. As mentioned above, the SV damping term affects the steady-state of the grid, and in the event of variations in the system load, the SV tends to deliver more active power to the grid. In the other strategies, the active power has similar steady-state behaviour in each case; however, there are some small differences, primarily caused by each technique's type of reactive power regulation. Concerning the frequency behaviour, all cases show better damping of the oscillations than when the power reference is varied. Fig. 4.10-c shows the frequency behaviour, where the techniques have a similar RoCoF. Nevertheless, the MC exhibits a higher frequency drop with a steeper slope because the dc capacitor is insufficient to deliver the same synthetic inertia as the other techniques studied.

Fig. 4.10-d depicts the voltage behaviour at the PCC. The dVOC achieves a fast and accurate voltage control while keeping load sharing capability. In comparison, the SV and VCVSM show a slight voltage drop, although the SV reaches steady-state more slowly due to the integrator and the division by $K$, which behaves like a low-pass filter.

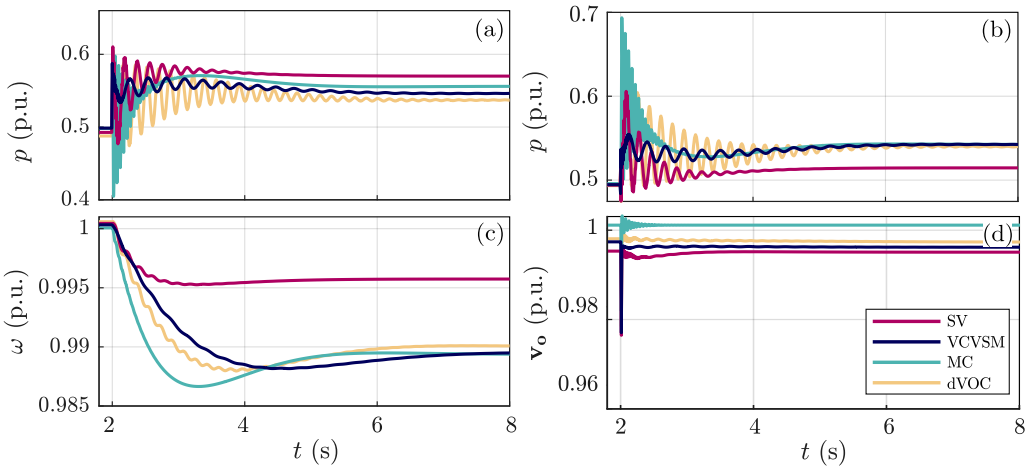


**Figure 4.10:** Response against load variations of the lineal model. a) active power of the converter. b) Synchronous generator active power. c) Grid frequency. d) Voltage of the PCC.

## 4.4.4 Modal analysis

A popular technique to assess the stability of power systems is to analyse the eigenvalues of the matrix **A** of the linearized state-space model in Eq. (4.16). The properties of these eigenvalues provide helpful information about the system dynamics such as the damping factor, the sensitivity to parameter deviations, the relation between states and oscillation modes (via the participation factors) and the oscillation frequencies.

The properties of the most relevant eigenvalues for the investigated control techniques are gathered in Table 4.1. Critical eigenvalues are defined as those with a real part greater than $-15$ and a damping ratio lower than 15%.

The modes that are most influenced by the grid-forming control reveal that the SME techniques present similar oscillation frequencies and damping factors. However, the VCVSM at-

**Table 4.1:** Critical eigenvalues and their most relevant information.

| Case | Eigenvalue | $\zeta$ | $f_{osc}$ (Hz) | Participating state | Parameter sensitivities |
|---|---|---|---|---|---|
| SV | $-0.99 \pm 28.05j$ | 0.03 | 4.46 | $\theta_c\ \omega_c\ \omega$ | $k_{ffi}\ R_f\ R_g\ H$ |
| | $-1.39 \pm 0.62j$ | 0.91 | 0.09 | $\tau_m\ \omega\ \omega_c$ | $t_t\ t_g\ H_g\ H$ |
| | $-4.69$ | 1 | 0 | $i_f$ | $k_v\ K\ k_q$ |
| | $-5.66 \pm 25j$ | 0.21 | 4.20 | $v_{dc}\ i_{dc}$ | $t_{idc}$ |
| | $-8.84 \pm 370j$ | 0.02 | 59 | $i_{s_d} i_{s_q}\ i_{c_d}\ i_{c_q}$ | $R_g\ k_{ffi}\ R_f$ |
| | $-10$ | 1 | 0 | $g$ | $t_g$ |
| VCVSM | $-0.74 \pm 0.74j$ | 0.70 | 0.1 | $\tau_m\ \omega\ \omega_c$ | $t_t\ t_g\ k_{d_g}\ H_g$ |
| | $-0.81 \pm 22.49j$ | 0.03 | 3.60 | $\theta_c\ \omega\ \omega_c$ | $k_{p_{pll}}\ R_v\ k_{ffv}$ |
| | $-5.68 \pm 25j$ | 0.21 | 4.20 | $v_{dc}\ i_{dc}$ | $t_{idc}\ C_{dc}$ |
| | $-8.73 \pm 16j$ | 0.47 | 2.50 | $\varepsilon_{pll}\ \theta_{pll}$ | $k_{p_{pll}}$ |
| | $-10$ | 1 | 0 | $g$ | $t_g$ |
| | $-14.25 \pm 501j$ | 0.02 | 79 | $i_{s_d}\ i_{s_q}$ | $R_v\ k_{ffi}\ L_v$ |
| MC | $-1.14 \pm 1.11j$ | 0.71 | 0.20 | $\omega\ \tau_m$ | $t_g\ t_t\ R_g$ |
| | $-3.57$ | 1 | 0 | $\gamma i_v$ | $k_{p_c}\ k_{ffi}\ k_{i_v}$ |
| | $-5.96 \pm 123j$ | 0.04 | 19.7 | $v_{dc}\ \theta_c$ | $R_g\ k_{ffi}\ R_f$ |
| | $-7.34 \pm 365j$ | 0.02 | 58 | $i_{s_d}\ i_{s_q}$ | $R_g\ k_{ffi}\ R_f$ |
| | $-10$ | 1 | 0 | $g$ | $t_t$ |
| | $-15.42 \pm 114j$ | 0.74 | 2.20 | $p_o\ i_{dc}$ | $k_{ffi}\ L_g\ R_f$ |
| dVOC | $-0.92 \pm 36j$ | 0.02 | 5.73 | $\theta_c\ p_o\ \omega$ | $R_f\ k_{ffi}\ R_g$ |
| | $-0.60$ | 1 | 0 | $v^*_{o_d}$ | $\eta\ k_v$ |
| | $-0.87 \pm 0.90j$ | 0.70 | 0.10 | $\tau_m\ \omega\ p_o$ | $\eta\ t_g\ t_t$ |
| | $-5.67 \pm 25.67j$ | 0.21 | 4.08 | $v_{dc}\ i_{dc}$ | $t_{idc}\ C_{dc}$ |
| | $-10$ | 1 | 0 | $g$ | $t_g$ |
| | $-9.27 \pm 369j$ | 0.02 | 58 | $i_{s_d}\ i_{s_q}\ i_{c_d}\ i_{c_q}$ | $R_g\ k_{ffi}\ R_f$ |

Modes associated to the grid-forming control.
DC circuit modes.
Modes associated to inductance currents ($\mathbf{i}_{PCC}$).
Aggregated grid related modes.

tenuates the oscillations better due to the virtual impedance and a higher damping factor, which is provided by estimating the frequency with a PLL and does not impact the droop response. On the other hand, the dVOC modes show that it is possible to achieve a similar inertial response to SME techniques thanks to the delay added by the first-order filter in the active power. However, the oscillations present a very low damping and it is not possible to attenuate them by modifying the control parameters. In the case of MC, the delivered synthetic inertia is proportional to the energy stored in the dc-link capacitor (Eq. (4.14)). Therefore, achieving a level of inertia comparable to that of the other techniques would require a large bus capacitor. This fact becomes evident in the behaviour of the modes associated with the GFM control, which exhibit a frequency of oscillation as a consequence of the lower inertia that is higher than in the other cases. Therefore, achieving inertia comparable to the other

techniques would require a significantly large bus capacitor.

The modes associated with the electro-mechanical behaviour of the grid are very dependent on the slow dynamics of the turbine and the governor of the network. However, in the case of the MC, the modes associated to the grid oscillate slightly faster, since the converter delivers less synthetic inertia and synchronises faster. On the other hand, the SV, VCVSM, and dVOC exhibit similar oscillation modes related to the dc bus, because they decouple the ac and dc sides by dividing the modulation signal by the bus voltage ($\mathbf{m}_c/v_{dc}$). In the MC, the dc bus voltage $v_{dc}$ determines the electrical frequency behaviour of the grid, resulting in interactions between the ac and dc side. The parametric sensitivity of the eigenvalues associated to $\theta_c$ shows that they are strongly linked to the equivalent impedance at the connection node and the *LC* filter. Therefore, if the damping of the MC-controlled converter needs to be improved, the size of the *LC* filter must be modified.

The modes associated with the inductance currents are determined by the synchronous frequency resonance and depend on the equivalent grid impedance $[(R_g + R_f) + j\omega(L_f + L_g)]$ [147]. Analyzing the parametric sensitivities of these modes in the four cases, it can be concluded that the voltage regulator of the inner loops plays an essential role in the dynamics of these modes since it is possible to modify the *LC* filter dynamics through the constants of these regulators. Additionally, these modes are affected by network and filter resistance parameters because they provide damping; however, increasing their values would mean an increase in power losses. The VCVSM resolves this by incorporating a virtual impedance, which modifies the impedance seen by the converter and adding a great versatility over these modes. Regarding the SV, MC and dVOC, they show a lower flexibility to modify these oscillation modes, but e.g. the dVOC achieves a higher damping thanks to its robust voltage control.

## 4.5 Parametric sensitivity analysis

In this section a systematic parameter sensitivity analysis for each case is presented. The purpose of the section is twofold: on the one hand, the influence of physical or control parameter variations in the oscillation modes of the system is studied; on the other hand, the performance of the controllers is evaluated for different grid conditions such as aggregated inertia, damping and grid-side impedance.

### 4.5.1 Control parameter variation

The first part consists of studying the impact of the control parameters to demonstrate possible ways of tuning each of the grid-forming techniques.

#### Synchronverter

The synchronverter features a swing equation-based active power regulator that includes a $k_d$ gain for the damping, an inertia constant $H$ and a frequency droop regulator with a $k_\omega$ droop gain to mimic the governor of a classical SM.

The parameter $K$ and the reactive power low-pass filter time constant ($t_q$) are equivalent considering that they act on the reactive power loop dynamics adding a delay on the virtual flux current. The droop parameters $k_\omega$ and $k_q$ define the steady-state behaviour of the active and reactive power and, during transients, they add damping to the critical modes related to grid frequency and currents.

Fig. 4.11 represents the loci of eigenvalues for different parametric sweeps. As the inertia constant $H$ decreases, the dynamics associated to the GFM become faster. However, for very low levels of inertia, the modes related to $\mathbf{i}_{PCC}$ become unstable because the electromechanical dynamics of the converter are in conflict with the inner loops of the converter and the electrical components of the grid. In contrast, high values of inertia constants imply more oscillatory and less damped systems, increasing the time required for the settling between the converter and the grid. Fig. 4.11-b illustrates how, as the damping gain $k_d$ increases, the frequency of the GFM modes raises as well. Finally, the constant $K$ acts as the time constant of a low-pass filter, determining the dynamics of the reactive power loop. Increasing $K$, the eigenvalue related to $i_f$ slows down and delays the reactive power regulation improving the damping of the modes associated to $\mathbf{i}_{PCC}$.

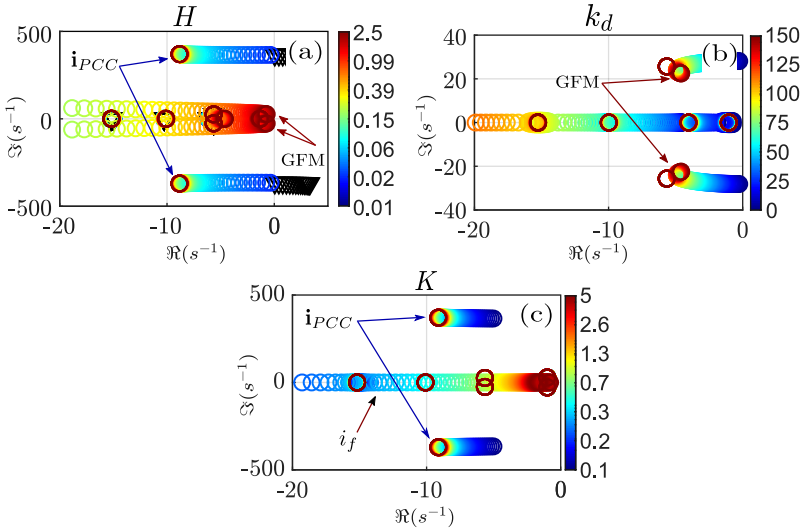


**Figure 4.11:** SV parameter sweep. a) inertia constant ($H$). b) Damping constant ($k_d$). c) Constant $K$.

### Voltage-controlled virtual synchronous machine

Fig. 4.12 presents a sweep of the control parameters related to the critical modes of the system. Varying the inertia constant $H$ affects the eigenvalue trajectories as those seen in the SV. However, in this case, varying $k_d$ improves the damping and, thus, the stability margins without affecting the active power-sharing. The reason is that a PLL is used to estimate the grid frequency, meaning that the damping will only react during transients but not affect the steady-state response. This behaviour is more in accordance with the damping effect of a synchronous machine. The virtual impedance values give great flexibility to the VCVSM because as $R_v$ increases, the modes associated to $\mathbf{i}_{PCC}$ move across the real axis. Nonetheless, one limitation is that it affects the behaviour of the voltage in steady-state [6]. As $L_v$ becomes larger, the modes of $\mathbf{i}_{PCC}$ are damped faster, thus, the virtual impedance can be tuned to adjust the position of the eigenvalues related to the synchronous frequency resonance.

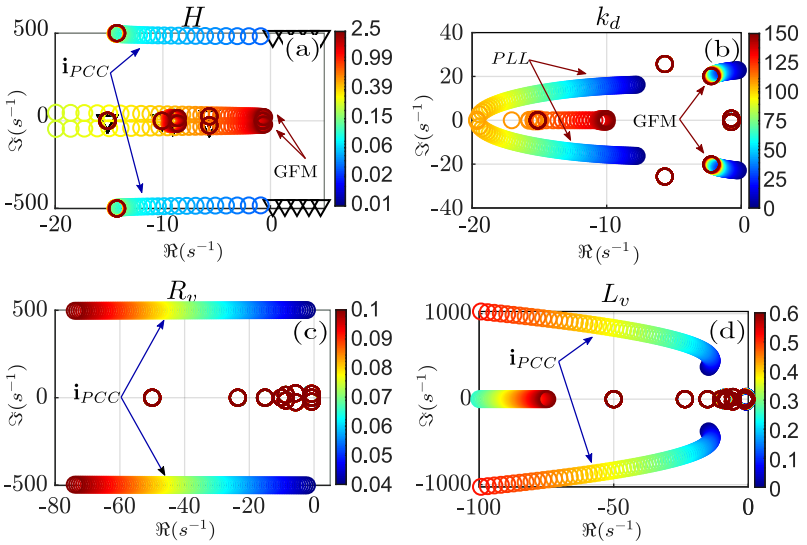


**Figure 4.12:** VCVSM parameter sweep. a) inertia constant ($H$). b) Damping constant ($k_d$). c) Virtual resistance ($R_v$). d) Virtual inductance ($L_v$).

### Matching control

In the MC control the emulated inertia $H_{dc}$ is directly related to the bus capacitor $C_{dc}$ as:

$$H_{dc} = \frac{1}{2}\frac{C_{dc} v_{dc_b}^2}{S_b} \tag{4.17}$$

where $v_{dc_b}$ is the base dc voltage.

From this equation it can be observed that even for relatively high bus capacitors, the equivalent inertia constant is very low. For instance, for $C_{dc} = 6.28\,p.u.$, the inertia constant is $H_{dc} = 0.01\,s$. Fig. 4.13-a shows the variation of the inertia constant (i.e. the bus capacitor size).

When the values are low, the GFM-related modes become unstable due to the incapacity of the dc bus to maintain the system frequency. However, the system becomes stable when the inertia constant is $H_{dc} = 0.024\,s$ ($C_{dc} = 15.07\,p.u.$). As the capacitor stores more energy, the system gains damping. However, to improve the RoCoF similar to an SME under the same grid conditions, the inertia constant needs to be around $H_{dc} = 2\,s$, which is equivalent to $C_{dc} = 2513\,p.u.$ Therefore, this type of control exhibits a limitation to emulate a higher inertial behaviour due to the physical constraints with the bus capacitor size. In any case, the dc supply emulates the response of a governor, so by making the response of this supply faster (i.e. reducing $t_{idc}$), the GFM could respond more quickly to power imbalances and thus keeping the size of the bus capacitor at more realistic values (Fig. 4.13-b). Concerning the voltage control, the system shows better performance at reduced values of $k_{p_{\hat{v}}}$ and $k_{i\hat{v}}$ (Fig. 4.13-c and d).

### Dispatchable virtual oscillator control

The dVOC is composed of the active power droop gain $\eta$ and a reactive power droop gain $\alpha$, which at the same time determines the speed of the integrator of $v_{o_d}^*$. As previously mentioned, the dVOC does not provide synthetic inertia to the grid, so the active power filter

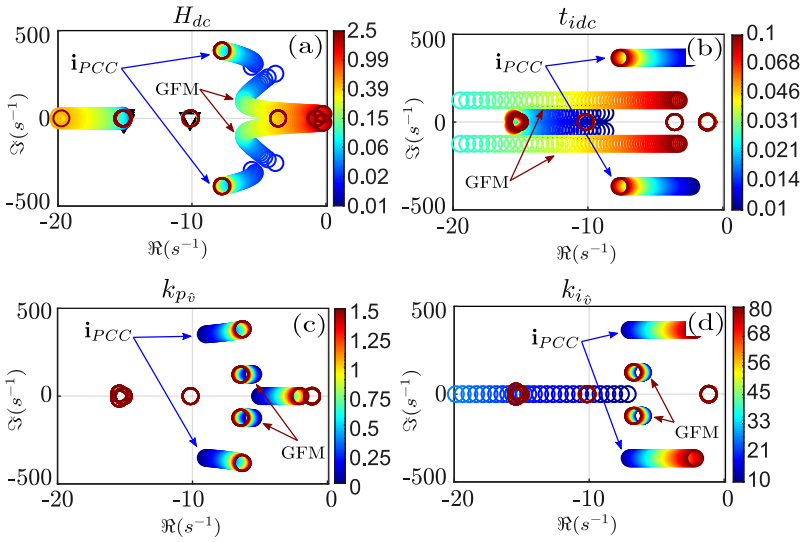


**Figure 4.13:** MC parameter sweep. a) Inertia provided by the dc-bus capacitor ($H_{dc}$). b) Constant time of the dc source ($t_{idc}$). c) Proportional gain of the voltage regulator ($k_{p\hat{v}}$). d) Integral gain of the voltage regulator ($k_{i\hat{v}}$).

has an essential role in this control technique since it is the only way to modify the dynamic of the active power delivered by the converter to the grid during transients.

The parametric sweep of the dVOC control parameters shows that the constant $\eta$ makes the system stable only in a very narrow range of values. When $\alpha$ increases, the mode associated to $v^*_{o_d}$ moves on the real axis, although at the same time, the $\alpha$-$\eta$ ratio is lost, and the converter decreases its participation in the regulation of the reactive power. On the other hand, the time constant of the active power filter $t_p$ slows down the mechanical modes but the dominant eigenvalues related to $\mathbf{i}_{PCC}$ increase their speed with the same behaviour of the SME inertia constant ($H$). In general, the dVOC is modelled as a resonant circuit, and has the advantage of providing a fast and reliable voltage and frequency loop in a way that allows it to respond quickly to changes in the grid. However, the sweep of its parameters reveals the difficulty of improving the damping to the modes related to the GFM control.

### 4.5.2 Grid condition variation

Due to all the different devices connected to power systems, their operation points constantly vary, whether due to generation/load variations, contingencies or market operations. In the following sections, a study is carried out to analyse the behaviour of the controllers under various grid conditions. The parameters that are varied include the load power, the grid-side impedance ($L_g$) and the converter rated power.

#### Load variation

In an electrical network, the load is one of the most frequently changing variables, which means that the grid operator has to constantly forecast the power demand and ensure an adequate grid operation. To examine the stability of the system against load variations, a sweep of the load resistance connected at the PCC in Fig. 4.1 is carried out. The results in Fig. 4.15 show that the critical modes associated with the PCC currents $\mathbf{i}_{PCC}$ lose damping as

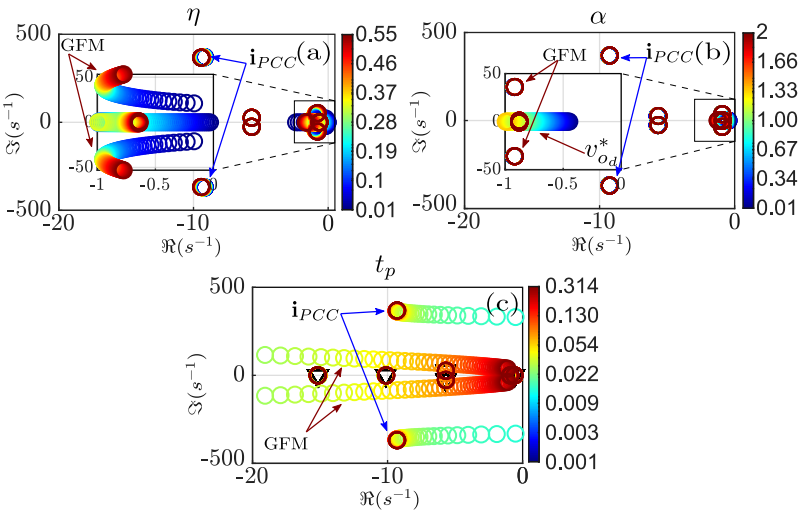


**Figure 4.14:** dVOC parameter sweep. a) ($\eta$) gain. b) ($\alpha$) gain. c) Active power filter time constant ($t_p$).

the load increases—i.e. as the power consumed by the load increases. This is caused by the damping added by the resistive load. In particular, these modes are slightly affected in the SV, while in the VCVSM and dVOC, they are more dependent on the equivalent impedance in the PCC due to its reactive power regulator. In the MC, the modes related to $\mathbf{i}_{PCC}$ are more sensitive to load variations than the rest of controllers, even to the point of becoming unstable when the load is close to the rated power of the inverter. Likewise, in the MC the modes associated to the GFM have faster dynamics than the other approaches; thus, the equivalent impedance at the PCC strongly affects the behaviour of the grid frequency against power imbalances.

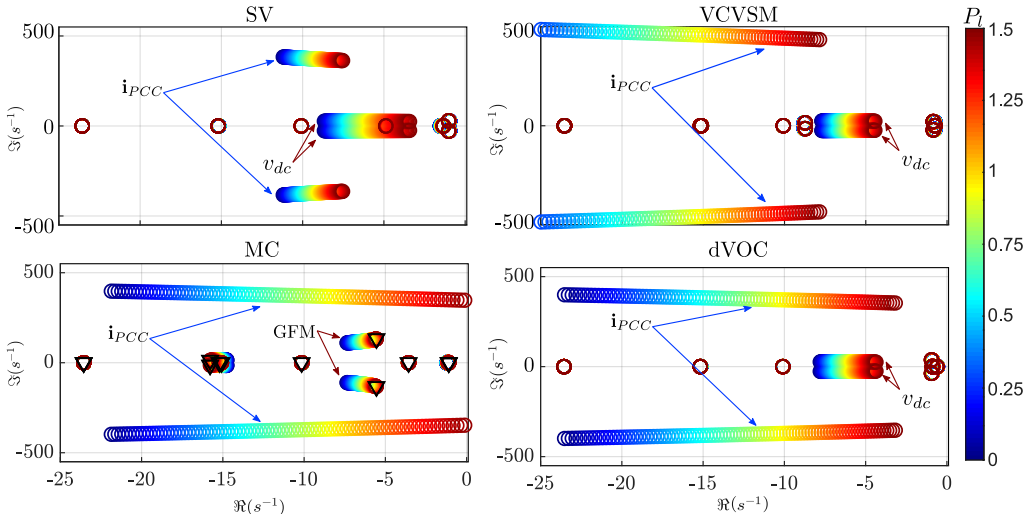


**Figure 4.15:** Eigenvalue trajectory for different load operation points.

### Grid-side impedance variation

Several articles in the literature have recently shown that the equivalent grid inductance at the PCC plays a key role in the stability of GFM converters [102, 103]. Fig. 4.16 shows the loci of eigenvalues for variations of the equivalent inductance of the grid ($L_g$), for each of the GFMs. The results reveal that in all cases, the modes associated with the GFM lose damping at reduced values of $L_g$ since a slight variation in the frequency can lead to a significant increase in the power delivered by the converter. This causes a reduction in the stability margins, and can result in instabilities. The VCVSM achieves a better performance thanks to the virtual inductance ($L_v$) and the damping term, which improves the damping of the GFM modes as has been previously shown in Fig. 4.12. The SV does not have the same degrees of freedom as the VCVSM and has limitations to increase the damping; this makes the GFM modes more vulnerable to grid-side inductance variations. The dVOC shows unstable points, but this can be solved by changing $\kappa = 0$ to adapt the controller to a resistive line [132]. Concerning the MC, it does not exhibit an electromechanical behaviour with the same time scales as the other controllers. This aspect makes it more susceptible to grid impedance variations.

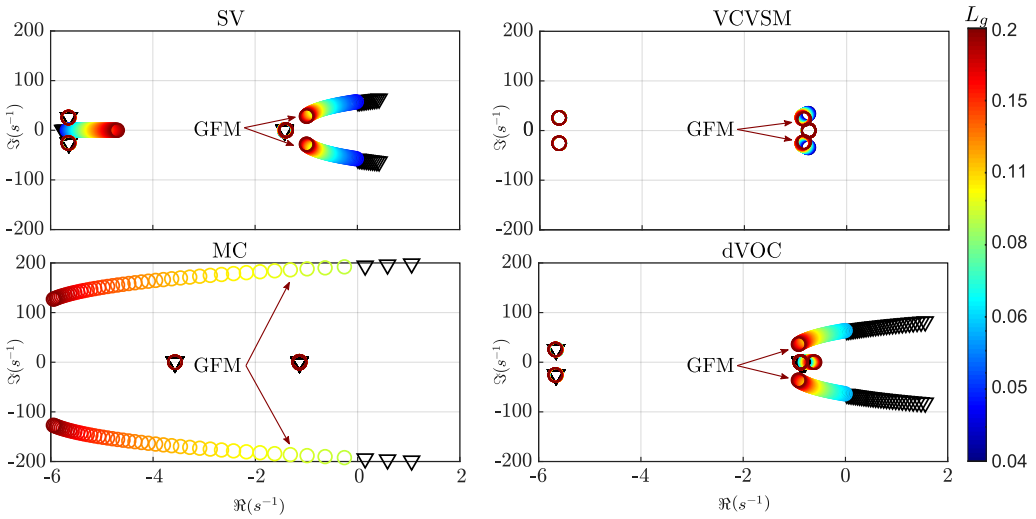


**Figure 4.16:** Eigenvalue trajectory for different grid-side impedance values.

### Grid inertia variation

In recent years, the inertial response of power systems has gained importance because the integration of RES into the power system leads to a reduction of the physical inertia connected to the grid, endangering the frequency stability under power disturbances. Fig. 4.17 illustrates the loci of eigenvalues of the four controllers for different inertia values of the grid. The results indicate that the SV achieves higher damping than the other techniques since the droop and the damping term changes the power-sharing of the converter in the frequency regulation, causing the converter dynamics to be more dominant and in a higher proportion concerning the grid. Therefore, the GFM modes are more excited by changes in the network frequency. Regarding VCVSM, MC and dVOC, as the grid delivers higher inertia, the GFM modes become slightly faster, improving the system's stability.

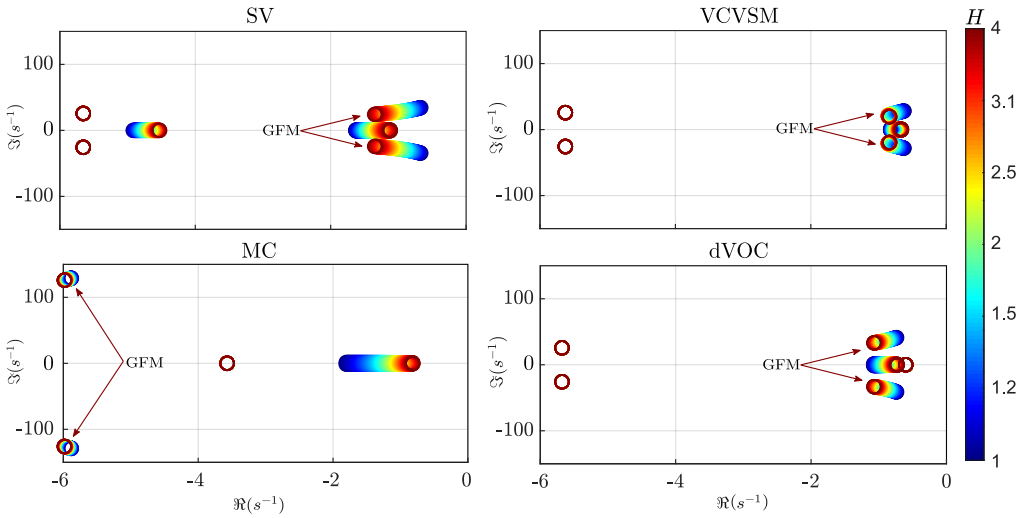


**Figure 4.17:** Eigenvalue trajectory for different grid inertia constants.

### Converter rated power variation

As stated above, the number of grid-connected inverters is increasing to the point where a large percentage of generation will be delivered to the grid by electronic converters. Fig. 4.18 depicts the eigenvalues associated to the electromechanical dynamics as the GFM converters change their participation in the system. The parametric sweep consists of modifying the rated power of the inverter, from 0.5 to 1.5 $p.u.$, while keeping the base power (and hence, the grid-side parameters) constant. A modification in the rated power of the inverter impacts not only on the power it provides, but also in the design of the output $LC$ filter and the tuning of the inner control loops. When the rated power of the converter is increased, the dominant modes of the SV and VCVSM show a very similar behaviour and move further from the unstable region; hence, these modes gain damping but maintain their oscillation frequency. This response happens because GFM converters provide more damping to the system. Therefore, it can be stated that the dynamics of the frequency in a low-inertia power system tend to improve with a higher penetration of GFM converters.The MC moves its modes in the same direction as the SME, although it gains more damping due to the rise in $R_f$ filter resistance. Regarding the dVOC, its eigenvalues move differently from the SV, VCVSM and MC control due to the difficulty of the controller to providing damping to the grid. Anyhow, the conclusion is that the power ratio is not a critical source of instability in the tested scenario.

## 4.6 Real-Time Implementation and Validation

In order to validate the proposed small-signal models and the subsequent stability analysis, a hardware-in-the-loop (HIL) testbed based on an OPAL-RT as shown in Fig. 4.19 has been used. The semiconductors of the converter, the $LC$ filter, the load and the synchronous machine have been implemented on this OPAL-RT, whereas the grid-forming control, inner loops and space vector modulation (SVPWM) have been integrated on a TMS320F28379D launchpad from Texas Instruments.

The experimental results in Fig. 4.20 show that with a variation of 0.05 $p.u.$ in the active power reference of the converter, the real-time simulations show a very similar behaviour in

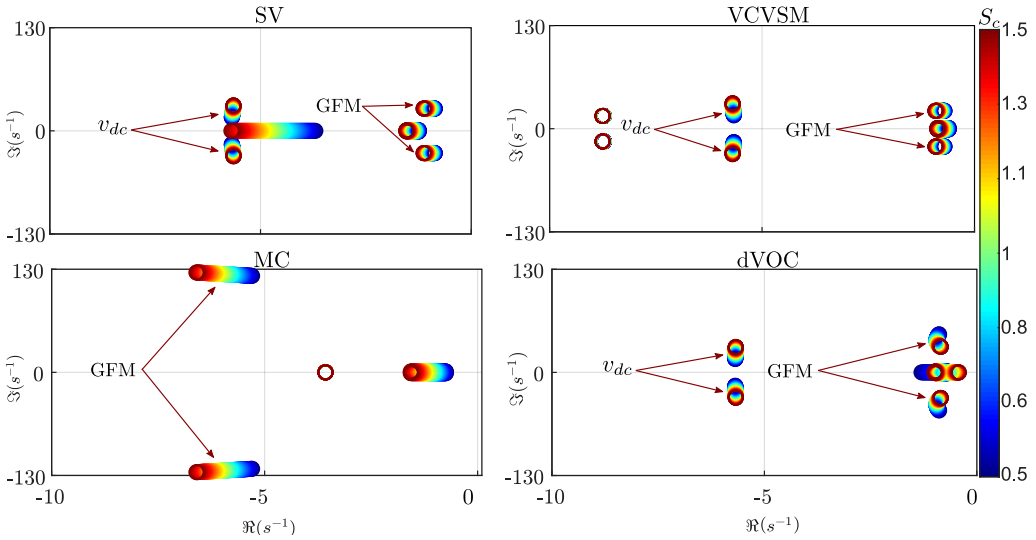


**Figure 4.18:** Eigenvalue trajectory for a parametric sweep of the converter rated power for the four implementations.


**Figure 4.19:** Opal-RT based real-time HIL testbed.

the frequency and amplitude of the power oscillations compared to the small-signal models. Moreover, despite the $0.02\,p.u.$ ripple in the HIL testbed caused by the converter switching, the results converge to the same operating point in steady-state. The only difference between experimental and small-signal simulation results are observed in the amplitude of the oscillations of the dVOC. This is due to the large amplitude of these oscillations, that saturates the

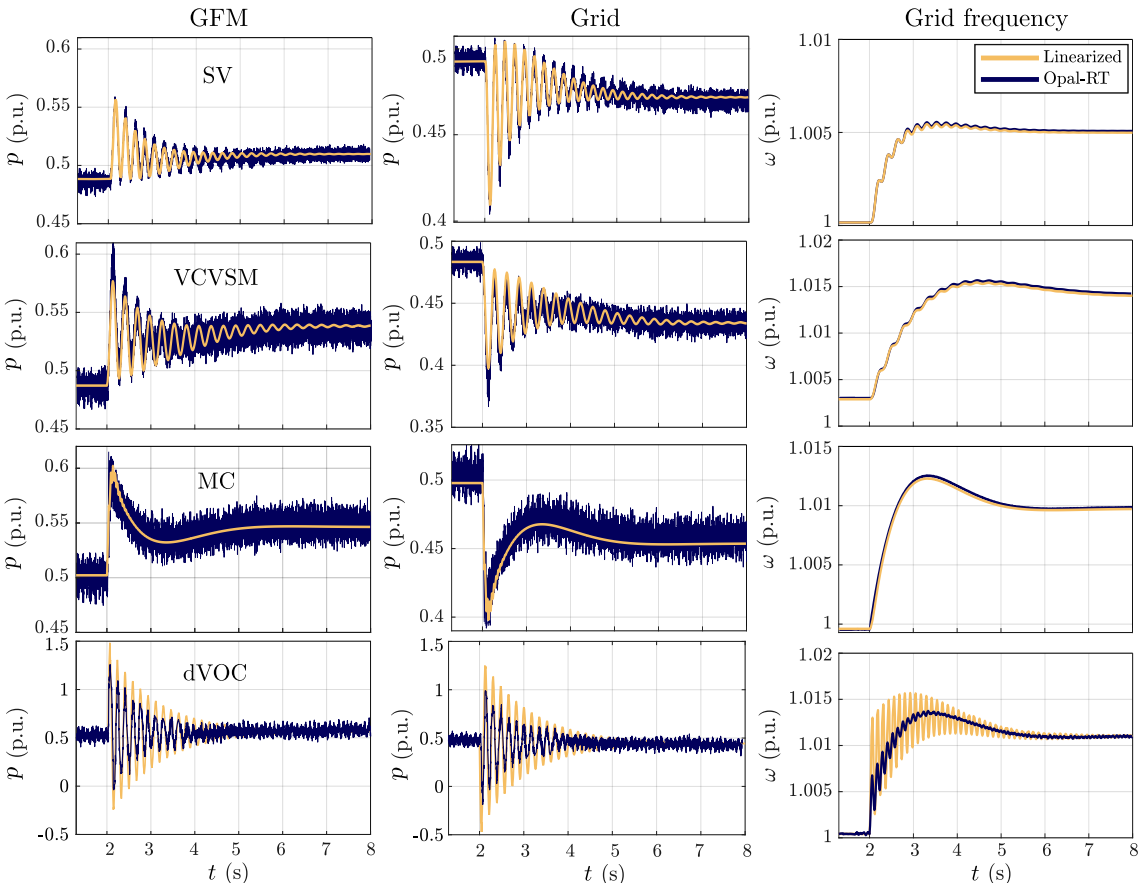


**Figure 4.20:** Validation of the linearized model against real-time simulation based on Opal-RT. From left to right, GFM power, SM power and grid frequency in each case.

currents and voltage measurements of the experimental setup. This saturation has not been considered in the analytical small-signal model. In any case, the frequency of the oscillations is the same both for the simulation and for the experimental results.

## 4.7 Summary

This chapter has studied and compared the time-domain and small-signal behaviour of four of the most relevant grid-forming control implementations: a synchronverter, a voltage-controlled virtual synchronous machine, a dispatchable virtual oscillator, and a matching control. Unlike previous studies in the literature, the performance of the controllers has been tested for varying grid conditions such as the equivalent inertia constant, damping and grid-side impedance.

The results reveal that the dVOC has similar inertial behaviour to the SV and the VCVSM when a low-pass filter is added to the active power measurement, since the time constant of the filter is equivalent to the inertial term of the swing equation. However, the dVOC does not have a damping term that allows attenuation of modes associated to the electromechanical response of the converter. The MC presents some challenges because the provided inertial behaviour depends directly on the size of the bus capacitor, and its stability is strongly dependent on the passive elements of the system. The VCVSM is a more reliable representation of the synchronous machine, allowing better attenuation of electromechanical oscillations thanks to its damping term. In contrast, the SV does not correctly represent the damping term in variable frequency grids, impacting the active power-sharing of the other generators in the system.

Regarding reactive power regulation, the VCVSM provides more flexibility due to the integration of a virtual impedance, allowing the GFM converter to operate even in very low-impedance grids. Nevertheless, its stability is very sensitive to the droop gain of the reactive power controller. This is not the case for the SV, which has less sensitivity to the droop gain, nor for the dVOC, that has a reactive power control faster and more robust than that of the VCVSM and whose stability is not drastically affected by the droop gain.

The final experimental results have shown a good match with the response of the developed analytical models, corroborating the validity of the results in the study of the small-signal stability.

# Chapter 5

# Second-order filter-based inertia emulation (SOFIE) for low inertia power systems

*The massive integration of power electronic converters into the power grid has led to a decrease in the mechanical inertia of the power system, causing an increase in the RoCoF that may lead to stability problems. In this direction, the grid-supporting approaches, are an interesting alternative to add frequency support to the grid while preserving the original control structure of the converter. This chapter proposes three new grid-supporting control techniques based on the dynamic behaviour of a synchronous machine and its equivalence with a second-order low-pass filter. They endow the converter with the capability of providing synthetic inertia, damping, droop-based p/f primary response and virtual reactance. The dynamics of the proposed implementations are compared with those of a reduced-order synchronous machine by means of time-domain simulations and in-depth state-space-based small signal analyses. Besides, their operation is validated in a nine-bus low-inertia power system. HIL laboratory results are used to validate experimentally the proposed techniques.*

## 5.1 Introduction

As mentioned in previous chapters, GSC technologies offer frequency support through small changes to the GFL structure [148]. Therefore, the inverter works as a current source and it needs to synchronise with the grid to regulate the exchanged power. These techniques are an interesting alternative to provide frequency support through the emulation of inertia and have been successfully applied, e.g. in wind farms [45, 46], energy storage systems [47, 48] or HVDC links [49, 50]. Broadly speaking, GSCs can be categorised in two different groups: droop-based and inertia emulation. Both approaches employ a PLL for synchronisation and internal loops to regulate the output current [148]. In droop-based GSCs, the frequency support is provided by injecting active power proportionally to the deviation of the frequency, following a $p/f$ droop characteristic. This approach is simple and easily implementable, but its dynamic response against power perturbations highly depends on the dynamics of the PLL [149] and it does not provide inertial support. In inertia emulation GSCs, the active power injections are proportional to the rate of change of the frequency (RoCoF or $d\omega/dt$), thus providing synthetic inertia. Nonetheless, their main disadvantages are that the derivative term make them susceptible to the noise of the estimated frequency and the system response is strongly linked to the dynamics of the PLL [150]. To overcome these challenges, the first-order filter-based inertia emulation (FOFIE) was proposed [77, 151].

Unlike GFMs that are capable of emulating effectively the behaviour of a SM, the main problem of GSCs is that their dynamic operation under power perturbations deviates from the expected behaviour of a SM. The first-order filter adopted to cope with sudden frequency variations does not provide a response equivalent to the well-known swing equation. Besides, some authors have reported stability problems due to adverse interactions induced by the FOFIE control and the *LC* resonances of the power system [77, 150]. As a solution, a proposal is to slow down the PLL dynamics to avoid strong transients [77], but this modification affects the converter synchronisation and its voltage regulation. Recently, the so-called external inertial emulation technique has been proposed to approximate the response of GSCs to that of SMs [152]. It consists of an external control based on the swing equation that provides an active power reference to a traditional GFL control structure. However, there have been no studies of the impact of the PLL or a detailed analysis of its equivalence to a synchronous machine.

Motivated by the need to overcome the previous issues, this work proposes an alternative GSC controller named second-order filter-based inertia emulation (SOFIE). As the name suggests, this control technique is based on an equivalence between a second-order low-pass filter and the reduced model of a classical SM. Its main features and novelties with regards to previous GSCs are:

1. Reproducing accurately the main dynamics defined by the swing-equation of SMs on which frequency stability relies.

2. Solving the stability problems of traditional first-order filter-based inertia emulation techniques, which are caused by the interactions of the GSC control with the *LC* resonances of the power system. This aspect is discussed thoroughly in [J4].

3. Providing fully independent and configurable virtual inertia constant, droop and damping gains, and virtual inductance.

4. Facilitating the seamless integration with existing GFL controllers. State-of-the-art inertia emulation algorithms based on derivative terms can quickly adopt the proposed

technique by replacing the first-order filter with a second-order one. These facts enable the conversion/upgrade of existing converters already in use to accurately reproduce the dynamics of SMs.

5. Providing virtual damping to attenuate power oscillations without affecting the steady-state value of the frequency.

6. Decoupling PLL dynamics with inertia emulation control, allowing fast PLLs without compromising the system stability.

This chapter introduces the principles and mathematical formulation of the SOFIE controllers. Three different implementations, each one with its own technical features, advantages and limitations are proposed. The performance of the SOFIE controllers is thoroughly characterised by means of large signal time domain simulations and state-space-based small signal analysis. Based on the results of these analyses, the dynamic performance of the SOFIE controllers are benchmarked against that of the conventional FOFIE controllers for several control configurations and grid conditions. Special attention is paid to the influence of the PLL on the dynamic response and on the closed-loop stability of the system. Besides, the dominant low-frequency oscillatory modes introduced by the SOFIE controllers are compared against those of a synchronous machine and a synchronverter.

## 5.2 Principles and analytical derivation of the SOFIE control

The purpose of this section is to lay the foundations of the proposed SOFIE technique, which is based on an equivalence between the simplified model of a SM and a second-order filter. Initially, the swing equation that represents the electromechanical response of a synchronous generator is described, as it is the basis of the proposed control philosophy. Then, the analytical rationale behind the proposed technique is described, and three different SOFIE control variants are proposed. The last subsection introduces how to incorporate these variants in the typical control structure of a power converter.

### 5.2.1 Simplified synchronous machine

The generator model studied is based on a simplified electromechanical model of a SM, which is driven by a turbine whose governor is controlled by an APC. It must be noted that in the following the response of the governor and the turbine is assumed to be instantaneous—i.e., no delay is considered in their response.

The dynamic equation describing the time evolution of the angular speed of the rotor using a per unit notation and assuming that $\omega_r \approx 1\,p.u.$ is given by [22]:

$$\frac{d\omega_r}{dt} = \frac{p_m - p_e - k_d(\omega - \omega_g)}{2H} \tag{5.1}$$

where $p_e$ and $p_m$ are the electrical and mechanical power, respectively. $k_d$ is the damping constant, $H$ is the inertia constant and $\omega_g$ is the grid frequency at the machine terminals. The mechanical speed of the rotor $\omega_r$ is related to the electrical speed of the induced electromotive force ($\omega$) through the number of pole pairs ($p_l$) as $\omega = \omega_r p_l$. To simplify the notation and without loss of generality, in the rest of the chapter the system is considered to have a single pair of poles, thus $\omega = \omega_r$.

Since no delays are considered in the turbine and the governor, the mechanical power is set by the APC, which is comprised by a $p/f$ droop control described as:

$$p_m = p^* + k_\omega (\omega^* - \omega) \tag{5.2}$$

where $p^*$ and $\omega^*$ are the output power and grid frequency setpoints, respectively, and $k_\omega$ is the droop constant.

The stator winding of a SM can be modelled as a series *RL* impedance. The current through that winding can be represented by the following differential equation:

$$\frac{d\mathbf{i}_s}{dt} = \frac{\omega_b}{L_s} [\mathbf{e}_s - \mathbf{v_o} - (R_s + j\,\omega L_s)\,\mathbf{i}_s] \tag{5.3}$$

where $\mathbf{i}_s$ is the stator current represented in a *dq* reference frame using a vector notation ($\mathbf{i}_s = i_d + j i_q$). $\mathbf{v}_o$ is the voltage at the PCC, and $L_s$ and $R_s$ are the inductance and armature resistance, respectively. $\mathbf{e}_s$ is the vector representing the internal voltage of the generator. To simplify the comparison to a second-order filter, it is assumed that $\mathbf{e}_s = e_{s_d} + j e_{s_q} = 1 + j0$ p.u.

The electrical power that the SM exchanges with the grid can be expressed in a simplified manner by [22]:

$$p_e = \frac{|\mathbf{e}_s|\,|\mathbf{v}_o|}{X_s} \sin\delta \tag{5.4}$$

where $X_s = \omega L_s$ and $\delta$ is the angle difference between $\mathbf{e}_s$ and $\mathbf{v}_o$. This angle difference can be calculated from the SM electrical frequency and the grid-side frequency as:

$$\frac{d\delta}{dt} = \omega_b \left(\omega - \omega_g\right) \tag{5.5}$$

where $\omega_b$ is the base angular frequency used in the per unit notation.

When the angle difference is very small $\sin(\delta) \approx \delta$. Moreover, when assuming that in per unit $\mathbf{e}_s \approx \mathbf{v}_o \approx 1$ p.u., Eq. (5.4) can be linearised around an operating point as:

$$p_e \approx \frac{1}{X_s}\delta \tag{5.6}$$

Eqs. (5.1), (5.3), and (5.5) are the state-space equations that represent the electromechanical motion of a simplified SM. Taking the Laplace transformation of these expressions and after some manipulations, the following transfer function can be defined:

$$p_e(s) = G_1(s)p^* + G_2(s)\omega^* + G_3(s)\omega_g(s) \tag{5.7}$$

where $G_1(s)$, $G_2(s)$ and $G_3(s)$ are defined as:

$$G_1(s) = \frac{\omega_b}{2HX_s\left(s^2 + \dfrac{(k_d + k_\omega)s}{2H} + \dfrac{\omega_b}{2HX_s}\right)} \tag{5.8}$$

$$G_2(s) = \frac{\omega_b\, k_\omega}{2HX_s\left(s^2 + \dfrac{(k_d + k_\omega)s}{2H} + \dfrac{\omega_b}{2HX_s}\right)} \tag{5.9}$$

$$G_3(s) = \frac{-\dfrac{\omega_b\, s}{X_s} - \dfrac{\omega_b\, k_\omega}{2HX_s}}{s^2 + \dfrac{(k_d + k_\omega)}{2H}s + \dfrac{\omega_b}{2HX_s}} \tag{5.10}$$

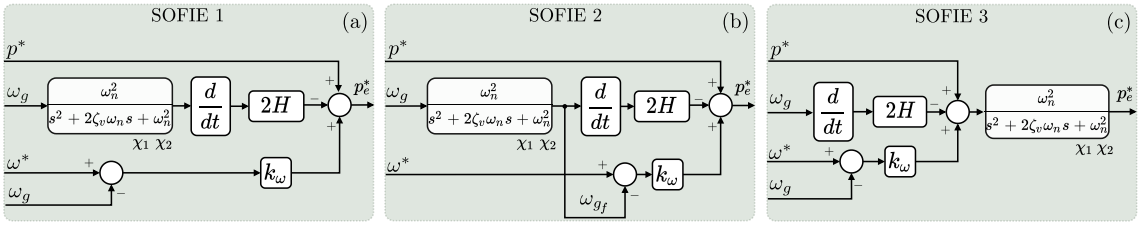


**Figure 5.1:** Proposed SOFIE implementations.

### 5.2.2 SOFIE control approaches

Assuming that the internal power control of a converter is very fast (i.e., that $p_e \approx p_e^*$), the dynamic response of a classical inertia emulation GSC can be represented by the following transfer function [77, 150]:

$$p_e(s) = -2H \frac{\omega_{cut}\, s}{s + \omega_{cut}} \omega_g(s) + k_\omega (\omega^* - \omega_g(s)) + p^* \tag{5.11}$$

where $\omega_{cut}$ is the cutoff frequency of the first-order low-pass filter used to avoid sudden frequency variations. The value of this low-pass filter is then passed through a derivative term to emulate an inertial behaviour. Moreover, a droop controller with gain $k_\omega$ is provided to simultaneously carry out the primary regulation and to damp the output response, meaning that these two terms are not decoupled [153, 154]. These characteristics cause the dynamic response of this type of control to differ significantly from the behaviour expected in a simplified SM. This can be also concluded from the differences observed between Eqs. (5.8) - (5.10) and (5.11).

The purpose of the SOFIE control is to approximate the behaviour of a power converter to that of a simplified SM, but without the need to modify the original control structure as it is done in other SM emulation techniques. For that purpose, the first-order filter used in the power control of classical inertia emulation techniques is replaced by a second-order low-pass filter. This way the dynamic response of a converter controlled with a SOFIE technique will be more similar to the one observed in Eq. (5.7) - (5.10).

Fig. 5.1 shows three different implementations of the SOFIE technique. Below their equivalent transfer functions are analysed to illustrate the similarities compared to Eq. (5.7) - (5.10). The first implementation, named SOFIE 1, is formed by replacing the first-order filter in Eq. (5.11) by a second-order filter. Based on the diagram depicted in Fig. 5.1(a) and following the notation in Eq. (5.7), the equivalent transfer functions that represent the electrical power ($p_e$) provided by converters controlled with this technique are:

$$G_1(s) = 1 \tag{5.12}$$

$$G_2(s) = k_\omega \tag{5.13}$$

$$G_3(s) = \frac{-k_\omega s^2 + (2H\omega_n^2 - 2k_\omega \omega_n \zeta_v)s - k_\omega \omega_n^2}{s^2 + 2\omega_n \zeta_v s + \omega_n^2} \tag{5.14}$$

The denominator of Eq. (5.14) has the same order as that of the simplified SM in Eq. (5.10). Therefore, the natural frequency ($\omega_n$) and damping term ($\zeta_v$) of the second-order filter in Eq. (5.14) can be defined as:

$$\omega_n = \sqrt{\frac{\omega_b}{2HX_s}} \tag{5.15}$$

$$\zeta_v = \frac{(k_d + k_\omega)\sqrt{2}}{4\sqrt{\frac{\omega_b H}{Xs}}} \tag{5.16}$$

Note how $\omega_n$ and $\zeta_v$ can be designed as a function of SM parameters to provide a response similar to a simplified SM under grid-side frequency variations ($\omega_g$). Replacing (5.15) and (5.16) into (5.12)–(5.14), the following transfer functions are obtained:

$$G_1(s) = 1 \tag{5.17}$$

$$G_2(s) = k_\omega \tag{5.18}$$

$$G_3(s) = \frac{-k_\omega s^2 + \left(-\frac{\omega_b}{X_s} - \frac{k_\omega (k_d + k_\omega)}{2H}\right)s - \frac{k_\omega \omega_b}{2HX_s}}{s^2 + \frac{(k_d + k_\omega)}{2H}s + \frac{\omega_b}{2HX_s}} \tag{5.19}$$

Comparing Eqs. (5.19) and (5.10), one can conclude that the dynamics of the SOFIE 1 controller, defined by the poles of (5.19), are the same than those of the swing-equation in Eq. (5.10). However, the zeros of both transfer functions are different, meaning that SOFIE 1 approximates the electromechanical response of a synchronous machine in the presence of frequency variations but does not completely match it due to the divergence in the zeros. Besides, the dynamic response of SOFIE 1 under power or frequency reference variations—given by Eqs. (5.17) and (5.18), respectively—differ from those defined in Eqs. (5.8) and (5.9). In this sense, it can be concluded that SOFIE 1 can provide emulated inertia against frequency changes, but it does not provide an accurate representation of a synchronous machine.

Fig. 5.1(b) shows a second implementation (SOFIE 2), where the second-order filter also operates over the frequency input used to implement the droop controller. Following the same reasoning as in the previous case, and making use of Eqs. (5.15) and (5.16), the transfer functions that define the response of SOFIE 2 take the form given by Eq. (5.7) where:

$$G_1(s) = 1 \tag{5.20}$$

$$G_2(s) = k_\omega \tag{5.21}$$

$$G_3(s) = \frac{-\frac{\omega_b s}{X_s} - \frac{\omega_b k_\omega}{2HX_s}}{s^2 + \frac{(k_d + k_\omega)}{2H}s + \frac{\omega_b}{2HX_s}} \tag{5.22}$$

Eqs. (5.22) and (5.10) are now identical since they have the same zeros and poles. Hence, one can conclude that the response provided by SOFIE 2 to frequency changes in the grid replicates with accuracy that of the simplified model of the SM. The electrical power injected in the grid by the SOFIE 2 controller to respond against variations in the grid frequency emulates the electrical power of an equivalent synchronous machine with a defined inertia, impedance, and droop and damping gains. However, Eqs. (5.20) and (5.21) are different from (5.8) and (5.9), indicating that the response of SOFIE 2 to changes in the power or frequency references does not match that of a SM.

In the third implementation, named SOFIE 3, the second-order filter operates over the electrical power reference instead of only over the grid frequency (Fig. 5.1c). The transfer functions that determine the dynamic response of SOFIE 3, provided that the equivalences in Eqs. (5.15) and (5.16) are used, takes the same form as Eq. (5.7), where:

$$G_1(s) = \frac{\omega_b}{2HX\left(s^2 + \dfrac{(k_d + k_\omega)s}{2H} + \dfrac{\omega_b}{2HX}\right)} \tag{5.23}$$

$$G_2(s) = \frac{\omega_b\, k_\omega}{2HX_s\left(s^2 + \dfrac{(k_d + k_\omega)s}{2H} + \dfrac{\omega_b}{2HX_s}\right)} \tag{5.24}$$

$$G_3(s) = \frac{-\dfrac{\omega_b\, s}{X_s} - \dfrac{\omega_b\, k_\omega}{2HX_s}}{s^2 + \dfrac{(k_d + k_\omega)}{2H}s + \dfrac{\omega_b}{2HX_s}} \tag{5.25}$$

In the SOFIE 3 implementation, Eqs. (5.23)–(5.25) are identical to (5.8)–(5.10), so it can be concluded that this controller provides a response that matches that of the simplified SM model under variations in the grid frequency, the reference power and the reference frequency.

Among the proposed implementations, SOFIE 3 is the approach that most accurately replicates the response of a simplified SM. Nevertheless, its implementation implies a slight variation

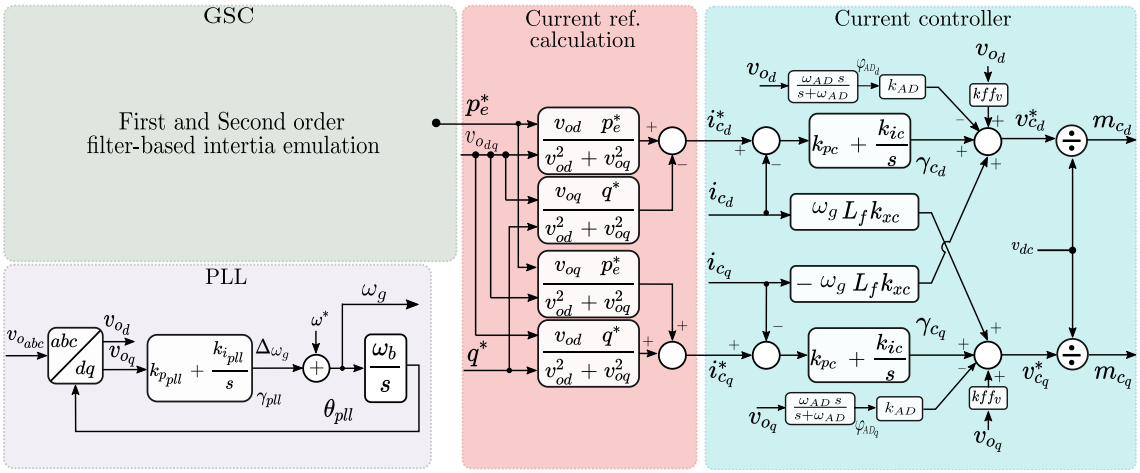


**Figure 5.2:** Control structure of the converter.

on the structure of classical inertia emulation techniques as the filter does not only operate on the grid frequency. SOFIE 1 and SOFIE 2 require almost no variation on the structure of classical inertia emulation controllers. However, they replicate the operation of SMs with a minor degree of accuracy.

### 5.2.3 Integration of SOFIE controllers in the control structure of a grid-tied converter

The diagram in Fig. 5.2 illustrates how SOFIE controllers can be integrated within the typical structure of a grid-connected converter developed in the $dq$ synchronous reference frame. This controller basically consists of PI regulators to control the current, including the coupling terms ($k_{xc}$) and feed-forward terms ($k_{ffv}$). As depicted in Fig. 5.1, the output of SOFIE controllers is the electrical power reference of the converter ($p_e^*$), which is converted into current set-points ($\mathbf{i}_c^*$) taking into account the measured terminal voltage ($\mathbf{v}_o$). Consequently, the integration with the inner converter control loops is seamless. The integration with other control implementations on the natural or stationary reference frame is also possible, since SOFIE controllers are agnostic of the structure of the inner control loops.

It is also convenient to remark that the frequency of the grid that is used as an input to the SOFIE controller is estimated using a classical synchronous reference frame PLL. The transfer functions of the SOFIE controllers in the previous section have been obtained neglecting the dynamics of the PLL and the inner current control loops. However, they will play a role in the final dynamic response of the converter. The effect of synchronisation algorithms in the dynamic response is usually neglected in the literature related to GSC, so this aspect is addressed in the following section.

## 5.3 Time-domain performance of SOFIE control

The aim of this section is to corroborate the hypotheses made in the analytical description of the three SOFIE implementations. For that purpose, initially the testing scenario is described, and then the performance of the SOFIE control is evaluated by providing the time-domain response under various disturbances and by comparing the system oscillation modes. The simplified model of a SM is taken as the benchmark system in the performance evaluation.

### 5.3.1 Description of the testing scenario

Since the SOFIE controller is a GSC, another grid-connected device must be responsible for setting the grid voltage and frequency. In this case, the testing scenario shown in Fig. 5.3 consists of an inverter with a series inductive filter ($L_f$) connected to an infinite bus via an inductive transmission line ($L_g$). A small resistance, accounting for the line and filter losses, has been considered as well.

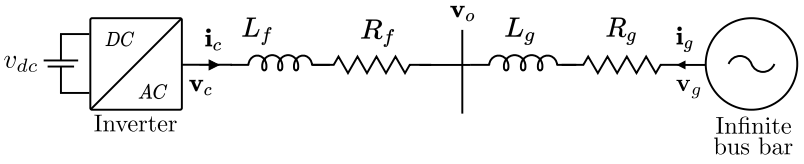


**Figure 5.3:** Testing scenario: power converter connected to an infinite grid model.

The configuration employed to obtain the results of the simplified SM model is the same as the one shown in Fig. 5.3, but the inverter and its filter is replaced by the SM modelled in 5.2.1.

The parameters and set-points employed in the following tests are gathered in Appendix B - Tab. B.2. The control parameters of the SOFIE controllers (i.e., $\omega_n, \zeta_\nu,$) are calculated using Eqs. (5.15) and (5.16) and taking the SM parameters as a reference. The modulus optimum criterion technique is used to tune the current PI regulators [146]. Moreover, the PLL is tuned employing the symmetric optimal criterion technique to ensure the maximum phase margin at the crossover frequency of the open-loop transfer function [155].

### 5.3.2 Performance tests

#### Active power reference variation

Fig. 5.4 depicts the behaviour of the electrical system described in Fig. 5.3 under a step-shaped variation of $0.1\,p.u.$ in the active power reference ($p^*$) of the SOFIE implementations and the simplified SM model at $t = 1\,s$.

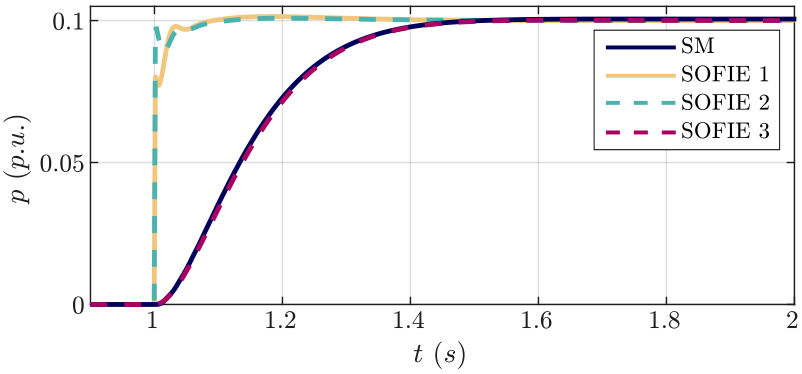


**Figure 5.4:** Active power for a $0.1\,p.u.$ variation in the power reference ($p^*$)

The results show that the dynamic response of SOFIE 1 and SOFIE 2 implementations is significantly faster than that of the SOFIE 3 implementation and the SM. As stated in Section 5.2.2, the reason is that the power reference is not being filtered in SOFIE 1 and 2 (refer to Fig. 5.1). However, under the power set-point variation, the SOFIE 3 implementation emulates the behaviour of the SM very closely, confirming the hypothesis made with the equivalent Eqs. (5.23)–(5.25).

#### Grid frequency variation

The behaviour under grid-side frequency variations is studied by making a step-shaped change of $-0.01\,p.u.$ in the infinite bus frequency at $t = 1\,s$. Fig. 5.5 shows the time-domain evolution of the active power supplied by the SOFIE implementations and the SM.

The active power in the steady state takes the same value for all the cases; this makes sense as it only depends on the droop gain $k_\omega$. Regarding the transient response, all the systems have similar behaviour, but SOFIE 1 exhibits a faster transient response and a higher overshoot caused by the instantaneous $p/f$ droop, which is directly driven by the PLL frequency estimation, causing different zeros in its transfer function. This effect cannot be observed in SOFIE 2 and SOFIE 3 implementations because the estimated frequency is filtered before applying

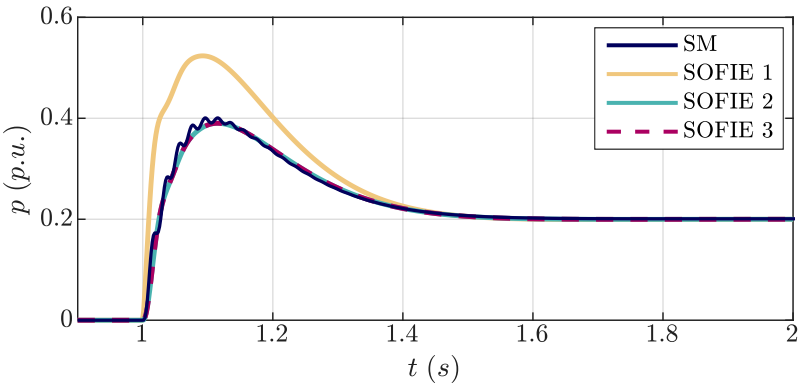


**Figure 5.5:** Active power for a $-0.01\,p.u.$ variation in the grid frequency ($\omega_g$)

the droop constant and the derivative term; thus, the frequency used in the $p/f$ droop takes the same dynamics as the rotor speed mimic by the SOFIE control. Therefore, the dynamic behaviour of these two SOFIE implementations matches very well the response expected from a SM.

The time-domain results provided in these two sections demonstrate that, even if the SOFIE controller depends on an estimation algorithm such as a PLL to synchronise with the grid, their transient behaviour can be designed to be equivalent to the simplified model of a SM.

### 5.3.3 Modal analysis

This section aims to provide a brief analysis of the eigenvalues of the proposed SOFIE implementations compared to the simplified model of a SM introduced before. The equations are first constructed in a state-space form, and then their eigenvalues are analysed by using the CSTEP tool, developed in chapter 3.

Table 5.1 displays the most relevant information of these eigenvalues, including the damping factor ($\zeta$), oscillation frequency ($f_{osc}$), the relation between states variables and oscillation modes via the participation factors, and the parameters to which eigenvalues are most susceptible (named parametric sensitivity).

The two eigenvalues with lowest oscillation frequency, highlighted in yellow in table 5.1, are related to the state variables of the second order filter used in the SOFIE implementations and are equivalent to the electromechanical eigenvalues of the SM. The remaining eigenvalues are related to the integrator of the current controllers ($\gamma_{c_d}$, $\gamma_{c_q}$), PLL and filter. Focusing on the electromechanical eigenvalues, it can be observed how the three SOFIE implementations reveal a behaviour similar to that of the swing equation of the SM. The location in the complex plane, damping factors and oscillations frequencies of the electromechanical eigenvalues are similar, but not equal, to those of the SM. The small differences observed between the SM and SOFIE are attributable to the influence of the current control loops and the PLL. As fast dynamics have been considered for tuning the current control loop and the PLL, their influence on the electromechanical eigenvalues is minimal and the analytical approach in Section 5.2 is verified. However, this could not be necessarily the case if slow PLL is assumed, as will be further developed in Section 5.5.

**Table 5.1:** System eigenvalues and their most relevant information.

| | Eigenvalue | $\zeta$ | $f_{osc}$ (Hz) | Participating state | Parametric sensitivity |
|---|---|---|---|---|---|
| SOFIE 1 | $-10.43 \pm 5.18j$ | 0.89 | 0.82 | $\chi_1\ \chi_2$ | $L_g\ \zeta_v$ |
| | $-77.24 \pm 24.56j$ | 0.88 | 6.61 | $\gamma_{pll}\ \theta_{pll}$ | $L_g\ k_{p_{pll}}$ |
| | $-23.56$ | 1 | 0 | $\gamma_{c_d}$ | $R_f\ k_{p_c}$ |
| | $-23.56$ | 1 | 0 | $\gamma_{c_q}$ | $R_f\ k_{p_c}$ |
| | $-2809$ | 1 | 0 | $i_{c_d}$ | $L_f\ L_g\ k_{p_c}$ |
| | $-2120$ | 1 | 0 | $i_{c_q}$ | $L_f\ R_f\ k_{p_c}$ |
| SOFIE 2 | $-10.58 \pm 4.90j$ | 0.90 | 0.78 | $\chi_1\ \chi_2$ | $L_g\ \zeta_v$ |
| | $-93 \pm 39j$ | 0.92 | 6.29 | $\gamma_{pll}\ \theta_{pll}$ | $L_g\ k_{p_{pll}}$ |
| | $-23.56$ | 1 | 0 | $\gamma_{c_d}$ | $R_f\ k_{p_c}$ |
| | $-23.56$ | 1 | 0 | $\gamma_{c_q}$ | $R_f\ k_{p_c}$ |
| | $-2102$ | 1 | 0 | $i_{c_d}$ | $L_f\ R_f$ |
| | $-2120$ | 1 | 0 | $i_{c_q}$ | $L_f\ R_f$ |
| SOFIE 3 | $-10.58 \pm 4.90j$ | 0.90 | 0.78 | $\chi_1\ \chi_2$ | $L_g\ \zeta_v$ |
| | $-93.20 \pm 39.55j$ | 16.11 | 6.29 | $\gamma_{pll}\ \theta_{pll}$ | $L_g\ k_{p_{pll}}$ |
| | $-23.56$ | 1 | 0 | $\gamma_{c_d}$ | $R_f\ k_{p_c}$ |
| | $-23.56$ | 1 | 0 | $\gamma_{c_q}$ | $R_f\ k_{p_c}$ |
| | $-2102$ | 1 | 0 | $i_{c_d}$ | $L_f\ R_f$ |
| | $-2120$ | 1 | 0 | $i_{c_q}$ | $L_f\ R_f$ |
| SM | $-11.49 \pm 4.17j$ | 0.94 | 0.66 | $\omega\ \theta$ | $H\ R_s$ |
| | $-16.76 \pm 314j$ | 0.05 | 50.03 | $i_{L_d}\ i_{L_q}$ | $R_s\ R_g$ |

Associated to the second-order filter (SOFIE cases) or the swing equation (SM case).

## 5.4 Parametric sensitivity analysis

This section further evaluates how the variation of several physical or control parameters influences the location of eigenvalues in the complex plane. This study will identify the similarities between the proposed SOFIE implementations and the SM and tune the control parameters of SOFIE implementations to improve the stability margins.

### 5.4.1 Inertia constant ($H$) variation

Fig. 5.6 shows the location of the electromechanical eigenvalues in the complex plane for the three SOFIE implementations (SOF) and the SM machine ($\omega$) as the value of the inertia ($H$) changes. The eigenvalues move almost identically in the four cases, corroborating once again the similarities in the behaviour of the proposed SOFIE controllers and the SM.

For low inertia constants, the eigenvalues are real, revealing a non-oscillatory nature of the electromechanical modes. However, as the inertia increases, the poles describe a circumference with diameter $(2\,\omega_b)/((k_d + k_\omega)X_s)$. Consequently, as $H$ increases the eigenvalues become complex numbers and the electromechanical modes exhibit an under-damped oscillatory behaviour. The damping factor of the modes decreases as $H$ increases.

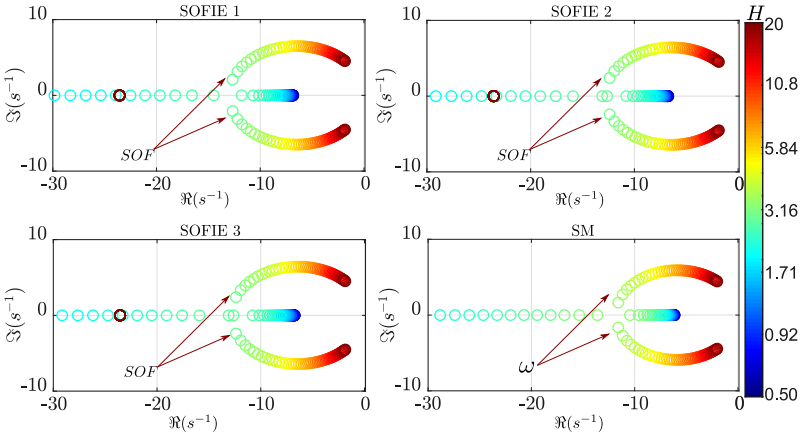


**Figure 5.6:** Root-locus under a variation of the inertia constant ($H$).

### 5.4.2 Damping constant ($k_d$) variation

Fig. 5.7 shows the root locus for the damping gain parametric sweep. As $k_d$ increases the electromechanical eigenvalues describe a semi-circumference with centre at the origin and radius equal to the natural frequency (5.16). This tendency continues until a threshold point is reached where the eigenvalues become real. For the proposed case study, this threshold value is $k_d = 151$. Results shows that for $k_d < 151$ the damping factor of the electromechanical eigenvalues of the SM and the SOFIE implementations is lower than 1, resulting in an under-damped system. For all the implementations, the imaginary part of the electromechanical eigenvalues decreases as $k_d$ increases. For $k_d > 151$, the damping factor becomes $\zeta > 1$, thus the eigenvalues associated to the electromechanical response become real and begin to separate from each other in the real axis. These results illustrates how, for high values of emulated inertia $H$, the damping gain $k_d$ of the SOFIE controllers can be properly adjusted to increase the damping of the electromechanical modes.

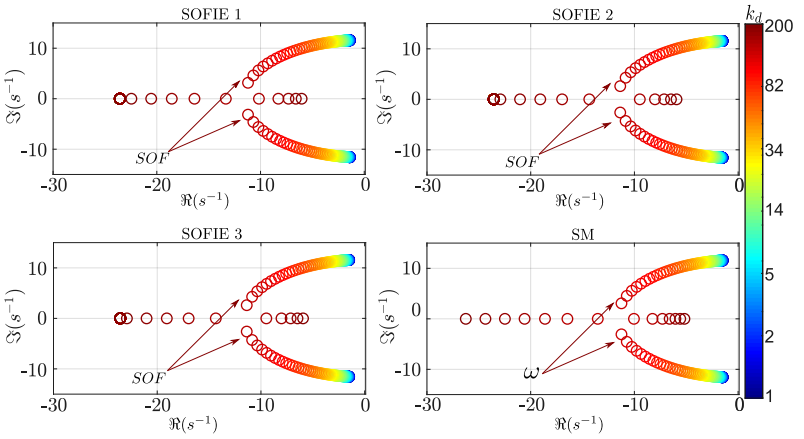


**Figure 5.7:** Root-locus under a variation of the damping gain ($k_d$).

### 5.4.3 Droop constant ($k_\omega$) variation

The analysis of the droop constant is fundamental because it determines how active power is shared among the devices participating in the frequency regulation of the grid. Its value is usually defined according to the maximum power of the device and the critical frequency boundaries established by the grid operator. Depending on the value of this droop constant, a converter might be constrained to work in certain operation conditions because it might cause undesired oscillations or instabilities. It can be observed in the zoomed regions of Fig. 5.8 that the electromechanical eigenvalues of the SOFIE controllers and those of the SM exhibit a similar behaviour as $k_\omega$ is swept, thus certifying that the SOFIE implementation approximates the dynamic response of SMs. As $k_\omega$ increases, the damping factor of the electromechanical modes increases as well. This behaviour is similar to that exhibited in Fig. 5.7 when $k_d$ increased, being possible to conclude that in the proposed SOFIE controllers, the damping and droop gains play an equivalent role in defining the damping factor. This is aligned with the analytical expression of the damping factor provided in (5.16). However, it is important to note that, while the droop gain modifies the point of operation of the converter in steady-state (because it is a proportional gain), the damping term only reacts under frequency variations ($\Delta\omega$), and therefore it should not cause a steady-state deviation.

In addition, the eigenvalues associated to the PLL are also displayed in Fig. 5.8. While in the SOFIE 2 and 3 the variation of the droop gain does not have any influence in their location, in SOFIE 1 the attenuation constant of these eigenvalues decreases (the eigenvalues move towards the right half plane) as the droop gain decreases. Therefore, it takes more time to damp these oscillatory modes. This is due to the fact that the dynamic response of the droop loop in SOFIE 1 is directly coupled to the PLL because the estimated frequency is not filtered.

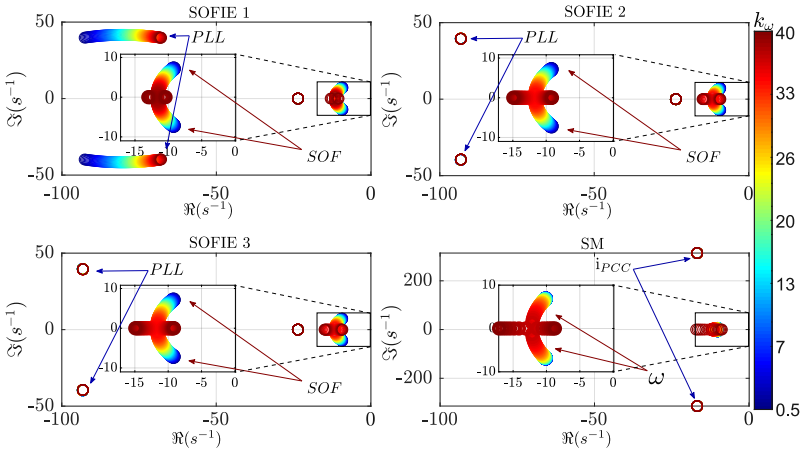


**Figure 5.8:** Root-locus under a variation of the droop gain ($k_\omega$).

### 5.4.4 Series reactance ($X_s$) variation

The influence of a variation of the virtual series reactance of SOFIE implementations and the SM stator reactance are shown in Fig. 5.9.

It can be observed in the zoomed regions of Fig. 5.9 that, as the virtual reactance increases, the electromechanical modes of the three SOFIE implementations and those of the SM move towards the real axis of the complex plane, thus becoming more damped. This is aligned with

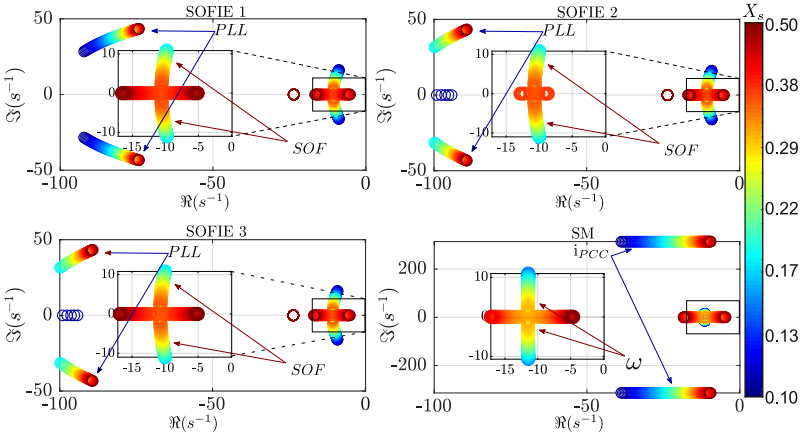


**Figure 5.9:** Root-locus under a variation of the virtual reactance ($X_s$).

the analytical expression found for the damping factor in (5.16). Above a threshold value of the virtual reactance, the damping factor becomes higher than 1 and the electromechanical modes become real numbers. For virtual reactances higher than this threshold, one of the eigenvalues moves toward the right half plane, thus implying longer attenuation times. Thus, the SOFIE controllers offer the possibility of selecting a proper virtual reactance to improve the damping of the electromechanical modes. In general, the higher the reactance, the more damped the electromechanical modes are. However, it is not recommended to select values that exceed the threshold. Otherwise, the system may become too slow and, additionally, angle stability may be compromised. Besides, it can be observed in Fig. 5.9 how the variation of the virtual reactance plays also an important role in the location of the high frequency eigenvalues associated the PLL of the SOFIE implementations. The higher the reactance, the lower the damping factor of these eigenvalues. Consequently, these results suggest the need to achieve a trade-off in the selection of the virtual reactance to properly attenuate both electromechanical and PLL modes.

### 5.4.5 Grid-side inductance ($L_g$) variation

The zoomed area of Fig. 5.10 shows the influence of the grid inductance on the position of the electromechanical eigenvalues. Unlike in previous cases, a qualitative difference can be observed in the evolution of the electromechanical eigenvalues between the SM and SOFIE implementations as $L_g$ is changed. This is attributed to the approximation made to estimate the active power (Eq. (5.6)), where the influence of the grid inductance is neglected. Nevertheless, despite this simplification, the electromechanical eigenvalues of the proposed SOFIE controllers are located in proximity to those of the SM.

## 5.5 Impact of the PLL in the performance of the SOFIE control

The aim of this section is to provide a more in depth analysis of the impact of the PLL dynamics on the proposed SOFIE 2 and 3 implementations.

As mentioned previously, the gains of the PI regulator of the PLL are calculated using the Symmetrical Optimum method, which determines the controller constants based on the output filter time constant ($\tau_f$), and on a factor $a$ that determines the crossover frequency and sets

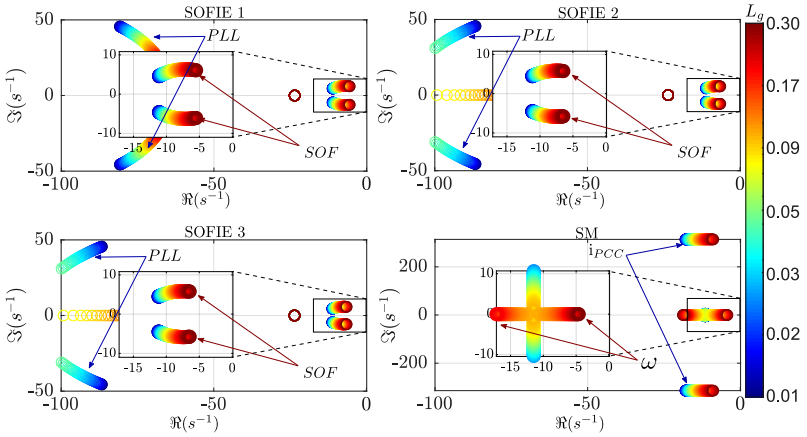


**Figure 5.10:** Root-locus under a variation of the grid impedance ($L_g$).

the damping. The values of the PI gains can be obtained as [155].

$$k_{p_{pll}} = \frac{1}{a\ \tau_f\ \omega_b} \qquad k_{i_{pll}} = \frac{k_{p_{pll}}}{a^2\ \tau_f} \tag{5.26}$$

The filter time constant $\tau_f$ is proportional to the response time of the PLL; the smaller the value of $\tau_f$, the faster can the PLL react under frequency variations. This phenomena can be clearly observed in Fig. 5.11, where the eigenvalues of the SOFIE 3 implementation are illustrated for different $\tau_f$ values.

Fig. 5.11 shows the PLL and electromechanical eigenvalues of the SOFIE 3 implementation for different values of $\tau_f$. If $\tau_f$ is below a threshold, meaning that the PLL is slow, the electromechanical eigenvalues are displaced towards the right half-plane, and the response of the SOFIE controllers starts to diverge from that of the SM. However, when $\tau_f$ is above the threshold, and the PLL is fast enough, the PLL dynamics do not affect the electromechanical eigenvalues. This is an interesting feature of the proposed SOFIE 2 and 3 controllers that make possible to uncouple the dynamics of the electromechanical modes from those of the PLL loop. In this sense, these controllers are indicated for power systems that are weak in terms of inertia but allow the use of a fast PLL to improve the dynamics of the converter. In these situations, the PLL eigenvalues do not affect the electromechanical eigenvalues of SOFIE controllers to approximate those of a SM properly.

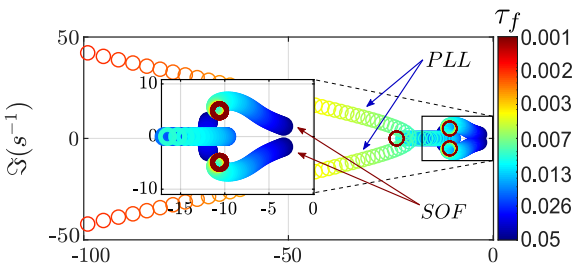


**Figure 5.11:** Root-locus under a variation of the time constant ($T_f$).

Fig. 5.12 (a) depicts the time-domain wave-forms of the active power of the SOFIE 3 controller for different values of $\tau_f$ under a $-0.01\,p.u.$ grid frequency variation and compares

them against that of a SM. Alternatively, Fig. 5.12 (b) display the frequency estimated by the PLL. The results reveal that when the PLL is faster, the frequency variation is detected much faster and hence the SOFIE controller reproduce more accurately the behaviour expected from a SM.

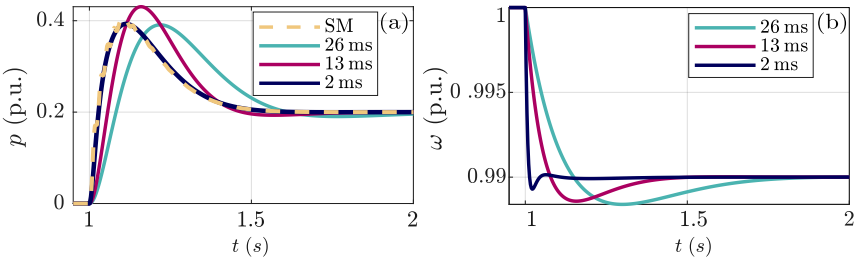


**Figure 5.12:** SOFIE 3 performance under a $-0.01\,p.u.$ grid frequency variation for different $\tau_f$ values: a) Active power of the converter and the SM, b) Frequency estimated by the PLL and mechanical frequency of the SM.

## 5.6 Comparison of control SOFIE and SM in low inertia power system.

To study the dynamics of SOFIE control and its equivalence to a SM in a low inertia power system, the IEEE 9 test case shown in Fig. 5.13 is modelled [156]. The inverters and the SM have been connected to the grid via an *RL* series impedance ($Z_g = Z_c = 0.006 + 0.08j$). The SM is in charge of forming the grid and is modelled by a reduced-order system with a turbine and governor, as described in the section 4.2.2. The parameters of the study can be found in Appendix Appendix B - Tab. B.2. Several studies have emphasised the need to use dynamic models to represent the transmission lines in converter-dominated networks, due to the adverse interaction that can take place between the converter and the lines and endanger the system's stability [25]. Thus, the transmission lines have been implemented as equivalent $\pi$ models. The loads are implemented as constant *RL* impedances. In order to analyse the dynamic operation of the proposed control, the following case studies are proposed: i) inverters 1 and 2 are controlled with a classical droop control, but without inertia emulation (Droop case); ii) inverters 1 and 2 are equipped with SOFIE control (SOFIE case); iii) the inverters are replaced by the SM studied in the previous sections (SM case).

To analyse the inertial behaviour of the grid in the presence of power imbalances, a load variation of $0.05\,p.u.$ at $t = 1\,s$ is applied at bus 6. Fig. 5.14 shows how, when the converters do not provide emulated inertia (droop case), the grid frequency exhibits a significantly higher RoCoF and nadir. On the other hand, when the converters provide frequency support through the use of the SOFIE control, the system remains stable and their dynamic response matches accurately that of SMs', even for different inertia constants.

As mentioned above, one of the main challenges of the massive integration of converters into the power grid is the adverse interactions between the converter dynamics and the *LC* resonances of transmission lines. Therefore, to study these interactions, the eigenvalues of the nine-bus system are analysed. Fig. 5.15 shows the root loci for the three proposed scenarios.

The eigenvalues associated to the electromechanical part are shown in the zoomed-in area. Outside the zoomed-in area are the modes associated with the resonances of the transmission

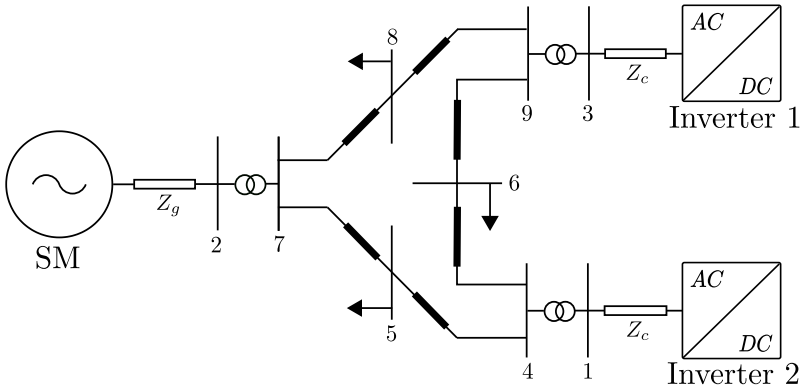


**Figure 5.13:** Nine-bus power transmission system diagram [156].

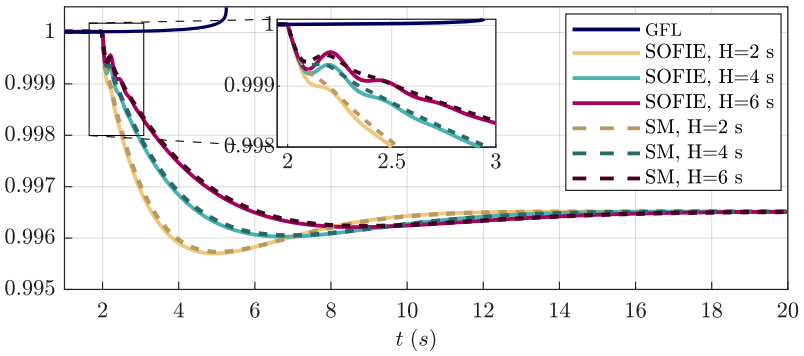


**Figure 5.14:** Frequency behaviour under power imbalance, varying the inertia.

lines.

The resonant modes in the droop case exhibit adverse interactions between the droop control and the transmission line resonances, causing these eigenvalues to move towards the right half plane. To achieve a stable point of operation the PLL speed has been reduced by setting the time constant as $\tau_f = 0.01$ (refer to Eq. (5.26)).

On the other hand, in the SOFIE case, the poles linked with the transmission line resonances remain in very similar positions compared to the SM scenario because the converter dynamics do not interact with the passive components of the grid. This means that the SOFIE

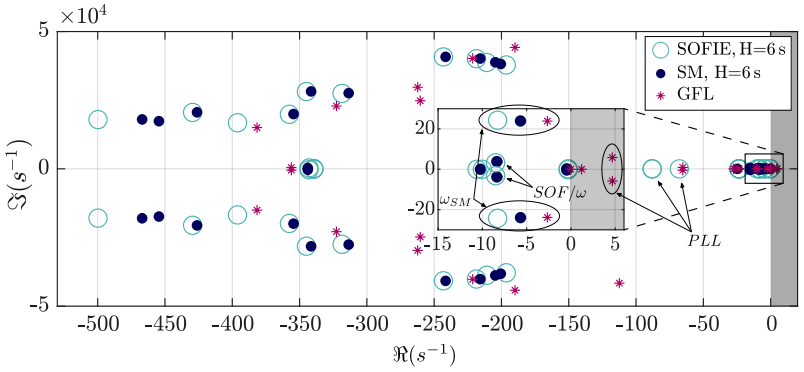


**Figure 5.15:** Resonant and electromechanical modes behaviour.

control keeps the system stability without exciting the modes associated with the *LC* resonances in a similar way to a SM in a traditional power system. It overcomes the stability drawbacks of classical GSCs based on droop control and first-order filter inertia emulation caused by interactions between the GSC control, the PLL and the *LC* resonances described in [77, 150].

## 5.7 Analysis and comparative evaluation of SOFIE vs. FOFIE control

This section carries out an exhaustive comparative evaluation of FOFIE and SOFIE control techniques for several control configurations and grid conditions. Initially, an analytical comparison is made and then the study is carried out via detailed time-domain simulations and frequency-domain responses. SOFIE 2 has been taken as the basis for the comparison. Unlike other studies, the influence of the PLL dynamics in the performance of the inertia emulation techniques is clearly assessed. Besides, different low-level control bandwidths and grid conditions are considered to perform the small-signal stability analysis. As it will be shown, the often neglected dynamic of the current control loops have a considerable impact on the stability of FOFIE techniques.

### 5.7.1 Time-domain performance comparison

The aim of this section is twofold. It compares in detail the dynamical behaviour of the SOFIE and FOFIE controllers through time and frequency-domain simulations. Besides, it provides a discussion on the effect of the PLL in their inertial behaviour and stability. Fig. 5.16 shows the system that has been considered to make this study. It is composed by an ideal grid with a series impedance, connected to an inverter through an *LC* filter. The series impedance and *LC* filter are modelled through differential state-space equations as in chapter 3 to evaluate the interactions among the inertia emulation techniques and the power system. The configuration parameters and the set-points employed in the analysis are shown in Appendix B - Tab. B.3. The control parameters of the SOFIE controllers (i.e., $\omega_n$ and $\zeta_v$) are calculated using Eqs. (5.15) and (5.16) and considering typical values of a SM. Regarding the FOFIE parameters, the cutoff frequency of the low-pass filter is set to be the same as the one calculated in the SOFIE; this is to ensure a fair comparison among both techniques. The inverter control structure is depicted in Fig. 5.2. It is equipped with the well-known internal current control loops in the $dq$ reference frame. An active damping term, intended to attenuate the resonances of the *LC* filter [157], is included as well. The current controllers are tuned following the "modulus optimum" method [146, 157].

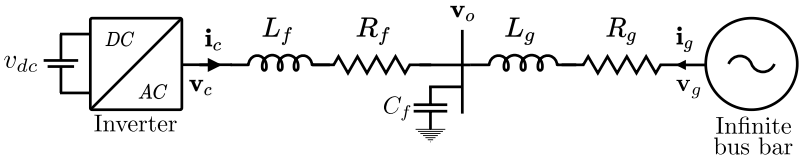


**Figure 5.16:** Testing scenario: power converter connected to an infinite grid model.

### Analysis with ideal PLL

In order to investigate the interactions of the inertia emulation techniques with the filter capacitor and the equivalent impedance of the grid, the system performance is first studied assuming an ideal PLL. This means that the frequency estimated by the converter is exactly the same as the grid frequency.

Fig. 5.17 illustrates the time-domain simulations of the active power and the direct and quadrature axis components of the voltage at the point of common coupling $\mathbf{v}_o$, for a $-0.003\,p.u.$ step change in the grid frequency at $t = 1\,s$. To provide a fair comparison the cutoff frequency of the low-pass filter is set to be the same on the FOFIE and SOFIE controllers.

The inertial response of the active power injected by the converter (Fig. 5.17-(a)) reveals an almost instantaneous transient in the case of the FOFIE control. Such behaviour is characteristic of a first order high-pass filter, which is the case when a derivative term is cascaded with a first-order low-pass filter.

Such behaviour can be also explained by rewriting the Eq. (2.2) as follows:

$$p_e^* = \left[ \underbrace{2H\omega_n}_{\text{Term 1}} - \underbrace{\frac{(k_\omega + 2H\omega_n)\,\omega_n}{s+\omega_n}}_{\text{Term 2}} \right] \omega_g(s) \tag{5.27}$$

From this equation, it can be observed that the transient exhibits two different terms:

1. The term $2H\omega_n\omega_g(s)$ causes the converter to deliver a near-instantaneous active power peak for any change in the grid frequency, which is beneficial from the inertial response perspective. However, such an active power transient in the grid causes the excitation of the *LC* resonance, producing high-frequency oscillations in the voltage $v_{o_d}$ and $v_{o_q}$ (Fig. 5.17-(b) and (c)).

2. Once the power reaches its peak amplitude, the subsequent transient is characterised by the classical dynamics of a first order system (Term 2 in Eq. 5.27).

In the case of the SOFIE control, it can be observed that the active power response is much smoother. This is due to the effect of the second-order filter that emulates the inertial response of a SM behind a virtual reactance. This type of response decreases significantly the amplitude of the *LC* resonances of the voltage at the PCC after the frequency disturbance.

These results illustrate how the type of inertia emulation technique strongly influences the excited *LC* resonances, and hence it determines the transient response of the voltage. This is an important aspect to consider in the design of the controller, since these transient oscillations are fed back into the controller when a real PLL is used and the voltage measurement $v_{o_q}$ is used to estimate the system frequency.

To provide a more in depth comparison of the voltage $v_{o_q}$ against frequency perturbations, the bode diagram of both inertia emulation techniques is studied using the transfer function $v_{o_q}(s)/\omega_g(s)$. The frequency response shown in Fig. 5.18 reveals that in the SOFIE control the *LC* resonance is attenuated significantly thanks to the natural ability of the second-order filter to attenuate 40 dB per decade the voltage fluctuations. However, the FOFIE control exhibits the frequency behaviour of a classical high-pass filter, and it does not filter the oscillations associated to the *LC* resonance.

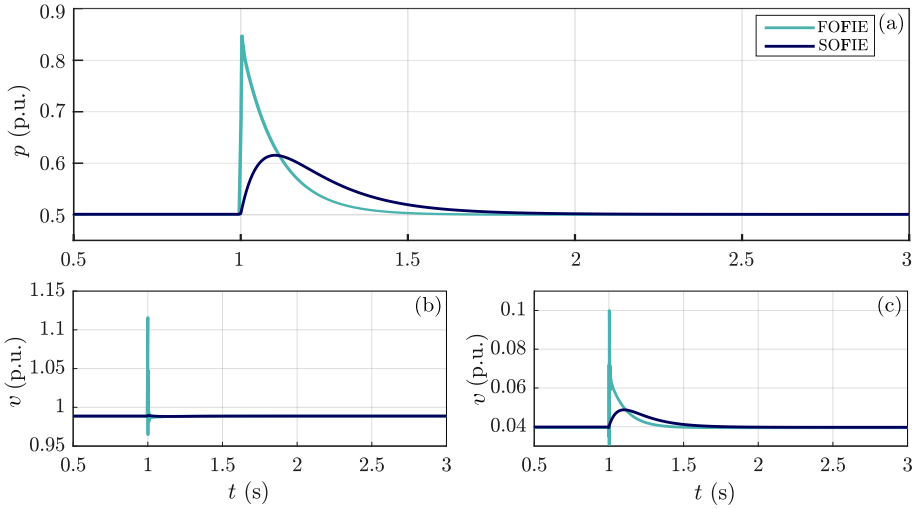


**Figure 5.17:** Time domain simulations with an ideal PLL: (a) Converter inertial response, (b) Direct axis voltage ($v_{o_d}$), and (c) Quadrature axis voltage ($v_{o_q}$).

### 5.7.2 Analysis including the PLL dynamics

Previous section illustrates the differences on the ideal dynamic response between the FOFIE and SOFIE controllers when an instantaneous frequency estimation and a perfect synchronisation with the grid voltage is assumed. This section analyses the effect a real PLL on the dynamic of the system of Fig. 5.2. A SRF-PLL has been considered in the analysis. The natural frequency of the PLL ($\omega_{n_{pll}}$) is calculated through its linearisation and subsequent equivalence with a second-order system [158], as follows:

$$\omega_{n_{pll}} = \frac{\pi - \arctan\left(\frac{\sqrt{1-\zeta_{pll}^2}}{\zeta_{pll}}\right)}{t_{pll}\sqrt{1-\zeta_{pll}^2}} \tag{5.28}$$

where $t_{pll}$ is the time response of the PLL and $\zeta_{pll}$ is the damping constant. A $\zeta_{pll} = 1/\sqrt{2}$ has been assumed in the analysis. The PI controller gains of the PLL are computed from the linearized models as follows:

$$k_{p_{pll}} = \frac{2\,\omega_{n_{pll}}\,v_b\,\zeta_{pll}\,\sqrt{2}}{v_{b_{ll-rms}}\,\omega_b} \tag{5.29}$$

$$k_{i_{pll}} = \frac{\omega_{n_{pll}}^2\,v_b\,\sqrt{2}}{v_{b_{ll-rms}}\,\omega_b} \tag{5.30}$$

where $v_{b_{ll-rms}}$ is the nominal line-line RMS voltage, and $v_b$ is the nominal peak phase voltage at the ac side.

Two different parametrisations, A and B, have been considered for each controller (see Table 5.2). In the parametrisations referred as FOFIE A and SOFIE A, the response time of current controllers (CR) and the cutoff frequency of the filters are assumed to be the same for a fair comparison between both controllers. However, due to high-frequency resonances excited by the interactions between the inertia emulation and the *LC* elements, the response time of the PLL in the FOFIE A parametrisation has to be much slower than in the SOFIE A case. Otherwise,the *LC* resonances excited by the FOFIE are fed back through the PLL to the control signals and destabilise the system. Another way to obtain the attenuation of these modes is by slowing down the current loops, which allows to increase the response time of the PLL. This is considered in the FOFIE B parametrisation. Finally, in the SOFIE B parametrisation, the controller is configured at its bandwidth limits to improve the inertial response while maintaining stability.

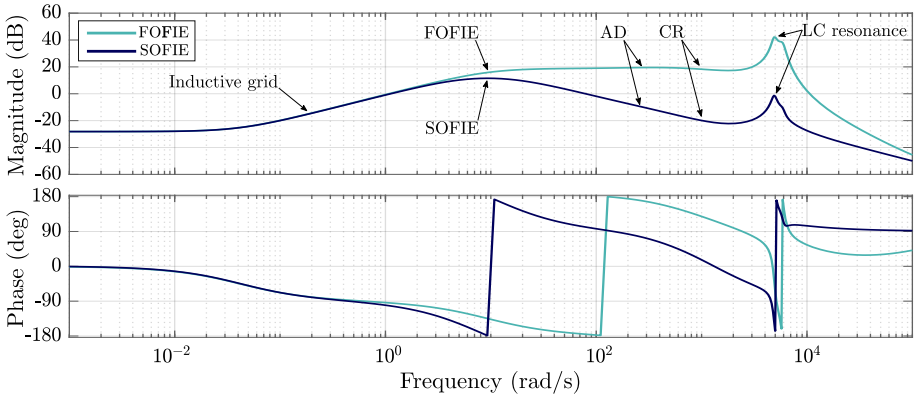


**Figure 5.18:** Bode diagram of $[v_{o_q}(s)/\omega_g(s)]$ with ideal PLL dynamics.

Fig. 5.19 shows the active power in response to a $-0.003\,p.u.$ step change on the grid frequency of the parametrisations. FOFIE A shows the worst performance in terms of power response, as the converter releases a delayed inertial response due to the slowness of the PLL to detect changes in the grid frequency. This means that a FOFIE control with a real PLL parametrised with these parameters will not be able to provide the ideal response showed on Fig. 5.17 and will not improve the rate of RoCoF when there is a sudden power perturbation of the grid. This drawback is fully overcome by the SOFIE A parametrisation, which makes use of the same cutoff-frequency and response time of the current controller than those used with FOFIE A but a fast PLL can be used. Fig. 5.19 illustrates how the response of SOFIE A is stable while providing better inertial response than FOFIE A. It is also worth noting that SOFIE

**Table 5.2:** Dynamics of the converter control loops for each scenario

| | CR time ($t_c$) | PLL time ($t_{pll}$) | Filter freq. ($\omega_n$) |
|---|---|---|---|
| FOFIE A | 2.5 *ms* | 1.2 *s* | 9.34 $rad/s$ |
| FOFIE B | 50 *ms* | 600 *ms* | 9.34 $rad/s$ |
| SOFIE A | 2.5 *ms* | 10 *ms* | 9.34 $rad/s$ |
| SOFIE B | 2.5 *ms* | 10 *ms* | 29.54 $rad/s$ |

A exhibits almost an identical response to that shown previously in Fig. 5.17 when an ideal synchronisation was assumed. This is due to the ability of SOFIE controllers to make use of fast current loops and PLL without compromising system stability.

FOFIE B is able to provide a faster and bigger power response to frequency variations than FOFIE A, thus improving the inertial response. It exhibits a dynamic performance comparable to that of the SOFIE A. Nevertheless, it is important to remark that to guarantee the system stability, the response time of the PLL still needs to be very slow. Besides, the response time of the current controller needs to be slow as well, which compromises its dynamic response and the rejection to voltage perturbations. All in all, FOFIE controllers requires parametrisations with slow PLL or slow current loops or a combination of both, which severely limits their practical application.

Lastly, the SOFIE B parametrisation provides the fastest power response under the frequency deviation thanks to the combination of fast current control loops and PLL and increased bandwidth of the second-order filter. As will be elaborated later, this controller will provide a performance similar to a SM or other grid-forming control approaches for improving the RoCoF of the grid frequency. This demonstrates the potential benefits of the SOFIE control for converters connected to grids that are weaker in terms of inertial response.

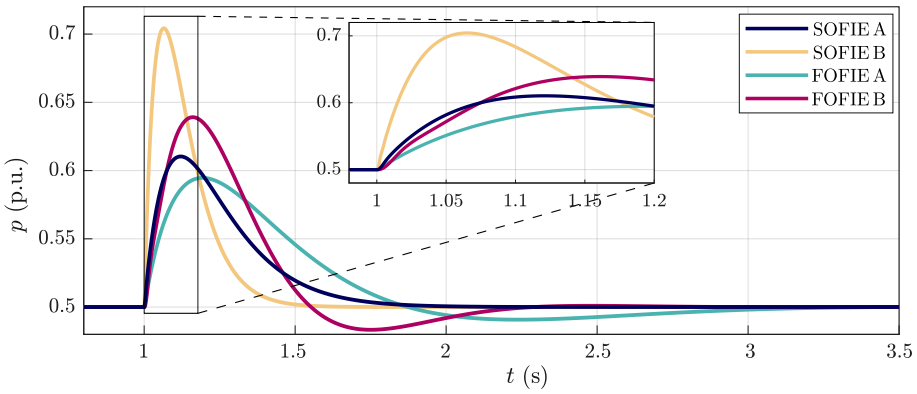


**Figure 5.19:** Behaviour of the converter power for the four scenarios studied..

### 5.7.3 Parametric sensitivity analysis

This section discusses the impact of the control techniques on the stability of the system. A parametric sensitivity analysis is performed for the system of Fig. 5.16 when the converter is equipped with the FOFIE B and SOFIE A parametrisations. The analysis reveals the system's stability under varying control parameters. The unstable cases are shown in black triangles.

#### Variation of the inertia constant ($H$)

Fig. 5.20 shows the location on the complex plane of the oscillatory modes of the system of Fig. 5.16 for the analysed techniques when the inertia constant ($H$) is modified. The results reveal that the modes associated with the *LC* resonance lose damping as the inertia constant increases and eventually become unstable when $H$ exceed a given threshold value in the FOFIE control. As demonstrated in (5.27), the inertia constant directly impacts the first stage of the transient that causes the excitation of the *LC* resonance, compromising the system stability. Thus, the inertia that FOFIE can emulate in resonant networks is limited. In the SOFIE case,

the eigenvalues remain always in the left half-plane even for the highest values of $H$ considered in the analysis. Thus, the system remains stable. Considering that the main objective of inertia emulation techniques is to provide synthetic inertia to the grid and given the limitations of FOFIE, it can be concluded that SOFIE represents a better solution. It allows the emulation of higher inertia constants without threatening the stability of the network.

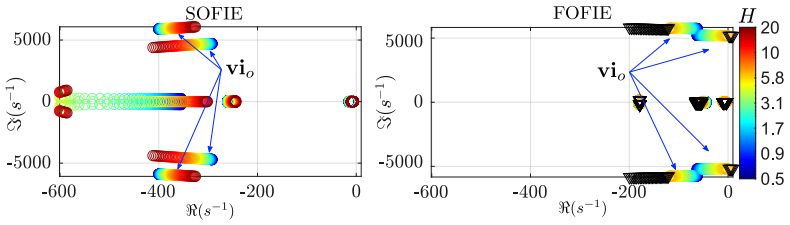


**Figure 5.20:** Root-locus under a variation of the inertia constant ($H$).

### Variation of the time constant ($t_{pll}$) of PLL

Fig. 5.21 shows how the location of the eigenvalues of the FOFIE B and SOFIE A parametrisations evolves as the response time of the PLL ($t_{pll}$) changes while the rest of the parameters remain as in Table 5.2. It can be observed how FOFIE eigenvalues move towards the right half-plane, and eventually, the system becomes unstable as the PLL becomes faster. This is since the *LC* resonances of the output voltage excited by FOFIE are fed back to the power reference calculation by the PLL. If the PLL is extremely slow, these resonances are filtered, but otherwise, the system becomes unstable. This is an issue since the need for very slow PLLs hampers the practical interest of FOFIE. However, this is overcome by SOFIE that, as it can be observed in Fig. 5.21, is stable over a broader range of PLL dynamics, thus enabling the use of fast PLLs without sacrificing grid stability.

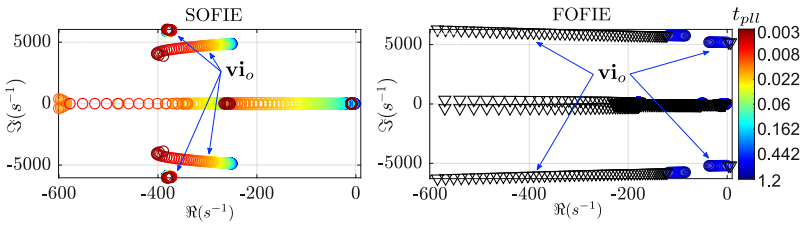


**Figure 5.21:** Root-locus under a variation of the filter time constant value ($t_{pll}$).

### Variation of the time constant of the current controller ($t_c$)

Fig. 5.22 shows the location of the eigenvalues in the complex plane as the response time of the current control loop changes and the rest of parameters remains as disclosed in Table 5.2 for the FOFIE B and SOFIE A paremetrisations. It can be observed how the FOFIE gets unstable as the response time of the internal current control loop decreases. Therefore, the current control loop bandwidth has to be reduced, which limits the ability to response fast to changes in the power set-points and to reject voltage perturbations at the PCC due to as for instance voltage sags. As in the previous case, SOFIE is able to overcome these issues by enabling the use of fast current controllers.

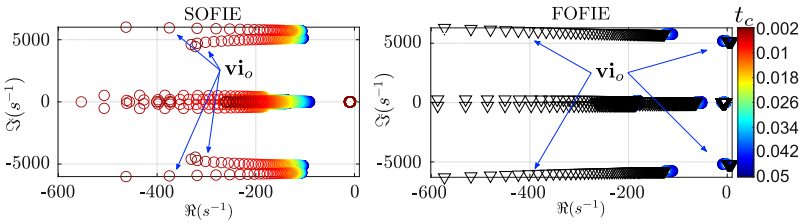


**Figure 5.22:** Root-locus under a variation of time of the inner loop ($t_c$).

### Variation of low-pass filter cut-off frequency ($\omega_n$)

Fig 5.23 presents the behaviour of the poles under the variation of the natural frequency of the filter ($\omega_n$). FOFIE is stable for a low value of $\omega_n$. However, according to (5.27), this limits the inertial response of the system. On the other hand, the SOFIE control system shows superior performance. It maintains system stability over the entire range of parameters analysed.

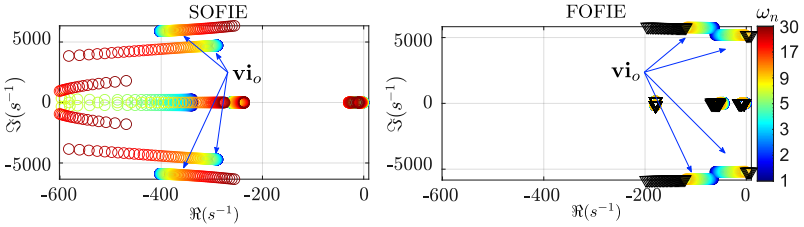


**Figure 5.23:** Root-locus under a variation of the cut-off frequency of the filters ($\omega_n$).

## 5.8 Grid-supporting and grid-forming: a brief analysis in low inertia power systems

The aim of this section is to validate the performance of the FOFIE B and SOFIE A controllers in a low power system and to benchmark their inertial response against that of a synchronverter (SV) [74]. To do it, a low inertia power system following the scheme of the 9-bus IEEE test case shown in Fig. 5.13 is considered. The inverters at buses 1 and 3 are simultaneously equipped with the control techniques that are the focus of each study.

The SM of bus 2 is in charge of forming the grid and is modelled by a reduced-order system with a turbine and governor, as described in chapter 4. The parameters of the SMs and the inverters are in Appendix B - Tab. B.3. Several studies have emphasised the need to model transmission lines as full-order dynamic models in converter-dominated networks, due to adverse interactions between inverter dynamics and the resonances of *LC* models [25]. Thus, the transmission lines have been assumed as a $\pi$ model and the loads as constant *RL* impedances.

In order to analyse the inertial behaviour of the grid frequency, a load variation of $0.05\,p.u.$ at $t = 1\,s$ is applied to bus 6.

Fig. 5.24 presents the frequency behaviour of the three scenarios studied for two synthetic inertia constants ($H$), revealing that the SOFIE control is capable of emulating the electromechanical behaviour of the SV in the two synthetic inertia scenarios studied. The FOFIE control

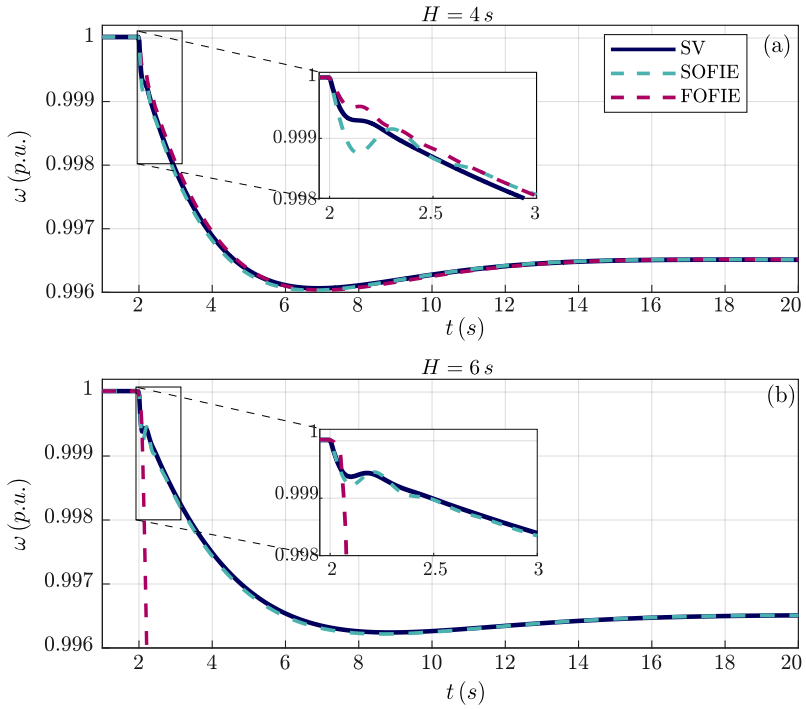


**Figure 5.24:** Frequency behaviour of the low inertia grid. (a) Synthetic inertia ($H = 4s$). (B) Synthetic inertia ($H = 6s$).

also manages to closely emulate the behaviour of the SV at $H = 4s$ (Fig. 5.24-a). However, when $H = 6s$ (Fig. 5.24-b) the FOFIE control becomes unstable, due to its limitation to emulate high inertia values.

One of the main challenges of massively integrating converters into the power system is the adverse interaction between the dynamics of the converter and the *LC* grid resonances. Therefore, to study these interactions, the eigenvalues of the linear system are analysed for scenario $H = 4$ s. Fig. 5.25 shows the position of the the oscillatory modes for the FOFIE B, SOFIE A and the SV. The dominant eigenvalues are shown in the zoomed-in area. Outside the zoomed-in area are the modes associated with the resonances of the transmission lines and the PLL poles. The results confirms the observations made in previous sections. The FOFIE control excites all associated *LC* resonant modes moving them towards the right half plane and limiting the converter dynamics. Conversely, the resonant *LC* modes when SOFIE controllers are considered are in close proximity to those of the SV. Although the converters equipped with SOFIE controllers add fast dynamics due to the PLL and the internal control loops, they does not excite adverse *LC* resonances due to the presence of the second-order filter. Besides, the low-frequency oscillatory modes associated with the emulation of inertia (noted as IE in the Fig. 5.25) are in close proximity to those of the SV as well, showing the capacity of the SOFIE controllers to emulate accurately the dynamics of the swing equation in which SV techniques are based.

A parametric sweep of the inertia constant ($H$) of the three compared techniques are performed to analyse the inertia emulation capacity, and their impact on the rest of the network components. Fig. 5.26 shows that the SV and SOFIE exhibit similar dynamic behaviour since their oscillatory modes are located in close proximity as the inertia constant is swept. On the contrary, the system with the FOFIE controller becomes unstable as the inertia constant

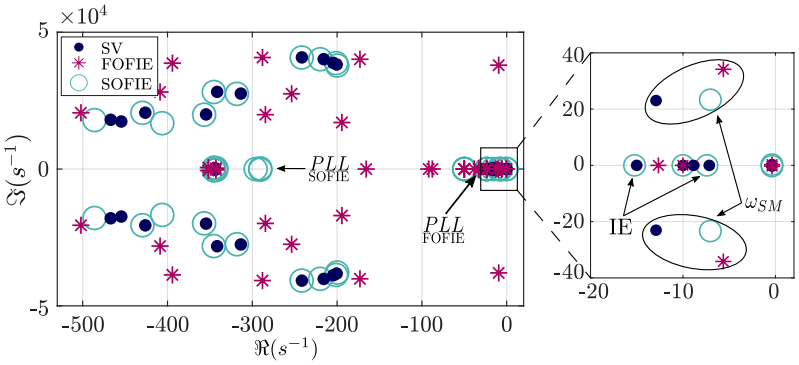


**Figure 5.25:** Behaviour of resonant and electromechanical modes at $H = 4s$.

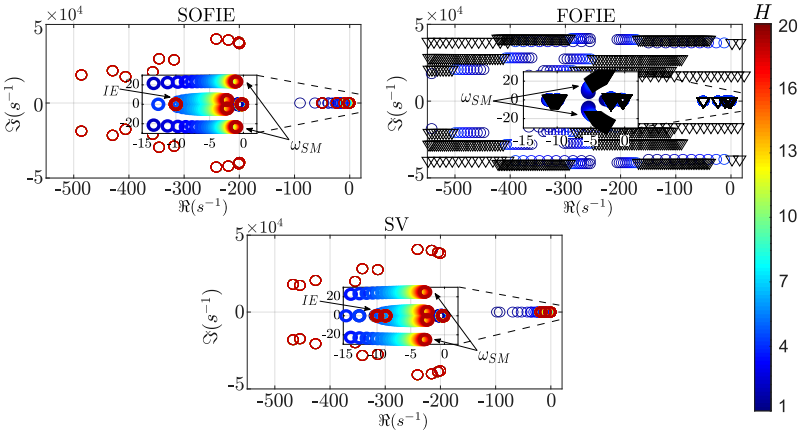


**Figure 5.26:** Root-locus under a variation of the inertia constant ($H$) in a low inertia power system.

increases. This analysis confirms the findings of previous sections and remarks how the limitations of inertia emulation techniques that follow a FOFIE implementation can be overcome by the SOFIE controllers.

## 5.9 Experimental validation

The aim of this section is to validate the performance of the proposed SOFIE implementations experimentally.

### 5.9.1 Validation of SOFIE control

For that purpose, a hardware-in-the-loop (HIL) test bench based on an OPAL-RT is used (Fig. 4.19). The inverter semiconductors, inductive filter, grid-side impedance and the infinite bus have been has been emulated in the FPGA of the OPAL-RT. In contrast, the converter control comprised by the SOFIE implementation, the current reference calculator, the current controller, the PLL and the space vector modulator are implemented on a Texas Instruments TMS320F28379D. The validation is carried out following the same methodology as in Section 5.3, which consists of testing the time-domain performance of the SOFIE implementations under a reference power ($p^*$) and a grid frequency variation ($\omega_g$).

The results in Fig. 5.27 show that for a $0.1\,p.u.$ variation in the active power reference, the experimental results matches the dynamic response of the small-signal models used to elaborate previous sections, thus validating them. As previously mentioned, the SOFIE 1 and 2 implementations modify their output power instantaneously because the power set-point is not filtered in the controller. The SOFIE 3 implementation, on the other hand, shows a slower power variation compared to the previous two. It is also worth noting how the experimental results of the SOFIE 1 implementation exhibit a significantly bigger noise than in the second and third configuration. This demonstrates the effectiveness of the second-order filter in the droop loop (refer to Fig. 5.1), since the frequency noise is not directly fed to the power controller. In SOFIE 2 and 3, the ripple is reduced to $0.02\,p.u.$ compared to the $0.1\,p.u.$ ripple of SOFIE 1.

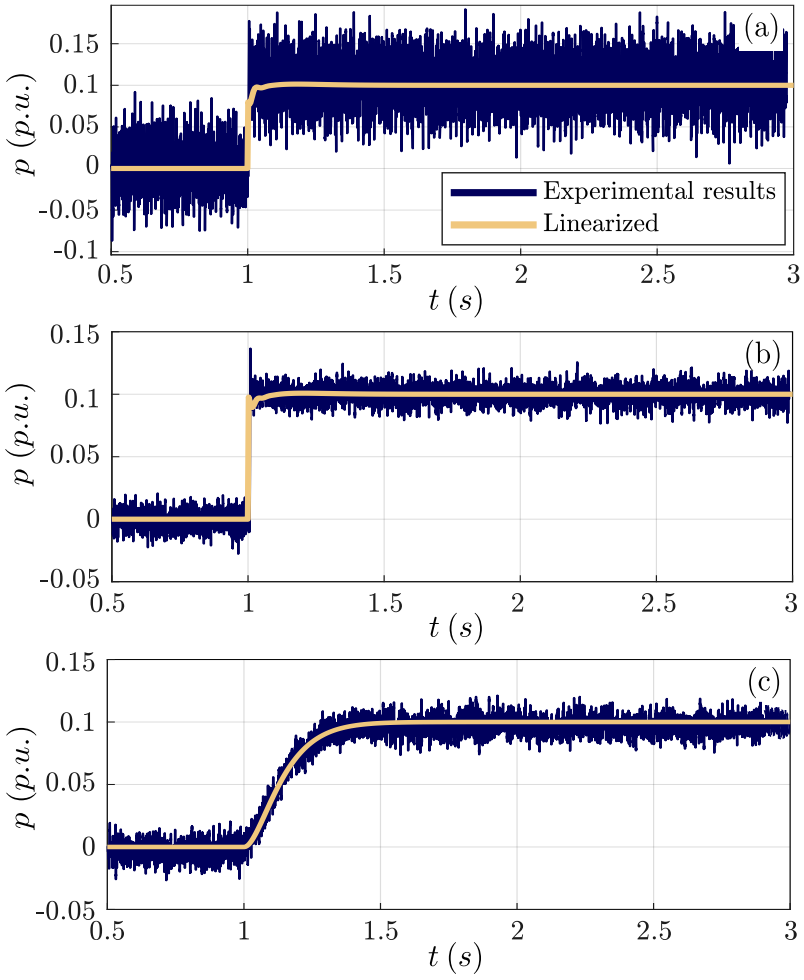


**Figure 5.27:** Validation of the linearized model against real-time simulation based on Opal-RT in the face of a change of $p^*$. a) SOFIE 1 implementation, b) SOFIE 2 implementation, v) SOFIE 3 implementation.

Fig. 5.28 illustrates the time-domain results for a $-0.01\,p.u.$ grid frequency variation. The experimental results also exhibit a good match with the analytical curves, and illustrate once again how the SOFIE 1 implementation has a higher power overshoot under sudden frequency variations compared to the other two implementations.

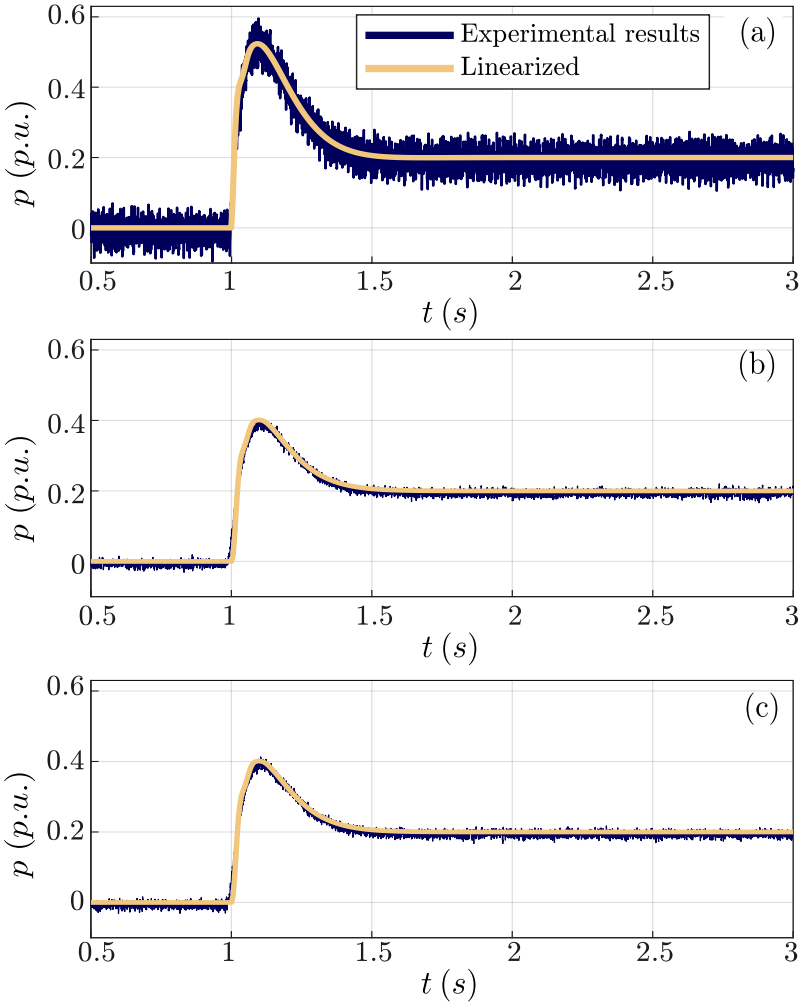


**Figure 5.28:** Validation of the linearized model against real-time simulation based on Opal-RT in the face of a change of grid frequency. a) SOFIE 1 implementation, b) SOFIE 2 implementation, c) SOFIE 3 implementation.

### 5.9.2 Validation of the inertial response of the FOFIE vs SOFIE control.

The aim of this subsection is to validate the performance of the FOFIE and SOFIE implementations experimentally.

The results of Fig. 5.29 show the active power inertial response of the converter to a step-change of 0.003 $p.u.$ in the grid frequency. The active power response of the small-signal model and the experimental results match perfectly in both implementations, thus validating the operation of both control techniques and proving the accuracy of the small-signal models used to support the conclusions achieved in previous sections. Furthermore, the SOFIE scenario active power has a ripple of 0.02 $p.u.$ despite having fast PLL and current loops (10 $ms$ and 2.5 $ms$, respectively); meanwhile, in the FOFIE control scenario, the ripple is 0.035 $p.u.$ Thus, the SOFIE control reduces the ripple generated by the modulation of the converter switches without affecting the converter's bandwidth.

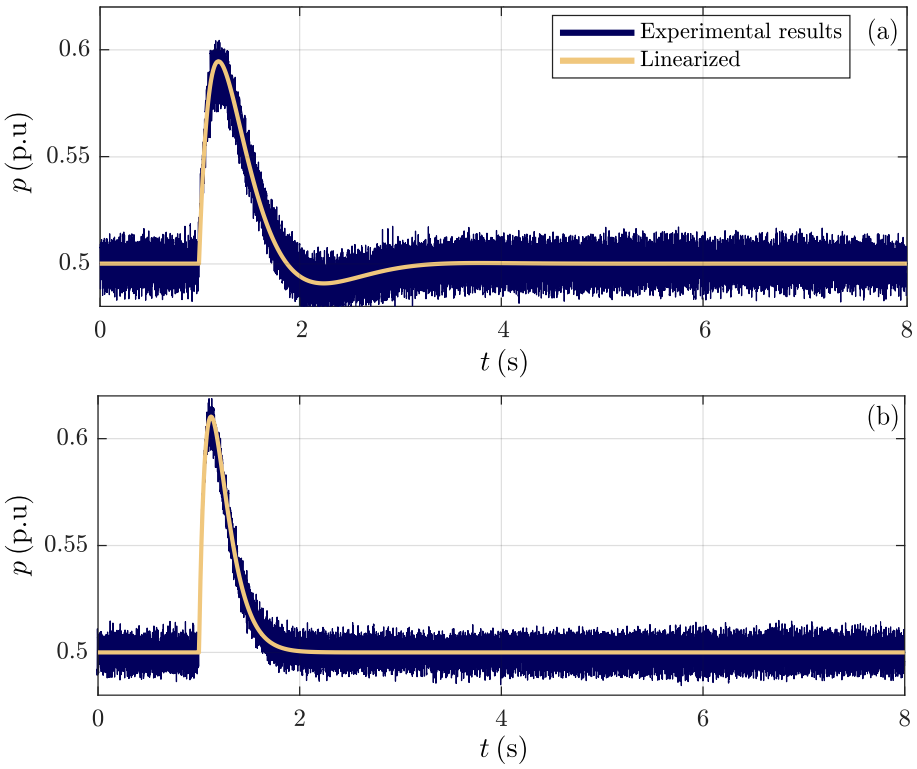


**Figure 5.29:** Validation of the linearized model against real-time simulation based on Opal-RT in the face of a change of grid frequency. a) FOFIE, b) SOFIE.

## 5.10 Summary

This chapter has presented a new grid-supporting control approach, with three different implementations, that allows the converter to support the grid frequency while providing the inertial behaviour, primary response and damping of a SM. To validate whether the converter can reproduce the dynamics of a SM, time-domain simulations and a detailed analysis of the eigenvalues of the system have been carried out. The results show how the proposed control implementations allow to a greater or lesser extent to operate a grid-connected converter with dynamics close to those of an ideal SM. Among the proposed implementations, SOFIE 3 is the approach that most accurately replicates the response of a simplified SM, while SOFIE 1 and 2 require almost no variation on the structure of classical inertia emulation controllers, but replicate the operation of SMs with a minor degree of accuracy. In this regard, SOFIE 2 is able to respond to grid frequency variations by emulating the same inertial response than that of an equivalent SM but, unlike SMs and SOFIE 3, it is capable of responding quasi-instantaneously to variations on the power setpoints of the primary controller. Therefore, SOFIE 2 is recommended for those applications where inertia emulation is required and the dynamics of the power set-point should not be modified. This is the case, for instance, of the converter of a photovoltaic or wind generation system where the power set-point is calculated with a MPPT algorithm. On the other hand, SOFIE 3 is recommended for applications in which sharp changes in the power set-point require filtering to avoid sudden power transients. This might be the case of a stationary energy storage system. The chapter has elaborated as well on the effect of the PLL on the closed-loop dynamics of the SOFIE controllers. If the PLL is fast

enough, the dynamics of the dominant modes of the proposed SOFIE 2 and 3 controllers are decoupled from those of the PLL. It has been also shown how the faster the PLL, the closer the behaviour of the converter to that of a synchronous machine. The low inertia network study showed that SOFIE control emulates the inertial behaviour of an SM, improving the stability of converter-dominated systems without exciting the LC resonances of the grid.

A comparison between the SOFIE and the conventional FOFIE control approaches has also been carried out. It is shown how FOFIE controllers can generate adverse interactions between the converter control loops and the *LC* components of the power system, which jeopardises the system stability. The main motivation behind these interactions is the derivative behaviour of the FOFIE, as it is equipped with a first order high-pass filter. This drawback can be mitigated by slowing down the PLL or the inner current control loops. However, this affects the dynamic response of the converter to set-point changes and the ability to reject perturbations due to voltage variations (as, for instance, voltage sags) at the point of common coupling. These issues seriously hinder the practical use of FOFIE techniques.

SOFIE can overcome the previous issues, thus enabling the practical use of inertia emulation techniques. It has been shown how SOFIE does not excite *LC* resonances, thanks to its 40dB/decade filtering capability, thus improving the stability margins for a wide range of emulated inertia constants and response times of the current control loops and PLLs. Therefore, SOFIE techniques can be equipped with fast PLLs and current control loops that increase the bandwidth of the internal controller and enable the provision of fast frequency response services. Besides, SOFIE can emulate a wide range of synthetic inertia constants without compromising system stability.

Even though SOFIE and SV follow completely different implementation approaches and grid synchronisation principles, both can exhibit a similar inertial response if SOFIE is properly parametrised. This feature is interesting since it enables, in line with the needs detected in recent studies [3], the coexistence of GFM and GSC techniques in modern grids to reinforce the system's robustness. GFM control techniques can provide services such as black-start or inertia and primary frequency response in weak grids (with high equivalent grid impedance). At the same time, they can have some issues synchronising and maintaining stability in stiff grids. In these cases, SOFIE GSC techniques are a good alternative since they can provide synthetic inertia and primary frequency response without synchronisation issues and preserve system stability.

# Chapter 6

# Conclusions and Outlook

*In this chapter, we summarise the most important observations of the thesis; the areas of research that we consider could be explored in future work and the lines of research we are currently pursuing.*

## 6.1 Conclusions

Power systems are undergoing one of the most significant paradigm shifts in recent decades due to the massive integration of non-conventional energy sources connected to the grid via electronic converters. This situation changes the dynamics of the power system and poses several challenges in the fields of control, protection and operation. This doctoral thesis focusses on the stability analysis and control of power electronics dominated power systems. It shows how the classical power system stability analyses need to be reformulated and proposes a new family of GSC techniques that overcomes the main limitations of the inertia emulation techniques present in the state-of-the-art.

The first objective of the thesis is the development of methodologies for dynamic analysis, which allows for studying the adverse interactions produced by the integration of converters into the grid. In this sense, chapter 3 presented the methodology and mathematical foundations of CSTEP, a tool for analysing the stability of converter-dominated grids using EMT models. This chapter demonstrated that stability studies based on EMT models are able to evaluate the small-signal stability beyond the electromechanical interactions - analysed in RMS models - allowing to assess the interactions between each of the converter dynamics and the passive elements of the network.

In subsequent chapters, the thesis studies the stability of networks dominated by GFM and GSC converters to characterise these control technologies. In this direction, chapter 4 presents the comparative small-signal analysis of some of the most relevant GFM techniques (VCVSM, SV, MC and dVOC). Likewise, to analyse the operation of the inverter under different grid scenarios, the inverter is connected to an equivalent grid that allows variations of essential parameters that will define the system's stability, such as inertia, equivalent impedance and system load. The results demonstrate the importance of maintaining a minimum of inertia in the system to prevent the electromechanical eigenvalues from becoming fast enough to interact with the resonant modes of the passive elements, generating instabilities in the network. Besides, to overcome the difficulty that GFM converters have to maintain stability in stiff grids - a small equivalent impedance - was demonstrated, revealing that the VCVSM achieves better stability limits in these scenarios thanks to the virtual impedance and the damping term that manage to attenuate the electromechanical oscillations.

Chapter 5 elaborates on GSC techniques. It shows how the high-pass characteristic of FOFIE controllers is the main root of the low damped or even unstable close loop modes that are stablished due to the interactions between the converter controllers and the LC passive elements of the grid. These modes can be attenuated by slowing down the PLL or the current control loops of the converter controllers. However, the required time response of the PLL and current control loops to stabilize the system is usually higher than that that makes physical sense to operate the system. Besides, chapter 5 also illustrates how FOFIE controllers do not replicate with accuracy the dynamics of a SM. Building on these observations, the thesis proposes a new family of second-order filter-based inertia emulation techniques that emulates the electromechanical behaviour of a SM while maintaining the traditional structure of the inertia emulation control. The proposed control was compared against a synchronous machine, demonstrating that the SOFIE perfectly emulates the transient and steady-state behaviour of a synchronous machine, allowing correct management of the damping of power oscillations and the integration of a virtual reactance. Additionally, to analyse the advantages of SOFIE control over FOFIE control, a comparison was made in an infinite grid and a low inertia system, revealing that SOFIE manages to increase the bandwidth of each control loop,

increasing the global stability limits of the system. Finally, the behaviour of the SOFIE control was compared against the synchronverter and the traditional FOFIE, revealing that the SOFIE control presents stability limits very similar to those of the synchronverter. Therefore, and in conclusion, SOFIE control is shown to be a very attractive alternative for emulating inertia and attenuating power oscillations in stiff grids.

## 6.2 Future Research Areas

This section introduces some lines that could be built on the results of the thesis but require further investigations:

1. This thesis demonstrates that EMT modelling converter-dominated grids is a valid methodology for performing small and large signal stability analysis. However, this type of modelling has limitations in dealing with large power systems due to the high consumption of computational resources. In this regard, it is necessary to develop new model reduction techniques, which allow the analysis of adverse interactions between passive grid elements and the inverter while reducing computational resources.

2. It has been considered all along the thesis that the proposed SOFIE controllers are connected to an ideal dc source that can provide the required power. This approach makes sense for stationary battery energy storage systems. Nevertheless, FOFIE controllers have also been proposed in the literature to emulate inertia in other applications, such as wind or PV. In this sense, it is necessary to analyse the advantages of upgrading FOFIE control to SOFIE control in this these applications, taking into account the ability of the SOFIE control to attenuate electromagnetic oscillations and increase the overall stabilisation limits of the system.

3. The SOFIE techniques described in the thesis have been designed to emulate the inertial response provided by SM as a way to support the ac grid and reduce its RoCoF. It seems interesting to extend the concept of SOFIE control approaches to the dc side, in such a way that the converter could emulate the operation of a virtual capacitor (the equivalent of a virtual inertia in ac) to reduce the rate of change of voltage (RoCoV) produced by load transients in the dc side. Besides, it would be desirable to endow the new dc control approach with a virtual damping term, totally decoupled from the droop characteristics, that would allow the controller to damp oscillatory modes without changing the load-sharing characteristic of the converter in the steady state.

## 6.3 Areas of research in development

This section develops further the third point discussed in the previous section. Its main objective is to briefly introduce some research aspects, that have been already carried out but are not concluded yet, to develop a control strategy to control converters in GFM or GSC mode in dc networks. The main goal of the proposed controller is the emulation of a virtual capacitor and a virtual impedance that improve the transient response on the dc side by reducing the RoCoV and by increasing the damping of critical oscillatory modes.

### 6.3.1 Second-order filter-based inertia emulation in dc grids

#### DC side control based on resonant *RLC* circuit

The proposed control to regulate the dc voltage of the grid is based on a resonant *RLC* circuit (as shown in Fig. 6.1). This second-order *RLC* circuit is composed of a virtual capacitor ($C_v$) to increase the capacitance of the network, a virtual conductance ($G_v$) and virtual inductance $L_{dc}$ to add damping to the bus voltage $v_{dc}$.

The differential equation expressed in *p.u.* (appendix C shows the methodology for calculating the base values.) that describes the behaviour of the virtual dc voltage $v_{dc_v}$ of the capacitor $C_v$, is given by:

$$\frac{dv_{dc_v}}{dt} = \frac{\omega_b}{C_v}\left[i_i - i_{L_{dc}} - G_v(v_{dc_v} - v_{dc})\right]. \tag{6.1}$$

where $v_{dc}$ is the measured dc-bus voltage.

The voltage $v_{dc_v}$ is regulated by a voltage droop with gain $k_{dc}$, as follows:

$$i_i = k_{dc}(v^*_{dc} - v_{dc_v}) + i^* \tag{6.2}$$

To make the capacitor $C_v$ resonate virtually, a virtual inductance $L_{dc}$ is integrated, which is described as:

$$\frac{di_{L_{dc}}}{dt} = \frac{\omega_b}{L_{dc}}\left[v_{dc_v} - v_{dc}\right]. \tag{6.3}$$

The output current $i^*_{dc}$ can be expressed as in (6.4).

$$i^*_{dc} = i_i - i_{cv} = i_{L_{dc}} + Gv(v_{dc_v} - v_{dc}) \tag{6.4}$$

Assuming that in *p.u.* $v_{dc_v} = 1$, the reference power provided by the proposed control is given by:

$$p_{dc} = i^*_{dc} \tag{6.5}$$

By implementing a controller that regulates the dc current of the converter as in (6.4) or the dc power as in (6.5), the converter behaves as the virtual circuit represented in Fig. 6.2, which provides virtual inertia to the dc side, due to the inclusion of a virtual capacitor, and virtual damping due to the use of a $L_{dc}/R_v$ impedance.

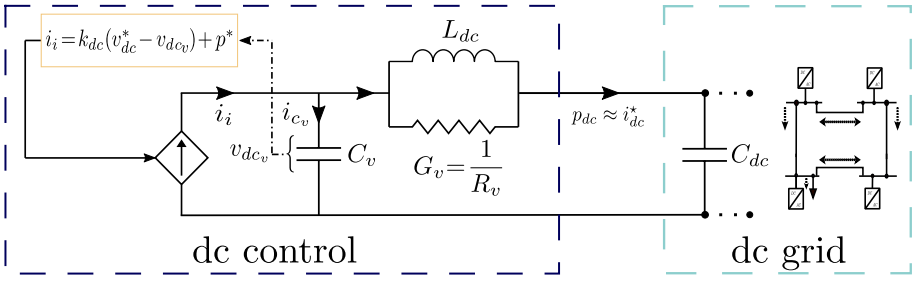


**Figure 6.1:** Resonant circuit used in dc control.

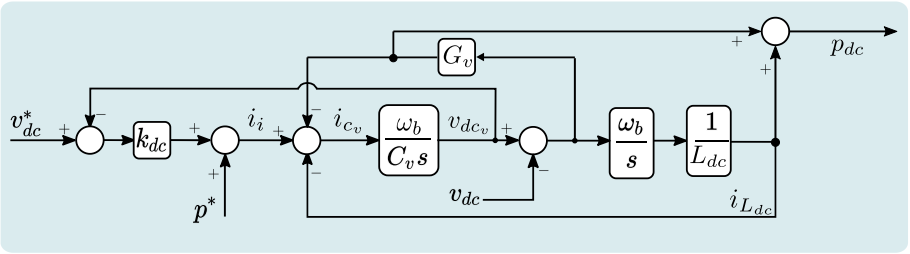


**Figure 6.2:** Block diagram of DC-SOFIE control based on differential equations.

## Introducing the DC-SOFIE controller

Equations (6.1)-(6.5) constitute the state-space model that represents the electrical performance of the proposed controller. Taking the Laplace transform of these expressions and after a few manipulations, the following transfer function for $p_{dc}$ can be defined:

$$p_{dc}(s) = G_1(s)\, v^*_{dc} + G_2(s)\, v_{dc} \tag{6.6}$$

$$G_1(s) = \frac{G_v\, L_{dc} k_{dc} \omega_b\, s + k_{dc} \omega_b^2}{C_v L_{dc}\, s^2 + (G_v L_{dc} \omega_b + L_{dc} k_{dc} \omega_b) s + \omega_b^2} \tag{6.7}$$

$$G_2(s) = -\frac{C_v G_v L_{dc}\, s^2 + (-G_v L_{dc} k_{dc} \omega_b - C_v \omega_b) s - k_{dc} \omega_b^2}{C_v L_{dc}\, s^2 + (G_v L_{dc} \omega_b + L_{dc} k_{dc} \omega_b) s + \omega_b^2} \tag{6.8}$$

Eqs. (6.7) and (6.8) compose a second order system with the natural frequency ($\omega_{n_{dc}}$) and damping ($\zeta_{v_{dc}}$) given by:

$$\omega_{n_{dc}} = \frac{\omega_b}{\sqrt{C_v\, L_{dc}}} \tag{6.9}$$

$$\zeta_{v_{dc}} = \frac{\sqrt{C_v\, L_{dc}}\,(G_v + k_{dc})}{2\, C_v} \tag{6.10}$$

Eqs. (6.7)-(6.10) represent the proposed control in the Laplace domain. It is a second order control system whose natural frequency and damping factor are correlated with the virtual circuit elements of Fig. 6.2 as given by (6.6) and (6.8). By making a block diagram representation of (6.7)-(6.10), the structure of the proposed DC-SOFIE is obtained as in Fig. 6.3.

### Time-domain performance of DC-SOFIE control

To determine the dynamic behaviour of the proposed control, the converter has been connected to an ideal dc voltage source which varies its amplitude from $1\,p.u.$ to $0.99\,p.u.$ at $t = 0.5\,s$. The parameters of the simulation are shown in the Appendix B - Tab.B.4. Fig. 6.4 reveals that the power response ($p_{dc}$) undergoes an almost instantaneous change because the virtual capacitor injects power into the grid quickly, preventing its discharge from the $C_v$. Besides, it is observed that the voltage of the virtual capacitor $v_{dc_v}$ is correctly damped, validating the virtual conductance's positive effect on the system's dynamic behaviour.

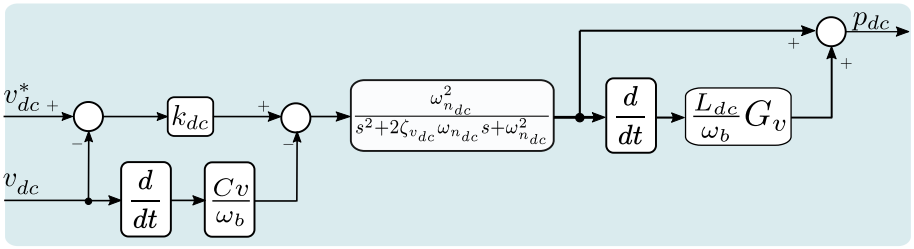


**Figure 6.3:** Block diagram of DC-SOFIE control implementation.

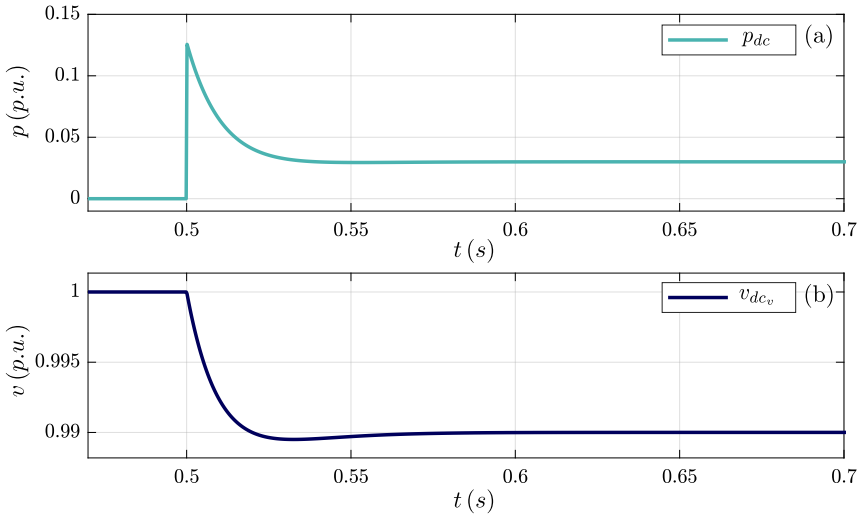


**Figure 6.4:** Block diagram of DC-SOFIE control implementation.

### 6.3.2 Dual Second-Order Filter-Based Inertia Emulation for HVDC and MTDC systems

Motivated by the need to improve the transient response of the future hybrid ac/dc grids, this section introduces a dual second-order filter-based inertia emulation (DSOFIE) controller for the ac/dc power converters that link both parts of the grid. The proposed DSOFIE controller combines the SOFIE introduced in Chapter 5 and the DC-SOFIE of the previous section in such a way that the power output of each of these controller is summed together to generate a new power reference ($p^*_e$) as in (6.11).

$$p^*_e = p^* + p_{ac} - p_{dc} \tag{6.11}$$

where the ac power reference ($p_{ac}$) is generated by SOFIE presented in section 5.2.2, while the dc power reference ($p_{dc}$) is generated by the DC-SOFIE controller presented in 6.3.1. The active power reference $p^+$ is added to dispatch the converter according to the optimum power flow.

The structure of the proposed DSOFIE is shown in Figure 6.5. By combining the SOFIE and DC-SOFIE in a single controller, the proposed DSOFIE takes benefit of the dc-side of the hybrid grid to provide virtual inertia support and damping to the ac-side. Alternatively, the ac-side is used to provide virtual capacitance support, thus contributing to improve the RoCoV, and

damping to the dc-side of the grid. The main expected advantages of the proposed controller over existing techniques are:

1. Provides damping against active power (in ac systems) and voltage (in dc systems) oscillations without affecting the power dispatched in steady state.

2. Allows the seamless collaboration of both sides of the hybrid grid through the interface converters, in such a way that the dc-side provides inertial support and damping to the ac-side and vice versa.

3. Facilitates the seamless integration with existing converter controllers. Classical inertia emulation algorithms (i.e. FOFIE approaches) based on derivative terms can be easily adapted to the proposed DSOFIE technique.

To determine the dynamic behaviour of the proposed control, the converter has been connected to an ideal dc voltage source which varies its amplitude from $1\,p.u.$ to $0.99\,p.u.$ at $t = 0.5\,s$. The parameters of the simulation are shown in the Appendix B - Tab.B.4. Fig. 6.4 reveals that the power response ($p_{dc}$) undergoes an almost instantaneous change because the virtual capacitor injects power into the grid quickly, preventing its discharge from the $C_v$. Besides, it is observed that the voltage of the virtual capacitor $v_{dc_v}$ is correctly damped, validating the virtual conductance's positive effect on the system's dynamic behaviour.

Finally, for the correct integration of the DSOFIE in the inverter, the classical GSC converter control strategy presented in Fig. 5.2 is used.

Using the methodology presented in 5.2.2, where a second-order filter is used to embed the dynamic behaviour of the controller, achieving a simpler implementation of the control system and additionally allowing an easy upgrade of the grid-supporting controller of the converters currently installed in the power grid, the structure of DSOFIE is shown in Fig. 6.5. In this sense, the cut-off frequencies ($\omega_{n_{ac}}$ and $\omega_{n_{dc}}$) and damping constants ($\zeta_{v_{ac}}$ and $\zeta_{v_{dc}}$) of the second filters are calculated according to Eqs. (5.15, (5.16), (6.9) and (6.10), respectively.

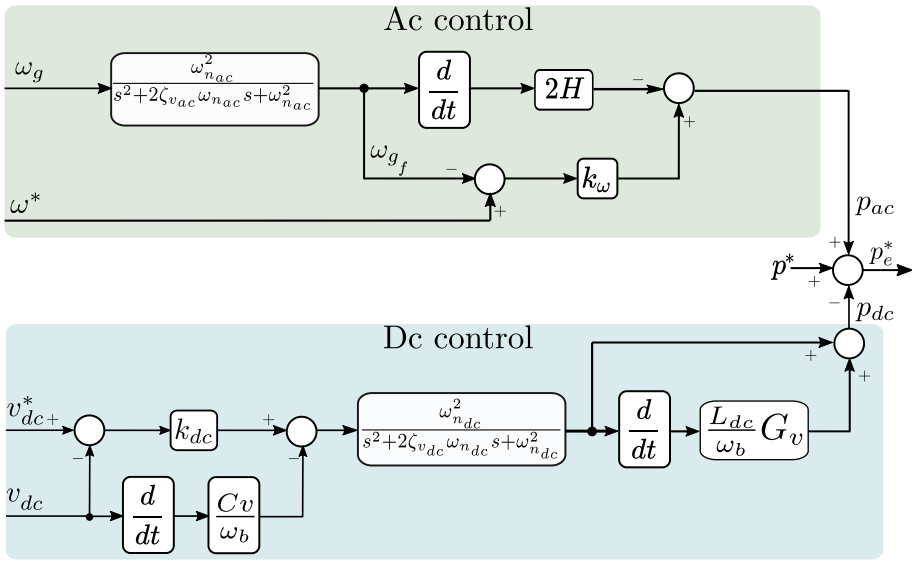


**Figure 6.5:** Block diagram of DC-SOFIE control implementation.

## Time-domain performance of DSOFIE control

### Description of the testing scenario

This section aims to corroborate the hypothesis made in the analytical description of the DSOFIE control by studying the dynamic behaviour of the converter using time-domain simulations. The electrical test system comprises two sources —ac and dc— connected to the inverter via transmission lines, as shown in Fig. 6.6. The ac and dc transmission lines have been assumed as $\pi$ models, to study interactions between the inverter and the resonances of the passive elements.

The control parameters of the DSOFIE controller are calculated using Eqs 5.15, (5.16), (6.9) and (6.10). On the other hand, the PLL parameters have been tuned according to the methodology proposed in [158]. Exploiting the ability of the SOFIE control to work with PLL with a high bandwidth (as concluded in chapter 5), its response time has been set to $t_{pll} = 0.01$ s. To guarantee that the time response of the current loop is several times faster than the GSC loop, its constants ($k_{p_c}$ and $k_{i_c}$) have been calculated using the "modulus optimum" method [146, 157]. The parameters and set-points employed in the following analyses are given in Appendix B - Tab. B.4.

### Performance test

Fig. 6.7 shows the power and dc-bus voltage behaviour against a change in the grid frequency of $-0.01\,p.u.$ in the form of a step at $t = 1s$. Next, in $2.5s$, a change of $0.01\,p.u.$ is made in the ideal dc source voltage.

The results reveals that during the change in frequency, the active power at the PCC (Fig. 6.7-(a)) presents an inertial response for the ac side during the $t = 1s$ and $2s$. This frequency disturbance will also be reflected in the bus voltage (Fig. 6.7-(b)) since the dc capacitor releases its stored energy. Subsequently, at the change in dc voltage ($t = 2.5s$), the converter quickly absorbs active power from the mains to avoid heavy discharges on the bus capacitor, thereby improving the RoCoV. These behaviours in the active power and bus voltage allow the converter to provide a fast transient response against power unbalances. On the other hand, in steady-state, the DSOFIE ensures the power dispatching on boths sides of the converter, enabling the interconnection of networks or the integration of dc generation systems through HVDC or MTDC links and removing the use of communication systems.

## Parametric sensitivity analysis

This section evaluates the influence of control parameters on oscillation modes using a stability analysis based on parameter sensitivity. To make the analysis, a state-space representation of the system of Fig. 6.6 has been made and their eigenvalues are computed by making use of the CSTEP tool introduced in chapter 2.

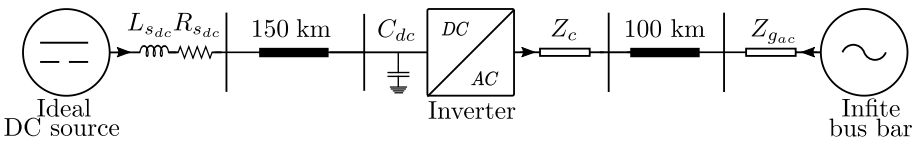


**Figure 6.6:** One-bus system comprised of GSC and infinite bus bar.

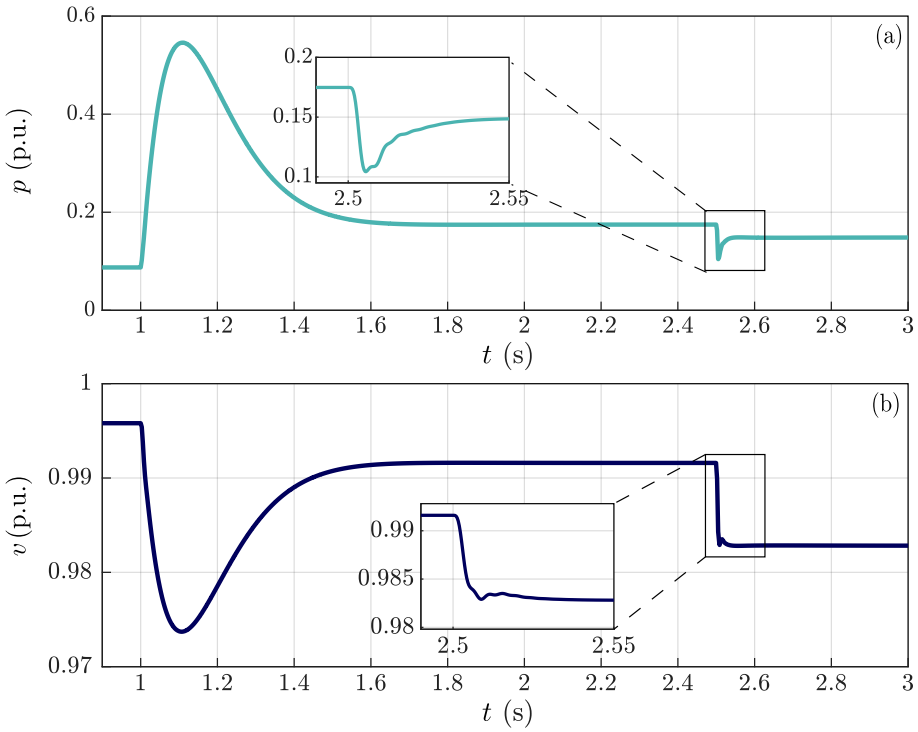


**Figure 6.7:** Time domain simulation in an ideal grid. (a) Active power at the PCC. (b) Dc bus voltage.

### Variation of synthetic inertia constants $H$ and $C_v$

Fig. 6.8 shows the location on the complex plane of the oscillatory modes of the system of the analysed system when $H$ and $(C_v)$) are modified. The results reveal that the electromechanical poles associated with the ac inertia emulation ($IE_{ac}$) move in response to the variation of the ac side inertia, creating a circumference with diameter $(2\,\omega_b)/((k_d+k_\omega)X_s)$ in the same way as an SM, as described in section 5.4.1. Consequently, as $H$ increases, the eigenvalues become complex numbers and the $IE_{ac}$ modes exhibit an under-damped oscillatory behaviour. Moreover, notice that the resonant modes related to the ac lines ($\mathbf{vi}_o$) are not excited, allowing a wide range of synthetic inertia values to be emulated, compared to techniques based on FOFIE control.

On the other hand, the sweep of $C_v$ reveals that as the size of the virtual capacitor increases, the eigenvalues related to dc inertia emulation ($IE_{dc}$) move in a semicircle in the same way as the SM (see section 5.4.1), confirming the equivalence between the inertia of the SM and a capacitor. Furthermore, it is shown that this behaviour of the modes ($IE_{dc}$) is replicated in the modes linked to the bus voltage ($v_{dc}$), demonstrating how the virtual capacitor achieves a fictitious increase in the capacity of the physical inverter capacitor.

### Damping factor $k_d$ and virtual conductance $G_v$ variation

Fig. 6.9 depicts the location of the eigenvalues in the complex plane as $k_d$ and $G_v$ vary. The results reveal that by increasing the damping gain ($kd$), the damping of the critical modes associated to the emulation of the SM ($IE_{ac}$) increases in the same way as in a real SM (see section 5.4.1). The eigevalues create a semi-circumference with a radius equal to the natural

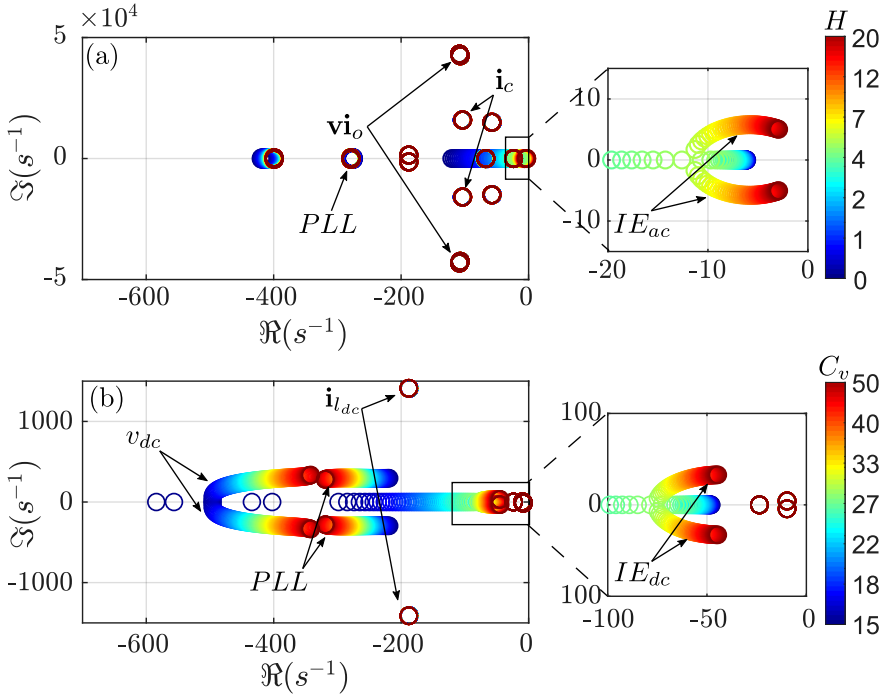


**Figure 6.8:** Root-locus under variations of the inertia constant. (a) Variation of the $H$. (b) Variation of the $C_v$

frequency ($\omega_{n_{ac}}$). This trend continues until $\zeta_{v_{ac}} = 1$ when the poles become real.

By varying virtual conductance $G_v$, the damping of the $IE_{dc}$ modes increases, permitting the DSOFIE control to attenuate the dc-bus voltage oscillations ($v_{dc}$). Additionally, the virtual conductance damps the oscillations of the resonant modes associated with the dc-lines ($\mathbf{i}_{l_{dc}}$), improving the stability margins of the dc-circuit.

### Virtual reactance $X_s$ and impedance $L_{dc}$ variation

Fig. 6.10 indicates the behaviour of the eigenvalues when varying the virtual reactance $X_s$ and virtual indutance $L_{dc}$. It can be observed in the zoomed regions of Fig. 6.10-a that, as the virtual reactance increases, the electromechanical modes $IE_{ac}$ move towards the real axis of the complex plane, thus becoming more damped, in the same way as an SM (see section 5.4.4).

On the other hand, Fig. 6.10-(b) shows how the modes associated with the $IE_{dc}$ behaves as the $L_{dc}$ inductance changes. These results can be used to select the $L_{dc}$ value to get an optimum damping of the $IE_{dc}$ modes.

## MTDC grid implementation

To study the dynamics of DSOFIE control and its performance in a multi-area system interconnected via an MTDC-link, the system shown in Fig. 6.11 is modelled. The system comprises of three aggregated network models shaped through reduced-order synchronous machines equipped with turbines and governors, as described in section 4.2.2. To evaluate the behaviour of DSOFIE control in low inertia systems, the aggregate network 1 has been assumed as

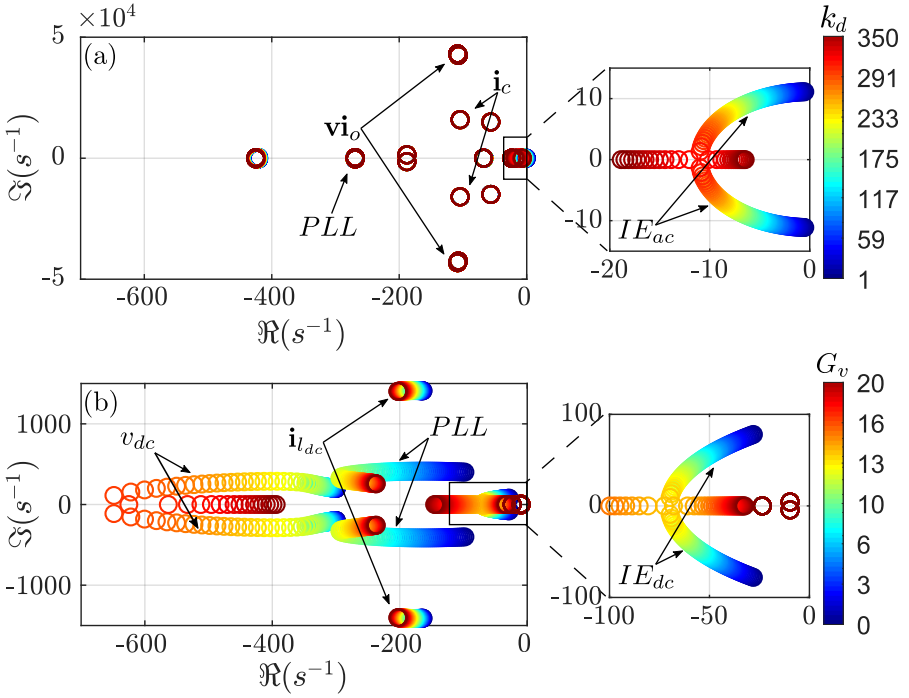


**Figure 6.9:** Root-locus under variations of the damping terms. (a) Variation of the $k_d$. (b)Virtual conductance $G_v$ variation.

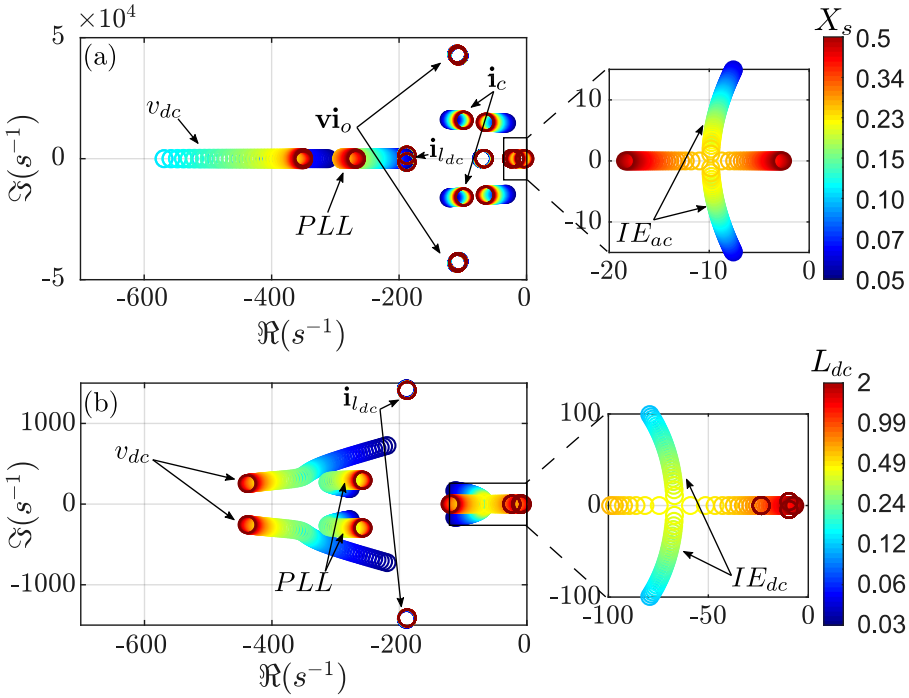


**Figure 6.10:** Root-locus under variations of virtual reactance and inductance. (a) Variation of the $X_s$. (b) Variation of the $L_{dc}$.

a low inertia grid ($H = 1\,s$). The parameters of the study can be found in Appendix B - Tab.B.4. The transmission lines of the ac and dc side have been implemented as equivalent $\pi$ models.

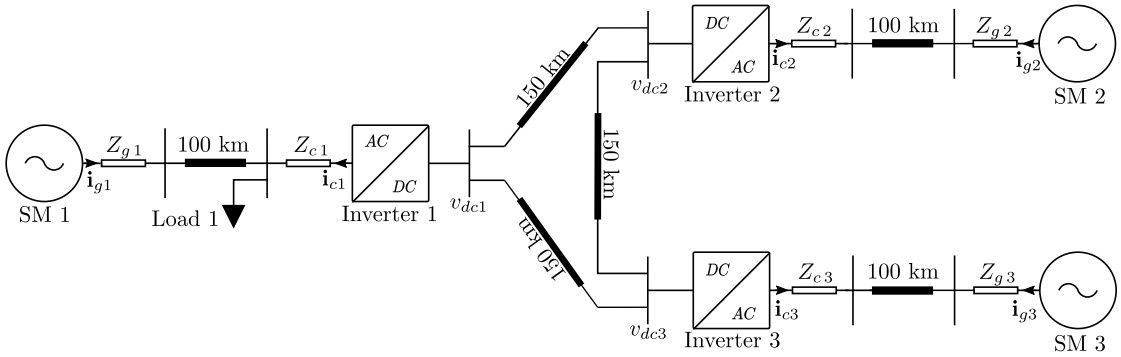


**Figure 6.11:** MTDC test network.

### Grid frequency inertial behaviour

To analyse the inertial behaviour of the grid in the presence of power imbalances, a load variation of $0.1\,p.u.$ at $t = 2.5$ s is applied at load 1. Fig. 6.12 demonstrates that the DSOFIE control manages to emulate inertia on the AC side, maintaining the dynamic behaviour of an SM even while providing a fast-frequency response (zero-inertia scanning). Therefore, the integration of DSOFIE control improves the RoCoF as the synthetic inertia added by the converter to the ac network increases.

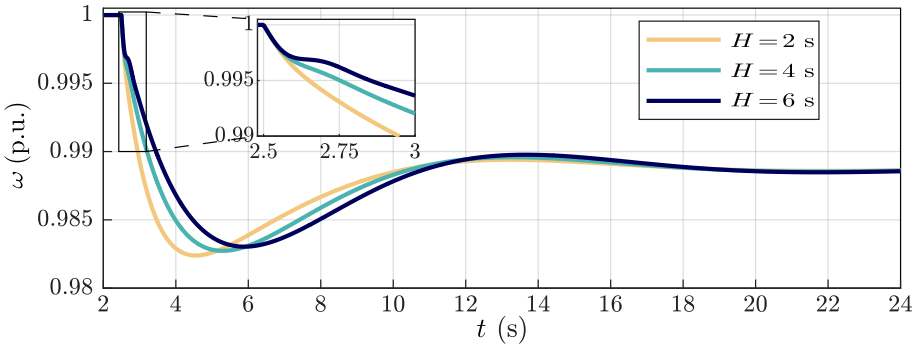


**Figure 6.12:** Behaviour of the grid frequency to changes in the synthetic inertia $H$.

## DC voltage inertial behaviour

To study the inertial performance of the dc bus voltage at different values of virtual capacitors, the power imbalance studied above is repeated. The test scenario is as mentioned above, a change in the active power of load 1 of $0.1\,pu.$ at $t = 2.5s$ s is applied. The values of the virtual dc capacitor have been selected according to the time constant of a capacitor in seconds. Fig. 6.13 demonstrate that effectively increasing the virtual capacitor $C_v$ enhances the performance of the RoCoV. Besides, the frequency disturbance caused by the change of load 1 is transmitted via the dc voltage to the second and third aggregated networks to ensure active power sharing in the power system.

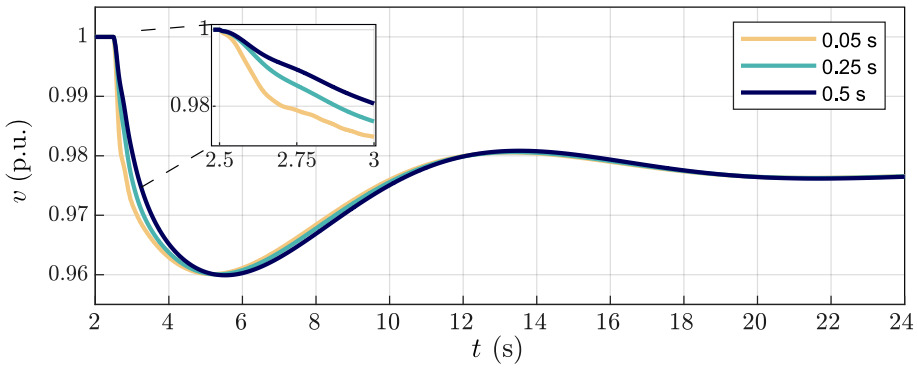


**Figure 6.13:** Performance of the dc voltage at different values of virtual capacitor $C_v$.

### Discussion

The integration of the DC-SOFIE to the SOFIE control presented in this thesis was presented to create a new grid-supporting control strategy (DSOFIE) for the interconnection of ac-dc networks, improving the dynamic response of ac and dc circuits under power variations independently on each side of the inverter. On the ac side, it supports frequency while providing the equivalent inertial behaviour, primary response and damping of a SM. On the dc side, it allows virtually increasing the capacitor size to reduce the RoCoV and add virtual damping to the electrical oscillations. Furthermore, since the control is standardised on a per unit system, it can be used to interconnect any electrical grid (ac or dc, different voltage levels, frequency values, etc.).

The results demonstrated that the DSOFIE is able to emulate a wide range of inertia values on the ac side without any adverse interactions between the controller control loops and the $LC$-resonant modes. Likewise, the DSOFIE successfully manages to virtually increase the value of the bus capacitor, improving the RoCoV on the dc side.

On the other hand, one of the main advantages of the proposed control is its ability to add virtual damping on both sides of the converter without altering the steady state set by the grid operator. This allows the converter to attenuate the power oscillations on the ac side and the bus voltage on the dc side, thereby improving the stability limits of the power system.

The DSOFIE control allows to emulate a virtual reactance (ac side) and inductance (dc side). The virtual reactance of the ac side attenuates the electromechanical oscillations of the grid. Meanwhile, on the dc side, a further degree of freedom is added to attenuate bus voltage oscillations.

To illustrate its ability to interconnect networks, the DSOFIE control has been used to interconnect three networks via an MTDC link. The results demonstrate its proper operation and ability to improve frequency and bus voltage performance in low inertia grids.

# Appendix A

# Taylor series expansion

According to the Taylor series expansion, an arbitrary function $f(x)$ can be expanded around the equilibrium point $\overline{x}$ as:

$$f(x) = f(\bar{x}) + \left.\frac{df}{dx}\right|_{x=\bar{x}} (x-\bar{x}) + \frac{1}{2!}\left.\frac{d^2f}{dx^2}\right|_{x=\bar{x}} (x-\bar{x})^2 + \frac{1}{3!}\left.\frac{d^3f}{dx^3}\right|_{x=\bar{x}} (x-\bar{x})^3 + \mathrm{L} \quad \text{(A.1)}$$

When $x$ is near $\overline{x}$, second and higher-order terms are very close to zero and therefore they can be neglected, obtaining the following approximation:

$$f(x) \approx f(\bar{x}) + \left.\frac{df}{dx}\right|_{x=\pi} (x-\bar{x}) \quad \text{(A.2)}$$

By defining the variation of the state as , Eq. (A.2) can be rewritten as:

$$\Delta x \approx \left.\frac{df}{dx}\right|_{x=\overline{x}} \Delta x \quad \text{(A.3)}$$

In a power system, equations depend not only on states but also on algebraic variables and inputs. Eq. (A.3) can be generalised to consider the effect of algebraic and input variables as:

$$\Delta x_l \approx \sum_{l=1}^{m} \left.\frac{\partial f_i}{\partial x_l}\right|_{x_l=\bar{x}_l} \Delta x_l + \sum_{l=1}^{n} \left.\frac{\partial f_i}{\partial z_j}\right|_{z_l=\bar{z}_l} \Delta z_l + \sum_{l=1}^{o} \left.\frac{\partial f_i}{\partial u_l}\right|_{u_l=\bar{u}_l} \Delta u_l \quad \text{(A.4)}$$

where $\overline{x}$, $\overline{z}$ and $\overline{u}$ are the values of the states, algebraic variables, and inputs at the equilibrium point, respectively. These values are calculated by setting all the derivatives equal to zero (meaning the system is in steady-state) and solving the system of equations for $x$, $z$ and $u$. The indices $m$, $n$ and $o$ represent the number of states, algebraic variables, and inputs, respectively. The matrices that group the partial derivatives of all system equations obtained according to Eq. (A.4) are known as Jacobian matrices, and they can be easily calculated by applying the jacobian command in MATLAB. The compact and grouped matrix form of the Jacobian matrices in Eq. (A.4) is shown in Eq. (3.17).

# Appendix B

# Parameter tables

**Table B.1:** Parameters of chapter four.

| | | | | | |
|---|---|---|---|---|---|
| System general values | | | | | |
| $S_b$ | 2.750 MVA | $v_b$ | 690 V | $\omega_b$ | $2\,\pi\,50$ rad/s |
| $v_{dc_b}$ | 1126.8 V | | | | |
| Aggregated grid | | | | | |
| $L_g$ | 0.2 p.u. | $R_g$ | 0.016 p.u. | $k_v$ | 0.270 |
| $H_g$ | 2 s | $k_{d_g}$ | 0 | $t_g$ | 0.1 s |
| $k_{w_g}$ | 4.430 | $t_t$ | 1 s | $R_l$ | 1 p.u. |
| Converter | | | | | |
| $S_c$ | 1 p.u. | $R_{dc}$ | 20 p.u. | $C_{dc}$ | 37.7 p.u. |
| $C_f$ | 0.078 p.u. | $R_f$ | 0.006 p.u. | $L_f$ | 0.08 p.u. |
| $t_{dc}$ | 0.066 s | $f_{sw}$ | 5.120 kHz | | |
| Control set-points of the converter and aggregated grid | | | | | |
| $v_{dc}^*$ | 1 p.u. | $q*$ | 0 p.u. | $p^*$ | 0.5 p.u. |
| $\omega^*$ | 1 p.u. | $\hat{v}^*$ | 1 p.u. | $p_g^*$ | 0.5 p.u. |
| Inner voltage and current loops | | | | | |
| $k_{pv}$ | 1.060 | $k_{pc}$ | 1.3 | $k_{ffv}$ | 1 |
| $k_{iv}$ | 16 | $k_{ic}$ | 30.7 | $k_{ffi}$ | 1 |
| MC | | | | | |
| $\psi$ | 1 | $k_{p\hat{v}}$ | 0.4 | $k_{i\hat{v}}$ | 5 |
| $k_{dc}$ | 6.016 | $t_p$ | $31.8 \cdot 10^{-3}$ s | | |
| dVOC | | | | | |
| $\eta$ | 0.204 | $\alpha$ | 0.4 | $\kappa$ | $\frac{\pi}{2}$ |
| $t_p$ | 0.360 s | $t_q$ | $5.263 \cdot 10^{-3}$ s | | |
| SV | | | | | |
| $k_d$ | 12 | $H$ | 2 s | $K$ | 1 |
| $k_\omega$ | 4.430 | $k_q$ | 2 | $t_q$ | $5.263 \cdot 10^{-3}$ s |
| $t_p$ | $4 \cdot 10^{-4}$ | | | | |
| VCVSM | | | | | |
| $k_d$ | 12 | $H$ | 2 s | $k_w$ | 4.930 |
| $k_q$ | 2 | $k_{p_{pll}}$ | 0.050 | $k_{i_{pll}}$ | 1 |
| $\omega_{f_{pll}}$ | 500 rad/s | $L_v$ | 0.1 p.u. | $R_v$ | 0.050 p.u. |
| $t_q$ | 0.0370 s | $t_p$ | $4 \cdot 10^{-4}$ s | | |

**Table B.2:** parameters of chapter five.

| | | | | | |
|---|---|---|---|---|---|
| System general values | | | | | |
| $S_b$ | 2.75 MVA | $v_{b_{ll-rms}}$ | 690 V | $\omega_b$ | $2\pi 50$ rad/s |
| Stiff grid | | | | | |
| $L_g$ | 0.03 p.u. | $R_g$ | 0.01 p.u. | $\omega_g^*$ | 1 p.u. |
| Synchronous machine | | | | | |
| $S$ | 1 p.u. | $L_s$ | 0.27 p.u. | $R_s$ | 0.006 p.u |
| $k_d$ | 141 | $k_\omega$ | 20 | $H$ | 3.50 s |
| Converter | | | | | |
| $S$ | 1 p.u. | $L_f$ | 0.08 p.u | $R_f$ | 0.006 p.u. |
| $f_{sw}$ | 2.12 kHz | | | | |
| Control set-points | | | | | |
| $p^*$ | 0 p.u. | $Q^*$ | 0 p.u. | $\omega^*$, $v_{dc}$ | 1 p.u. |
| Inner Current loop | | | | | |
| $k_{pc}$ | 0.54 | $k_{ic}$ | 12.72 | $k_{ffv}$, $k_{xc}$ | 1 |
| SOFIE | | | | | |
| $k_d$ | 141 | $H$ | 3.50 s | $k_\omega$ | 20 |
| $X_s$ | 0.03 | $\omega_n$ | 12.23 rad/s | $\zeta_v$ | 0.94 |
| $k_{p_{pll}}$ | 0.53 | $k_{i_{pll}}$ | 29.47 | $\tau_f$ | 0.002 s |
| Low inertia power system (Sec. 5.8) | | | | | |
| SM (connected at bus 2) | | | | | |
| $H$ | 1 s | $k_{\omega_g}$ | 4 | $k_{d_g}$ | 0 |
| $t_T$ | 1 s | $t_G$ | 0.1 s | $k_v$ | 0.1 |
| SM (connected at buses 1 and 3) | | | | | |
| $L_s$ | 0.3 p.u. | $R_s$ | 0.006 p.u. | $H$ | 2, 4, 6 s |
| $k_d$ | 206 | $k_\omega$ | 4 | | |
| SOFIE | | | | | |
| $k_d$ | 206 | $H$ | 2, 4, 6 s | $k_\omega$ | 4 |
| $X_s$ | 0.30 | $\omega_n$ | 9.34 rad/s | $\zeta_v$ | 0.94 |
| $k_{p_{pll}}$ | 0.53 | $k_{i_{pll}}$ | 29.47 | $\tau_f$ | 0.002 s |

**Table B.3:** Parameter values for the comparison between SOFIE and FOFIE, section 5.7.

| | | | | | |
|---|---|---|---|---|---|
| System general values | | | | | |
| $S_b$ | 40 kVA | $v_{b_{ll-rms}}$ | 400 V | $\omega_b$ | $2\pi 50$ rad/s |
| Grid | | | | | |
| $L_g$ | $7.85^{-2}$ p.u. | $R_g$ | $2.50^{-3}$ p.u. | | |
| Converter | | | | | |
| $L_f$ | $7.85^{-2}$ p.u. | $R_f$ | $2.50^{-3}$ p.u. | $f_{sw}$ | 10 kHz |
| $\omega_{AD}$ | 250 rad/s | $k_{AD}$ | 0.5 | | |
| Control set-points | | | | | |
| $p^*$ | 0.5 p.u. | $q^*$ | -0.2 p.u. | $\omega^*$ | 1 p.u. |
| $\hat{v}^*$ | 1 p.u. | | | | |
| Analysis with ideal PLL (sec. 5.7.1) | | | | | |
| SOFIE | | | | | |
| $k_d$ | 250.10 | $X_s$ | 0.3 p.u. | $k_\omega$ | 0 |
| $H$ | 6 s | $\zeta_v$ | 1.12 | $\omega_n$ | 9.34 rad/s |
| $kp_c$ | 0.44 | $ki_c$ | 4.44 | $t_c$ | 2.5 ms |
| FOFIE | | | | | |
| $H$ | 6 s | $\omega_n$ | 9.34 rad/s | $k_\omega$ | 0 |
| $kp_c$ | 0.44 | $ki_c$ | 4.44 | $t_c$ | 2.5 ms |
| Analysis adding the PLL dynamics (sec. 5.7.2) | | | | | |
| FOFIE A | | | | | |
| $H$ | 6 s | $\omega_n$ | 9.34 rad/s | $k_\omega$ | 0 |
| $kp_c$ | 0.44 | $ki_c$ | 4.44 | $t_c$ | 2.5 ms |
| $kp_{pll}$ | $1.44^{-2}$ | $ki_{pll}$ | $2.83^{-2}$ | $t_{pll}$ | 1.2 s |
| FOFIE B | | | | | |
| $H$ | 6 s | $\omega_n$ | 9.34 rad/s | $k_\omega$ | 0 |
| $kp_c$ | $2.21^{-2}$ | $ki_c$ | 0.22 | $t_c$ | 50 ms |
| $kp_{pll}$ | $2.88^{-2}$ | $ki_{pll}$ | $11.33^{-2}$ | $t_{pll}$ | 600 ms |
| SOFIE A | | | | | |
| $k_d$ | 250.10 | $X_s$ | 0.3 p.u. | $k_\omega$ | 0 |
| $H$ | 6 s | $\zeta_v$ | 1.12 | $\omega_n$ | 9.34 rad/s |
| $kp_c$ | 0.44 | $ki_c$ | 4.44 | $t_c$ | 2.5 ms |
| $kp_{pll}$ | 1.73 | $ki_{pll}$ | 480 | $t_{pll}$ | 10 ms |

Continued on next page

| | | | | | |
|---|---|---|---|---|---|
| | | | SOFIE B | | |
| $k_d$ | 1350 | $X_s$ | 0.03 p.u. | $k_\omega$ | 0 |
| $H$ | 6 s | $\zeta_v$ | 1.91 | $\omega_n$ | 29.54 rad/s |
| $kp_c$ | 0.44 | $ki_c$ | 4.44 | $t_c$ | 2.5 ms |
| $kp_{pll}$ | 1.73 | $ki_{pll}$ | 480 | $t_{pll}$ | 10 ms |
| | | | Low inertia power system (sec. 5.8) | | |
| | | | System general values | | |
| $S_b$ | 100 MVA | $v_{b_{ll-rms}}$ | 230 kV | $\omega_b$ | $2\pi 50$ rad/s |
| | | | SM (connected at bus 2) | | |
| $H$ | 1 s | $k_{\omega_g}$ | 4 | $k_{d_g}$ | 0 |
| $t_T$ | 1 s | $t_G$ | 0.1 s | $k_v$ | 0.1 |
| | | | SOFIE | | |
| $k_d$ | 201 | $H$ | 4 s $k_\omega$ | 4 | |
| $X_s$ | 0.30 | $\omega_n$ | 9.34 rad/s | $\zeta_v$ | 1.12 |
| $kp_c$ | 0.44 | $ki_c$ | 4.44 | $t_c$ | 2.5 ms |
| $kp_{pll}$ | 1.73 | $ki_{pll}$ | 480 | $t_{pll}$ | 10 ms |
| | | | FOFIE | | |
| $H$ | 4 s | $k_\omega$ | 4 s $\omega_n$ | 9.34 rad/s | |
| $kp_c$ | 0.44 | $ki_c$ | 4.44 | $t_c$ | 2.5 ms |
| $kp_{pll}$ | 0.28 | $ki_{pll}$ | 11.33 | $t_{pll}$ | 600 ms |
| | | | SV (connected at bus 1 and 3) | | |
| $L_s$ | 0.3 p.u. | $R_s$ | 0.006 p.u. | $H$ | 4 s |
| $k_d$ | 201 | $k_\omega$ | 4 | $K$ | 0.15 |

**Table B.4:** Parameter values of chapter six.

| | | | | | |
|---|---|---|---|---|---|
| IDEAL GRID (sec. 6.3.2) | | | | | |
| System general values | | | | | |
| $S_b$ | 400 MVA | $v_{b_{RMS-LL}}$ | 244.95 kV | $\omega_b$ | $2\pi 50$ rad/s |
| Grid | | | | | |
| $Z_{g_{ac}}$ | | $0.01 + 0.02j$ p.u. | | $R_{s_{dc}}$ | 0.0037 p.u. |
| $L_{s_{dc}}$ | 0.0375 p.u. | | | | |
| Ac Transmission line | | | | | |
| $R_{l_{ac}}$ | 0.0119 p.u. | $L_{l_{ac}}$ | 0.016 p.u. | $B_{l_{ac}}$ | 0.0083 p.u. |
| Dc Transmission line | | | | | |
| $R_{l_{dc}}$ | $1.17^{-1}$ Ω/km | $L_{i_{dc}}$ | $2.28^{-4}$ H/km | $C_{l_{dc}}$ | $0.19^{-6}$ F/km |
| Converter | | | | | |
| $Z_c$ | | $0.006 + 0.08j$ | | $C_{dc}$ | 6.28 p.u. |
| $kp_c$ | 0.70 | $ki_c$ | 22.21 | $t_c$ | 2.00 ms |
| $kp_{pll}$ | 1.57 | $ki_{pll}$ | 337.27 | $t_{pll}$ | 11 ms |
| Control set-points | | | | | |
| $p^*$ | 0.1 p.u. | $q^*$ | 0.0 p.u. | $\omega^*$ | 1 p.u. |
| DSOFIE | | | | | |
| $k_d$ | 250.10 | $X_v$ | 0.20 p.u. | $k_\omega$ | 10 |
| $H$ | 6 s | $\zeta_{v_{ac}}$ | 0.98 | $\omega_{n_{ac}}$ | 11.44 rad/s |
| $G_v$ | 12.68 S | $L_{dc}$ | 1.60 mH | $k_{dc}$ | 3 |
| $C_v$ | 100 mF | $\omega_{n_{dc}}$ | 80 rad/s | $\zeta_{v_{dc}}$ | 0.98 |
| MTDC GRID IMPLEMENTATION (sec. 6.3.2) | | | | | |
| System general values | | | | | |
| $S_b$ | 400 MVA | $v_{b_{RMS-LL}}$ | 244.95 kV | $\omega_b$ | $2\pi 50$ rad/s |

Continued on next page

| | | | | | |
|---|---|---|---|---|---|
| | | Aggregated grid 2 and 3 | | | |
| $L_s$ | 0.02 p.u. | $R_s$ | 0.01 p.u. | $k_v$ | 0.10 |
| $H$ | 1 s | $k_d$ | 0 | $t_g$ | 0.1 s |
| $k_\omega$ | 5 | $t_t$ | 3 s | | |
| | | Ac Transmission line | | | |
| $R_{l_{ac}}$ | 0.0119 p.u. | $L_{l_{ac}}$ | 0.016 p.u. | $B_{l_{ac}}$ | 0.0083 p.u. |
| | | Dc Transmission line | | | |
| $R_{l_{dc}}$ | $1.17^{-1}$ Ω/km | $L_{i_{dc}}$ | $2.28^{-4}$ H/km | $C_{l_{dc}}$ | $0.19^{-6}$ F/km |
| | | DSOFIE | | | |
| $k_d$ | 250.10 | $X_v$ | 0.20 p.u. | $k_\omega$ | 10 |
| $H$ | 6 s | $\zeta_{v_{ac}}$ | 0.98 | $\omega_{n_{ac}}$ | 11.44 rad/s |
| $G_v$ | 12.68 p.u. | $L_{dc}$ | 0.49 p.u | $k_{dc}$ | 3 |
| $C_v$ | 31.41 p.u. | $\omega_{n_{dc}}$ | 80 rad/s | $\zeta_{v_{dc}}$ | 0.98 |

# Appendix C

# Base values for Per Unit System

This appendix describes the methodology for converting to per unit.

## C.1 Per unit ac side

The nominal power rating of the three-phase ac system is usually defined as the base power which is given as:

$$S_b = v_{ll_{rms}}\, i_n \sqrt{3} \tag{C.1}$$

where $S_b$ is the power base and $i_n$ is the nominal current.

$$\text{The base phase peak voltage} := v_b = v_{LL_{RMS}} \sqrt{2/3} \tag{C.2}$$

where $v_{ll_{rms}}$ is the nominal phase-to-phase RMS voltage of the system.

$$\text{base current} := i_b = i_n \sqrt{2} \tag{C.3}$$

$$\text{Base impedance} := z_b = \frac{v_b}{i_b} \tag{C.4}$$

$$\text{Base angular frequency} := \omega_b = 2\pi f_b \tag{C.5}$$

where $f_b$ is the frequency of the system in Hz.

$$\text{Base inductance} := L_b = \frac{Z_b}{\omega_b} \tag{C.6}$$

$$\text{Base capacitance} := C_b = \frac{1}{\omega_b\, Z_b} \tag{C.7}$$

## C.2 Per unit dc side

$$\text{Base dc power} := S_{b_{dc}} = S_b \tag{C.8}$$

$$\text{Base dc voltage} := v_{b_{dc}} = 2\,v_b \tag{C.9}$$

$$\text{Base dc current} := i_{b_{dc}} = \frac{S_{b_{dc}}}{v_{b_{dc}}} \tag{C.10}$$

$$\text{Base dc resistence} := R_{b_{dc}} = \frac{v_{b_{dc}}}{i_{b_{dc}}} \tag{C.11}$$

$$\text{Base dc capacitance} := C_{b_{dc}} = \frac{1}{R_{b_{dc}}\,\omega_b} \tag{C.12}$$

$$\text{Base dc inductance} := L_{b_{dc}} = \frac{R_{b_{dc}}}{\omega_b} \tag{C.13}$$

# List of Figures

# List of Tables

# List of References


[1] British petroleum, *bp Statistical Review of World Energy 2022*, 2022. [Online]. Available: https://www.bp.com/content/dam/bp/business-sites/en/global/corporate/pdfs/energy-economics/statistical-review/bp-stats-review-2022-full-report.pdf

[2] International Renewable Energy Agency, *IRENA (2019), Global Energy Transformation: A Roadmap to 2050*, 2019. [Online]. Available: https://www.irena.org/publications/2019/Apr/Global-energy-transformation-A-roadmap-to-2050-2019Edition

[3] P. Chunark, B. Limmeechokchai, S. Fujimori, and T. Masui, "Renewable energy achievements in CO2 mitigation in Thailand's NDCs," *Renew. Energy*, vol. 114, no. May 2016, pp. 1294–1305, 2017. [Online]. Available: http://dx.doi.org/10.1016/j.renene.2017.08.017

[4] B. Kroposki, B. Johnson, Y. Zhang, V. Gevorgian, P. Denholm, B.-M. Hodge, and B. Hannegan, "Achieving a 100% renewable grid: Operating electric power systems with extremely high levels of variable renewable energy," *IEEE Power and Energy Magazine*, vol. 15, no. 2, pp. 61–73, 2017.

[5] T. Ackermann, T. Prevost, V. Vittal, A. J. Roscoe, J. Matevosyan, and N. Miller, "Paving the way: A future without inertia is closer than you think," *IEEE Power and Energy Magazine*, vol. 15, no. 6, pp. 61–69, 2017.

[6] E. Unamuno, J. Paniagua, and J. A. Barrena, "Unified virtual inertia for ac and dc microgrids: And the role of interlinking converters," *IEEE Electrification Magazine*, vol. 7, no. 4, pp. 56–68, 2019.

[7] S. Widergren, R. Melton, A. Khandekar, B. Nordman, and M. Knight, "The plug-and-play electricity era: Interoperability to integrate anything, anywhere, anytime," *IEEE Power and Energy Magazine*, vol. 17, no. 5, pp. 47–58, 2019.

[8] M. Li, M. Yang, Y. Yu, and W.-J. Lee, "A wind speed correction method based on modified hidden markov model for enhancing wind power forecast," *IEEE Transactions on Industry Applications*, vol. 58, no. 1, pp. 656–666, 2022.

[9] Z. Wang, J. Zhang, Y. Zhang, C. Huang, and L. Wang, "Short-term wind speed forecasting based on information of neighboring wind farms," *IEEE Access*, vol. 8, pp. 16 760–16 770, 2020.

[10] H.-Y. Su, T.-Y. Liu, and H.-H. Hong, "Adaptive residual compensation ensemble models for improving solar energy generation forecasting," *IEEE Transactions on Sustainable Energy*, vol. 11, no. 2, pp. 1103–1105, 2020.

[11] ERCOT, "Future ancillary services in ercot," 2014.

[12] EirGrid and SONI, "All-island generation capacity statement," 2018. [Online]. Available: https://www.soni.ltd.uk/media/documents/Generation_Capacity_Statement_2018.pdf

[13] AEMO, "Black system event in south australia on28 september 2016 - final report," 3 2017. [Online]. Available: https://www.aemo.com.au/-/media/Files/Electricity/NEM/Market_Notices_and_Events/Power_System_Incident_Reports/2017/Integrated-Final-Report-SA-Black-System-28-September-2016.pdf

[14] R. Yan, N.-A. Masood, T. Kumar Saha, F. Bai, and H. Gu, "The anatomy of the 2016 south australia blackout: A catastrophic event in a high renewable network," *IEEE Transactions on Power Systems*, vol. 33, no. 5, pp. 5374–5388, 2018.

[15] W. Winter, K. Elkington, G. Bareux, and J. Kostevc, "Pushing the limits: Europe's new grid: Innovative tools to combat transmission bottlenecks and reduced inertia," *IEEE Power and Energy Magazine*, vol. 13, no. 1, pp. 60–74, 2015.

[16] J. Machowski, J. Bialek, and J. Bumby, *Power System Dynamics: Stability and Control*. Wiley, 2011. [Online]. Available: https://books.google.com.co/books?id=wZv92UdKxi4C

[17] F. Milano, F. Dörfler, G. Hug, D. J. Hill, and G. Verbič, "Foundations and challenges of low-inertia systems (Invited Paper)," in *20th Power Syst. Comput. Conf. PSCC 2018*, 2018, pp. 1–25.

[18] Q. Peng, Q. Jiang, Y. Yang, T. Liu, H. Wang, and F. Blaabjerg, "On the stability of power electronics-dominated systems: Challenges and potential solutions," *IEEE Transactions on Industry Applications*, vol. 55, no. 6, pp. 7657–7670, 2019.

[19] AEMO, "Quarterly energy dynamics q1 2022," 4 2022. [Online]. Available: https://www.aemo.com.au/-/media/files/major-publications/qed/2022/qed-q1-report.pdf?la=en&hash=981BA7016C0C9A25947F0F05198EDB96

[20] A. Tayyebi, A. Anta, and F. Dörfler, "Almost globally stable grid-forming hybrid angle control," in *2020 59th IEEE Conference on Decision and Control (CDC)*, 2020, pp. 830–835.

[21] F. D. Bianchi and J. L. Domnguez-Garca, "Coordinated frequency control using mt-hvdc grids with wind power plants," *IEEE Transactions on Sustainable Energy*, vol. 7, no. 1, pp. 213–220, 2016.

[22] P. Kundur and N. Balu, *Power System Stability and Control*, ser. EPRI power system engineering series. McGraw-Hill, 1994. [Online]. Available: https://books.google.es/books?id=0fPGngEACAAJ

[23] M. Klein, G. Rogers, and P. Kundur, "A fundamental study of inter-area oscillations in power systems," *IEEE Transactions on Power Systems*, vol. 6, no. 3, pp. 914–921, 1991.

[24] P. Kundur, M. Klein, G. Rogers, and M. Zywno, "Application of power system stabilizers for enhancement of overall system stability," *IEEE Transactions on Power Systems*, vol. 4, no. 2, pp. 614–626, 1989.

[25] U. Markovic, O. Stanojev, P. Aristidou, E. Vrettos, D. S. Callaway, and G. Hug, "Understanding Small-Signal Stability of Low-Inertia Systems," *IEEE Trans. Power Syst.*, p. 1, 2021.

[26] J. Matevosyan, B. Badrzadeh, T. Prevost, E. Quitmann, D. Ramasubramanian, H. Urdal, S. Achilles, J. MacDowell, S. H. Huang, V. Vital, J. O'Sullivan, and R. Quint, "Grid-forming inverters: Are they the key for high renewable penetration?" *IEEE Power and Energy Magazine*, vol. 17, no. 6, pp. 89–98, 2019.

[27] S. Golestan, J. M. Guerrero, and J. C. Vasquez, "Three-phase plls: A review of recent advances," *IEEE Transactions on Power Electronics*, vol. 32, no. 3, pp. 1894–1907, 2017.

[28] M. Amin, J. A. Suul, S. D'Arco, E. Tedeschi, and M. Molinas, "Impact of state-space modelling fidelity on the small-signal dynamics of vsc-hvdc systems," in *11th IET International Conference on AC and DC Power Transmission*, 2015, pp. 1–11.

[29] N. R. Chaudhuri, R. Majumder, B. Chaudhuri, and J. Pan, "Stability analysis of vsc mtdc grids connected to multimachine ac systems," *IEEE Transactions on Power Delivery*, vol. 26, no. 4, pp. 2774–2784, 2011.

[30] Q. Peng, Q. Jiang, Y. Yang, T. Liu, H. Wang, and F. Blaabjerg, "On the stability of power electronics-dominated systems: Challenges and potential solutions," *IEEE Transactions on Industry Applications*, vol. 55, no. 6, pp. 7657–7670, 2019.

[31] Y. Sun, E. C. W. E. de Jong, X. Wang, D. Yang, F. Blaabjerg, V. Cuk, and J. F. G. S. Cobben, "The impact of pll dynamics on the low inertia power grid: A case study of bonaire island power system," *Energies*, vol. 12, no. 7, 2019. [Online]. Available: https://www.mdpi.com/1996-1073/12/7/1259

[32] B. Wen, D. Boroyevich, P. Mattavelli, Z. Shen, and R. Burgos, "Influence of phase-locked loop on input admittance of three-phase voltage-source converters," in *2013 Twenty-Eighth Annual IEEE Applied Power Electronics Conference and Exposition (APEC)*, 2013, pp. 897–904.

[33] S. Golestan, J. M. Guerrero, and J. C. Vasquez, "Three-phase plls: A review of recent advances," *IEEE Transactions on Power Electronics*, vol. 32, no. 3, pp. 1894–1907, 2017.

[34] C. Subramanian and R. Kanagaraj, "Rapid tracking of grid variables using prefiltered synchronous reference frame pll," *IEEE Transactions on Instrumentation and Measurement*, vol. 64, no. 7, pp. 1826–1836, 2015.

[35] B. Liu, F. Zhuo, Y. Zhu, H. Yi, and F. Wang, "A three-phase pll algorithm based on signal reforming under distorted grid conditions," *IEEE Transactions on Power Electronics*, vol. 30, no. 9, pp. 5272–5283, 2015.

[36] T. Thacker, R. Wang, D. Dong, R. Burgos, F. Wang, and D. Boroyevich, "Phase-locked loops using state variable feedback for single-phase converter systems," in *2009 Twenty-Fourth Annual IEEE Applied Power Electronics Conference and Exposition*, 2009, pp. 864–870.

[37] T. Thacker, D. Boroyevich, R. Burgos, and F. Wang, "Phase-locked loop noise reduction via phase detector implementation for single-phase systems," *IEEE Transactions on Industrial Electronics*, vol. 58, no. 6, pp. 2482–2490, 2011.

[38] S. Vazquez, J. A. Sanchez, M. R. Reyes, J. I. Leon, and J. M. Carrasco, "Adaptive vectorial filter for grid synchronization of power converters under unbalanced and/or distorted grid conditions," *IEEE Transactions on Industrial Electronics*, vol. 61, no. 3, pp. 1355–1367, 2014.

[39] M. Ciobotaru, R. Teodorescu, and F. Blaabjerg, "A new single-phase pll structure based on second order generalized integrator," in *2006 37th IEEE Power Electronics Specialists Conference*, 2006, pp. 1–6.

[40] M. Karimi-Ghartemani, "Linear and pseudolinear enhanced phased-locked loop (epll) structures," *IEEE Transactions on Industrial Electronics*, vol. 61, no. 3, pp. 1464–1474, 2014.

[41] R. Eriksson, N. Modig, and K. Elkington, "Synthetic inertia versus fast frequency response: a definition," *IET Renewable Power Generation*, vol. 12, 09 2017.

[42] J. Fradley, R. Preece, and M. Barnes, "Adaptive fast frequency response for power electronic connected energy sources," in *2019 IEEE Milan PowerTech*, 2019, pp. 1–6.

[43] Q. Hong, M. Nedd, S. Norris, I. Abdulhadi, M. Karimi, V. Terzija, B. Marshall, K. Bell, and C. Booth, "Fast frequency response for effective frequency control in power systems with low inertia," *The Journal of Engineering*, vol. 2019, 03 2019.

[44] ENTSO-E, "Need for synthetic inertia (SI) for frequency regulation," ENTSO-E, Tech. Rep., 2018.

[45] J. Morren, J. Pierik, and S. W. de Haan, "Inertial response of variable speed wind turbines," *Electric Power Systems Research*, vol. 76, no. 11, pp. 980–987, 2006. [Online]. Available: https://www.sciencedirect.com/science/article/pii/S0378779605002713

[46] N. Julius, J. Nderu, and G. Irungu, "Frequency control and virtual inertia emulation techniques for grid connected wind energy conversion systems - a review," in *2019 IEEE AFRICON*, 2019, pp. 1–6.

[47] T. Kerdphol, F. Rahman, M. Watanabe, and Y. Mitani, *Virtual Inertia Synthesis and Control*, ser. Power Systems. Springer International Publishing, 2020. [Online]. Available: https://books.google.es/books?id=UTGjzQEACAAJ

[48] Y. Yoo, S. Jung, and G. Jang, "Dynamic inertia response support by energy storage system with renewable energy integration substation," *Journal of Modern Power Systems and Clean Energy*, vol. 8, no. 2, pp. 260–266, 2020.

[49] E. Rakhshani, D. Remon, A. Mir Cantarellas, and P. Rodriguez, "Analysis of derivative control based virtual inertia in multi-area high-voltage direct current interconnected power systems," *IET Generation, Transmission & Distribution*, vol. 10, no. 6, pp. 1458–1469, 2016. [Online]. Available: https://ietresearch.onlinelibrary.wiley.com/doi/abs/10.1049/iet-gtd.2015.1110

[50] J. Paniagua, E. Unamuno, and J. A. Barrena, "Dual inertia-emulation control for interlinking converters in grid-tying applications," *IEEE Transactions on Smart Grid*, vol. 12, no. 5, pp. 3868–3876, 2021.

[51] D. Pattabiraman, R. H. Lasseter., and T. M. Jahns, "Comparison of grid following and grid forming control for a high inverter penetration power system," in *2018 IEEE Power & Energy Society General Meeting (PESGM)*, 2018, pp. 1–5.

[52] O. Gomis-Bellmunt, S. D. Tavakoli, V. A. Lacerda, and E. Prieto-Araujo, "Grid-forming loads: Can the loads be in charge of forming the grid in modern power systems?" *IEEE Transactions on Smart Grid*, pp. 1–1, 2022.

[53] M. A. Roslan, S. A. Azmi, B. Ismail, M. M. Azizan, and S. S. Lee, "Centralize control power sharing scheme of parallel connected inverters for microgrids," in *2016 IEEE International Conference on Power and Energy (PECon)*, 2016, pp. 692–696.

[54] A. Bubshait, A. Alsaleem, and M. G. Simões, "Centralized power reserve algorithm of de-loaded wind farm for primary frequency regulation," in *2018 IEEE Energy Conversion Congress and Exposition (ECCE)*, 2018, pp. 423–429.

[55] M. A. Hossain, H. Pota, W. Issa, and M. Hossain, "Overview of ac microgrid controls with inverter-interfaced generations," *Energies*, vol. 10, 08 2017.

[56] V. C. Gungor, D. Sahin, T. Kocak, S. Ergut, C. Buccella, C. Cecati, and G. P. Hancke, "Smart grid technologies: Communication technologies and standards," *IEEE Transactions on Industrial Informatics*, vol. 7, no. 4, pp. 529–539, 2011.

[57] F. Katiraei and M. Iravani, "Power management strategies for a microgrid with multiple distributed generation units," *IEEE Transactions on Power Systems*, vol. 21, no. 4, pp. 1821–1831, 2006.

[58] J. C. Vasquez, J. M. Guerrero, A. Luna, P. Rodriguez, and R. Teodorescu, "Adaptive droop control applied to voltage-source inverters operating in grid-connected and islanded modes," *IEEE Transactions on Industrial Electronics*, vol. 56, no. 10, pp. 4088–4096, 2009.

[59] M. Hassanzahraee and A. Bakhshai, "Adaptive transient power control strategy for parallel-connected inverters in an islanded microgrid," in *IECON 2012 - 38th Annual Conference on IEEE Industrial Electronics Society*, 2012, pp. 5926–5931.

[60] M. Chandorkar, D. Divan, and R. Adapa, "Control of parallel connected inverters in standalone ac supply systems," *IEEE Transactions on Industry Applications*, vol. 29, no. 1, pp. 136–143, 1993.

[61] H. Bevrani and S. Shokoohi, "An intelligent droop control for simultaneous voltage and frequency regulation in islanded microgrids," *IEEE Transactions on Smart Grid*, vol. 4, no. 3, pp. 1505–1513, 2013.

[62] Y. A.-R. I. Mohamed and E. F. El-Saadany, "Adaptive decentralized droop controller to preserve power sharing stability of paralleled inverters in distributed generation microgrids," *IEEE Transactions on Power Electronics*, vol. 23, no. 6, pp. 2806–2816, 2008.

[63] A. K. Sahoo, K. Mahmud, M. Crittenden, J. Ravishankar, S. Padmanaban, and F. Blaabjerg, "Communication-less primary and secondary control in inverter-interfaced ac microgrid: An overview," *IEEE Journal of Emerging and Selected Topics in Power Electronics*, vol. 9, no. 5, pp. 5164–5182, 2021.

[64] J. Guerrero, L. de Vicuna, J. Matas, M. Castilla, and J. Miret, "A wireless controller to enhance dynamic performance of parallel inverters in distributed generation systems," *IEEE Transactions on Power Electronics*, vol. 19, no. 5, pp. 1205–1213, 2004.

[65] S. D'Arco and J. Suul, "Equivalence of virtual synchronous machines and frequency-droops for converter-based microgrids," *IEEE Transactions on Smart Grid*, vol. 5, pp. 394–395, 01 2014.

[66] R. Majumder, A. Ghosh, G. Ledwich, and F. Zare, "Angle droop versus frequency droop in a voltage source converter based autonomous microgrid," in *2009 IEEE Power & Energy Society General Meeting*, 2009, pp. 1–8.

[67] R. Majumder, B. Chaudhuri, A. Ghosh, R. Majumder, G. Ledwich, and F. Zare, "Improvement of stability and load sharing in an autonomous microgrid using supplementary droop control loop," *IEEE Transactions on Power Systems*, vol. 25, no. 2, pp. 796–808, 2010.

[68] W. Yao, M. Chen, J. Matas, J. M. Guerrero, and Z.-M. Qian, "Design and analysis of the droop control method for parallel inverters considering the impact of the complex impedance on the power sharing," *IEEE Transactions on Industrial Electronics*, vol. 58, no. 2, pp. 576–588, 2011.

[69] J. M. Guerrero, L. Hang, and J. Uceda, "Control of distributed uninterruptible power supply systems," *IEEE Transactions on Industrial Electronics*, vol. 55, no. 8, pp. 2845–2859, 2008.

[70] J. Guerrero, L. G. de Vicuna, J. Matas, M. Castilla, and J. Miret, "Output impedance design of parallel-connected ups inverters with wireless load-sharing control," *IEEE Transactions on Industrial Electronics*, vol. 52, no. 4, pp. 1126–1135, 2005.

[71] J. M. Guerrero, J. C. Vasquez, J. Matas, L. G. de Vicuna, and M. Castilla, "Hierarchical control of droop-controlled ac and dc microgrids—a general approach toward standardization," *IEEE Transactions on Industrial Electronics*, vol. 58, no. 1, pp. 158–172, 2011.

[72] C. N. Rowe, T. J. Summers, R. E. Betz, D. J. Cornforth, and T. G. Moore, "Arctan power–frequency droop for improved microgrid stability," *IEEE Transactions on Power Electronics*, vol. 28, no. 8, pp. 3747–3759, 2013.

[73] M. S. Golsorkhi and D. D. C. Lu, "A control method for inverter-based islanded microgrids based on v-i droop characteristics," *IEEE Transactions on Power Delivery*, vol. 30, no. 3, pp. 1196–1204, 2015.

[74] E. Unamuno, J. A. Suul, M. Molinas, and J. A. Barrena, "Comparative Eigenvalue Analysis of Synchronous Machine Emulations and Synchronous Machines," in *IECON 2019 - 45th Annual Conference of the IEEE Industrial Electronics Society*. IEEE, oct 2019, pp. 3863–3870. [Online]. Available: https://ieeexplore.ieee.org/document/8927826/

[75] D. Groß, M. Colombino, J.-S. Brouillon, and F. Dörfler, "The effect of transmission-line dynamics on grid-forming dispatchable virtual oscillator control," *IEEE Transactions on Control of Network Systems*, vol. 6, no. 3, pp. 1148–1160, 2019.

[76] S. D'Arco, J. A. Suul, and O. B. Fosso, "A Virtual Synchronous Machine implementation for distributed control of power converters in SmartGrids," *Electr. Power Syst. Res.*, vol. 122, pp. 180–197, 2015. [Online]. Available: http://dx.doi.org/10.1016/j.epsr.2015.01.001

[77] J. Are Suul and S. D'Arco, "Comparative analysis of small-signal dynamics in virtual synchronous machines and frequency-derivative-based inertia emulation," in *2018 IEEE 18th International Power Electronics and Motion Control Conference (PEMC)*, 2018, pp. 344–351.

[78] E. Avdiaj, J. A. Suul, S. D'Arco, and L. Piegari, "A virtual synchronous machine-based control for eliminating dc-side power oscillations of three-phase vscs under unbalanced grid voltages," in *2021 IEEE 15th International Conference on Compatibility, Power Electronics and Power Engineering (CPE-POWERENG)*, 2021, pp. 1–6.

[79] S. D'Arco and J. A. Suul, "Improving the power reference tracking of virtual synchronous machines by feed-forward control," in *2021 IEEE 19th International Power Electronics and Motion Control Conference (PEMC)*, 2021, pp. 102–107.

[80] S. D'Arco, J. A. Suul, and O. B. Fosso, "Small-signal modelling and parametric sensitivity of a virtual synchronous machine," in *2014 Power Systems Computation Conference*, 2014, pp. 1–9.

[81] E. Avdiaj, J. Are Suul, S. D'Arco, and L. Piegari, "A current controlled virtual synchronous machine adapted for operation under unbalanced conditions," in *2020 9th International Conference on Renewable Energy Research and Application (ICRERA)*, 2020, pp. 263–270.

[82] J. A. Suul, S. D'Arco, and G. Guidi, "Virtual synchronous machine-based control of a single-phase bi-directional battery charger for providing vehicle-to-grid services," in *2015 9th International Conference on Power Electronics and ECCE Asia (ICPE-ECCE Asia)*, 2015, pp. 742–749.

[83] L. Vetoshkin and Z. Müller, "A comparative study of synchronverter stability," in *2020 21st International Scientific Conference on Electric Power Engineering (EPE)*, 2020, pp. 1–6.

[84] S. S. Pore. and P. R. Jadhav., "Filters for grid connected self-synchronized synchronverter," in *2019 4th International Conference on Recent Trends on Electronics, Information, Communication & Technology (RTEICT)*, 2019, pp. 551–555.

[85] C.-H. Zhang, Q.-C. Zhong, J.-S. Meng, X. Chen, Q. Huang, S.-h. Chen, and Z.-p. Lv, "An improved synchronverter model and its dynamic behaviour comparison with synchronous generator," in *2nd IET Renewable Power Generation Conference (RPG 2013)*, 2013, pp. 1–4.

[86] Q.-C. Zhong and G. Weiss, "Synchronverters: Inverters that mimic synchronous generators," *IEEE Transactions on Industrial Electronics*, vol. 58, no. 4, pp. 1259–1267, 2011.

[87] Q.-C. Zhong, P.-L. Nguyen, Z. Ma, and W. Sheng, "Self-synchronized synchronverters: Inverters without a dedicated synchronization unit," *IEEE Transactions on Power Electronics*, vol. 29, no. 2, pp. 617–630, 2014.

[88] S. V. Raghavan and R. Jayabarathi, "Simulation and analysis of power synchronization control for voltage source inverter," in *2017 Recent Developments in Control, Automation & Power Engineering (RDCAPE)*, 2017, pp. 348–353.

[89] Q. Fu, W. Du, C. Chen, H. F. Wang, and L. L. Fan, "Vector and power synchronization control for connecting a vsc-mtdc to an ac power system — a comparative study of dynamic interactions between the dc and ac network based on pscad simulation," in *12th IET International Conference on AC and DC Power Transmission (ACDC 2016)*, 2016, pp. 1–6.

[90] D. Remon, A. M. Cantarellas, E. Rakhshani, I. Candela, and P. Rodriguez, "An active power synchronization control loop for grid-connected converters," in *2014 IEEE PES General Meeting | Conference & Exposition*, 2014, pp. 1–5.

[91] D. Remon, W. Zhang, A. Luna, I. Candela, and P. Rodriguez, "Grid synchronization of renewable generation systems using synchronous power controllers," in *2017 IEEE 6th International Conference on Renewable Energy Research and Applications (ICRERA)*, 2017, pp. 169–174.

[92] D. Remon, A. M. Cantarellas, J. Martinez-Garcia, J. M. Escaño, and P. Rodriguez, "Hybrid solar plant with synchronous power controllers contribution to power system stability," in *2017 IEEE Energy Conversion Congress and Exposition (ECCE)*, 2017, pp. 4069–4076.

[93] E. Rakhshani, D. Remon, A. M. Cantarellas, J. M. Garcia, and P. Rodriguez, "Virtual synchronous power strategy for multiple hvdc interconnections of multi-area agc power systems," *IEEE Transactions on Power Systems*, vol. 32, no. 3, pp. 1665–1677, 2017.

[94] W. Zhang, D. Remon, J. Rocabert, A. Luna, J. I. Candela, and P. Rodriguez, "Frequency support properties of the synchronous power control for grid-connected converters," in *2016 IEEE Energy Conversion Congress and Exposition (ECCE)*, 2016, pp. 1–8.

[95] W. Zhang, D. Remon, A. Mir, A. Luna, J. Rocabert, I. Candela, and P. Rodriguez, "Comparison of different power loop controllers for synchronous power controlled grid-interactive converters," in *2015 IEEE Energy Conversion Congress and Exposition (ECCE)*, 2015, pp. 3780–3787.

[96] H. Han, X. Hou, J. Yang, J. Wu, M. Su, and J. M. Guerrero, "Review of power sharing control strategies for islanding operation of ac microgrids," *IEEE Transactions on Smart Grid*, vol. 7, no. 1, pp. 200–215, 2016.

[97] M. Chandorkar, D. Divan, and R. Adapa, "Control of parallel connected inverters in standalone ac supply systems," *IEEE Transactions on Industry Applications*, vol. 29, no. 1, pp. 136–143, 1993.

[98] J. Guerrero, L. G. de Vicuna, J. Matas, M. Castilla, and J. Miret, "Output impedance design of parallel-connected ups inverters with wireless load-sharing control," *IEEE Transactions on Industrial Electronics*, vol. 52, no. 4, pp. 1126–1135, 2005.

[99] G.-S. Seo, M. Colombino, I. Subotic, B. Johnson, D. Groß, and F. Dörfler, "Dispatchable virtual oscillator control for decentralized inverter-dominated power systems: Analysis and experiments," in *2019 IEEE Applied Power Electronics Conference and Exposition (APEC)*, 2019, pp. 561–566.

[100] B. B. Johnson, S. V. Dhople, A. O. Hamadeh, and P. T. Krein, "Synchronization of parallel single-phase inverters with virtual oscillator control," *IEEE Transactions on Power Electronics*, vol. 29, no. 11, pp. 6124–6138, 2014.

[101] B. B. Johnson, S. V. Dhople, J. L. Cale, A. O. Hamadeh, and P. T. Krein, "Oscillator-based inverter control for islanded three-phase microgrids," *IEEE Journal of Photovoltaics*, vol. 4, no. 1, pp. 387–395, 2014.

[102] Y. Li, Y. Gu, and T. Green, "Revisiting grid-forming and grid-following inverters: A duality theory," *IEEE Transactions on Power Systems*, pp. 1–1, 2022.

[103] X. Wang, M. G. Taul, H. Wu, Y. Liao, F. Blaabjerg, and L. Harnefors, "Grid-synchronization stability of converter-based resources—an overview," *IEEE Open Journal of Industry Applications*, vol. 1, pp. 115–134, 2020.

[104] P. Kundur, J. Paserba, V. Ajjarapu, G. Andersson, A. Bose, C. Canizares, N. Hatziargyriou, D. Hill, A. Stankovic, C. Taylor, T. Van Cutsem, and V. Vittal, "Definition and classification of power system stability ieee/cigre joint task force on stability terms and definitions," *IEEE Transactions on Power Systems*, vol. 19, no. 3, pp. 1387–1401, 2004.

[105] M. Zhao, X. Yuan, J. Hu, and Y. Yan, "Voltage dynamics of current control time-scale in a vsc-connected weak grid," *IEEE Transactions on Power Systems*, vol. 31, no. 4, pp. 2925–2937, 2016.

[106] N. Hatziargyriou, J. Milanovic, C. Rahmann, V. Ajjarapu, C. Canizares, I. Erlich, D. Hill, I. Hiskens, I. Kamwa, B. Pal, P. Pourbeik, J. Sanchez-Gasca, A. Stankovic, T. Van Cutsem, V. Vittal, and C. Vournas, "Definition and classification of power system stability – revisited & extended," *IEEE Transactions on Power Systems*, vol. 36, no. 4, pp. 3271–3281, 2021.

[107] M. Farrokhabadi, C. A. Cañizares, J. W. Simpson-Porco, E. Nasr, L. Fan, P. A. Mendoza-Araya, R. Tonkoski, U. Tamrakar, N. Hatziargyriou, D. Lagos, R. W. Wies, M. Paolone, M. Liserre, L. Meegahapola, M. Kabalan, A. H. Hajimiragha, D. Peralta, M. A. Elizondo, K. P. Schneider, F. K. Tuffner, and J. Reilly, "Microgrid stability definitions, analysis, and examples," *IEEE Transactions on Power Systems*, vol. 35, no. 1, pp. 13–29, 2020.

[108] X. Wang and F. Blaabjerg, "Harmonic stability in power electronic-based power systems: Concept, modeling, and analysis," *IEEE Transactions on Smart Grid*, vol. 10, no. 3, pp. 2858–2870, 2019.

[109] G. Gaba, S. Lefebvre, and D. Mukhedkar, "Comparative analysis and study of the dynamic stability of ac/dc systems," *IEEE Transactions on Power Systems*, vol. 3, no. 3, pp. 978–985, 1988.

[110] E. Unamuno, A. Rygg, M. Amin, M. Molinas, and J. A. Barrena, "Impedance-based stability evaluation of virtual synchronous machine implementations in converter controllers," in *2018 International Power Electronics Conference (IPEC-Niigata 2018 -ECCE Asia)*, 2018, pp. 759–766.

[111] F. Milano and A. Ortega Manjavacas, *Data*, 2020, pp. 271–290.

[112] J. Mahseredjian, V. Dinavahi, and J. A. Martinez, "Simulation tools for electromagnetic transients in power systems: Overview and challenges," *IEEE Transactions on Power Delivery*, vol. 24, no. 3, pp. 1657–1669, 2009.

[113] R. W. Kenyon, M. Bossart, M. Marković, K. Doubleday, R. Matsuda-Dunn, S. Mitova, S. A. Julien, E. T. Hale, and B.-M. Hodge, "Stability and control of power systems with high penetrations of inverter-based resources: An accessible review of current knowledge and open questions," *Solar Energy*, vol. 210, pp. 149–168, 2020, special Issue on Grid Integration. [Online]. Available: https://www.sciencedirect.com/science/article/pii/S0038092X20305442

[114] C. Collados-Rodriguez, M. Cheah-Mane, E. Prieto-Araujo, and O. Gomis-Bellmunt, "Stability analysis of systems with high vsc penetration: Where is the limit?" *IEEE Transactions on Power Delivery*, vol. 35, no. 4, pp. 2021–2031, 2020.

[115] F. Shahnia and A. Arefi, "Eigenanalysis-based small signal stability of the system of coupled sustainable microgrids," *International Journal of Electrical Power & Energy Systems*, vol. 91, pp. 42–60, 2017. [Online]. Available: https://www.sciencedirect.com/science/article/pii/S0142061516313369

[116] Z. Li and M. Shahidehpour, "Small-signal modeling and stability analysis of hybrid ac/dc microgrids," *IEEE Transactions on Smart Grid*, vol. 10, no. 2, pp. 2080–2095, 2019.

[117] D. Rimorov, J. Huang, C. F. Mugombozi, T. Roudier, and I. Kamwa, "Power coupling for transient stability and electromagnetic transient collaborative simulation of power grids," *IEEE Transactions on Power Systems*, vol. 36, no. 6, pp. 5175–5184, 2021.

[118] R. Venkatraman, S. K. Khaitan, and V. Ajjarapu, "Dynamic co-simulation methods for combined transmission-distribution system with integration time step impact on convergence," *IEEE Transactions on Power Systems*, vol. 34, no. 2, pp. 1171–1181, 2019.

[119] N. Watson and J. Arrillaga, *Power Systems Electromagnetic Transients Simulation*, ser. Energy Engineering. Institution of Engineering and Technology, 2019. [Online]. Available: https://books.google.com.co/books?id=whoJtgEACAAJ

[120] I. Caduff, U. Markovic, C. Roberts, G. Hug, and E. Vrettos, "Reduced-order modeling of inverter-based generation using hybrid singular perturbation," *Electric Power Systems Research*, vol. 190, p. 106773, 01 2021.

[121] "Impedance-based modelling of hybrid ac/dc grids with synchronous generator for interaction study and dynamic improvement," *Electric Power Systems Research*, vol. 179, p. 106086, 2020. [Online]. Available: https://www.sciencedirect.com/science/article/pii/S0378779619304055

[122] P. De Rua, Özgür Can Sakinci, and J. Beerten, "Comparative study of dynamic phasor and harmonic state-space modeling for small-signal stability analysis," *Electric Power Systems Research*, vol. 189, p. 106626, 2020. [Online]. Available: https://www.sciencedirect.com/science/article/pii/S0378779620304296

[123] L. Nagel, *SPICE2: A Computer Program to Simulate Semiconductor Circuits*, ser. Electronics Research Laboratory Berkeley, Calif: Memorandum. Electronics Research Laboratory, College of Engineering, University of California, 1975. [Online]. Available: https://books.google.com.co/books?id=a1FGAQAAIAAJ

[124] K. Strunz, E. Abbasi, R. Fletcher, N. Hatziargyriou, R. Iravani, and G. Joos, *TF C6.04.02 : TB 575 – Benchmark Systems for Network Integration of Renewable and Distributed Energy Resources*, 04 2014.

[125] J. Beerten, S. D'Arco, and J. A. Suul, "Identification and small-signal analysis of interaction modes in vsc mtdc systems," *IEEE Transactions on Power Delivery*, vol. 31, no. 2, pp. 888–897, 2016.

[126] J. Macias, A. Exposito, and A. Soler, "A comparison of techniques for state-space transient analysis of transmission lines," *IEEE Transactions on Power Delivery*, vol. 20, no. 2, pp. 894–903, 2005.

[127] J. O'Sullivan, A. Rogers, D. Flynn, P. Smith, A. Mullane, and M. O'Malley, "Studying the Maximum Instantaneous Non-Synchronous Generation in an Island System-Frequency Stability Challenges in Ireland," *IEEE Trans. Power Syst.*, vol. 29, no. 6, pp. 2943–2951, 2014.

[128] T. L. Vandoorn, J. D. M. De Kooning, B. Meersman, and L. Vandevelde, "Review of primary control strategies for islanded microgrids with power-electronic interfaces," *Renew. Sustain. Energy Rev.*, vol. 19, pp. 613–628, 2013. [Online]. Available: https://www.sciencedirect.com/science/article/pii/S1364032112006764

[129] J. M. Guerrero, J. C. Vasquez, and R. Teodorescu, "Hierarchical control of droop-controlled DC and AC microgrids - a general approach towards standardization," *2009 35th Annu. Conf. IEEE Ind. Electron.*, pp. 4305–4310, 2009.

[130] T. Jouini, C. Arghir, and F. Dörfler, "Grid-friendly matching of synchronous machines by tapping into the dc storage," *IFAC-PapersOnLine*, vol. 49, no. 22, pp. 192–197, 2016, 6th IFAC Workshop on Distributed Estimation and Control in Networked Systems NECSYS 2016. [Online]. Available: https://www.sciencedirect.com/science/article/pii/S2405896316319826

[131] B. B. Johnson, M. Sinha, N. G. Ainsworth, F. Dörfler, and S. V. Dhople, "Synthesizing virtual oscillators to control islanded inverters," *IEEE Transactions on Power Electronics*, vol. 31, no. 8, pp. 6002–6015, 2016.

[132] G.-S. Seo, M. Colombino, I. Subotic, B. Johnson, D. Groß, and F. Dörfler, "Dispatchable virtual oscillator control for decentralized inverter-dominated power systems: Analysis and experiments," pp. 561–566, 2019.

[133] O. Mo, S. D'Arco, and J. A. Suul, "Evaluation of virtual synchronous machines with dynamic or quasi-stationary machine models," *IEEE Transactions on Industrial Electronics*, vol. 64, no. 7, pp. 5952–5962, 2017.

[134] O. Saborío, "Small-signal modelling and stability analysis of a traditional generation unit and a virtual synchronous machine in grid- connected operation," 2015. [Online]. Available: https://brage.bibsys.no/xmlui/bitstream/handle/11250/2368222/12531{_}FULLTEXT.pdf?sequence=1{&}isAllowed=y

[135] N. Pogaku, M. Prodanovic, and T. C. Green, "Modeling, analysis and testing of autonomous operation of an inverter-based microgrid," *IEEE Transactions on Power Electronics*, vol. 22, no. 2, pp. 613–625, 2007.

[136] A. Tayyebi, D. Groß, A. Anta, F. Kupzog, and F. Dörfler, "Frequency stability of synchronous machines and grid-forming power converters," *IEEE Journal of Emerging and Selected Topics in Power Electronics*, vol. 8, no. 2, pp. 1004–1018, 2020.

[137] Y. Lin, B. Johnson, V. Gevorgian, V. Purba, and S. Dhople, "Stability assessment of a system comprising a single machine and inverter with scalable ratings," in *2017 North American Power Symposium (NAPS)*, 2017, pp. 1–6.

[138] M. M. Siraj Khan, Y. Lin, B. Johnson, M. Sinha, and S. Dhople, "Stability assessment of a system comprising a single machine and a virtual oscillator controlled inverter with scalable ratings," in *IECON 2018 - 44th Annual Conference of the IEEE Industrial Electronics Society*, 2018, pp. 4057–4062.

[139] D. Pan, X. Wang, F. Liu, and R. Shi, "Transient Stability of Voltage-Source Converters With Grid-Forming Control: A Design-Oriented Study," *IEEE J. Emerg. Sel. Top. Power Electron.*, vol. 8, no. 2, pp. 1019–1033, 2020.

[140] L. Huang, H. Xin, Z. Wang, K. Wu, H. Wang, J. Hu, and C. Lu, "A Virtual Synchronous Control for Voltage-Source Converters Utilizing Dynamics of DC-Link Capacitor to Realize Self-Synchronization," *IEEE J. Emerg. Sel. Top. Power Electron.*, vol. 5, no. 4, pp. 1565–1577, 2017.

[141] Q.-C. Zhong, P.-L. Nguyen, Z. Ma, and W. Sheng, "Self-Synchronized Synchronverters: Inverters Without a Dedicated Synchronization Unit," *IEEE Trans. Power Electron.*, vol. 29, no. 2, pp. 617–630, 2014.

[142] I. Cvetkovic, D. Boroyevich, R. Burgos, C. Li, and P. Mattavelli, "Modeling and control of grid-connected voltage-source converters emulating isotropic and anisotropic synchronous machines," *2015 IEEE 16th Work. Control Model. Power Electron.*, pp. 1–5, 2015.

[143] C. Arghir and F. Dörfler, "The Electronic Realization of Synchronous Machines: Model Matching, Angle Tracking, and Energy Shaping Techniques," *IEEE Trans. Power Electron.*, vol. 35, no. 4, pp. 4398–4410, 2020.

[144] C. Arghir, T. Jouini, and F. Dörfler, "Grid-forming control for power converters based on matching of synchronous machines," *Automatica*, vol. 95, pp. 273–282, 2018. [Online]. Available: https://www.sciencedirect.com/science/article/pii/S0005109818302796

[145] M. Colombino, D. Groß, J.-S. Brouillon, and F. Dörfler, "Global Phase and Magnitude Synchronization of Coupled Oscillators With Application to the Control of Grid-Forming Power Inverters," *IEEE Trans. Automat. Contr.*, vol. 64, no. 11, pp. 4496–4511, 2019.

[146] S. D'Arco, J. A. Suul, and O. B. Fosso, "Automatic tuning of cascaded controllers for power converters using eigenvalue parametric sensitivities," *IEEE Transactions on Industry Applications*, vol. 51, no. 2, pp. 1743–1753, 2015.

[147] J. Wang, Y. Wang, Y. Gu, W. Li, and X. He, "Synchronous frequency resonance of virtual synchronous generators and damping control," in *2015 9th International Conference on Power Electronics and ECCE Asia (ICPE-ECCE Asia)*, 2015, pp. 1011–1016.

[148] B. K. Poolla, D. Groß, and F. Dörfler, "Placement and implementation of grid-forming and grid-following virtual inertia and fast frequency response," *IEEE Transactions on Power Systems*, vol. 34, no. 4, pp. 3035–3046, 2019.

[149] M. S. Golsorkhi and D. D. Lu, "A decentralized power flow control method for islanded microgrids using V-I droop," *22nd Iran. Conf. Electr. Eng. ICEE 2014*, no. Icee, pp. 604–609, 2014.

[150] D. Duckwitz and B. Fischer, "Modeling and Design of df/dt -Based Inertia Control for Power Converters," *IEEE J. Emerg. Sel. Top. Power Electron.*, vol. 5, no. 4, pp. 1553–1564, 2017.

[151] Z. Ahmad, J. Rueda, N. Kumar, E. Rakhshani, P. Palensky, and M. Meijden, "A power hardware-in-the-loop based method for fapr compliance testing of the wind turbine converters control," *Energies*, vol. 13, 10 2020.

[152] N.-B. Lai, A. Tarraso, G. Baltas, L. V. Marin Arevalo, and P. Rodriguez, "External Inertia Emulation Controller for Grid-following Power Converter," *IEEE Trans. Ind. Appl.*, vol. 9994, no. c, pp. 1–1, 2021.

[153] M. S. Alam, F. S. Al-Ismail, A. Salem, and M. A. Abido, "High-level penetration of renewable energy sources into grid utility: Challenges and solutions," *IEEE Access*, vol. 8, pp. 190 277–190 299, 2020.

[154] T. Kerdphol, F. S. Rahman, M. Watanabe, Y. Mitani, D. Turschner, and H.-P. Beck, "Enhanced virtual inertia control based on derivative technique to emulate simultaneous inertia and damping properties for microgrid frequency regulation," *IEEE Access*, vol. 7, pp. 14 422–14 433, 2019.

[155] J. A. Suul, K. Ljokelsoy, and T. Undeland, "Design, tuning and testing of a flexible PLL for grid synchronization of three-phase power converters," in *2009 13th Eur. Conf. Power Electron. Appl.*, 2009, pp. 1–10.

[156] P. Anderson, A. Fouad, I. of Electrical, E. Engineers, and I. P. E. Society, *Power System Control and Stability*, ser. IEEE Press power engineering series Power system control and stability. Wiley, 2003. [Online]. Available: https://books.google.es/books?id=8-xSAAAAMAAJ

[157] C. Bajracharya, M. Molinas, J. Suul, and T. Undeland, "Understanding of tuning techniques of converter controllers for vsc-hvdc," 06 2008.

[158] Eider Robles Sestafe, “Grid connection and control of multipole synchronous wind turbines,” Ph.D. dissertation, Universidad del País Vasco, 2010.